Vortex induced vibrations of free span pipelines

A thesis submitted in fulfillment of the
requirements for the degree of
doctor philosophia
by

Kamran Koushan

Centre for Ships and Ocean Structures (CeSOS)
Norwegian University of Science and Technology (NTNU)

Trondheim (2009)

Abstract

Pipelines from offshore petroleum fields must frequently pass over areas with uneven seafloor. In such cases the pipeline may have free spans when crossing depressions. Hence, if dynamic loads can occur, the free span may oscillate and time varying stresses may give unacceptable fatigue damage. A major source for dynamic stresses in free span pipelines is vortex induced vibrations (VIV) caused by steady current. This effect is in fact dominating on deep water pipelines since wave induced velocities and accelerations will decay with increasing water depth. The challenge for the industry is then to verify that such spans can sustain the influence from the environment throughout the lifetime of the pipeline.

The aim of the present project is to improve the understanding of vortex induced vibrations (VIV) of free span pipelines, and thereby improve methods, existing computer programs and guidelines needed for design verification. This will result in more cost effective and reliable offshore pipelines when laid on a very rugged seafloor.

VIV for multiple span pipeline is investigated and the dynamical interaction between adjacent spans has been shown. The interaction may lead to increased or decreased response of each spans depending on the current speed and the properties for the two spans. The extension of the contact zone between the spans and seafloor parameters will of course also be important for the interaction effect.

The influence from temperature variation on vortex induced vibrations has been demonstrated. The response frequency is influenced through changes in pipe tension and sag. Both increase and decrease of the response frequency may be experienced. Moreover, it is shown that the influence from snaking of the pipe on the temperature effect is small, at least for large diameter pipes.

A free span pipeline will necessarily oscillate close to the seabed. The presence of the seabed will therefore have some influences on the ambient flow profile and also on the flow pattern around the cylinder during oscillation. Hydrodynamic pa-

rameters may therefore vary when the pipe is close to the seabed. In the present work, the influence from spatial varying current profiles is investigated for both single and multiple span pipeline. It is shown that the difference between using uniform and spatial varying current profiles is significant for some current speeds. It is also shown that use of spatial varying current profiles can be even more important for multiple span pipeline.

The comparison of VIVANA analysis results with MARINTEK test results has been given. It shows VIVANA predicts the cross-flow response generally much higher than the test measurements, especially for the higher mode responses. To improve understanding of this phenomena, the VIVANA model was tuned to the test model and results are compared in different cases. Attempts were made to obtain a better agreement by adjusting some of the input parameters to VIAVANA. The reference point is tuned by changing various hydrodynamic properties, i.e. C_L, St and added mass. The response frequencies are also tuned in order to have a better agreement on the results. It is been concluded that the method used here by VIVANA is not able to describe VIV for free spanning pipelines adequately. It is not possible to find a set of parameter in a rational way that will give reasonably correct results. The discrepancy between the analysis and test results are highlighted which confirms the interaction between the in-line and cross-flow vibrations. Discussions are given and addressed on different reasons which may cause this phenomena.

An improved strategy for non-linear analysis of free span pipeline is outlined. Time domain analysis for free span pipeline has been performed. The difference between time and frequency domain analysis has also been investigated by varying boundary conditions, pipe properties and axial tension. A significant difference is shown between results from time and frequency domain analysis at each end of the span where the pipe is started to interact with the seafloor. Due to high fatigue at this point, the importance of using non-linear time domain analysis is therefor obvious and highly recommended.

Acknowledgements

I would like to gratefully appreciate my supervisor Professor Carl Martin Larsen for his support during this study. His much knowledge in the area of Marine technology and specially in VIV was always highly accessible to me. I wish also to thank him for his help for providing me with a scholar-ship on my Ph.D. program and valuable comments and many good ideas and advices patiently given during this thesis.

I wish to appreciate Dr. Kourosh Koushan, Research director of MARINTEK Ship technology, for his great support and encouragement. Without his kind help this Ph.D. was not possible. I was also inspired by his nice family during my Ph.D. study.

I wish to give a special thank to Professor Odd M. Faltinsen for his great soul and attitude. His support and encouragement made this Ph.D. to be happened. He has always been a great help to me.

I would like to thank Professor Jørgen Juncher Jensen, Denmark Technical University, for his good comments on my thesis. I want also to thank Professor Finn Gunnar Nielsen for his support for providing me with the scholar-ship and his good comments given on my thesis.

I shall acknowledge Norsk Hydro for granting the scholar-ship on some part of my Ph.D. program. I joined CeSOS at the last year of my study in NTNU. Their nice academic atmosphere and also their financial support is gratefully acknowledged.

Finally, I would like to thank my good company FMC Technologies for giving me the opportunity to finalize and defend my thesis.

At last, but not least many thanks are extended to my parents for everything I have, and to my lovely wife Mrs. Sheida Sherkat for her much understanding, encouragement and patient during this thesis. Happy ending of this thesis coincided with the birth of my little girl Melina who made my life full of love!

Nomenclature

General

- Symbols are generally defined where they appear in the text for the first time.
- Only the most used symbols are listed in the following section.
- Symbols and identifiers are kept unique, as far as practical.
- Over-dots signify differentiation with respect to time.

Roman symbols

A	Displacement amplitude, Cross section area
(A/D)	Non-dimensional amplitude
$(A/D)_0$	Non-dimensional amplitude when $C_L = 0$
$(A/D)_{max}$	Maximum non-dimensional amplitude
A_x	Oscillation amplitude in in-line vibration
A_y	Oscillation amplitude in cross-flow vibration
$a_{(n)}$	Amplitude
C	Total damping
C_a	Added mass coefficient
C_B	Damping matrix for pipe/seafloor interaction
C_{cr}	Critical damping coefficient
C_D	Drag coefficient in the flow direction
$C_{D_{osc}}$	Oscillating drag coefficient in the flow direction
C_d	Drag coefficient (quadratic) in the cross-flow direction
$\bar{C}_d$	mean drag coefficient

C_H	Hydrodynamic damping matrix
C_L	Lift force coefficient
C_{L_T}	Total lift force coefficient
$\bar{C}_L$	Mean Lift force coefficient
$C_{L,0}$	Lift coefficient when $A = 0$
$C_{L_{A_0}}$	Lift coefficient in phase with acceleration
$C_{L,max}$	Maximum lift coefficient
$C_{L_{V_0}}$	Lift coefficient in phase with velocity
C_n	n^{th} damping coefficient
C_{M_0}	Normalized added mass
C_s	Structural damping coefficient
D	Cylinder diameter
D_i	External diameter of pipe
D_0	Internal diameter of pipe
dt	Time step
E	Young's modulus
E_s	Young's modulus of soil
F	Force
$\bar{F}$	Mean force
F_0	Amplitude value of force
F_D	Drag force
F_H	Resultant force
F_v,F_L	Lift force
$\bar{F}_L$	Mean lift force
f	Frequency, $\frac{1}{T}$
$\hat{f}$	Non-dimensional frequency, $\frac{fD}{U}$
$\hat{f}_{min}$	Minimum non-dimensional frequency
$\hat{f}_{max}$	Maximum non-dimensional frequency
f_0	Natural frequency in still water
f_{0i}	Eigen frequency by using still water values for added mass, mode i
f_{air}	Natural frequency in air
f_n	Natural frequency
f_{osc}	Oscillation frequency
f_{v_0}	Vortex shedding frequency
f_{true}	Natural frequency computed including added mass
$f_{(resp)}$	Response frequency found from added mass iteration in VIVANA

G	Shear modulus
g	Gravity constant 9.81 m/s^2
H	Depth of the pipe below the water surface
I	Cross section moment of inertia
i	Used in subscripts to indicate different numbers
K	Stiffness matrix, Curvature
KC	Keulegan-Carpenter number
K_s	Reduced damping parameter
k	Size of roughness
$\bar{k}$	Modal stiffness
k_s	Soil stiffeness
L, l	Length, Span length
L_{corr}	Displacement amplitude
M	Mass
M	Mass matrix
m	Mass per unit length
M_{A_0}, m_a	Added mass
M_b	Bending moment
M_H	Hydrodynamical mass
M_s	Structural mass
m_{dry}	Dry mass, i.e. total mass without added mass
m_{wet}	Wet mass, i.e. total mass with added mass
N	A number
N_s	Number of excitation frequencies
n	Integer number, mode number, normal vector
n_{osc}	Number of oscillation
p	Pressure
p_0	Hydrostatic pressure
Q	Transverse shear load
q	Submerged weight
$\bar{q}$	Weight per unit length
q_p	Lateral pressure load
R	Excitation matrix, Radius of curvature
R_e	Reynolds number, $\frac{UD}{\nu}$
r	Displacement matrix
r	Displacement, time domain

$\dot{r}$	Velocity, time domain
$\ddot{r}$	Acceleration, time domain
St_G	Strouhal number in Gopalkrishnan's tests
St	Strouhal number, $\frac{f_v D}{U}$
T	Oscillatory period
t	Time
T	Tension
T_{nl}	Non-linear sag tension
t	Time variable
U	Flow velocity, Stream velocity
U_r	Reduced flow velocity, $\frac{U}{f_0 D}$
$U_{r_{true}}$	True reduced velocity, $\frac{U}{f_{osc} D}$
u	Local fluid velocity component in x direction
V	Current speed
X_ω	Complex load vector, frequency domain
x_ω	Complex displacement vector, frequency domain
x	x-coordinate in a global coordinate system
x_i	x-coordinate in a local coordinate system
Y_{max}	Maximum value of the mode shape
z	Height
z_b	Water depth

Greek symbols

α	Thermal expansion coefficient, Phase angle
β	Phase angle
δ	Logarithmic decrement
δ	Boundary layer thickness
δ^*	Displacement thickness
$\delta_{0.99}$	Thickness parameter
ε	Strain
ε_{nl}	Non-linear strain
ζ	Modal damping ratio
ζ_{str}	Modal structural damping ratio
η	Similarity parameter
θ	Angle on the cylinder, Momentum thickness
μ	Viscosity

ν	Kinematic viscosity, $\frac{\mu}{\rho}$
ν_s	Poisson's ratio of soil
π	3.14159265...
ρ	Density of water, 1000 kg/m^3
ρ_s	Density of the cylinder
ρ_c	Density of the coating
ρ_i	Density of contents
ρ_w	Density fluid flow
σ	Material stress
τ	Shear stress
Φ_n	Mode shape
ϕ	Velocity potential
$\omega, \omega_i, \omega_n$	Circular frequency, 2π
ω_s	Vortex shedding frequency

Mathematical operators

∇	Gradient operator
∇^2	Laplace operator
Σ	Summation

Abbreviations

$2D$	Two dimensional
$3D$	Three dimensional
AM	Added mass
AR	Arbitrary
Bot	Bottom
CF	Cross-flow
CFD	Computational Fluid Dynamics
$cf.$	Refer to
cm	Centimeter
DNV	Det Norske Veritas
$e.g.$	Exempli gratia (eng: for example)
FEM	Finite Element Method

$i.e.$	Id est (eng: that is)
IL	In line
kg	Kilogram
kN	Kilo Newton
m	Meter
max	Maximum value
min	Minimum value
MIT	Massachusetts Institute of Technology
MPa	Mega Pascal
N	Newton
NTH	The Norwegian Institute of Technology (NTNU at present)
$NTNU$	Norwegian University of Science and Technology
$RIFLEX$	Static and dynamic analysis program for slender marine structures
rad	Radians
rms	Root Mean Square
SD	Standard deviation
$Temp$	Temperature
VIV	Vortex induce vibration
$VIVANA$	Vortex induced vibrations analysis program

Contents

List of Figures

List of Tables

Chapter 1

Introduction

1.1 Background and motivation

Pipelines from offshore petroleum fields must frequently pass over areas with uneven seafloor. One of the serious problems for the structural safety of pipelines is uneven areas in the seafloor as they enhance the formation of free spans. Route selection, therefore, plays an important part in design, Matteelli (1982). However, due to many obstacles it is difficult to find a totally obstruction free route. In such cases the pipeline may have free spans when crossing depressions. Hence, if dynamic loads can occur, the free span may oscillate and time varying stresses may give unacceptable fatigue damage. A major source for dynamic stresses in free span pipelines is vortex induced vibrations (VIV) caused by steady current. This effect is in fact dominating on deep water pipelines since wave induced velocities and accelerations will decay with increasing water depth. The challenge for the industry is then to verify that such spans can sustain the influence from the environment throughout the lifetime of the pipeline.

The aim of the present project is to improve the understanding of vortex induced vibrations (VIV) of free span pipelines, and thereby improve methods, existing computer programs and guidelines needed for design verification. This will result in more cost effective and reliable offshore pipelines when laid on a very rugged seafloor.

The Ormen Lange field in the Norwegian Sea is one of the examples where the pipeline will have a large number of long spans even for the best possible route (see Figure 1.1). It was decided to evaluate two different strategies for field devel-

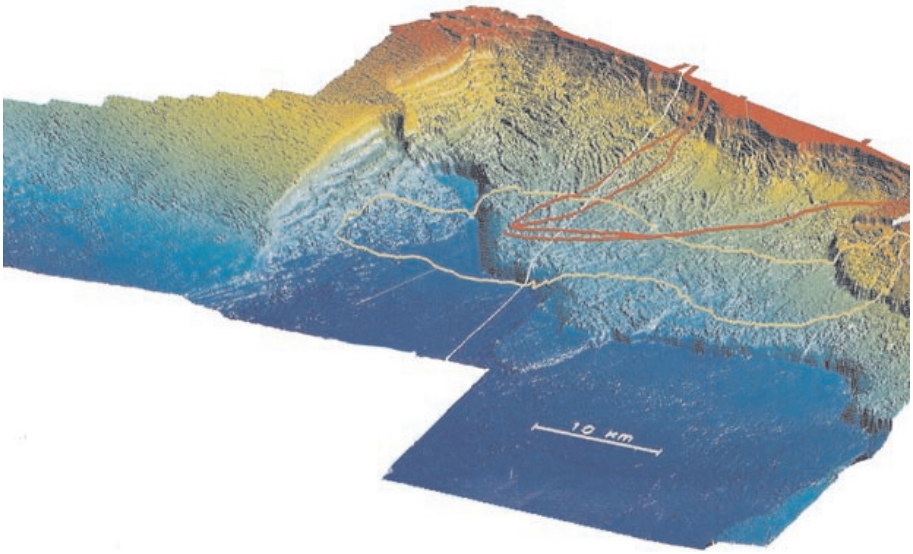

Figure 1.1: 3D map of the slope, showing the Storegga slide, (Norsk Hydro)

opment; one based on offshore loading and the other on a pipeline to an onshore gas terminal. A key problem for the last alternative is that the seafloor between these fields and the coast is extremely rugged meaning that a pipeline must have more and longer free spans than what is seen for conventional pipelines. Today's knowledge and guidelines are inadequate for obtaining a cost effective and reliable pipeline under these conditions, Det Norske Veritas (1998). Significant uncertainties are related to the assessment of fatigue from vortex induced vibrations caused by ocean currents. An extensive research program has therefore been initiated. The aim has been to improve the understanding of VIV for free span pipelines and thereby identify potential unnecessary conservatism in existing guidelines. Some changes have been proposed by Det Norske Veritas (2002), but improved analysis models have not been developed so far.

Two alternative strategies for calculation of VIV are seen today. Practical engineering is still based on empirical models, while use of computational fluid dynamics (CFD) is considered immature mainly because of the needed computing resources. Most empirical models are based on frequency domain dynamic solutions and linear structural models Larsen (2000), but the free span pipeline case has indeed important nonlinearities that should be taken into consideration. Both tension variation and pipe-seafloor interaction will contribute to non-linear behavior, which means that most empirical models will have significant limitations when dealing with the free span case. CFD models may certainly be linked to a non-linear structural

model, but the needed computing time will become overwhelming. Then, one of the main focuses of the present research is investigation about time domain model for analysis of vortex induced vibrations for free span pipelines and the other is about multi free span pipelines where neighbor spans may interact dynamically. The interaction will depend on the length and stiffness of the pipe resting on the sea floor between the spans, and sea floor parameters such as stiffness, damping and friction. Each of them has important issues to investigate for improvement of our VIV knowledge.

Work on various aspects of slender marine structures has been going on at MARINTEK and Department of marine technology, NTNU for three decades. During the last ten years focus has been on vortex induced vibrations. Two commercial computer programs serve for the present project:

- **RIFLEX**
  a general finite element program for static and dynamic analysis of slender marine structures. The program can perform linear and non-linear dynamic analysis, and both frequency and time domain analysis are possible. Dynamic loads form waves can be considered, but RIFLEX has no capability to handle vortex induced vibrations.
- **VIVANA**
  a program for calculating vortex induced vibrations of marine risers and pipelines in current. The program applies a frequency domain method for dynamic analysis and is limited to predict oscillations perpendicular to the fluid flow direction. The reason why a frequency domain procedure is employed is that all data related to VIV are known on a frequency format and not easily transferable to time domain.

Some VIV experiments were conducted in MARINTEK in order to investigate the interaction between cross-flow (CF) and in-line (IL) response on free span pipelines. The results showed much reduction in CF response than expected. More investigations on these results and comparison of them with a VIV software tool such as VIVANA is obviously important.

Moreover, an important feature of the free span pipeline problem is that there are important non-linearities that will influence the dynamic behaviour. Such effects are:

- Coupling between dynamic response and pipe tension will alter the lateral stiffness and hence influence the eigenfrequency of the pipe.
- Contact between the pipe and seafloor will vary during vertical (out of the current plane) oscillations, meaning that the boundary conditions of the sus-

pended pipe will vary in time. The soil stiffness that determines this interaction is in general non-linear, and hysteresis effects will also contribute to damping.

- Interaction in terms of friction and non-linear stiffness between the pipe and seafloor during horizontal (in current plane) oscillations will lead to a "stick and slide" behaviour that is strongly non-linear with a significant damping contribution.

These non-linearities can be taken into account in a time domain analysis as implemented in RIFLEX, but can not be adequately represented in a VIVANA type of frequency domain method. The ideal situation is hence to combine the two programs.

1.2 Framework and scope of the present analysis

The project was divided into the following tasks:

- **Multiple free span pipeline:**

  Investigate the dynamical interaction between adjacent spans and influence on response amplitudes from this interaction. Some case studies including the analysis of double spans and comparing the results with single span pipelines are reported.

- **Temperature variation:**

  Investigate the influence from temperature variation of the internal flow on eigen and response frequency of free span pipeline. Perform some case studies to see this influence on a straight lined and curved pipeline.

- **Spatial current profile variation:**

  Compare the response from a uniform current profile and the response from a more realistic profile found by taking boundary layer effects into account.

- **Comparison between analysis and experiment:**

  Compare the results from VIVANA analyses and MARINTEK experiments. Discuses the differences and give some cases studies for a better interpretation of the results.

- **Combined time and frequency domain analysis:**

  Study time and frequency domain models and explore the potential by combing the two. Moreover, investigate the effect from laying conditions, seafloor properties and pipeline parameters by use of time and frequency domain analysis.

1.2.1 Multiple span pipeline

The irregular nature of seafloor topography and randomness of scouring, can create a wide variety of possible span geometries. However, in situations of multiple span configurations, in which adjacent spans are located in sufficiently close proximity of each other, care must be performed. Each span may not be considered individually, but rather the entire system of spans must be analyzed as a unit. Moreover, there might be some dynamic interaction between the adjacent spans. This case is often referred to as a multiple free span pipeline. If two adjacent spans have different length, tension or sag, VIV on one span might be influenced by the other. The amplitude of one span may become amplified or damped because of this interaction. This is of course depending on the length of each spans and the length of the contact zone between two spans.

1.2.2 Temperature variation

The influence from temperature variation of the internal flow on vortex induced vibrations has also been demonstrated in the present work. Varying temperature will change the stress-free length of a pipeline. Sag and tension in a free span will hence be influenced, but this influence will be controlled by the initial geometry of the pipe on the seafloor close to the free span, and the interaction forces between the pipe and the sea-floor. If the on-bottom pipe has a straight lined shape, the length variation from change of temperature will most likely accumulate in the free span and change sag and tension. If the pipe has a snaked geometry the length variation may be taken by a change of the horizontal projection instead of being accumulated in the sag.

1.2.3 Spatial current profile variation

A free span pipeline will necessarily oscillate close to the seabed. The seabed will therefore have some influences on the ambient flow profile and also on the flow pattern around the cylinder during oscillation. Hydrodynamic parameters can be

varied when the pipe is closing the seabed. Some researchers have worked on this topic and done some experiments such as Greenhow (1987) and Sumer (1994), but more data are still needed. In the present work, the influence from spatial varying current profile in comparison with uniform current is researched, but the influence from seafloor proximity on hydrodynamic coefficients has not been studied.

1.2.4 Comparison between analysis and experiment

To improve the understanding of multi modal and multi span VIV some experiments were conducted in MARINTEK in connection with the Ormen Lange pipeline project. The tests clearly proved the VIV response mode interactions resulted in major reduction in cross flow amplitudes.

VIVANA have been used to compare theses results with the program tools. Program showed the results are much higher than the test measurements. Some case studies have been performed to give a better understandings and explain these differences.

1.2.5 Combined time and frequency domain analysis

The use of a new method for VIV analysis of free span pipelines is shown in this thesis. The basic idea of this method is to use the results from a linear frequency domain model to identify key parameters in a non-linear time domain model that can account for varying contact conditions at the shoulders of the free span pipelines. Since fatigue damage is high at these shoulders, the importance of using non-linear time domain analysis is obvious and highly recommended.

1.3 Contributions of the thesis

Det Norske Veritas (1998) released a code for free span pipelines but was still needed to be improved by understanding more about the behaviour of the pipeline in a steady current regarding vortex induced vibrations and the pipe/soil interaction when this Ph.D. project was started. Note that Det Norske Veritas (2006) released a more complete code for free span pipelines at the end of this study.

The contribution of this present research is to understand more about this behaviour, and since the nature of vortex induced vibration is dynamical, one of the main consequences is to control the fatigue damage of free span pipelines.

According to what previously explained, three main topics are considered in the present research:

- Characterization and analysis of multiple free spans.
- The influence from space varying current and temperature fluctuations.
- Comparison of the analysis results with MARINTEK test measurements.
- The application of non-linear time domain analysis for vortex induced vibrations.

The method and coding was carried out as a MARINTEK project and published by Larsen, Koushan and Passano (2002). Investigating of snaking/temperature effects has been published by Koushan and Larsen (2003), study of the shoulder effect as a joint work by Larsen, Passano, Barholm and Koushan (2004) and also Larsen and Koushan (2005). This thesis explores the methods and potentials more in detail.

1.4 Outline of thesis

This thesis is divided in 7 chapters as follow:

- **Chapter 2:**
  Deals with the 2D cases, meaning a rigid, flexibly supported cylinder that may move in cross-flow, in-line or cross-flow and in-line directions. Describes the theory of flow induced vibrations and presents flow field, dimensionless flow and structural parameters, free and forced oscillation experiments, vortex induced excitation forces and a brief discussion on some experimental studies. Furthermore, gives the methods of VIV suppression.
- **Chapter 3:**
  Explains the theory on flexible beams. Presents the theory of vortex induced vibrations more in detail and describes the analysis procedure, VIVANA and the models and theory applied in this program.
- **Chapter 4:**
  Presents some case studies and describes multiple free span pipelines and gives more studies about the dynamical interaction between neighbor spans where the results from the analyses of double spans compared with the results from single span pipelines including the comparison of eigen- response frequencies.

Further, gives the description of spatial current profiles. Shows the results from some case studies and compared these results with those from uniform current profile. The influence from temperature variation is also described and the results from a straight lined and non-straight lined free span pipeline are discussed.

- **Chapter 5:**
  Presents comparison between analysis and experiment. In this chapter the results from MARINTEK tests on Ormen Lange project have been compared with the VIVANA results. Some case studies are given to improve the understanding of the difference between the results. The results are tuned in VIVANA to be more comparable with the tests on different cases. Discussions are given and addressed on the reasons causing the discrepancies between the results.

- **Chapter 6:**
  Discusses in detail time and frequency domain analysis and gives an outline of the analysis approach. Further, introduce the new strategy in time domain analysis and discovers its potentials. Moreover, shows the features of nonlinearity effects in free span pipeline by variation of boundary conditions, pipe properties and axial tension. Give the discussion and comparison of the results by using some case studies at the end.

- **Chapter 7:**
  Gives a summary on the conclusions from research findings. Also used to recommend further works following the work performed during this thesis.

Chapter 2

Introduction to vortex induced vibrations

A lot of researches have been done during the last century in the area of steady flow past a bluff body and hydroelastic problem due to flow induced vibration. One of the earliest contributions to this field was the recognition of the importance of the Reynolds number in describing the flow, Stokes (1851) and Reynolds (1883). Strouhal (1878) found the relation between the flow velocity, diameter and frequency of vortex shedding for a tensioned string. Further, the concept of the boundary layer due to viscous action and the consequent development of the theory of vortex street investigated by Prandtl (1904) and Karman (1912) respectively. The result of these investigations were at utmost importance in understanding of fluid/structure interaction problems. In the recent years, significant contributions to this field have made by Sarpkaya and Isaacson (1981), Sarpkaya (1977), Dean and Wooten (1977), King (1977), Blevins (1997) and Griffin (1980).

2.1 Vortex shedding

Vortex shedding is a result of the basic instability which exists between the two free shear layers released from the separation points at each side of the cylinder into the downstream flow from the separation points. These free shear layers roll-up and feed vorticity and circulation into large discrete vortices which form alternately on opposite sides of the generating cylinder. At a certain stage in the growth cycle of the individual vortex, it becomes sufficiently strong to draw the other free shear layer with its opposite signed vorticity across the wake. This action cuts off further

supply of vorticity to the vortex which ceases to grow in strength and is subsequently shed into the downstream flow. The process then repeats itself on the opposite side of the wake resulting in regular alternate vortex shedding, see Figure 2.1, J P Kenny (1993).

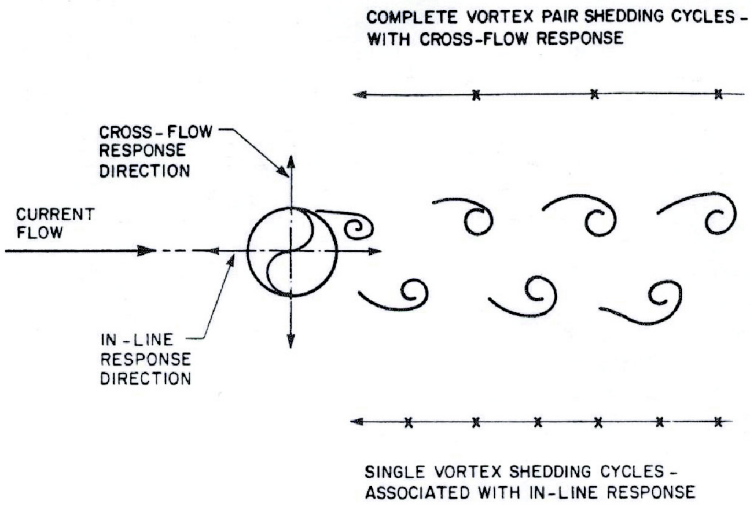

Figure 2.1: Staggered alternate vortex shedding - in-line and cross-flow response, J P Kenny (1993)

2.1.1 Flow field

The relation between the pressure gradient and acceleration in an incompressible inviscid fluid is demonstrated in Bernoulli equation

$$\rho\frac{\partial\phi}{\partial t} + p + \frac{1}{2}\rho U^2 + \rho g z = constant \tag{2.1}$$

where U is the fluid velocity, p is the pressure, ρ is the fluid density, g is acceleration of gravity and z is the height. For a stationary flow the above equation reduces to a more simple equation since the first term is equal to zero, $\partial\phi/\partial t = 0$ and the last term, $\rho g z$ is the static pressure and also in comparison with the other terms is neglected, then

$$p + \frac{1}{2}\rho U^2 = constant \tag{2.2}$$

The tangential velocity of particle on a stationary cylinder in uniform flow can be given by using potential theory, e.g. White (1991), as follow

$$u_t = -2U \sin\theta \tag{2.3}$$

here U is the free stream velocity and θ is the angle on the cylinder (see Figure 2.2). Therefore, by using Equation 2.1, the pressure distribution on the cylinder surface is given by

$$p = \frac{1}{2}\rho U^2 - 2\rho U^2 \sin^2\theta + p_0 \tag{2.4}$$

Using this equation shows the pressure distribution is symmetrical. Furthermore, the integrating of pressure around the cylinder surface will result to a net force equal to zero and confirm the so called d'Alembert's paradox which states that a body in an inviscid fluid, i.e. $\nabla^2\phi = 0$ has zero drag.

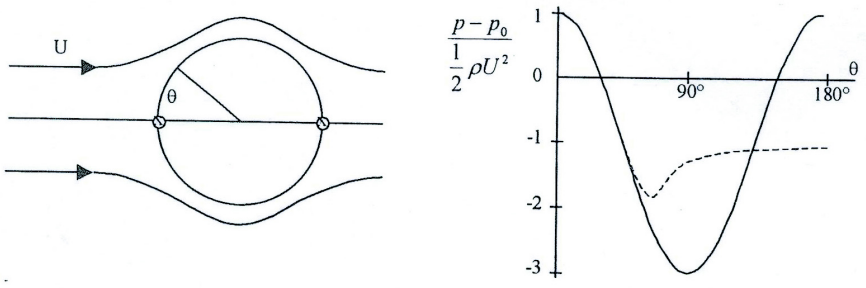

Figure 2.2: Flow and pressure distribution around a circular cylinder, — ideal fluid, - - experiments, stagnation point at $\theta = 0°$ and 180°, (Pettersen 1999)

Consideration of the flow as a potential flow or irrotational flow neglecting the viscous shear is not the actual situation that normally is found in reality. Flow retardation due to viscous action close to the surface of the cylinder leads to the development of a boundary layer on it.

2.1.2 Boundary layer

Schlichting (1987) and earlier than him, Prandtl (1904) have done many efforts for investigation on boundary layer theory. Prandtl (1904) divided the flow around the body into two regions:

- As a result of viscous friction a thin boundary layer is formed at the solid walls. The velocity of the flow is increased from zero at the body surface to the free flow with distance from the body surface. The fluid viscosity cannot be neglected in comparison with the *thickness*, δ of the boundary layer, even it is extremely small.
- The flow treated as inviscid (the viscosity may be neglected) in other regions outside the boundary layer.

The smaller the viscosity, the thinner is the boundary layer. Furthermore, according to Newman (1977), the boundary layer as seen in Figure 2.3 is the thin layer in which the flow velocity varies from the free stream value to zero at the wall where fluid adheres to the boundary. The velocity profile is uniform at the upstream of the plate, whereas the development of the boundary layer at downstream is apparent (see Figure 2.3). The boundary layer with a function proportional to $x^{1/2}$ grows in lateral direction. The outer limit of the boundary layer is defined by *thickness parameter*, $\delta_{0.99}$ which is defined as

$$u(\delta_{0.99}) = 0.99\, U_\infty \tag{2.5}$$

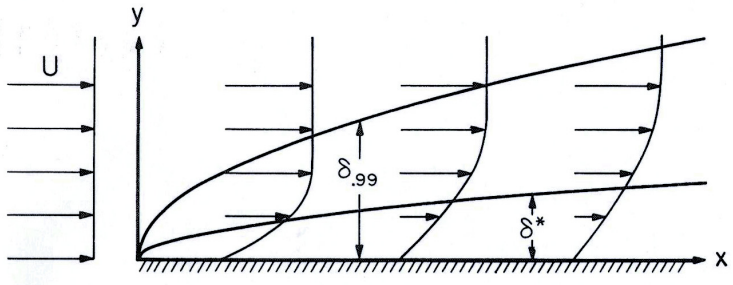

Figure 2.3: Development of laminar boundary layer along a flat plate, the lateral scale is magnified, (Newman 1977)

The *displacement thickness* is an alternative definition of the boundary layer thickness and defined as a region of width equal to the retardation of fluid flux in the boundary layer, divided by the flow velocity

$$\delta^* = \int_0^\infty \left(1 - \frac{u}{U}\right) dy \tag{2.6}$$

Blasius (1908) computed the boundary layer for a flat plate as shown in Figure 2.4. He predicted at the outer limit of the boundary layer $\eta = 4.9$ and also the boundary

layer thickness approximately as

$$\delta = 4.9 \left(\frac{\nu x}{U}\right)^{\frac{1}{2}} \tag{2.7}$$

where η is the *similarity parameter* and defined as

$$\eta = y\sqrt{\frac{U}{\nu x}} \tag{2.8}$$

In this regard the displacement thickness can be

$$\delta^* = 1.72 \left(\frac{\nu x}{U}\right)^{\frac{1}{2}} \tag{2.9}$$

where ν and u are the fluid kinematic viscosity and velocity respectively and U is the stream velocity (undisturbed flow).

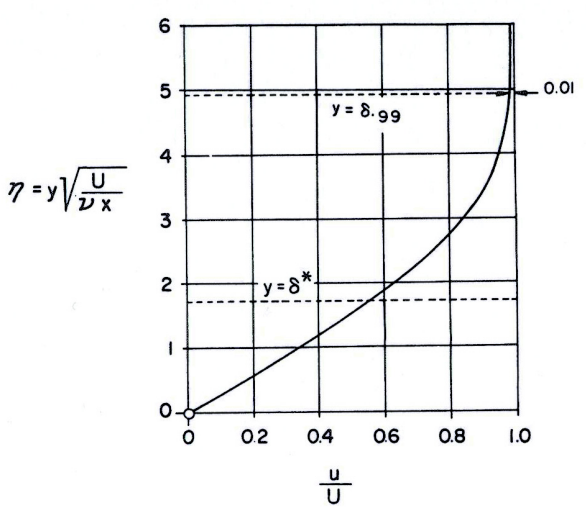

Figure 2.4: Distribution of velocity in a Blasius laminar boundary layer. The total area under the curve is equal to the area under the dashed line, corresponding to the flux defect and the displacement thickness δ^* , (Newman 1977)

The momentum thickness is another parameter which corresponds to the loss in momentum

$$\theta = \int_0^\infty \frac{u}{U}\left(1 - \frac{u}{U}\right) dy \tag{2.10}$$

and for a flat plate it can be calculated as

$$\theta = 0.664 \left(\frac{\nu x}{U}\right)^{\frac{1}{2}} \tag{2.11}$$

Studying the pressure gradient helps to understand more about the separation, *stagnation point* and boundary layer in general (see Figure 2.5). The separation occurs when the shear stress is zero and then there is no contact force between the flow and the body.

$$\left(\frac{\partial u}{\partial y}\right)_{y=0} = 0 \tag{2.12}$$

This is valid under the below condition

$$\left(\frac{\partial^2 u}{(\partial y)^2}\right)_{y=0} > 0 \tag{2.13}$$

The point which separation starts usually referred as the seperation point. At this point the streamline breaks away from the body enclosing a separated wake downstream of relatively high vorticity and low pressure. It is seen in Figure 2.5 that the tangential velocity is negative behind of this point and positive ahead of that.

Schlichting (1979) applied the laminar boundary theory to a far-wake behind a cylinder because the pressure is almost constant across the wake and the transverse component of velocity is small in comparison with the streamwise velocity. Also the rate of change of the streamwise velocity along the axis of the wake is small compared with the rate of change across the wake. By neglecting the the pressure gradient along the axis of the wake, equation of motion can be written as

$$u\frac{\partial u}{\partial x} + \upsilon\frac{\partial u}{\partial y} = \nu\frac{\partial^2 u}{\partial y^2} \tag{2.14}$$

At a very long distance downstream u is nearly equal to the free stream velocity, U and υ is small. By applying the velocity defect, $\Delta u = U - u$, the first approximation to Δu satisfies the equation

$$U\frac{\partial(\Delta u)}{\partial x} = \nu\frac{\partial^2(\Delta u)}{\partial y^2} \tag{2.15}$$

The drag force per unit span of the cylinder can be defined by consideration of the momentum as

$$D = \rho U \int \Delta u dy \tag{2.16}$$

by integrating across a section of the wake. As previously mentioned the the breath of the wake will increase as $x^{1/2}$ and by following Equation 2.15, Δu must be of the order of $x^{-1/2}$,

$$\Delta u = A x^{-1/2} f(\eta) \tag{2.17}$$

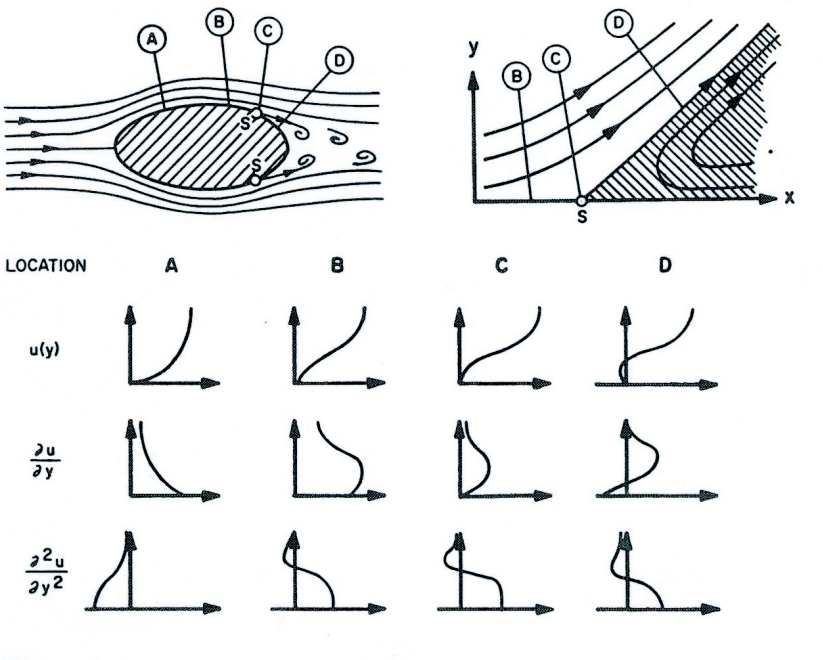

Figure 2.5: Viscous flow around a bluff body, (Newman 1977)

where $\eta = (U/2\nu x)^{1/2}y$, $f(\eta)$ is a universal function and A a constant. The boundary conditions for a symmetrical wake are

$$\begin{cases} \Delta u \to 0 & as \quad y \to \infty \\ \partial \Delta u/\partial \eta = 0 & when \quad \eta = 0 \end{cases}$$

and then the solution of Equation 2.14 is given by

$$f = C(1 - \eta^{3/2})^2 \tag{2.18}$$

By applying shearing stress hypothesis instead of the mixing length, we get

$$\Delta u = UC(\frac{x}{D})^{-1/2} \exp(-\frac{1}{4}\eta^2) \tag{2.19}$$

and

$$C = \frac{C_D}{4\sqrt{\pi}}\sqrt{\frac{UD}{\varepsilon_0}} \tag{2.20}$$

where ε_0 is virtual kinematic viscosity. Figure 2.6 shows that the curve 2 obtained by using Equation 2.18 is in the close agreement with curve 1 according to Equation 2.19 and both results are close to the measured velocity profile.

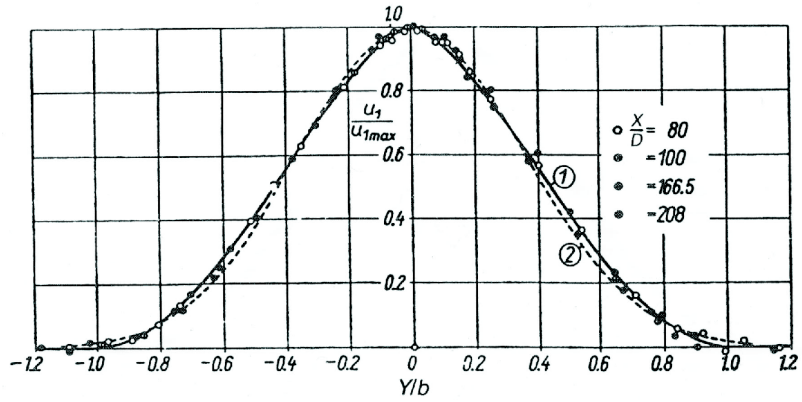

Figure 2.6: Velocity-deficit distribution across for wake, (Schlichting 1930)

2.2 Dimensionless parameters

Many researchers have been working on the area of flow around circular cylinder and vortex induced vibration over many years. They have used different parameters and put different meaning into them. However, it is important to define these parameters precisely. We try to summarize and define these parameters in this section. Those parameters divided into three categories; cf. Halse (1997) and Vikestad (1998). The first group parameters in the categories is flow parameters and the other two are related to the interaction between the fluid and the structures named as structure and interaction parameters respectively.

2.2.1 Flow parameters

The velocity properties of the flow are described in this subsection. These parameters are related to the fluid properties.

Reynolds number, R_e

The *Reynolds number* classifies dynamically similar flows, i.e. flows which have geometrical similar streamlines around geometrical similar bodies, Schlichting (1987) and defined as the ratio between the inertia forces and friction forces acting on a

body.

$$Re = \frac{U.D}{\nu} \tag{2.21}$$

Where U is the free stream velocity, D is a characteristic dimension of the body around which the fluid flows (in the case of a cylinder is its diameter) and ν is the kinematic viscosity coefficient of the fluid. The maximum flow velocity, U is used for the oscillatory flow.

Keulegan-Carpenter number, KC

The *Keulegan-Carpenter* number describes the harmonic oscillatory flows, as e.g. in waves. If the flow velocity, U is written as $U = U_M \sin(\omega t)$, the KC-number is defined as

$$KC = \frac{U_M T}{D} = \frac{2\pi A}{D} \tag{2.22}$$

where U_M is the maximum flow velocity during one period, T is the period of oscillations and A is the oscillation amplitude of the oscillating cylinder. For the constant flow KC corresponds to a very high number. This number was introduced by Keulegan and Carpenter (1958) and since then has been investigated by some researchers e.g. Sarpkaya (1977a) and Sarpkaya and Isaacson (1981).

The frequency parameter, β

The *frequency parameter* is defined as the ratio of Reynolds number over Keulegan-Carpenter number so that

$$\beta = \frac{R_e}{KC} = \frac{D^2}{\nu T} \tag{2.23}$$

where T is the period of oscillation. β parameter represents the ratio of diffusion rate through a distance δ to the diffusion rate through a distance D, Sarpkaya (1977a). δ is defined as the boundary layer thickness.

Turbulence intensity

Turbulence intensity parameter is dimensionless and used to describe the fluctuations in the mean incoming flow as follow

$$\frac{u_{rms}}{U_{mean}} \tag{2.24}$$

where u_{rms} is the root mean square (rms) of the velocity fluctuations, i.e. rms of $u(t) = U(t) - U_{mean}$.

Shear fraction of flow profile

Current profiles can be non-uniform. The amount of shear in the current profile describes the *shear fraction* as

$$\frac{\triangle U}{U_{max}} \tag{2.25}$$

where ΔU is the variation of velocity over the length of the current profile and can be written as $U_{max} - U_{min}$ where U_{max} is the maximum flow velocity which can be occurred in the current profile.

2.2.2 Structural parameters

These parameters represents the properties of the body, geometry, density and damping. These parameters are related to the structure properties.

Aspect ratio

The *aspect ratio* is about the geometric shape of the structure which for a cylinder defined as the length of the cylinder over the diameter

$$\frac{L}{D} = \frac{length}{width} \tag{2.26}$$

where L is the length and D is the cylinder diameter.

Roughness ratio

The *roughness ratio* describes the surface of the body and defined as

$$\frac{k}{D} \tag{2.27}$$

where k is a characteristic dimension of the roughness on the surface of the body. One of the parameter affects the friction of a body is roughness. The changes in the friction cause the change in the boundary layer and make it more turbulent and affect on the vortex shedding process since this process is highly depending upon the separation process on the body surface.

Mass ratio

The *mass ratio* for a structure is defined as the ratio of the cylinder mass per unit length, m, over ρD^2 as

$$\frac{m}{\rho D^2} \tag{2.28}$$

In literature, the mass is applied with or without including added mass but in the present work the added mass is not included in the mass ratio.

Specific gravity

The *specific gravity* is used to describe the ratio of the structural mass per unit length to the displaced fluid mass per unit length as

$$\frac{m}{\frac{\pi}{4}\rho D^2} \tag{2.29}$$

Like the mass ratio, also in this case the added mass is not included in the mass per unit length.

Damping ratio

The *damping ratio* for a given mode is the ratio of the linear damping coefficient to its critical value as follow

$$\zeta_n = \frac{c_n}{2m_n\omega_n} \tag{2.30}$$

where c_n is the $n'th$ damping coefficient, ω_n is the corresponding natural frequency and m_n is the corresponding mass to ω_n and the actual restoring force k_n. This ratio is usually referred to the *structural damping*.

Damping ratio or damping factor may also be defined in terms of the energy dissipation by a vibrating structure

$$\zeta = \frac{energy\ dissipation\ per\ cycle}{4\pi \times total\ energy\ of\ structure} \tag{2.31}$$

according to Figure 2.7, $2\pi\zeta$ is the natural logarithm of the ratio of the amplitudes of any two successive cycles in free decay.

Wave propagation parameter, $n\zeta_n$

Vandiver (1993) uses the product between the mode number n and the damping ratio ζ_n for the same mode, in order to identify the behavior of a cable (the damping

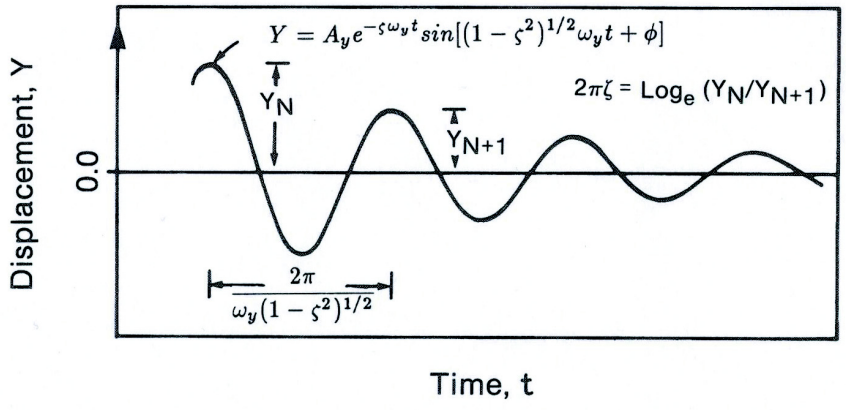

Figure 2.7: Free vibration of a viscously damped structure; ω_y is the natural frequency of vibration in radians per second, (Blevins 1990)

ratio here includes all damping, both structural and hydrodynamic). If the number is less than 0.2 the cable behave like a standing wave. Values greater than 2.0 means an infinite cable behavior. In between, there will be a mixed behavior.

- $n\zeta_n < 0.2$, a standing wave behavior can be expected
- $0.2 < n\zeta_n < 2.0$, a mix behavior will be happened
- $n\zeta_n > 2.0$, an infinite cable behavior can be expected

2.2.3 Interaction parameters

The interaction parameters are related to the interaction between the structure and the fluid.

Non-dimensional amplitude, A_y/D

The cross-flow response is important for studying vortex induced vibration. This response is non-dimensional and defined as

$$\frac{A}{D} \tag{2.32}$$

It is important to note that this parameter can also be defined for in-line vibration in the same way, but since this work only focuss on cross-flow vibration it is not mentioned here.

Reduced velocity, U_r

Path length per cycle for steady vibrations can be defined by the distance the undisturbed flow is traveling during one cycle, U/f. The reduced velocity is the ratio of the path length per cycle to the model width as follow

$$U_r = \frac{path\ length\ per\ cycle}{model\ width} = \frac{U}{f_n D} \tag{2.33}$$

where the $f_\circ$ is the natural frequency in still water. Moe and Wu (1990) proposed reduced velocity with the natural frequency in air which is called *nominal reduced velocity* and also with true vibration frequency which is called *true reduced velocity*.

True reduced velocity, U_{true}

The true reduced velocity is defined as

$$U_{true} = \frac{U}{f_{osc} D} \tag{2.34}$$

Added mass is known to vary with varying flow velocity. Consequently, the observed frequency of the cylinder changes and can be different from the natural frequency of the system in still water. In fact, the observed frequency, f_{osc} is a compromise between the natural frequency of the cylinder in still water, $f_\circ$ and the vortex shedding frequency for a fixed cylinder, $f_{v\circ}$.

Non-dimensional vibration frequency, $\hat{f}$

The *Non-dimensional vibration frequency* is used to define the condition for a cylinder with forced motions. This parameter is the inverse of the true reduced velocity parameter.

$$\hat{f} = \frac{f_{osc} D}{U} \tag{2.35}$$

The Strouhal number, St

The *Strouhal number* is a non-dimensional parameter and is defined as

$$St = \frac{f_{v_\circ}.D}{U} \tag{2.36}$$

There is an almost constant relation between the vortex shedding frequency for a fixed cylinder, $f_{v\circ}$, and the ambient velocity divided by the cylinder diameter, U/D. The proportionality constant of this relation is called the Strouhal number (see Figure 2.17).

Response parameter, S_G

The combination of the product of mass ratio and damping ratio is defined as *response parameter*; cf. Griffin and Koopmann (1977) and Griffin and Ramberg (1982). The other names which have been used for this parameter are *stability parameter*, *reduced damping*, *Scruton parameter* and *mass damping*.

$$S_G = 2\pi S_t^2 K_s = \frac{\zeta_s}{\mu} \tag{2.37}$$

where K_s is the reduced damping parameter

$$K_s = \frac{2m\delta}{\rho D^2} \tag{2.38}$$

m is the cylinder mass per unit length and $\delta = 2\pi\zeta$ is the logarithmic decrement. Gopalkrishnan (1993) shows that in a lock-in condition if the frequency of the excitation forces and the natural frequency of the system (by taking added mass into account) are equal, the lift force component which is in phase with cylinder velocity and the damping of the system will balance each other. Then, the incoming energy to the system from excitation forces is zero or is equivalent to the energy dissipated by the damping from other sources.

$$2S_G\frac{A}{D} = C_{Lv_0}(A/D) \tag{2.39}$$

where $C_{L_{V_0}}(A/D)$ is the lift force coefficient in phase with cylinder velocity. Regarding Equation 2.39, the maximum oscillation amplitude in a lock-in condition occurs when there is no damping in the system. In the other meaning, the maximum oscillation amplitude will be for $C_{L_{V_0}}(A/D) = 0$ that corresponds to $S_G = 0$ which means zero structural damping.

By using Equation 2.37 and 2.38, one may conclude that increasing mass ratio

reduces the maximum oscillation amplitude. However, Vandiver (1993) shows that by substituting $\delta = 2\pi\zeta$, $2\pi S_t = \omega D/U$ and $\zeta = r/2\omega m$ into Equation 2.37, the response parameter reduces to

$$S_G = \frac{r\omega}{\rho U^2} \tag{2.40}$$

he also shows the fact that Equation 2.40, is independent of the cylinder mass.

2.3 Lock-in

In the condition of the constant Strouhal number, when the vortex shedding frequency for a stationary cylinder approaches the natural frequency of oscillation of the cylinder from below, the cylinder will start oscillating and vortex shedding will start to *correlate* along the cylinder axis. This leads to a large increase in the forces acting on the cylinder. By increasing the current velocity further, the vortex shedding frequency will finally jump back to the linear curve defined by the Strouhal number.

The changes taking place in the vortex shedding frequency, $f_{v\circ}$ in the synchronization range are shown by Larsen (2000) in Figure 2.8. In this range, vortex shedding frequency, $f_{v\circ}$ and the oscillation frequency, f_{osc} collapse into the natural frequency of the system in flow $f_\circ$. It is interesting to note here that sustained oscillations extend over a range of U values and the vortex shedding is controlled by the vibrating cylinder. This figure also shows that the response frequency is a function of flow velocity.

2.4 The hydrodynamic force

Fluid flow around a cylinder with low structural damping properties will force them to vibrate in the transverse (cross-flow) and to a certain extent in the in line directions due to vortex shedding. When the frequency of vortex shedding is close to the natural frequency of the structure or one of its harmonics the vibrations occur. The cross flow force happens due to the difference in the pressure at the top and bottom of the cylinder. This is due to changing in the velocity of the flow passing the body. An opposite circulation around the cylinder occurs when a vortex is shed. This gives an increased velocity at the top of the cylinder, and a reduced velocity at the bottom. The pressure at the bottom will then be larger than at the top according to Bernoulli's equation. This induces pressure forces which will be directed upwards. The other vortices is shed from the opposite side, resulting in a force directed downwards. Each complete cross-flow excitation cycle therefore comprises

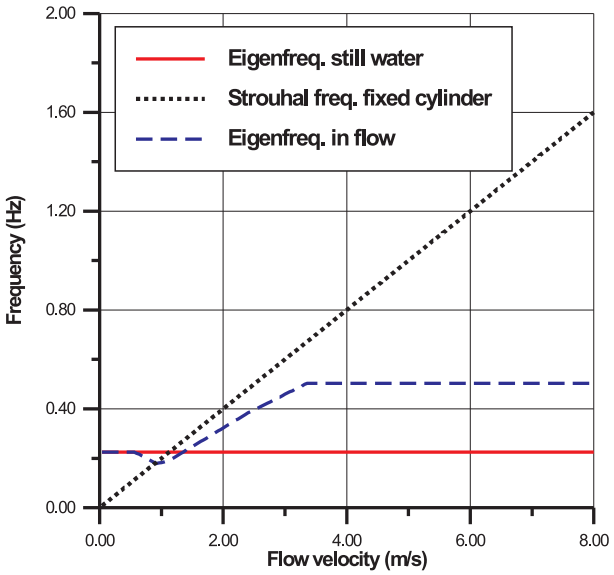

Figure 2.8: Lock-in or synchronization of vortex shedding cross-flow oscillations, added mass is assumed to follow the VIVANA model, Larsen et.al. (2002)

the effects of a complementary pair of vortices, acting first in one given direction and then in the vertically opposite direction. The pressure resultant, F_H changes sign and oscillates with the same frequency as the vortex shedding frequency, $f_{v\circ}$. If there is a single vortex shedding frequency, the relationship between F_H and the shedding of the vortices with respect to $\omega = 2\pi f_{v\circ}$, can be approximated as

$$F_H(t) = |F_H| \sin(\omega t + \alpha) \tag{2.41}$$

where α is the phase angle between the the hydrodynamic force and the body motion.

$$y(t) = y_0 \sin(\omega t) \tag{2.42}$$

The hydrodynamic force can be decomposed into one component in phase with the acceleration known as added mass and one component in phase with the velocity known as lift force.

$$F_H(t) = F_A \sin(\omega t) + F_L \cos(\omega t) \tag{2.43}$$

where $F_A = |F_H| \cos(\alpha)$ and $F_L = |F_H| \sin(\alpha)$ correspond to added mass and lift force respectively.

2.4.1 The lift coefficient

Lift force, F_L can be given in terms of lift coefficient, C_L as

$$F_L = \frac{1}{2}\rho C_L D L U^2 \tag{2.44}$$

where L is the length of the cylinder and ρ is the density of the fluid.

2.5 Free oscillation, 2D case

Figure 2.9 shows a cylinder supported by a spring in steady flow. This is a simple 2D case with free oscillation. Understanding of this model is the basic step to understand the behaviour of a more complicated case.

In this case, eigenfrequency of the cylinder in still water, $f_\circ$ is known if k, m (including added mass in still water) and D as stiffness, mass and diameter of the cylinder are known. Moreover, the vortex shedding frequency when the cylinder is fixed, $f_{v\circ}$ is known if U and D are known and finally, the oscillation frequency of the cylinder, f_{osc} can be observed if k, m, D and U are known.

After starting the oscillation, it takes time that the system gets stable. From that period with stable oscillation, the lift coefficient is zero and there is no energy in or dissipated from the system (in the case of zero mechanical damping).

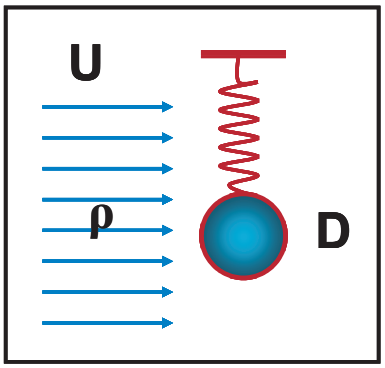

Figure 2.9: Free oscillation, 2D case, Figure from Larsen (2005)

2.5.1 Equation of motion, Free oscillation

The equation of motion for the free oscillation system with zero mechanical damping can be written as

$$m\ddot{y} + ky = |F_A| \sin(\omega t) \tag{2.45}$$

where m and k are mass and stiffness respectively. By inserting Equation 2.42 in Equation 2.45 we have

$$-\omega^2 m y_0 \sin(\omega t) + k y_0 \sin(\omega t) = |F_A| \sin(\omega t) \tag{2.46}$$

The hydrodynamic force must be in phase with acceleration, contributes to added mass

$$(m + m_a)(-\omega^2 y_0) \sin(\omega t) + k y_0 \sin(\omega t) = 0 \tag{2.47}$$

2.5.2 Added mass from free oscillation test

Figure 2.10 shows added mass from measured force under free oscillations. As seen in the figure, the added mass is very high for low reduced velocity, U_R and decrease by increasing of reduced velocity. At low reduced velocity, response amplitudes are small and the response frequency is much lower than the still water eigenfrequency, $f_\circ$. For high reduced velocities the added mass is seen to become negative, and the response frequency will be much higher than the original eigenfrequency.

2.5.3 Amplitude and frequency ratio

From free oscillation tests, added mass can be found from the measured force as well as measured frequency

$$\omega = \sqrt{\frac{k}{m}} = \sqrt{\frac{k}{m_{dry} + m_a}} = \sqrt{\frac{k}{m_{dry} + \frac{\pi D^2}{4} \rho C_a L}} \tag{2.48}$$

where the added mass coefficient, C_a can be calculated by measuring ω.

Figure 2.11 shows the results from Vikestad's free oscillation tests. In the figure, response amplitude and frequency are shown as function of the reduced velocity. Here, the response frequency is given in terms of the measured frequency, f_{osc} divided by the calculated eigenfrequency based on the measured added mass. The A/D curve can be found in many publications, e.g. Blevins (1977). The true resonance occurs when the frequency ratio is 1.0. As seen in the figure, the curve has a weak tendency to deviate from 1.0, but is seen to be fairly constant. However, it shows a good agreement and confirms that lock-in is a response at resonance.

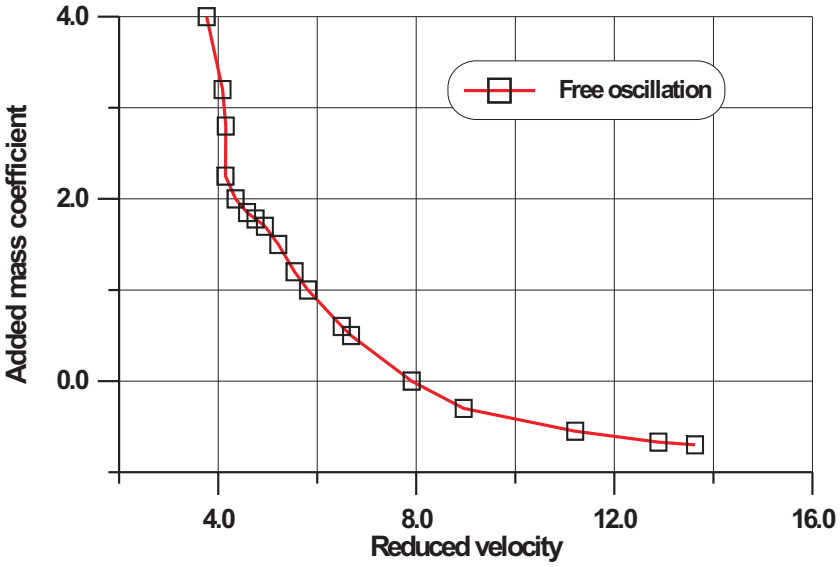

Figure 2.10: Added mass from free oscillation test, Vikestad (1998)

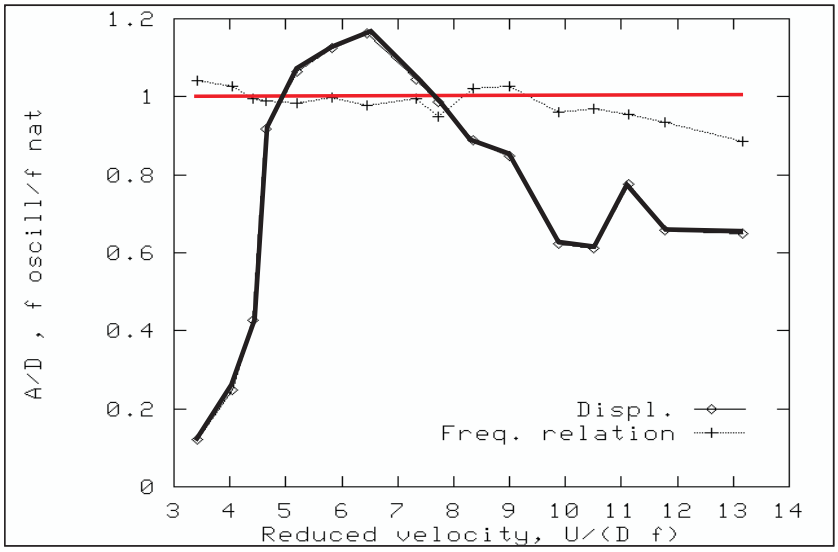

Figure 2.11: Amplitude and frequency ratio, Vikestad (1998)

2.6 Forced oscillation

Forced oscillation test is one of the methods to investigate the vortex induced vibrations. In this method, the cylinder is given a predefined motion orthogonal to the flow. The motion is hence defined by its amplitude and frequency, and the non-dimensional frequency ratio, $\hat{f} = f_{osc}D/U$ must be used to present results.

The lift and added mass coefficients are found by measuring forces in phase and out of phase with the velocity of the cylinder respectively.

In this method, added mass and lift coefficient can be found for any combinations of amplitude and frequency.

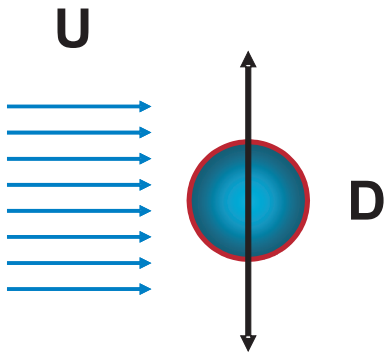

Figure 2.12: Forced oscillation model, Figure from Larsen (2005)

2.6.1 Equation of motion, Forced oscillation

The equation of motion for one single frequency, $\omega = 2\pi f_{v\circ}$ can be written as

$$m\ddot{y} + c\dot{y} + ky = F_y(t) \tag{2.49}$$

where m, c, k are mass, damping and stiffness respectively and $F_y(t) = |F_L|\sin(\omega t + \alpha)$. By inserting Equation 2.42 in Equation 2.49 and considering zero damping and stiffness for the system we have

$$-\omega^2 m y_0 \sin(\omega t) = F_A \sin(\omega t) + F_L \cos(\omega t) \tag{2.50}$$

The first term in the right hand side is in phase with cylinder acceleration and then contributes to the added mass and the second term is in phase with cylinder

velocity which contributes to either excitation or damping, depending on the sign.

$$(m + m_a)(-\omega^2 y_0)\sin(\omega t) = F_L \cos(\omega t) \tag{2.51}$$

2.6.2 Lift coefficient

Figure 2.13 shows contour lines for the lift coefficient as function of the non-dimensional frequency and motion amplitude ratio, A/D. In the case of zero mechanical damping, the ideal lock-in occurs when the lift coefficient is zero. At this situation, no energy is transmitted between the cylinder and the flow.

As seen in the figure, excitation occurs if energy goes from the fluid to the cylinder (lift coefficient is positive), while damping occurs when the lift coefficient is negative and energy takes away from the cylinder.

According to this figure, the maximum A/D for zero lift is 0.85, which should correspond to maximum response amplitude for free oscillation tests. In Vikestad's tests for force oscillations, this value is 1.15, see Figure 3.8. This discrepancy is not fully understood, but the explanation might be that the two sets of experiments were carried out with different Reynolds number or that the free cylinder has motions that contains higher order harmonics in contrast to the harmonic forced motions.

Lift coefficient in phase with cylinder velocity, $C_{L_{V_0}}$

The lift coefficient in phase with cylinder velocity, $C_{L_{V_0}} = C_L \sin(\alpha)$ is defined by Gopalkrishnan (1993) as

$$C_{L_{V_0}} = \frac{|F_L|\sin(\alpha)}{\frac{1}{2}\rho D L U^2} \tag{2.52}$$

where D is the cylinder diameter, L is the length of the cylinder, α is the phase angle and U is the free stream velocity.

Further with using

$$\frac{1}{2}\omega y_0 |F_L|\sin(\alpha) = \lim_{T\to\infty} \frac{\int_t^{t+T} F_y \dot{y} dt}{T} \tag{2.53}$$

we get

$$C_{L_{V_0}} = \frac{\lim_{T\to\infty} \frac{1}{T}\int_t^{t+T} F_y \dot{y} dt}{\frac{1}{4}\omega y_0 \rho D L U^2} \tag{2.54}$$

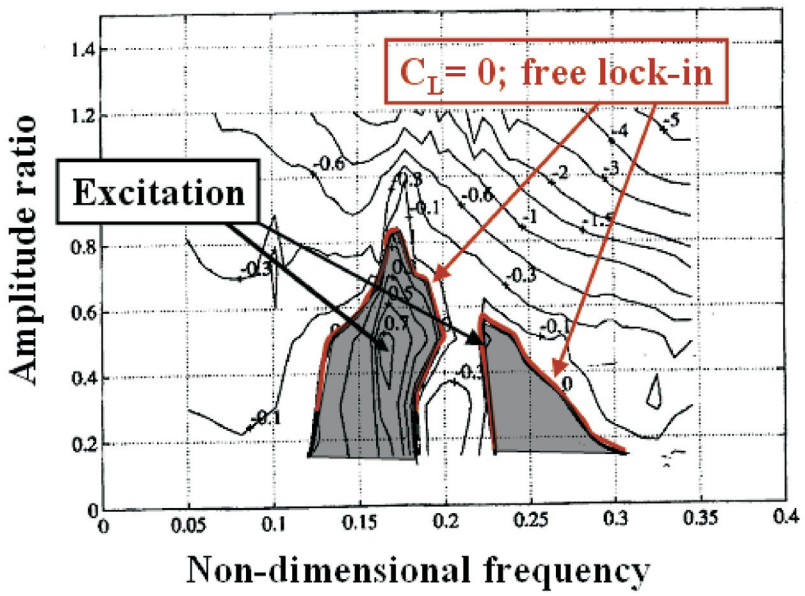

Figure 2.13: Lift coefficient referred to force in phase with cylinder velocity, Gopalkrishnan (1993)

Lift coefficient in phase with cylinder acceleration, $C_{L_{A_0}}$

Lift coefficient in phase with cylinder acceleration, $C_{L_{A_0}} = C_L \cos(\alpha)$ can be written as

$$C_{L_{A_0}} = \frac{|F_L| \cos(\alpha)}{\frac{1}{2}\rho D L U^2} \tag{2.55}$$

with using

$$\frac{1}{2}\omega^2 y_0 |F_L| \cos(\alpha) = \lim_{T\to\infty} \frac{\int_t^{t+T} F_y \ddot{y} dt}{T} \tag{2.56}$$

and

$$C_{L_{A_0}} = \frac{\lim_{T\to\infty} \frac{1}{T} \int_t^{t+T} F_y \ddot{y} dt}{\frac{1}{4}\omega^2 y_0 \rho D L U^2} \tag{2.57}$$

Relation between the lift coefficients

The relation between C_{L_T}, $C_{L_{V_0}}$ and $C_{L_{A_0}}$ for a circular cylinder with the length, L, is written as

$$C_{L_T}^2 = C_{L_{V_0}}^2 + C_{L_{A_0}}^2 \tag{2.58}$$

and by using Equation 2.52 and 2.55 in this equation we find the *total lift coefficient*

$$C_{L_T} = \frac{|F_L|}{\frac{1}{2}\rho DLU^2} \tag{2.59}$$

The lift force can be written also in the terms of the mean lift force, $\overline{F}_L$ and the mean lift coefficient, $\overline{C}_L$ simply as

$$\overline{F}_L = \frac{1}{2}\rho \overline{C}_L DLU^2 \tag{2.60}$$

2.6.3 Added mass coefficient

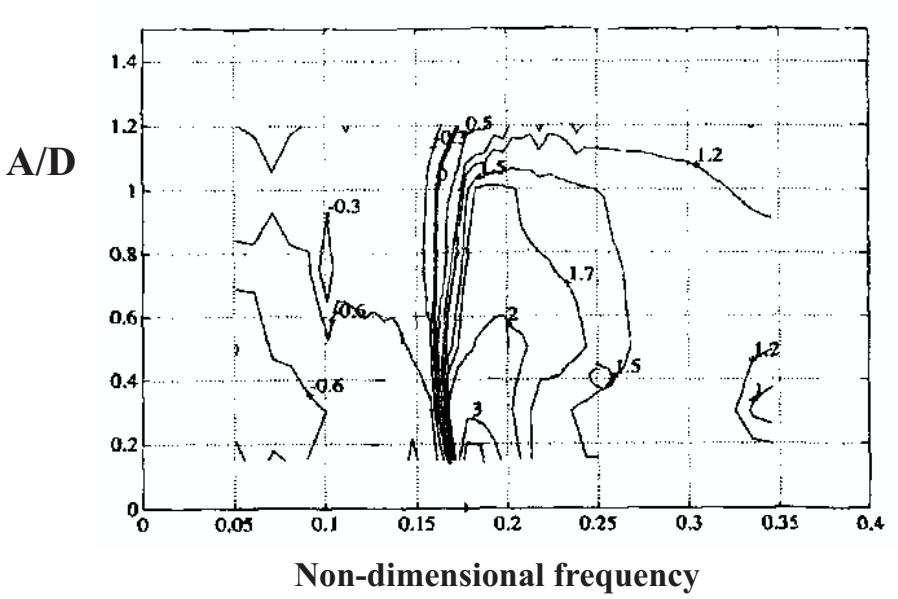

Figure 2.14: The added mass coefficient plots, Gopalkrishnan (1993)

Figure 2.14 shows contour lines for the added mass as function of the non-dimensional amplitude and frequency. The contours are close to vertical where the added mass

has its strongest gradients. This means that added mass is almost independent on the amplitude in this region.

The added mass coefficient, C_{M0}

The added mass is given from the hydrodynamic force by

$$M_{A0} = \frac{|F_L|\cos(\alpha)}{\omega^2 y_0} = \frac{\frac{1}{2}\rho D L U^2 C_{L_{A_0}}}{\omega^2 y_0} \tag{2.61}$$

The added mass which is normalized by the mass of the displaced fluid is defined as

$$C_{M0} = \frac{M_{A0}}{\rho\frac{\pi D^2}{4}L} = \frac{2}{\pi}\frac{U^2 C_{L_{A_0}}}{\omega^2 y_0 D} \tag{2.62}$$

Inserting Equation 2.57 in Equation 2.62, we get the expression for the added mass coefficient

$$C_a = -\frac{\lim_{T\to\infty}\frac{1}{T}\int_t^{t+T} F_y \ddot{y} dt}{\frac{\pi}{8}\rho(\omega^2 y_0)^2 L D^2} \tag{2.63}$$

2.6.4 Drag coefficient

The in-line (drag) force component has a different behavior than what explained in the previous sections. This force is created due to the pressure differentials induced between upstream and downstream faces of the cylinder for each time an individual vortex is created.

The drag oscillation frequency will be twice the vortex shedding frequency, $2f_{v\circ}$ since the upward movement effects in-line drag the same way as downward (see Figure 2.15). The drag force in the time domain can be approximated as

$$F_D(t) = F_D + |F_D| \sin(4\pi f_{v\circ} t + \beta) \tag{2.64}$$

where A_D is the amplitude of the oscillatory part of the drag force and β is phase angle and vary strongly along the cylinder axis. F_D is time independent and is the basis for the normally defined drag coefficients.

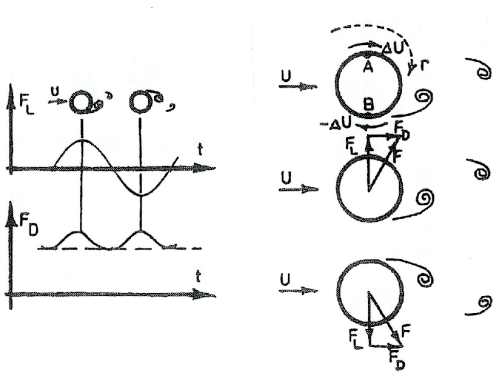

Figure 2.15: Drag and lift forces

Quadratic cross-flow drag coefficient, C_d

This coefficient is based on the *not true!* assumption that the cross-flow force is in phase with the velocity of the cylinder, and is proportional to the square of the cylinder velocity. The time averaged power from the structure to the fluid should be the same both in the experiment and when using the mathematical model, and this determines the value of C_d.

$$C_d = -\frac{\lim_{T\to\infty} \frac{1}{T} \int_t^{t+T} F_y \dot{y} dt}{\frac{2}{3\pi}\rho(\omega^2 y_0)^3 LD} \tag{2.65}$$

Mean drag coefficient, $\overline{C}_d$

The drag force also can be defined in the terms of $\overline{F}_D$ and $\overline{C}_d$, which are the mean drag force and mean drag coefficient respectively as

$$\overline{F}_D = \frac{1}{2}\overline{C}_d \rho DLU^2 \tag{2.66}$$

2.7 Experimental studies

2.7.1 Steady flow around a stationary cylinder

As the transition from a lower Reynolds number, Re to a higher Re occurs in the flow and subsequently at a sufficiently large Re a flow structure comprising of a laminar region followed by a transition region and a turbulent region develops.

The free stream velocity and turbulence intensity of the flow together with the surface roughness of the boundary controls the location of the transition region.

This dependence on the Reynolds number usually is divided into different flow regimes. However, there are many different definitions in the literatures. For a smooth circular cylinder, the major Reynolds number regimes of vortex shedding given by Lienhard (1966). This is shown in Figure 2.16. According to Lienhard (1966), at Reynolds number < 5, the flow is laminar and no separation takes place. In the range 5 to $15 \leq Re < 40$, two symmetrical standing eddies are formed and the flow separates from the back of the cylinder. The extension of these eddies increase in the streamwise direction by increasing of Reynolds number, and can be reached to a length of three cylinder diameters at $Re = 45$. Further that Reynolds number, one of the vortices breaks away in an unstable wake and the other vortices in the opposite sign of vortex street are formed as a laminar periodic wake. $150 \leq Re < 300$, transient from laminar to turbulent vortex street happens, even though the boundary layer on the cylinder remains laminar. In the *subcritical* range, $300 < Re < 1.5 \times 10^5$, the vortex shedding is strong and periodic. In this range, the boundary layer separates at about 80° aft of the cylinder nose. The Reynolds number range $1.5 \times 10^5 < Re < 3.5 \times 10^6$, is called *transitional*. In this range the boundary layer on the cylinder becomes turbulent and the separation points move aft to 140°. This causes a high decrease in the drag coefficient to 0.2-0.3. Simultaneously, the Strouhal number increases from $St \simeq 0.2$ to a maximum of 0.46. regular vortex shedding is re-established with a turbulent boundary layer on the cylinder in the *supercritical* range, $Re > 3.5 \times 10^6$.

Existence of a relationship between the vortex shedding frequency, cylinder diameter and the velocity of the flow was first recognized by Strouhal (1878) as

$$St = \frac{f_{v_\circ}.D}{U} \tag{2.67}$$

The relationship that exists between the Strouhal number and the Reynolds number can be seen in Figure 2.17, Lienhard (1966). The value of St remains at about 0.2 in the subcritical regime as a result of a narrow band vortex shedding. In the critical regime where changes in laminar to turbulent separation occurs as a result of formation of separation bubble, the value of St varies due to a rather broad

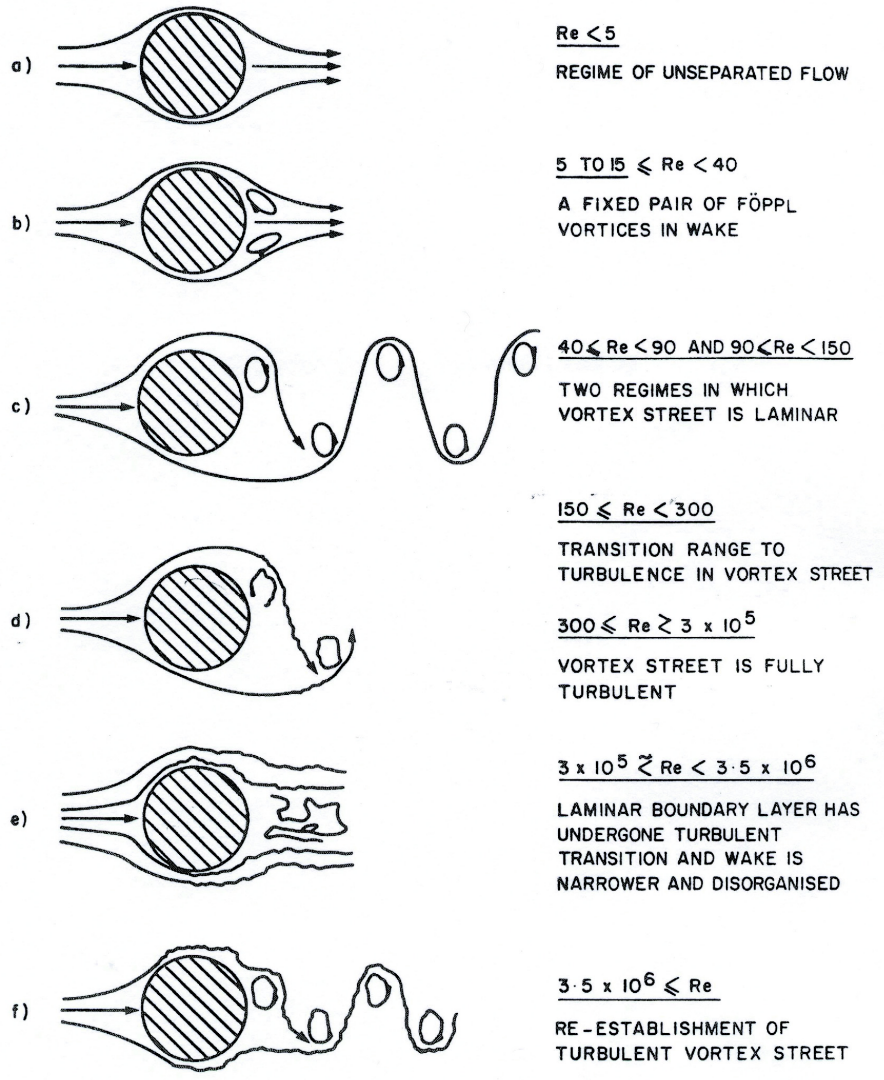

Figure 2.16: Flow regime across smooth circular cylinder, Linehard (1966)

band vortex shedding. A similar behavior in the value of St could be noticed in the supercritical regime where the wake is highly turbulent and non periodic. At higher Re where the vortex shedding becomes some what periodic, values of St rises to about 0.27, Roshko (1961). Gerrard (1966) describes the vortex shedding mechanism for subcritical Reynolds number above 500. He states that while the

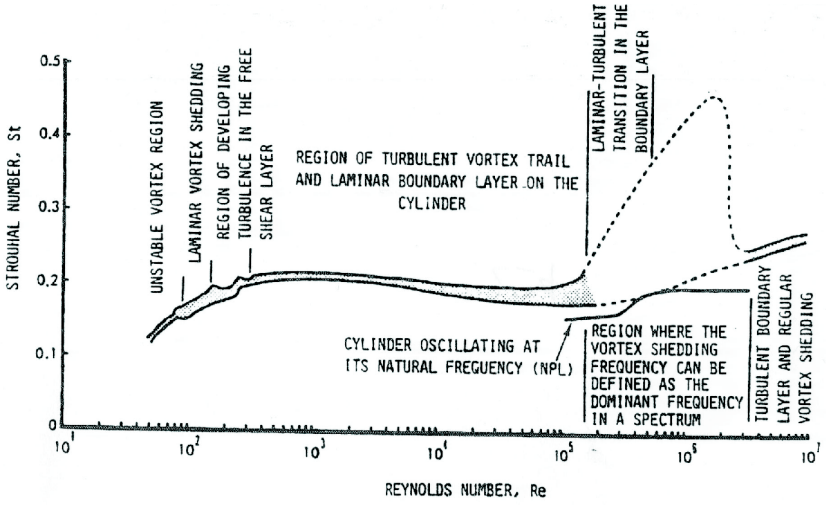

Figure 2.17: Strouhal-Reynolds number relationship

vortex is fed by circulation from the separated shear layer, then the growing vortex remains stationary relative to the cylinder. In another article Green and Gerrard (1993) describe also the behavior of vortex shedding for the low R_e flows. For lower R_e, diffusion of the vortices becomes significantly important. Griffin (1995) has introduced $R_e = 350$ to form the border between low R_e flows and high R_e flows. Before, in an article, Green and Gerrard (1993) also describes the behavior of vortex shedding for the low R_e flows and presents the fact that the vortex shedding needs some time to develop and get enough strength depending on the Reynolds number. Williamson (1988) defines a universal and continuous relations between Strouhal and Reynolds numbers for the laminar vortex shedding of a circular cylinder as seen in Figure 2.18.

2.7.2 Steady flow around an oscillating cylinder

The above discussed behavior of St is for a fixed smooth circular cylinder. Cylinder vibration result changes in the boundary layer characteristics like, formation of separation bubble and the the vortex shedding. From Sarpkaya and Isaacson (1981) it is found that the experiments conducted at the National Physical Laboratory (1968) as seen in Figure 2.17, showed the cylinder vibration prevents the occupance of sharp rise in the value of St. On the contrary the value of St was found to remain rather close to that observed in the subcritical regime.

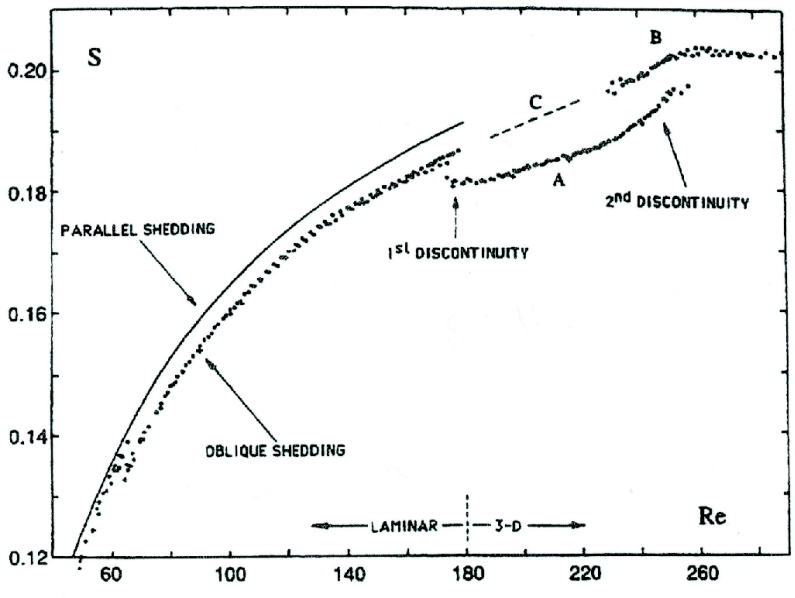

Figure 2.18: Strouhal-Reynolds relation, (Williamson 1991)

Periodic shedding of the vortices results in an alternating force on a circular cylinder normal to the flow which acts in a direction away from the last shed vortex. Variation of the lift force coefficient is not as clear as compared to the drag coefficient and the Strouhal number.

Figure 2.19, from Sarpkaya and Isaacson (1981) show a large scatter in the values of the lift force coefficient, C_L. C_L is found to be rather sensitive to end gaps, cylinder mounting (fixed or free to vibrate, as in the case of free cylinders, vibrations are found to increase the lift force due to increase in force correlation), and the flow characteristics like free stream turbulence etc.

Elastically mounted cylinder

Griffin and Koopmann (1977) have performed some experiments to establish amplitude, frequency and phase angle of a vibrating cylinder for various reduced velocities, U_R and with different mass ratio, $m/\rho D^2$ and damping ratio, ζ and the combined response parameter, S_G. They have also done some experiments to show the lock-in phenomena in cross-flow vibration. Furthermore, Anagnostopoulos and Bearman (1992) also have done the same attempt to show this phenomena.

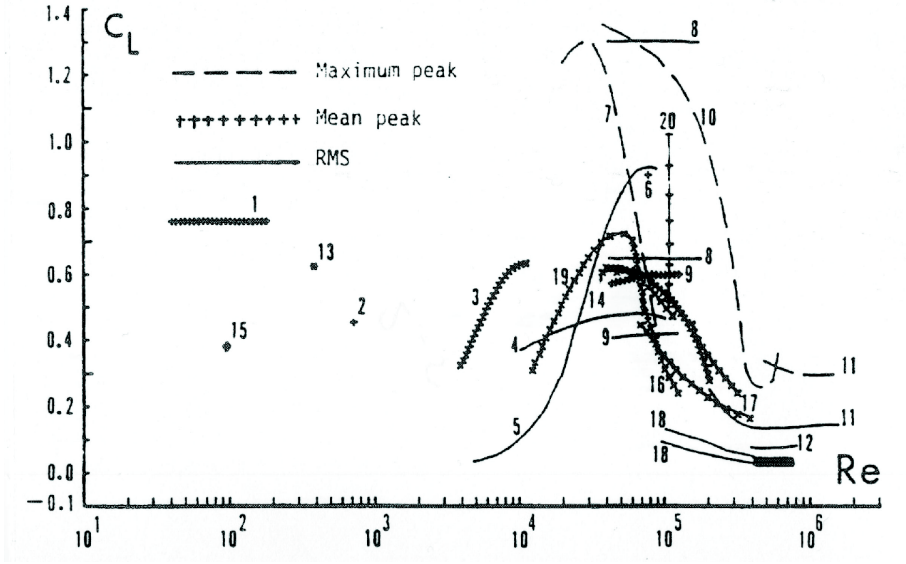

Figure 2.19: Lift coefficient as a function of the Reynolds number for circular cylinders, (Sarpkaya & Isaacson 1981)

King (1977) states the first instability region to be in the range $1.25 < U_R < 2.5$ and the second instability region in the range $2.7 < U_R < 3.8$, even though, slightly different ranges reported by the other researchers, (see Sarpkaya and Isaacson (1981)).

Moe and Wu (1990) have done some experiments with both a freely oscillating cylinder and a cylinder with force motion. They show that the actual frequency of vibrations are not constant in two oscillations and state that the frequency of oscillation can be affected by the variation of the added mass. They found the same lock-in ranges in both cases by correcting the actual vibrating frequency in the reduced velocity of the free vibrating case. Griffin and Ramberg (1982) have performed some flow induced vibration both in air and in water and show that the lock-in range of the experiments in water are wider than the lock-in range from the experiments performed in air. Some experiments have done by Brika and Laneville (1993) on a free oscillation cylinder in a wind tunnel and the results compared with results on a flexible mounted cylinder in with free oscillation by Feng (1968). The results have been in good agreements in main points but due to the different experimental set up, some significance differences are found in the details of the results.

Cylinder with forced motion

Bishop and Hassan (1964) have performed many experiments on a cylinder with forced motion in a fluid flow and got some interesting results. They observed a discontinuity in the phase between the lift force and cylinder displacement (see Figure 2.20). They also noted the hysteresis effect in experiments.

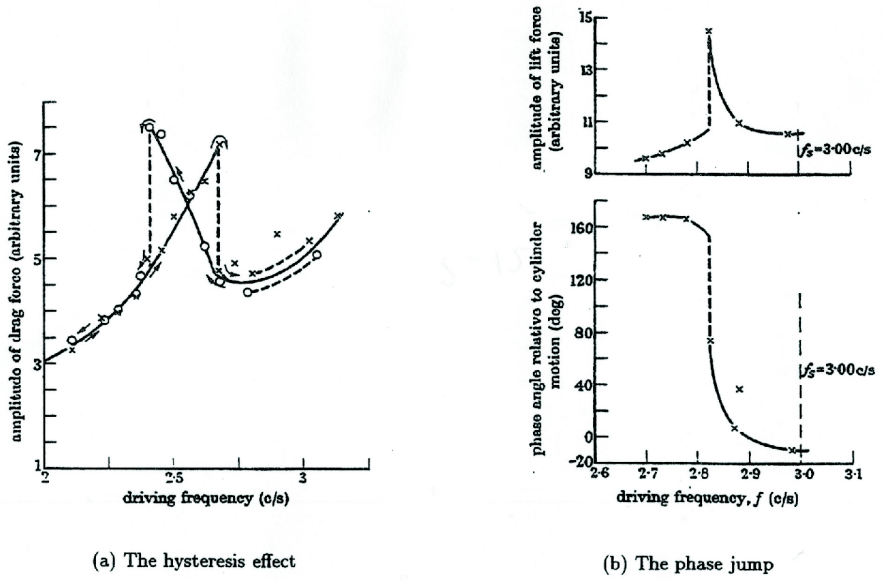

(a) The hysteresis effect (b) The phase jump

Figure 2.20: (a) The hysteresis effect (x, f is increasing, O, f is decreasing); (b) The jump in the lift force amplitude is shown together with a corresponding jump in the phase angle between lift force and cylinder motion, (Bishop & Hassan 1964)

Sarpkaya (1978) carried out a large research program in order to determine the in-phase and out-of-phase component of the forces acting on a cylinder forced to have cross-fellow oscillation in a uniform flow. As previously mentioned, Moe and Wu (1990) have also conducted forced oscillation tests rather than the free oscillation tests. They emphasizes the importance of the possible added-mass variation within the lock-in range. They reported the narrower lock-in range of forced vibration tests and the wider range for free vibrations. The other researchers like Staubli (1983) and Gopalkrishnan (1993) also have conducted forced oscillation experiments of a circular cylinder in cross-flow (see Figure 2.21).

Williamson and Roshko (1988) have performed some experiments with a cylinder

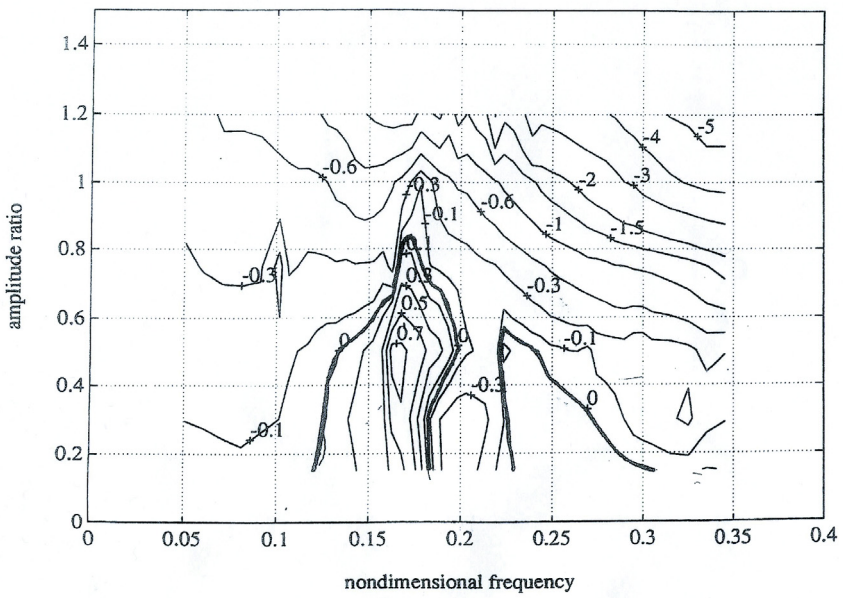

Figure 2.21: Contours of the lift coefficient in phase with velocity; sinusoidal oscillations, (Gopalkrishnan 1993)

forced to vibrate over a large range of frequencies and amplitudes. They provided a clear picture of the patterns forming behind an oscillating cylinder with uniform section, as a function of amplitude and frequency of oscillation, and for Reynolds numbers in the range 300-1000. Brika and Laneville (1993) have shown that the results from free oscillation tests can be related to results found in forced oscillation cases.

2.8 Suppression of VIV

The suppression of VIV can be achieved with many different methods; see also Skaugset (2003). In this section we try to categorize these methods and briefly explain about each of them. One of this method is to use of hydrodynamic devices. Zdravkovich (1981) divides the suppression options into three categories:

- **Surface protrusions**
  These devices are used to modify the cylinder's surface and thus causes the amplitude of VIV to be reduced. They can be strakes, wires, fins and studs. They disrupt or prevent the initiation of an organized, two-dimensional vortex street.

- **Shrouds**
  These devices such as perforated shrouds, axial rods and axial slats are placed at a distance from the cylinder and disrupt the vortex to be grown up and break the flow to many small vortices.

- **Near-wake stabilizers**
  These devices affect the wake of the cylinder to make them more stabilized. They are such as splitter plates, guiding vanes, base-bleeds and slits cut along the cylinder.

Blevins (1990) determines that the suppression can be achieved by modifying either the structure or the flow and presents the suppression options in four categories as follows:

- **Increase reduced damping**
  The amplitude of vibration can be reduced, by increasing of the reduced damping, K_s. According to Blevins (1990), if the reduced damping is greater than about 64, then peak amplitudes at resonance is decreased to less than 1% of the diameter. It can be done by using viscoelastic materials, rubber and wood, or by using external dampers. But we have to mention that for marine structures is difficult to have this kind of reduction since the damping can not be that high for them.

- **Avoid resonance**
  It can be achieved by stiffening the structure so that the reduced velocity is kept below 1. For a slender structure it is possible when the highest Strouhal frequency for the cross section will be lower than the first natural frequency. The combination of shear flow and the excitation of the higher modes (more than 100) reduces the probability of lock-in.

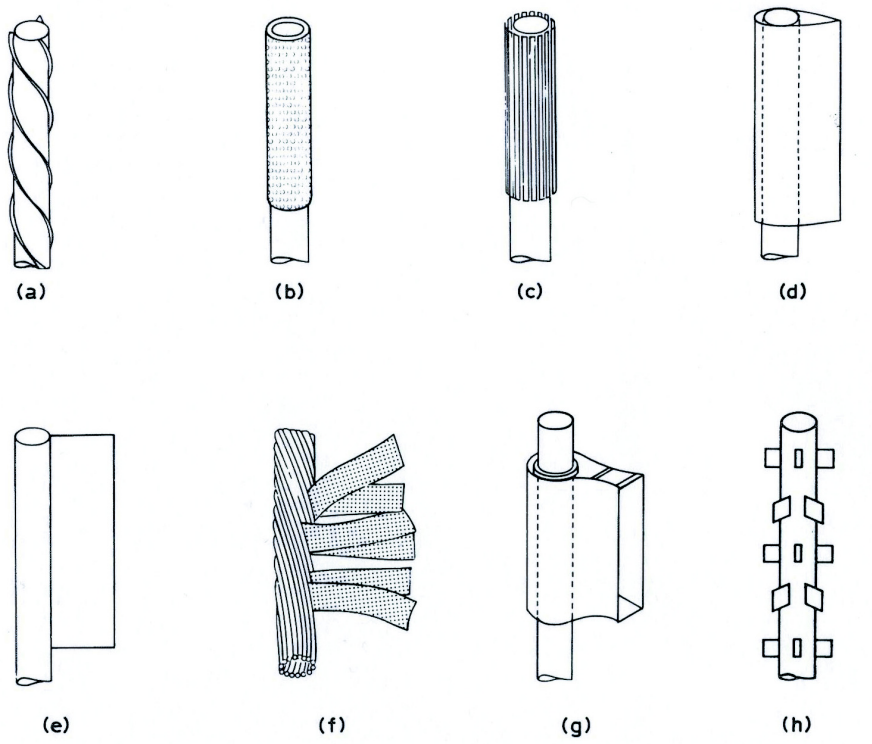

Figure 2.22: Add-on devices for suppression of vortex-induced vibration of cylinders: (a) helical strake; (b) shroud; (c) axial slats; (d) streamlined fairing; (e) splitter; (f) ribboned cable; (g) pivoted guiding vane; (h) spoiler plates, (Blevins 1990)

- **Streamline cross section**
  Vortex shedding can be minimized if separation from the structure is minimized by streamlining the cross section and thus drag will be reduced.

- **Add a vortex suppression device**
  Those are suppression devices as introduced by Zdravkovich (1981) and explained previously. They interfere with boundary layer separation by introducing an artificial turbulence, or forcing uncorrelated spanwise shedding (see Figure 2.22).

Chapter 3

Vortex induced vibrations of slender marine structures

Pipelines and risers are slender marine structures. These structures have unique behaviours and are hence demanding special analysis methods.

One of the major problems for these structures is vortex induced vibrations which has been under investigation over decades.

A substantial research effort related to various aspects of VIV has been seen during the last years.

Flow induced vibration was investigated by Blevins. Blevins (1977) focuses on applications for offshore platforms and piping; wind-induced vibration of buildings, bridges, and towers; and acoustic and mechanical vibration of heat exchangers, power lines, and process ducting.

Full scale measurement of free span pipeline response was performed by (Bruschi et.al. 1989). He performed a data acquisition programme within the '*Submarine Vortex Shedding*' (S.V.S.) research project to check the response of a full scale free spanning pipeline in real environment subject to the action of predominant wave flow (first site) and predominant steady current (second site). Full scale models were arranged and instrumented in each site, and thorough environmental monitoring systems were employed.

Some laboratory tests on long slender beams were carried out, (Bryndum et al. 1989) and also (Marchesani et.al. 1995). They described a model test programme

in which the hydro-elastic vibrations of free spanning marine pipelines are studied. In this programme, a large variety of environmental conditions are covered including steady currents, regular waves, irregular waves and combined steady currents and regular/irregular waves. They used two types of models simulating a prototype pipeline span. One, a relatively short rigid pipe segment mounted in elastic springs and two, a long flexible pipe. They have also performed extensive measurements of displacements and hydrodynamic forces combined with detailed analysis established a number of parameters characterizing the hydroelastic response in each test. However, methods for direct calculation of VIV on free span pipeline have been published by (Tura et.al. 1990).

Moe and Wu (1990) conducted an experimental program with forced and free vibration tests of a rigid cylinder and showed that when the cylinder is allowed to move in both in-line and cross-flow directions, the lock-in region becomes wider in terms of true reduced velocity than the case with only cross-flow motion.

The maximum cross-flow vibration amplitude is reported by Vandiver (1993) and several others to be in order of one diameter.

Some experiments on driven cylinders have been performed by Gopalkrishnan (1993) which later widely adopted through the international research community. He produced exceptionally detailed contour plots, e.g. of lift force in phase with velocity as function of amplitude and dimensionless frequency.

Vikestad (1998) investigated an elastically mounted rigid smooth cylinder. Pure VIV tests were performed in a test rig which proved to give exceptionally low mechanical damping. The results from his and Goplakrishnan's experiments have been used in VIVANA.

Det Norske Veritas (1998) issued guidelines and recommendations regarding free spanning pipeline, often referred to as DNV-G14. Some improvements of these guidelines have been proposed by Det Norske Veritas (2002). Important implications of the guidelines were published by (Mørk et al. 1998).

Halse and Larsen (1998) used the combination of two-dimensional (2D) solutions of Navier-Stokes in combination with a 3D beam model. Multi-Strip numerical analysis method for flexible riser response has performed by Sulz and Meling (2004). In this method, combining solution of the incompressible Reynolds Averaged Navier-Stokes (RANS) equations with a finite-element structural dynamics response, has been developed to analyze the flow-structure interaction of long, flexible risers. This solution methodology combines a number of individual hydrodynamic simulations corresponding to individual axial strips along the riser section with a full 3D structural analysis to predict overall VIV loads and displacements. Sulz and Meling (2005) expanded on the previous work using the tool to numerically compute the

VIV loads and motions of a vertically tensioned riser in a stepped current. In addition to the stepped current, the multi-strip method was extended to accommodate a three-dimensional skew current exposed to a vertically tensioned riser. Willden and Graham (2005) report results from two strip theory CFD investigations of the Vortex-Induced Vibrations of model riser pipes. The first investigation is concerned with the vibrations of a vertical riser pipe that was subjected to a stepped current profile. They conducted an axial spatial resolution study to determine the number of simulation planes required to achieve tolerably converged numerical solutions. They found that six to seven simulation planes are required per half-wavelength of pipe vibration in order to obtain convergence. The second investigation was concerned with the simultaneous in-plane and out-of-plane vibrations of a model Steel Catenary Riser that was subjected to a uniform current profile. They concluded that the pipe's simulated vibrations found to be agree very well with those determined experimentally.

Another important aspect is the interaction between in-line and cross-flow response that has been discussed by (Huse et.al. 2002). Nielsen (2002)discussed the observed VIV response of long free spanning pipelines during model testing and gave the hypotheses that could explain the observed behaviour.

Mørk (2003)has been investigated the assessment of VIV induced fatigue in long free spanning pipelines. Ilstad (2005) discussed the fatigue calculations of multimode VIV based on the implementation of test results into detail design on Ormen Lange project.

3.1 Simple empirical model for VIV analysis

Figure 3.1 to Figure 3.3 shows Locari test program based on the results from 2D tests. The method was implemented in the LOCARI program and based on an extensive test program with short cylinder sections supported by IL and CF springs. Ordinary circular cross sections and cylinders with satellite pipes were tested. Note that in these figures Locari used TR (Transverse) instead of CF to illustrates the cross flow oscillation.

Figure 3.4 shows a vertical riser with a uniform cross section exposing to a uniform current profile. In this model, the response will take place at an eigen frequency and will have the shape of the associated mode. Another step is to select the dominating eigen frequency that will become excited.

There are different methods for selecting mode, (i.e. uniform and sheared current):

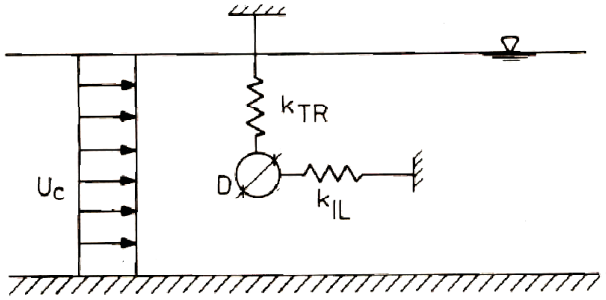

Figure 3.1: Locari test set up

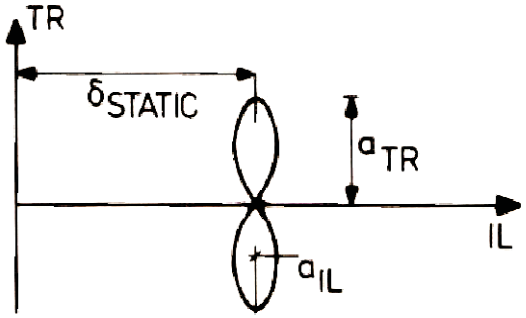

Figure 3.2: General behavior at lock-in, Locari

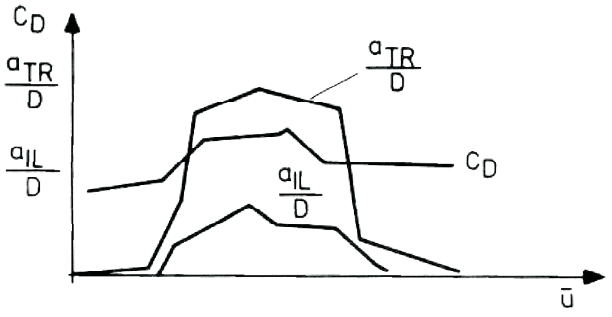

Figure 3.3: Format of results, Locari

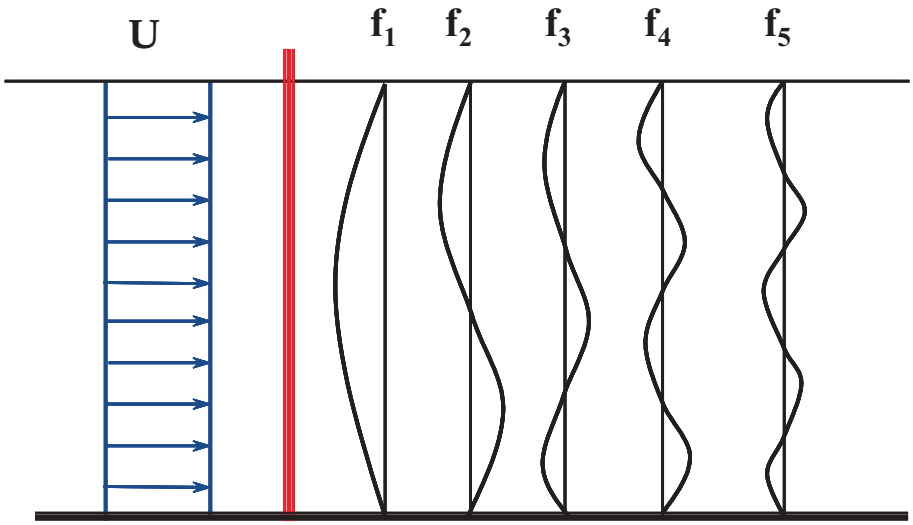

Figure 3.4: Vertical riser in uniform current, Figure from Larsen (2005)

3.1.1 Uniform current

In this approach, the mode is selected that has the largest response amplitude for free oscillation tests, see Figure 3.5.

By calculating the reduced velocity, the dominating eigen frequency is selected as the frequency that will have the largest cross flow response on the A/D - U_R plot. Each eigen frequency will give a unique reduced velocity since the current speed is constant along the riser.

As seen in the figure, in-line motion (IL) amplitude and the drag coefficient for the selected mode are also given in addition to the cross flow (CF) amplitude. In the case of uniform current, the total response is found as the mode shape with a maximum amplitude equal to the free oscillation 2D test amplitude multiplied by an empirical shape factor, h_{shape} valid for the actual mode shape, ϕ_n. For sine-shaped mode, this factor will be equal to 1.14.

In-line response frequency must be twice the CF response frequency, and the mode, ϕ'_n is selected as the mode associated to the IL eigenfrequency that is closest to this value.

$$x_{CF}(z,t) = h_{shape} y_{0,CF} \phi_n(z) \sin(\omega_n t) \tag{3.1}$$

$$y_{IL}(z,t) = h_{shape} y_{0,IL} \phi'_n(z) \sin(2\omega_n t) \tag{3.2}$$

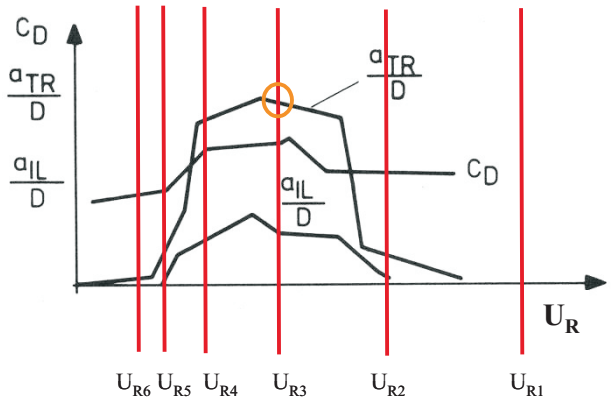

Figure 3.5: Selecting the mode with the largest response amplitude, Larsen (2005)

This method is conservative since the maximum amplitude for a flexible beam will be smaller than for the 2D test.

An even simpler method is to say that the response frequency is an eigenfrequency closest to the Strouhal frequency: $f = St.U/D$, where $St = 0.19$. IL frequency and mode as for the former method. The maximum response amplitude for CF can be set to D (diameter), and IL amplitude = 0.2 D. However, the ratio between IL and CF amplitudes varies considerably, and will in most cases be between 0.2 and 0.4, Swithenbank (2008).

This method will normally be conservative and can give an upper estimate for stresses for a slender marine structure subjected to uniform current.

3.1.2 Sheared current

Figure 3.6 shows a vertical riser with varying cross section diameter in sheared current. Along the riser, the vortex shedding frequency varies due to diameter and flow speed variations.

The riser has many eigenfrequencies and among them the frequency or frequencies that will be excited shall be found.

A more complete empirical response model must handle cross section and current velocity variations, be able to find the response frequency (or frequencies) and find added mass as well as lift coefficient along the riser.

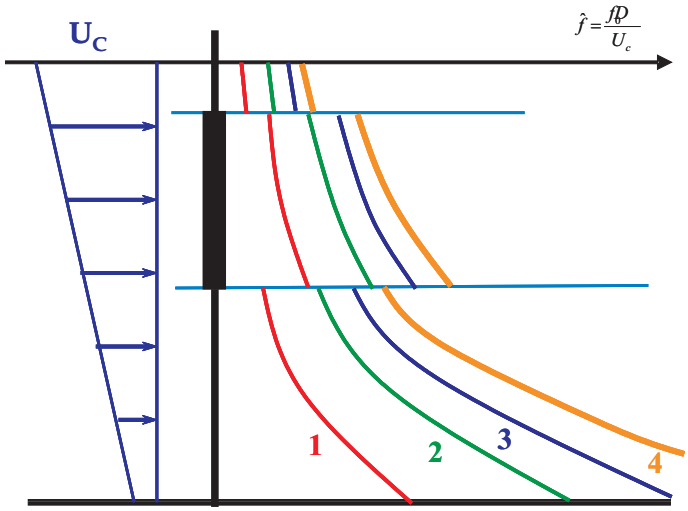

Figure 3.6: Sheared current and varying cross section diameter, Larsen (2005)

3.2 VIVANA

VIVANA is a software program tailor made for VIV analysis of slender marine structures in current, see VIVANA User Manual, Larsen et.al. (2000).

3.2.1 Analysis procedure

- **Step 1.** *Static analysis*

  The eigenfrequencies and mode shapes for the pipeline in still water are found. Added mass is applied as for a pipe in still water according to data given by the user. The results will be given in terms of eigenvectors and associated eigenfrequencies.

- **Step 2** *Eigenvalue analysis*

  A subset of all calculated eigenfrequencies will define the complete set of possibly active eigenfrequencies. These are found from a excitation range criterion defined in terms of an interval for the non-dimensional frequency where excitation can take place. The present study applied an interval of, $0.125 < \hat{f} < 0.3$, which is somewhat wider than traditionally used for VIV analysis. This decision was taken on the basis of observations form model tests; see (Huse et

al. 2002). Note that even if the current speed and diameter are constant along a pipe, more than one eigenfrequency might become active since the non-dimensional frequency depends on the eigenfrequency itself.

- **Step 3** *Identification of possible and dominating excitation frequencies*

  The response is always assumed to take place at an eigenfrequency, but the initial eigenfrequencies will not become true response frequencies since added mass will depend on the non-dimensional frequency and hence also on the eigenfrequency itself. An iteration is hence necessary to obtain consistency between added mass and eigenfrequency. Note that the result will be a response frequency that is different from the original eigenfrequency and also different from the Strouhal frequency defined as the vortex shedding frequency for a fixed cylinder. The new frequency will in fact become a compromise between the two, and will normally increase for increasing current speed due to a continuous reduction of added mass; see (Larsen et.al. 2001)

- **Step 4** *Analysis of the response at the dominating frequency*

  The next step is to decide which eigenfrequency will dominate. The following criterion is proposed:

$$\int_{L_E} U^2 D^3 \left(\frac{A}{D}\right)_0 dl \tag{3.3}$$

  where $(A/D)_0$ is the maximum possible response for a rigid cylinder under the actual conditions. This value can be found from the lift coefficient curve, (see Figure 3.9). This curve is defined by four parameters that all are given as functions of the non-dimensional frequency, (see Figure 3.10). The integral is taken within the excitation zone, which normally will include the total length of a free span.

- **Step 5** *Response analysis for other frequencies than the dominating frequency*

  The frequency response method is used to calculate the dynamic response at the dominating frequency identified in the previous step. The analysis applies an iteration that converges when the response is in accordance with the non-linear models for excitation and damping. The result of this analysis is hence complete information of exciting forces and damping coefficients along the pipe.

- **Step 6** *Post-processing of results*

  Post-processing includes fatigue analysis and calculations of amplified drag coefficients.

3.2.2 Added mass model in VIVANA

The added mass model in VIVANA is applied based on the results from Gopalkrishnan (1993). It is assumed that added mass is independent on the oscillation amplitude, and the curve on Figure 3.7 is found by applying data for $A/D = 0.5$ in Goplakrishnan's database (Figure 2.13).

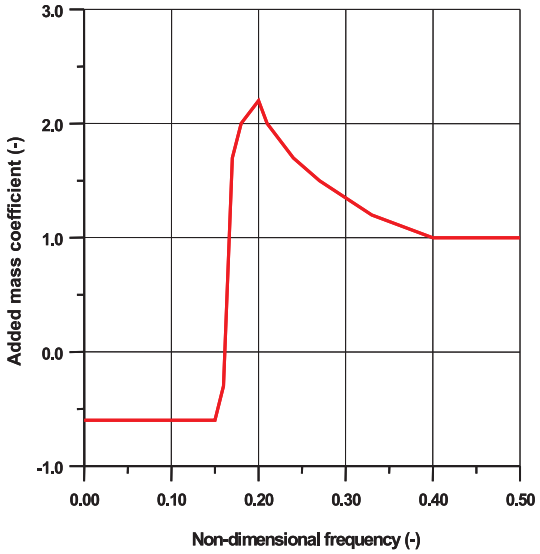

Figure 3.7: Added mass as function of non-dimensional frequency as applied by VIVANA, VIVANA Theory Manual (2005)

By using this approach it is possible to find the response frequency independent on the response amplitude, and independent iteration for the frequency and amplitude can be carried out.

3.2.3 VIVANA lift coefficient model

The lift coefficient model in VIVANA is based on the coefficients found by Gopalkrishnan (1993), but the curves have been modified with respect to maximum oscillation amplitude according to findings by Vikestad (1998). Gopalkrishnan (1993) performed some forced oscillation tests in order to get these results. In continuation, Vikestad (1998) investigated the response amplitude by some free oscillation tests along $C_L = 0$ contour line and found that the maximum response amplitude

is significantly lower for forced oscillation than for the free oscillation tests, (see Figure 3.8).

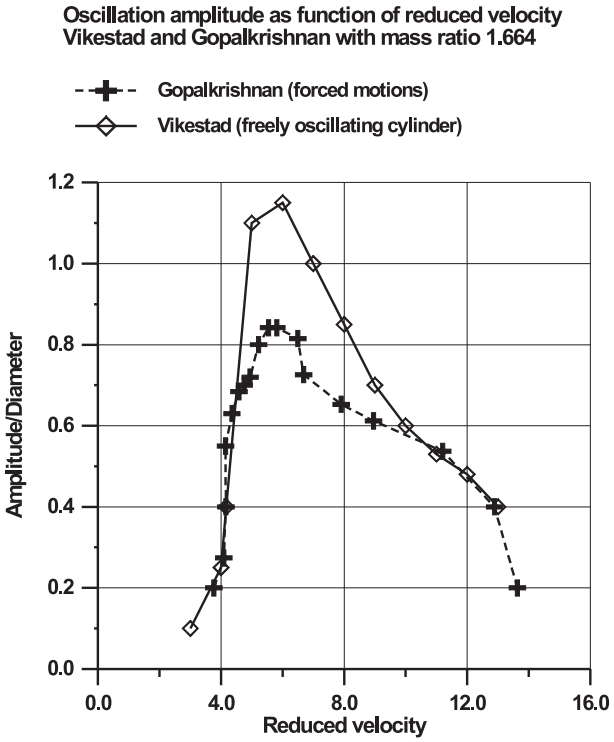

Figure 3.8: Results from forced motion tests and free oscillation tests

VIVANA applies a set of lift coefficient curves where each curve is defined by three points as seen from Figure 3.9. The points are given as functions of the non-dimensional frequency as seen from Figure 3.10. The curve is assumed to have a maximum value at B, meaning that the lines AB and BC can be found as two second order polynomial when the three points A, B and C are defined.

Lock-in vibrations of a short cylinder in a spring is known to have a self-limiting amplitude even if no mechanical damping exists. This feature can be illustrated by the lift coefficient curve on Figure 3.9. If $C_L = 0$ there is no net energy transport between the fluid and the cylinder, meaning that the oscillation is stationary. $(A/D)_0$ on the figure represents hence the lock-in amplitude. Larger amplitudes will give negative lift coefficient, meaning that we will have hydrodynamic damping, while smaller amplitudes will give excitation needed to drive an oscillation with

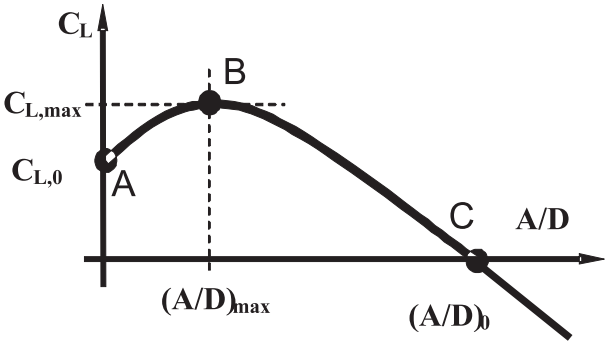

Figure 3.9: Lift coefficient curve as defined in VIVANA, VIVANA Theory Manual

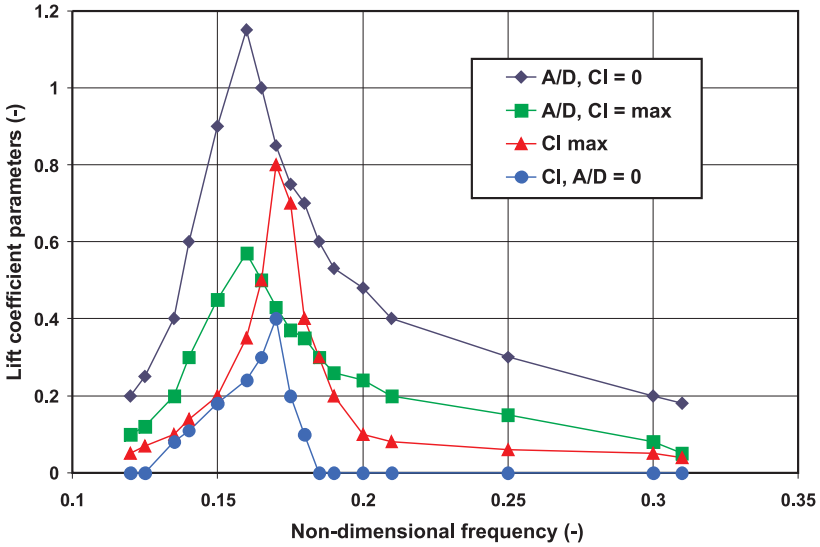

Figure 3.10: Parameters to define the lift coefficient as function of the non-dimensional frequency. (Note that the parameters for the non-dimensional frequency more than 0.2 are only relevant for on-set of mode 1)

some mechanical damping.

If the seafloor damping is low, excitation will take place at moderate amplitudes, while we will have some damping at the largest amplitudes and at the shoulders

(Figure 3.12). Increasing soil damping will reduce the response and the total span length may enter the excitation zone. This way of modeling implies that the lift coefficient curve will define both excitation and damping.

3.2.4 VIVANA excitation and damping model

Most empirical models for risers in sheared current will define an excitation bandwidth in terms of reduced velocity U_R or non-dimensional frequency. This bandwidth will identify an excitation zone along the riser for a given eigenfrequency. Damping will take place outside this zone. There is hence an energy balance between the excitation and damping zones as illustrated on Figure 3.11.

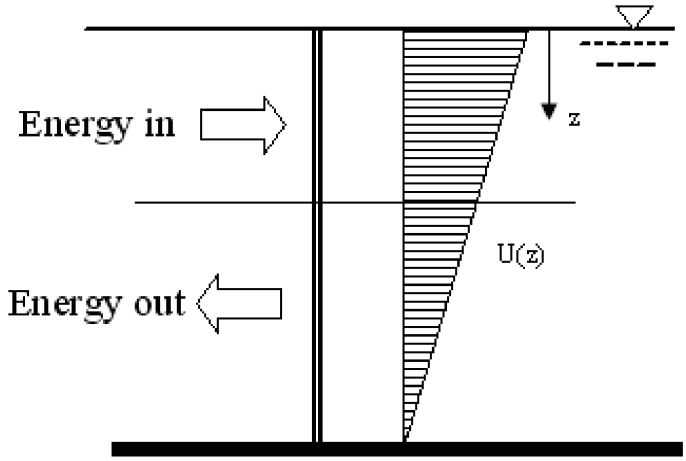

Figure 3.11: Energy balance for riser in sheared current, Figure from Larsen (2005)

The damping model proposed by Venugopal (1996) is used by VIVANA. It is partly based on Gopalkrishnan (1993) experiments on an oscillating cylinder. Vikestad (2000) made other experiments and confirmed that the damping model is conservative; meaning that real damping most often is higher that what is predicted by the model. A riser in sheared current will normally have damping outside the excitation zone along the riser, and energy balance is obtained by equalizing the energy input within the zone and dissipation outside. However, for a free span case the current speed will normally be constant along the pipe. Hence, the excitation zone will formally cover the entire length, and the damping mechanism will become different.

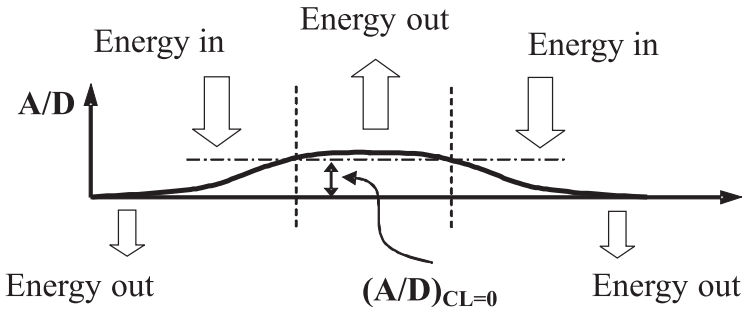

Figure 3.12: Energy balance for free span pipeline, Figure from Larsen (2005)

This can be illustrated by showing the energy balance of the pipeline in Figure 3.12. Soil-structure interaction at shoulders will introduce damping, but the main contribution will origin from large oscillation amplitudes. If the amplitude exceeds $(A/D)_0$ (see Figure 3.9) the lift coefficient will become negative and hence become a damping coefficient. This approach is applied in VIVANA and is an essential feature when dealing with VIV analysis of free span pipelines.

3.2.5 Modifications of excitation range and lift coefficient

An excitation range in terms of upper and lower values for the non-dimensional frequency defines the excitation zone on a structure in a practical flow profile. The interval

$$\hat{f}_{min} = 0.12; \qquad \hat{f}_{max} = 0.2 \tag{3.4}$$

was originally used in VIVANA. This interval was chosen on the basis of Gopalkrishnan's (1993) data, see Figure 3.13.

This figure illustrates how excitation is limited to the area enclosed by the $C_L = 0$ contour curve, and the original interval is seen to contain the high lift coefficient part of the $\{C_L; \hat{f}\}$ space. It is also seen from the curves that there is an area to the right of the selected interval (lower flow speed) with zero lift, but with very low C_L values inside. This area was originally excluded from the excitation range definition.

VIVANA excitation range and lift coefficient have been modified by MARINTEK. Hence, excitation range was extended to

$$\hat{f}_{min} = 0.12; \qquad \hat{f}_{max} = 0.3 \tag{3.5}$$

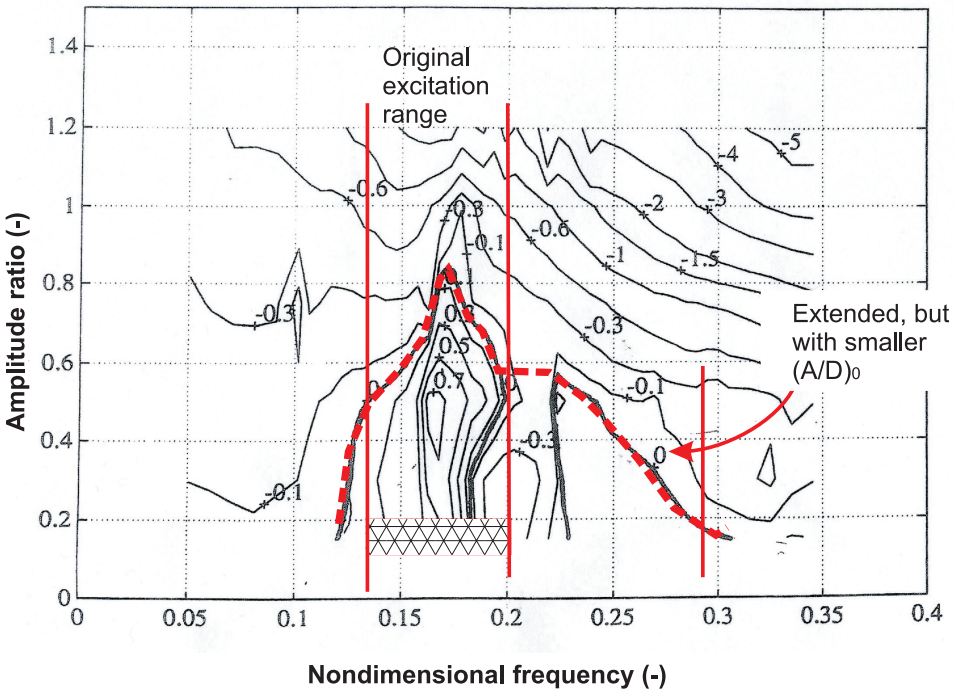

Figure 3.13: Lift coefficient versus non-dimensional frequency, Gopalkrishnan (1993)

and a new set of lift coefficient curves were given. According to Figure 3.9 by defining $(A/D)_0$ (the A/D value that give zero lift) in agreement with Figure 3.13, a significant improvement of VIVANA prediction was obtained. An earlier onset of VIV is seen, and also a more gradual increase of the response amplitude for increasing speed. This improvement is in particular important for free span pipelines since low current velocities often will have a major impact on accumulated fatigue damage. This is normally not the case for long slender beam since response at the primary mode will give very small stresses and therefor be insignificant.

3.2.6 Drag amplification

Drag amplification occurs during VIV. Equation 3.6 by Blevins (1990) and Equation 3.7 by Vandiver (1983) are commonly used for calculating of the drag amplification factor. Figure 3.14 shows the drag amplification which are found using these equations.

$$\frac{C_d(\frac{A}{D})_t}{C_d(A=0)_t} = 1 + 2.1(\frac{A}{D})_t \tag{3.6}$$

$$\frac{C_d(\frac{A}{D})_t}{C_d(A=0)_t} = 1 + 1.043(\frac{2.A_{rms}}{D})_t \tag{3.7}$$

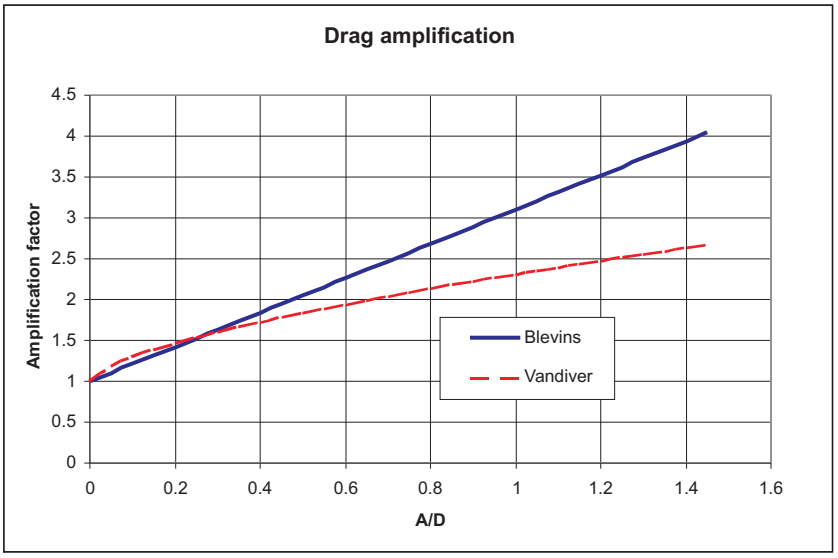

Figure 3.14: Drag amplification factor

3.2.7 Mathematical approach - frequency domain

The frequency response method combined with a three-dimensional finite element model is applied to solve the dynamic equilibrium problem. This method is well suited for this application since the loads are assumed to be acting at one frequency or at a limited number of discrete frequencies. The equation of dynamic equilibrium may be written

$$M\ddot{r} + C\dot{r} + Kr = R \tag{3.8}$$

where M is the mass matrix, C is the damping matrix, K is the stiffness matrix, r is the displacement matrix and R is the excitation matrix. The external loads will in this case be harmonic, but loads at all degrees of freedom are not necessarily in phase. It is convenient to describe this type of load pattern by a complex load vector with harmonic time variation

$$R = Xe^{i\omega t} \tag{3.9}$$

The response vector will also be given by a complex vector and a harmonic time variation. Hence we have

$$r = xe^{i\omega t} \tag{3.10}$$

By introducing the hydrodynamic mass, M_H and damping matrices, dynamic equilibrium can now be expressed as

$$-\omega^2(M_s + M_H)x + i\omega(C_s + C_B)x + Kx = X \tag{3.11}$$

The damping matrix C_S represents structural damping and will normally be proportional to the stiffness matrix. C_B contains damping terms from pipe-seafloor interaction. Elements in the excitation vector X are always in phase with the local response velocity, but a negative lift coefficient will imply a 180° phase shift and hence turn excitation to damping. Since the magnitude of the lift coefficient depends on the response amplitude (see Figure 3.9), iteration is needed to solve the equation. Note that the response frequency is fixed during this iteration. The iteration will identify a response shape and amplitude that gives consistency between the response level, lift coefficients and the local flow condition. The mode shape corresponding to the selected response frequency is used as an initial estimate for the response vector, but the final result is not defined in terms of normal modes.

3.3 Free span pipelines

Vortex induced vibrations may cause large response amplitude on free span pipelines and in consequence, time varying stresses may give unacceptable fatigue damage. A major source for dynamic stresses in deep water free span pipelines is vortex induced vibrations (VIV) caused by current, (see Figure 3.15).

Free span may be caused by seabed unevenness and change of seabed topology such as scouring or sand wave (see Figure 3.16).

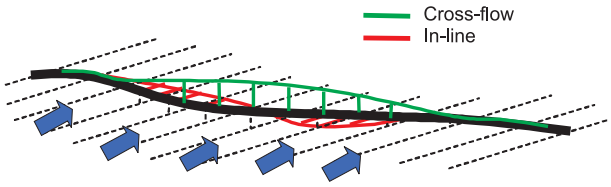

Figure 3.15: Static shape and VIV of free span pipeline

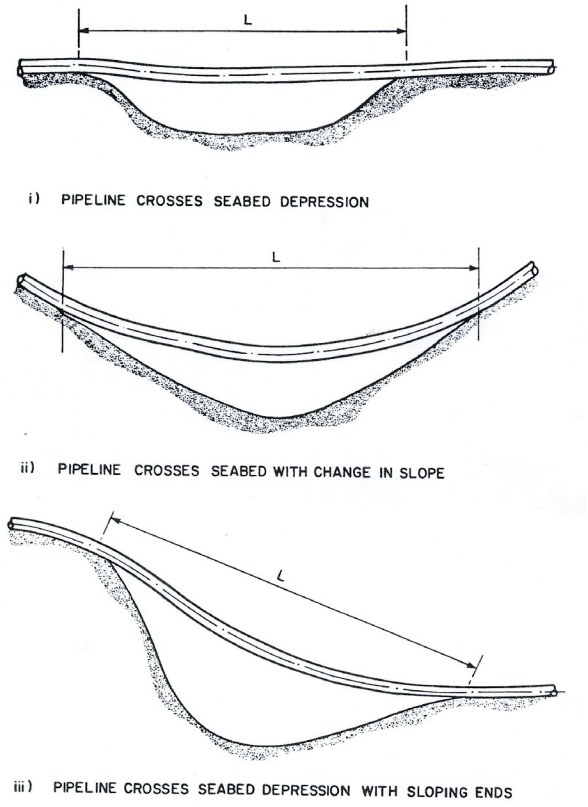

Figure 3.16: Typical examples of free span pipelines, J P Kenny (1993)

3.4 The ideal VIV model for free span pipelines

A structural model will normally include the free span and represent the influence from the pipeline at both ends by proper boundary conditions. Such conditions may consist of a combination of springs, dampers, and external forces, but always represent a simplification as compared to a more complete model. However, an ideal model for analysis of VIV for free span pipelines should be able to take into account effects as follows:

- Start with a correct static condition found from a non-linear static analysis that gives a correct tension, seafloor contact and 3D shape of the pipe. Such an analysis must know the tension during installation and consider later changes in pressure, density of content and temperature. This condition will define the in-line and cross-flow eigenfrequencies for the pipe.
- Describe needed hydrodynamic coefficients (added mass, lift, drag and damping) for a pipe that oscillates in current close to a wall.
- Describe the local current profile including boundary layer effects close to the seafloor.
- Handle any current direction relative to the pipeline and also the combination of current and wave induced forces.
- Predict the correct dominating modes for in-line and cross-flow response for a given current condition.
- Describe the interaction between in-line and cross-flow VIV.
- Describe the interaction between the pipe and seafloor in terms of non-linear stiffness and damping including friction for in-line oscillations of a pipe with seafloor contact.
- Take into account the influence from tension variation on stiffness and hence also on the actual eigenfrequency.
- Be able to analyze adjacent spans and the dynamic interaction between them.

Many researchers have worked on free span pipelines in the recent years, but there are still many challenges regarding this problem. Some of the specific free span needs are:

- Pipe / seafloor interaction
- Multi-span pipelines

- Spatial current profiles
- Oscillations close to sea-floor
- In-line VIV
- Interaction between In-line and Cross-flow VIV
- Damping from large amplitudes

Due to time limitation and scope of works, the first three items have been discussed in this study and the rest addressed as further works.

Chapter 4

Case studies

Multiple spans pipeline, spatial variation of current and effect from temperature variation are presented in this chapter.

4.1 Pipeline with multiple spans

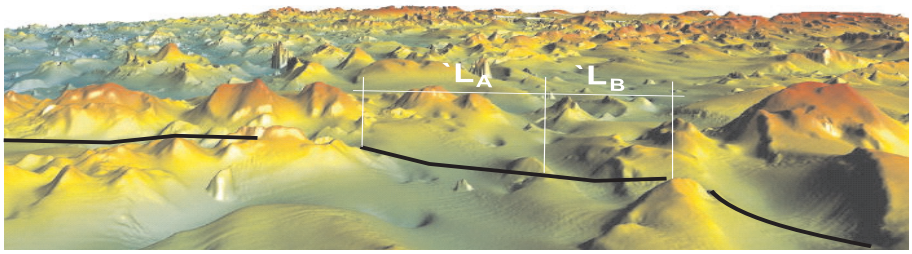

Figure 4.1: Multiple spans on a rugged seafloor, (Norsk Hydro)

Offshore pipelines may frequently pass over the area with uneven sea floor. This causes the pipeline to have multiple spans (see Figure 4.1). Depending on the length

of each spans and the length of the shoulder between the neighboring spans, these spans may interact with each other. It is therefore needed to investigate this interaction and thereby improve the understanding of multiple spanning pipelines.

In this chapter we will try to investigate the dynamical interaction between neighboring spans and compare each of them to an identical single span.

4.1.1 Introduction

For a pipeline laid on a very rugged sea floor it has been shown that the single span approach has some limitations due to the following reasons:

- Neighboring spans may be separated only by short sections of contact with the seabed. In such situations the static and the dynamic interference between adjacent free spans is such that it is not possible to define a limiting free span length beyond which it is necessary to take remedial measures, both for temporary and permanent conditions. The concepts of maximum allowable free span length, as conventionally applied to offshore pipelines, fails.
- The dynamic response of one span can not be calculated by considering this span only. The neighboring spans must also be taken into account since the loads and response there may have significant influence.
- The irregular sea floor topography has a strong influence on current velocities close to the seabed and further studies are needed to correlate measurements of on-bottom currents flowing over rough seabeds and characteristic estimates to be used for the pipe structural integrity.
- The free stream turbulence is such as to influence the hydroelastic loads acting on the pipe and further insight is necessary on the subject matter.

4.1.2 Initial study of the behavior of a single span

Calculation of VIV has been carried out for the single free span. Data for the pipe cross section are given in Table 4.1, and results from the computations are presented in Figure 4.2, Figure 4.3 and Figure 4.4. Figure 4.2 illustrates how the eigenfrequency for constant added mass and the response frequency varies with increasing current speed. The eigenfrequency is influenced by the 3-dimensional shape of the span and the tension, while the response frequency is found from the added mass iteration that was described previously, see Larsen et al. (2002).

Pipe properties		
Outer diameter	0.556	m
Inner diameter	0.508	m
Wall thickness	0.024	m
Modulus of elasticity	2.06E+11	N/m^2
Density of pipe material	7850	kg/m^3
Density of content	148.07	kg/m^3
Submerged weight	942	N/m

Table 4.1: Key data for the pipe

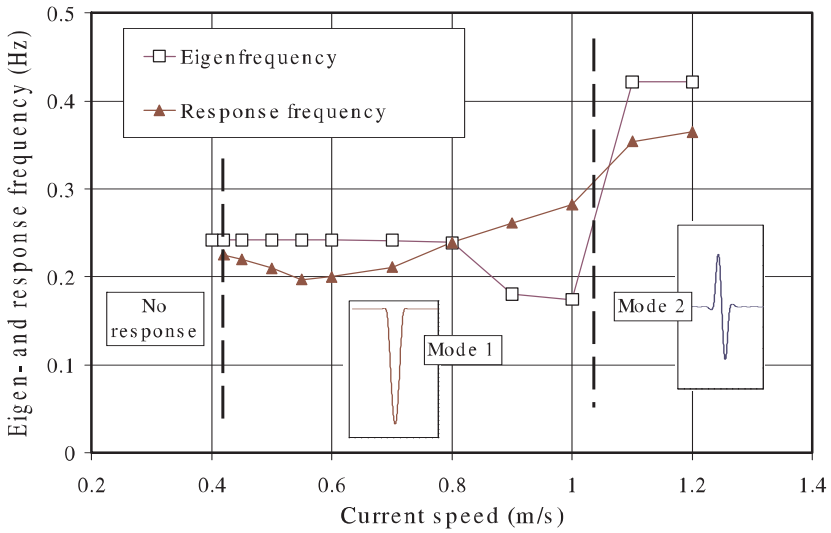

Figure 4.2: Frequency and mode evaluation for increasing current speed with constant added mass, Larsen et al. (2002)

The response frequency is seen to be lower than the initial eigenfrequency for low current speeds. This is a consequence of high added mass for the associated non-dimensional frequency. Increasing speed beyond 0.8 m/s gives higher response frequencies even if the initial eigenfrequency is seen to be reduced due to changes in the static pipe condition. The added mass will here be low and even experience negative values. The transition from first to second eigenfrequency is also clearly seen on the figure. This is a result of the applied criterion for dominating response frequency given in Equation 3.3. The response frequency is again seen to be lower than the original eigenfrequency since added mass again is higher than for the still water case.

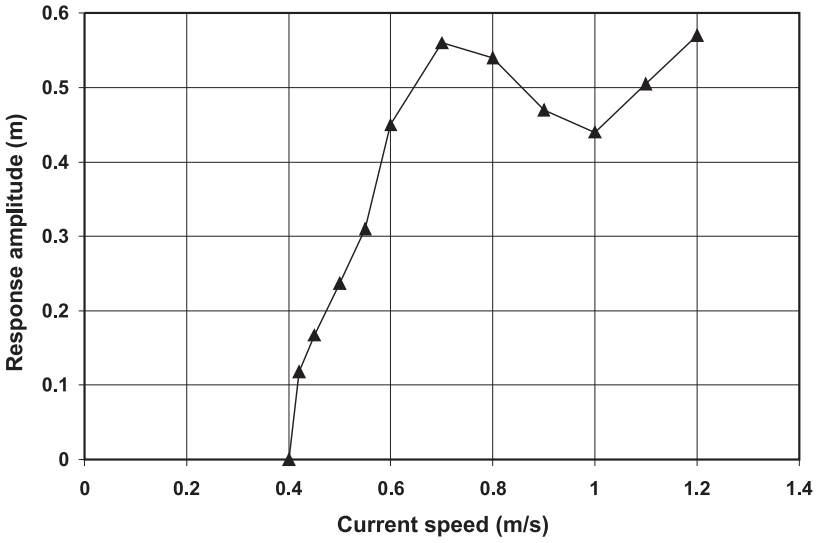

Figure 4.3: Maximum response amplitude for increasing current speed

Figure 4.3 presents maximum response amplitude as function of current speed. Cross-flow response is seen to start at a speed of 0.4 m/s for this case. In-line VIV is known to take place at lower speeds, but this is not included here. A maximum value is seen at a speed of 0.7 m/s, and the response is seen to drop after this level. A new increasing tendency is seen for speeds above 1 m/s, where the transition from first to second eigenfrequency takes place.

Reduced velocity is often used when presenting VIV amplitudes. Consistent use of this parameter means that the initial eigenfrequency must be used as reference, and not the response frequency. Figure 4.4 shows the variation of maximum response amplitude versus reduced velocity. The dotted line links results for increasing values of the current velocity. The results for second mode will have a higher eigenfrequency, which means that the reduced velocity will drop. The results are compared to the response curve applied by Det Norske Veritas (1998), where the reduced velocity is used as controlling parameter. Results are seen to follow the DNV curve quite well. The disagreement for the highest reduced velocity might be caused by the mass ratio that will influence the computed results but is not considered by the DNV guideline.

One may say that there is no reason to have a sophisticated analysis tool that

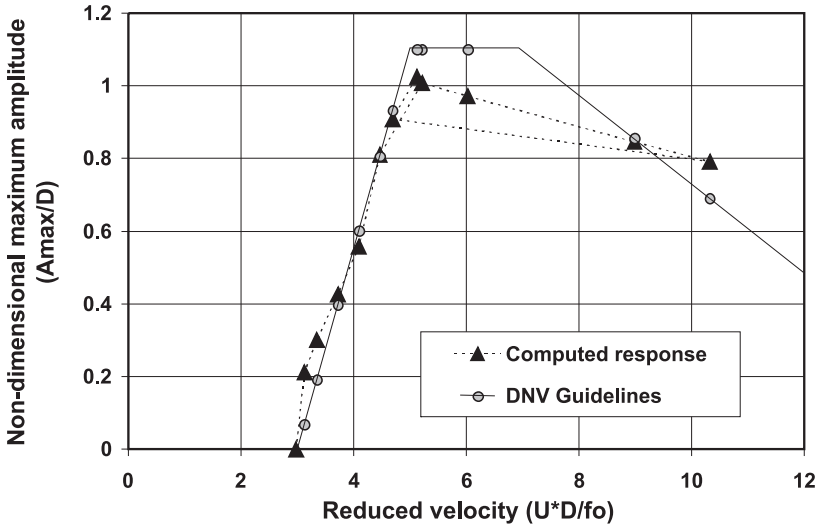

Figure 4.4: Non-dimensional maximum response amplitude versus reduced velocity

solely reproduces a simple guideline curve. This is of course correct, but the benefit of the analysis tool presented here is its capability to calculate the eigenfrequencies for complex cases and also compute VIV response under other current and boundary conditions than what is offered by the guidelines. It is possible to apply the present method on cases with current speed gradients along the pipe that are caused by the boundary layer effect, and also to account for complex damping mechanisms from pipe/fluid/seafloor interaction. This will be a subject for further investigations at shoulders.

4.1.3 Response amplitudes

If two spans are close to each other, there might be some dynamic interaction between them. This case is often referred to as a multiple free span pipeline. If two adjacent spans are different, VIV on one span might be influenced by the other. This influence may lead to increased or decreased response depending on the current speed and the properties for the two spans. The extension of the contact zone between the spans and seafloor parameters will of course also be important for the interaction effect.

A double span has been analyzed (see Figure 4.5) and results are compared to

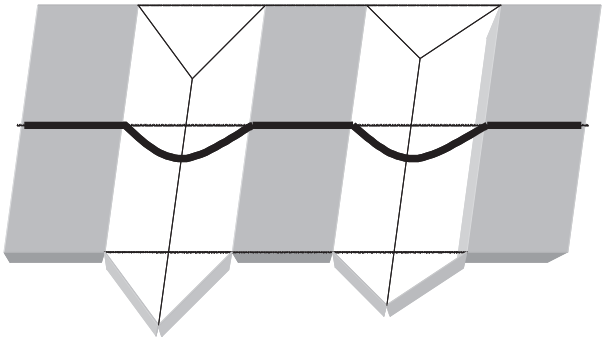

Figure 4.5: Multi free span pipeline

two single spans with identical properties as each individual span in the multi span case. The span lengths were 156 m and 92 m respectively.

The length of the contact zone was 25 m. Soil stiffness has been chosen from DNV recommended practice for free span pipelines (2001), using data for a very soft soil. Friction coefficients are taken from sub sea pipeline code (BS 8010). The current speed varies from 0.36 to 0.8 m/s.

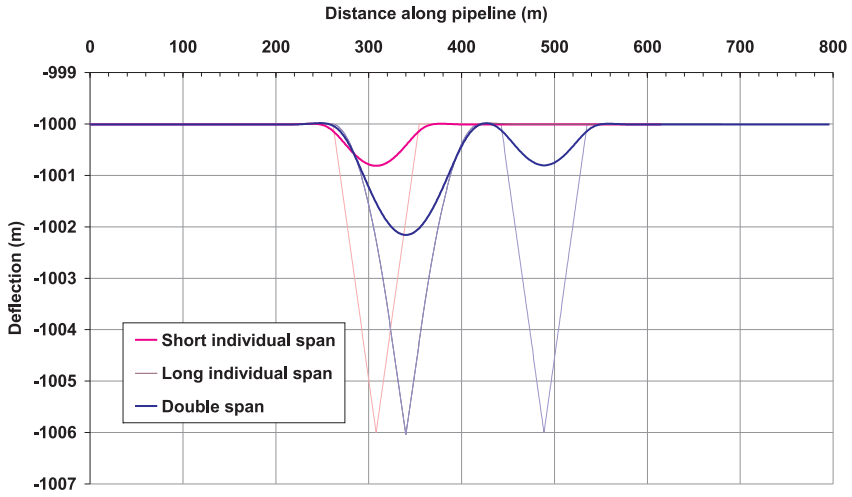

Figure 4.6: Static deformation of pipeline related to bottom profile

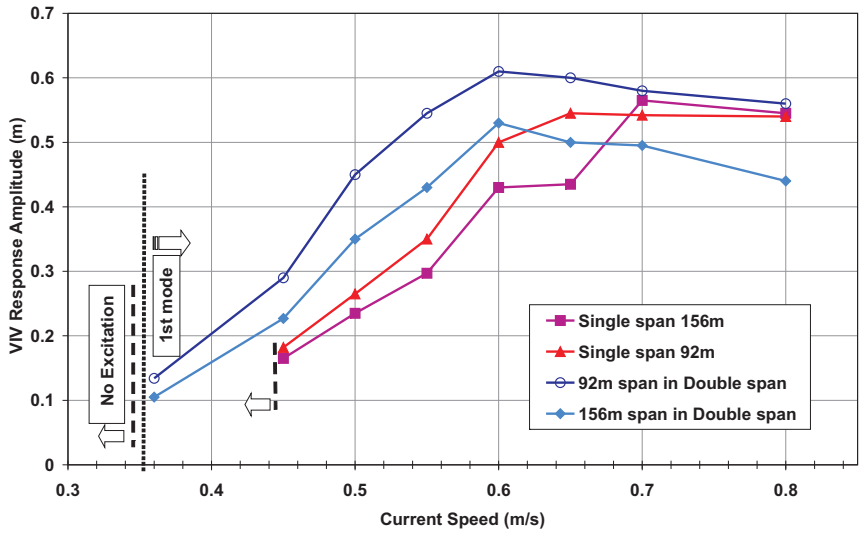

Figure 4.7: VIV response amplitude of single span and double span pipeline

The position of the static deformation of the double and single span pipelines related to the bottom profiles shown in Figure 4.6.

VIV response amplitudes from the multiple span cases are compared with the single span cases in Figure 4.7. In the case of double span there is no excitation at lower current speed than 0.36 m/s, while for single span cases this limit was found to be 0.45 m/s. All cases are excited in mode one.

It is interesting to observe that the response for the double span case is higher than for the single spans up to 0.6 m/s. After this point the trend is different for the cases. The amplitude amplification in one of the span caused by influence from the other span can also be seen in this figure.

The results from the short individual span and long individual span is very close when current speed is lower than 0.6 m/s, but it can be different in the general case since the sag in this case is comparably lower in the shorter span.

Figure 4.8 shows the response amplitudes for the double span and the two individual spans for current speed equal to 0.6 m/s. Note that the horizontal scale is not correct for the three plots since the individual spans have identical lengths as the spans in the double span case. The figure clearly illustrates that the response of the double span is larger than the individual spans. The reason for this

is found to be that the phase angle between the responses for the two spans in the double span case is 180 degrees, meaning that both spans will feel an active boundary that amplifies its response. The analysis model is able to capture this effect since consistency of response phase along the pipe is a part of the iteration process.

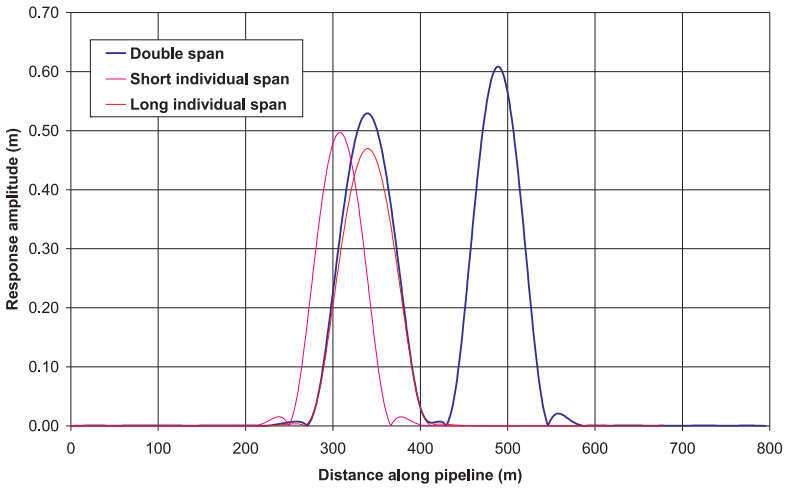

Figure 4.8: Response amplitudes for double and individual spans, current speed = 0.6 m/s

Figure 4.9 shows the lift coefficient curve for the double span pipeline at current speed 0.6 m/s. As seen in the figure, the energy transfers from the longer span to the shorter span and that amplifies response amplitude in the shorter span.

The reason for the response amplification in one of the span is illustrated by energy transfer hypothesis in Figure 4.10.

The lift coefficient C_L defines the component of hydrodynamic force which is in phase with oscillation velocity and can be used to define the energy balance in the system.

For a steady state system, the lift coefficient is zero and there is no energy in or dissipated from the system (in the case of zero mechanical damping). However, in an oscillating system, there is a balance between the energy in and out from the system so that the energy gets into the system should be dissipated at the other part of the system.

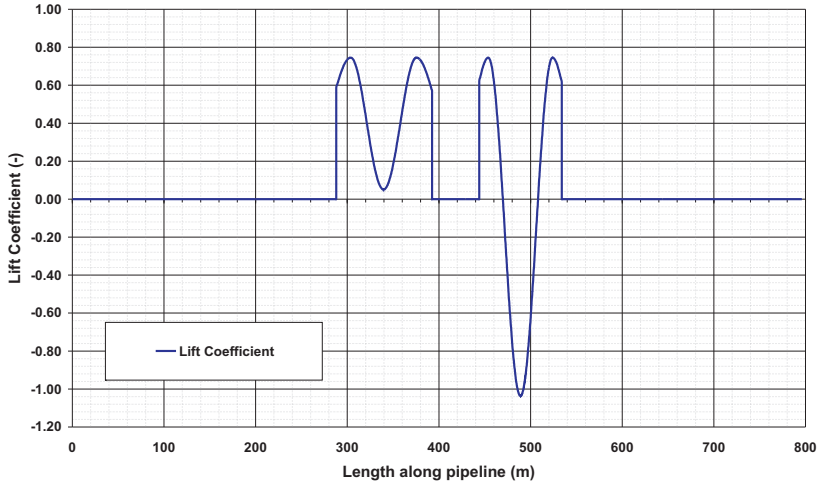

Figure 4.9: Lift coefficient for double span pipeline, current speed = 0.6 m/s

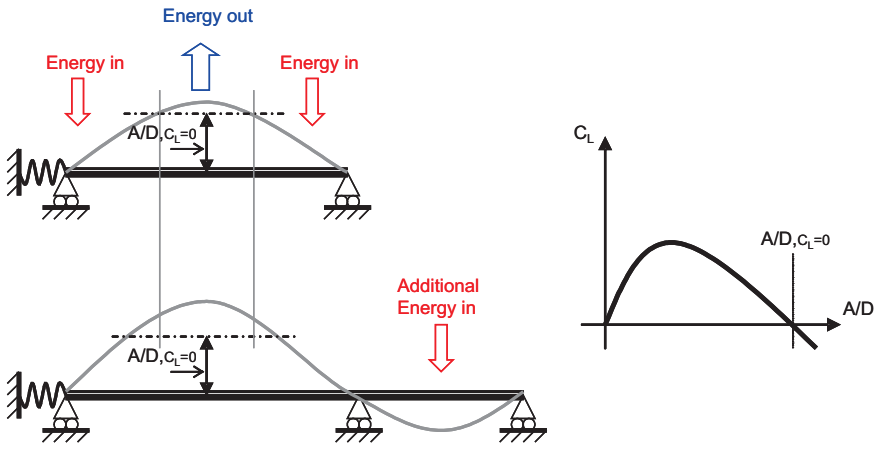

Figure 4.10: Energy transfer between two adjacent spans

As seen in the lift coefficient curve in Figure 4.10, the system is in excitation for the positive value of the lift coefficient where the response amplitude is less than the amplitude which gives $C_L = 0$, and in damping for the negative value of the lift coefficient where the response amplitude is larger than this amplitude. This is the reason that a system under vortex induced vibration is self limited.

For a single span pipe it means that the response amplitude will be found as a balance between energy out at the middle of the span with larger amplitude and energy in at both side of the pipe with lower amplitudes.

For a multiple span pipe, however, one span can influence the adjacent span so that the energy can be transferred from the span with lower response amplitude to the part of the adjacent span with larger amplitudes in order to keep the energy balance in the whole system and this may be appeared as the response amplification in one of the span.

Soni and Larsen (2005) have investigated the interaction between the adjacent spans more in detail and can be referred to for more information.

4.1.4 Response frequency

Mode shapes for the double span and the longest single span are presented in Figure 4.11 for a static condition corresponding to a current speed of 0.7 m/s. The dominating second mode for the double span has large response for the shortest span and almost no displacement for the longest span. This explains why the response of the longest span is significantly reduced as soon as the second eigenfrequency becomes active.

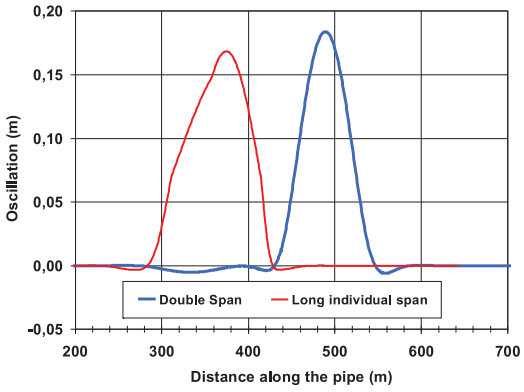

Figure 4.11: First mode for the longest individual span and second mode for the double span

The variation of eigen- and response frequencies for increasing current speed is shown for the double span case in Figure 4.12.

The eigenfrequency is almost constant except for a small jump when the dominating mode changes from the first to the second mode. The response frequency, however, decreases until the current speed reaches 0.5 m/s and then increases. This trend is similar to what was shown for the single span in Figure 4.2, and the reason for this trend is also the same.

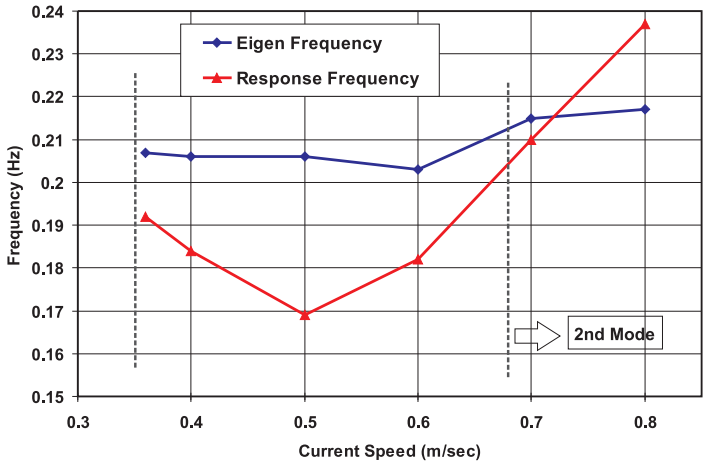

Figure 4.12: VIV response frequency and eigen frequency from the double free span pipeline

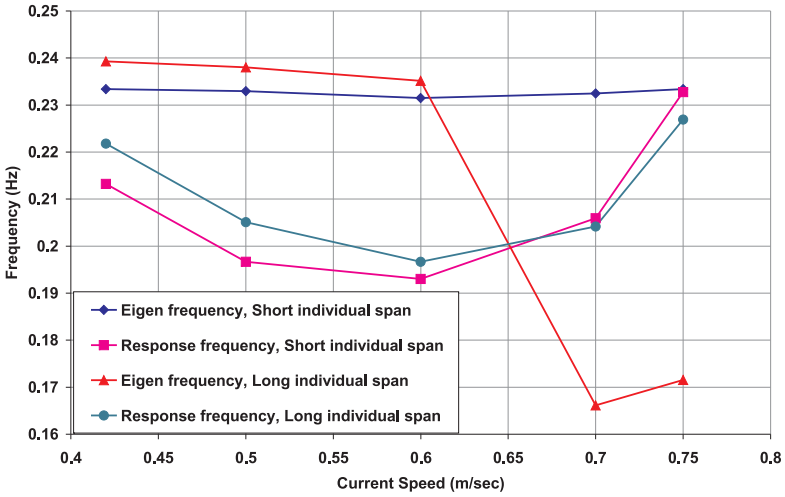

Figure 4.13: VIV response frequency and eigen frequency from single free span pipelines

Figure 4.13 shows the same variation for the two single span cases. The response

frequencies decrease until 0.6 m/s and then increases. There is a drop in the eigen-frequency for 156 m span case after the current speed equals 0.6 m/s. The reason is changes in the static pipe condition as previously discussed for Figure 4.2. Note that the sag is different for the short and long individual span with the same current speed and is lower in the short one.

4.1.5 Results in time domain

Time domain analysis of double span pipeline has been performed to investigate more about the interaction of neighbor spans. In this regard, the same pipeline as the previous section with contact zone length 25 m between two spans has been chosen. The current speed is 0.6 m/sec and axial tension set to 250 kN.

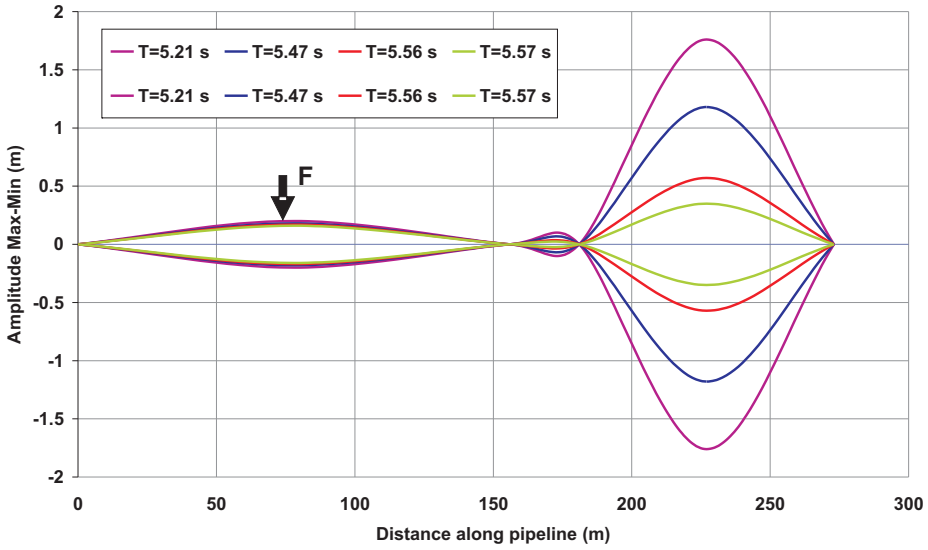

Figure 4.14: Amplitude envelope curves

In the time domain analysis, a unit dynamical force is applied at the middle of the longer span. The purpose is to show the interaction from longer span on the adjacent span by varying the dynamical force period.

Figure 4.14 shows amplitude envelope curve for the double span pipeline with different dynamical force periods. The period is changing from 5.21 *sec* to 5.57 *sec*.

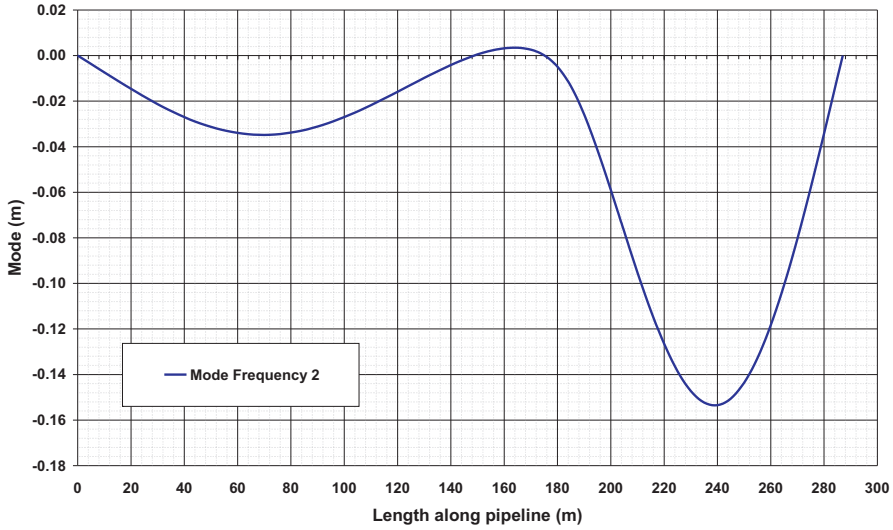

Figure 4.15: Mode shape, double span pipeline, $T = 5.56sec$

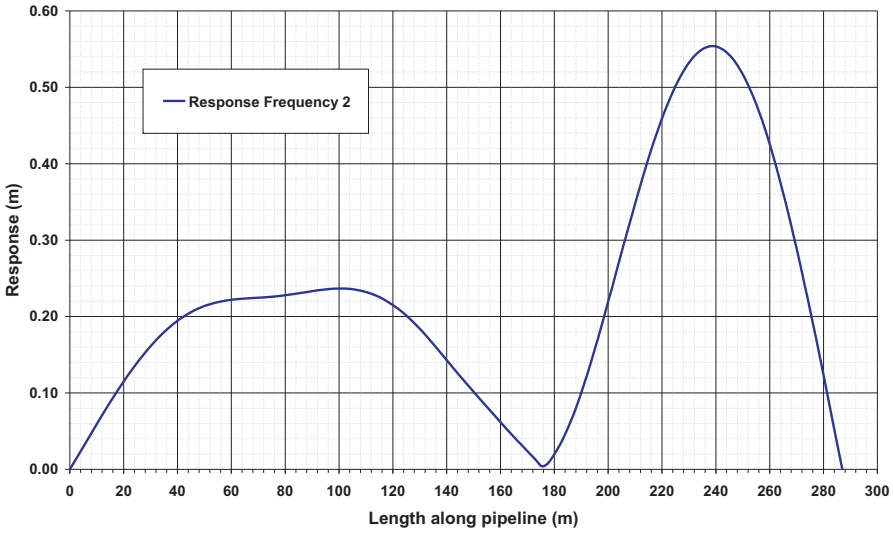

Figure 4.16: Response amplitude, double span pipeline, $T = 5.56sec$

As seen in the figure, the amplitude shows small variation for the longer span by changing the force period, while far larger variation are seen for the adjacent span.

Figure 4.15 and Figure 4.16 shows the mode shape and response amplitude for the second mode while the period is 5.56 *sec*. The amplitude amplification on shorter span which is influenced by the vibration in longer span can be seen clearly.

While the period is 5.57 *sec*, the amplitude for shorter span is 0.35 m. This value is 1.76 m when the period is 5.21 *sec*. This significant difference happened by changing the period 0.36 *sec* and since the force is applied only on the longer span, obviously shown that the excitation in the shorter span occurs by dynamical interaction between the spans.

4.2 Influence from local current profile

4.2.1 Introduction

The influence on VIV from local variation of current velocity along the free span is of practical importance and theoretical interest.

A free span pipeline will necessarily oscillate close to the seafloor. The seafloor will therefore has some influences on the ambient flow profile and also on the flow pattern around the cylinder during oscillation (see Figure 4.17). Hydrodynamic parameters such as added mass and lift force coefficients may vary as a function of gap G and oscillation amplitude A. Some researchers have worked on this problem and done some experiments such as Greenhow (1987) and Sumer (1994), but there is still lack of data. A significant improvement of the response model with respect to this effect is therefore not possible without an extensive test program.

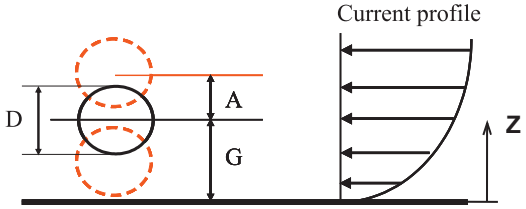

Figure 4.17: Pipe oscillation close to a wall, C_L and C_A as function of A/D, G/D and ω

4.2.2 Spatial current profile

Soulsby (1997) studied the dynamics of marine sands and clays and found the local current profile above seabed. According to Soulsby, the most commonly used measure of the current speed at a particular time and place is the *depth-averaged current speed*, $\bar{U}$. This is related to the velocity profile $U(z)$ through the definition

$$\bar{U} = \frac{1}{h}\int_0^h U(z)dz \tag{4.1}$$

where $\bar{U}$ is depth-averaged current speed, h is water depth, $U(z)$ is current speed at hight z and z is hight above seafloor.

The lower limit of the integral has to be changed from 0 to z_0 if the velocity profile becomes zero at a hight $z = z_0$ (e.g. for a logarithmic velocity profile).

Close to the bottom the current velocity U varies with the height z above the bed according to the logarithmic velocity profile

$$U(z) = \frac{u_*}{\kappa} \ln(\frac{z}{z_0}) \tag{4.2}$$

where u_* is friction velocity, z_0 is bed roughness length and κ is Von Karman's constant (=0.40).

The friction velocity u_* is related to the bed shear stress through the relationship.

$$\tau_0 = \rho u_*^2 \tag{4.3}$$

The bed shear stress is most closely related to the current velocity near the bed. Consequently, the above relation can be written by relating τ_0 to the current speed U_{100} at a hight of 1 m above the bed:

$$\tau_0 = \rho C_{100} U_{100}^2 \tag{4.4}$$

For clay $z_0 = 0.2mm$ and $C_{100} = 0.0022$, then Equation 4.2 can be expressed as

$$U(z) = 2.5\sqrt{0.0022} U_{100} \ln(\frac{z}{0.0002}) \tag{4.5}$$

The range of heights for which Equation 4.2 is valid is from a few centimeters above the bed up to about 20-30% of the water depth in shallow water (say, up to z=2 to 3 m), or 20-30% of the boundary-layer thickness in deep water (say, up to z=20 to 30 m).

Equation 4.2 applies to steady flow without density stratification over a flat (but possibly rippled) seabed, well away from structures, and outside the surf zone.

4.2.3 Analysis results

Figure 4.18 shows the spatial varying current profiles that used in the case studies. To investigate the influence from spatial current variation, three different pipelines are investigated. Two of them are single spans with 156 m and 92 m span respectively. The third one is a double span pipeline with the spans identical to the span

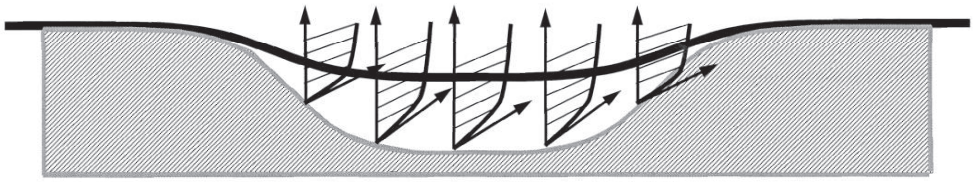

Figure 4.18: Spatial varying current profiles

in each single spans. The bottom profile under each span in the double span is also identical to the bottom profile for each single span case. The contact zone between two spans in the double span is 25 m. The key data for all pipeline presented in the analysis is the same and given in Table 4.2. Regarding the explanation in the previous section, different spatial current profiles are created for each seafloor.

Pipe properties		
Outer diameter	0.556	m
Inner diameter	0.508	m
Wall thickness	0.024	m
Modulus of elasticity	2.06E+11	N/m^2
Density of pipe material	7850	kg/m^3
Density of content	148.07	kg/m^3
Submerged weight	942	N/m

Table 4.2: Key data for the pipe

The bottom profile for a double span pipeline shown in Figure 4.19. 9 different spatial current profiles are made for this bottom profile.

Figure 4.20 illustrates the spatial current profile for two single pipelines, one with 156 m span and the other with 92 m which both corresponds to the reference current speed 0.7 m/sec. The same current profiles is also presented for each span of the double span correspondent to the same span in the single span pipeline. As seen in this figure, the value of the spatial varying current profile at the mid span is almost the same with the uniform current speed which corresponds to 0.7 m/sec. But, the significant difference can be seen at the shoulders -at the end of each span- where the pipeline is gradually getting off from the seafloor.

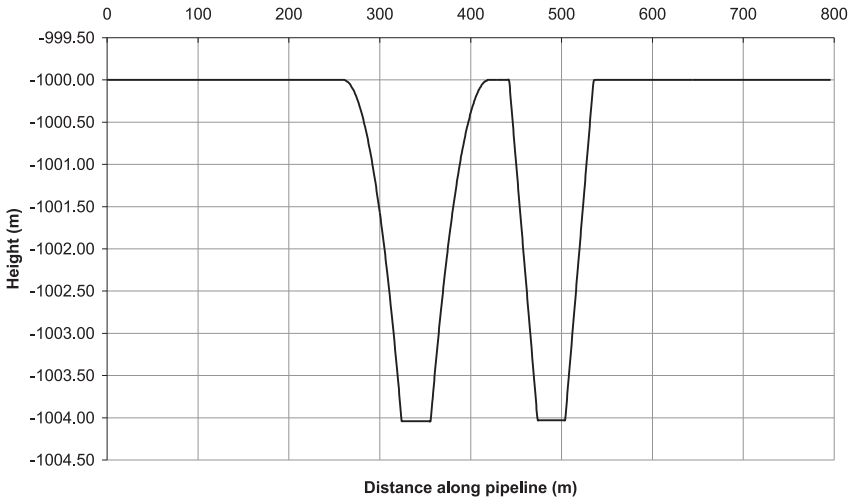

Figure 4.19: Bottom profile for the double span pipeline

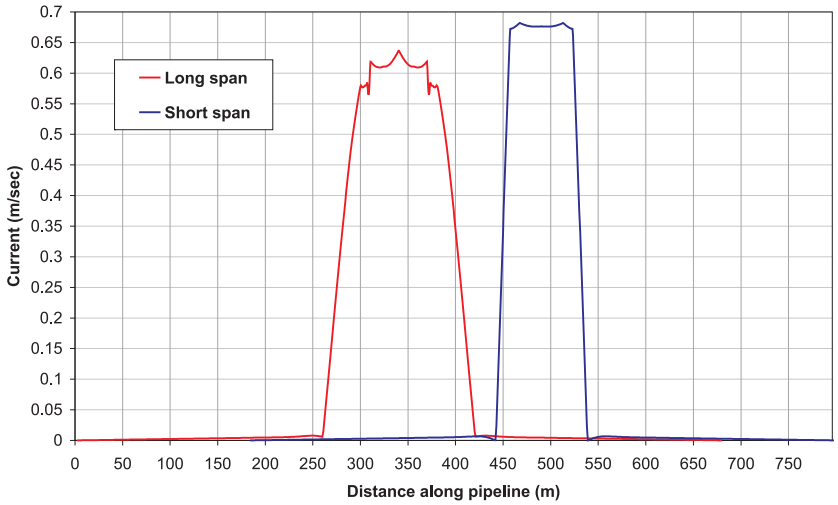

Figure 4.20: Spatial varying current profile, the reference current speed at level -1000 m is V=0.7 m/sec

In the following, results from the pipeline -both single and double spans- with spatial varying current profile will be compared with the same pipeline exposed to the uniform current with the same reference speed.

Figure 4.21 and Figure 4.22 respectively show the dimensionless response amplitude and response frequency for a pipeline with 156 m span for both spatial and uniform current conditions. Figure 4.21 shows that the pipeline in both conditions starts to vibrate at the same current speed 0.5 m/sec. For higher current speeds, there is a significant difference between the response amplitude for the two conditions until the current speed reaches 0.8 m/sec. The response amplitude is almost the same for both cases when the speed is 0.85 to 1.2, but one may note that the response frequencies are different (see Figure 4.22). That means different frequency and current velocity from one case cause a non-dimensional frequency which corresponds to the same lift coefficient value as the other case and then lead to the same response amplitude for both cases.

Figure 4.23 shows the dimensionless response amplitude for the pipeline with 92 m span for both spatial and uniform current cases. The excitation begins at current speed 0.5 m/sec for both cases. Some significant differences are observed before 0.8 m/sec.

The differences are less than the case with 156 m span. The reason may be that the sag is larger in the longer span case than the short span. hence, the long span pipe will be closer to the bottom and hence have a lower current speed than the short span for the same reference speed. In addition, as illustrated in Figure 4.20, the current profile for the shorter span case is closer to uniform than for the long span, which will give a larger response.

The response frequency of the pipeline for the both current cases is shown in Figure 4.24. There is some differences in the response frequency of uniform and spatial current. The response frequency for the uniform case has a drop at $1.1m/sec$, that as already explained in section 7.2, may be caused by changing in the static condition of the pipeline.

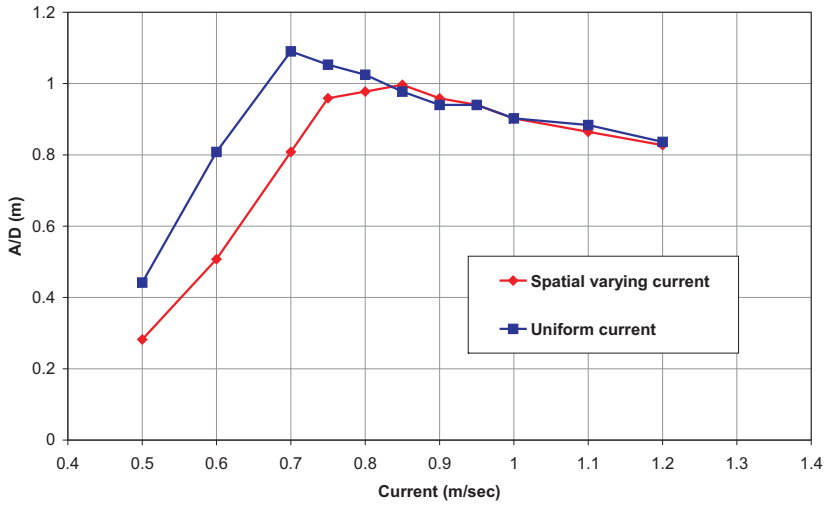

Figure 4.21: Dimensionless response amplitude versus reference current speed for single span pipeline, Span length 156m

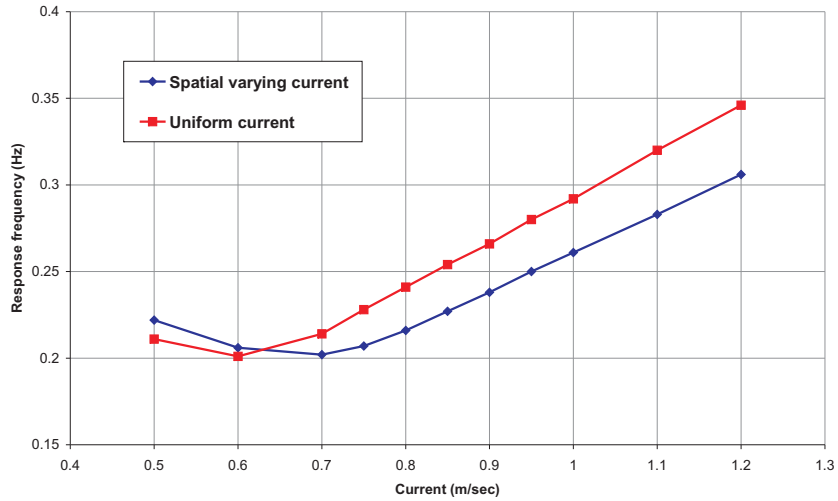

Figure 4.22: Response frequency versus reference current speed for single span pipeline, Span length 156m

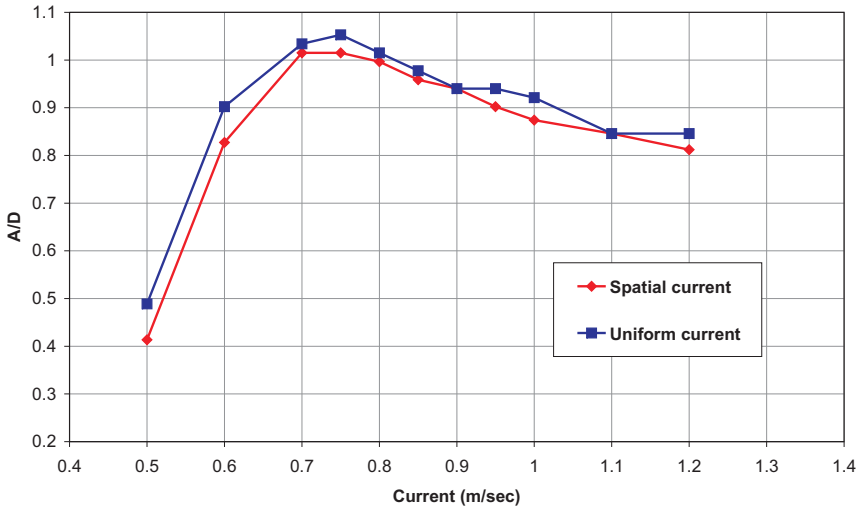

Figure 4.23: Dimensionless response amplitude versus reference current speed for single span pipeline, Span length $92m$

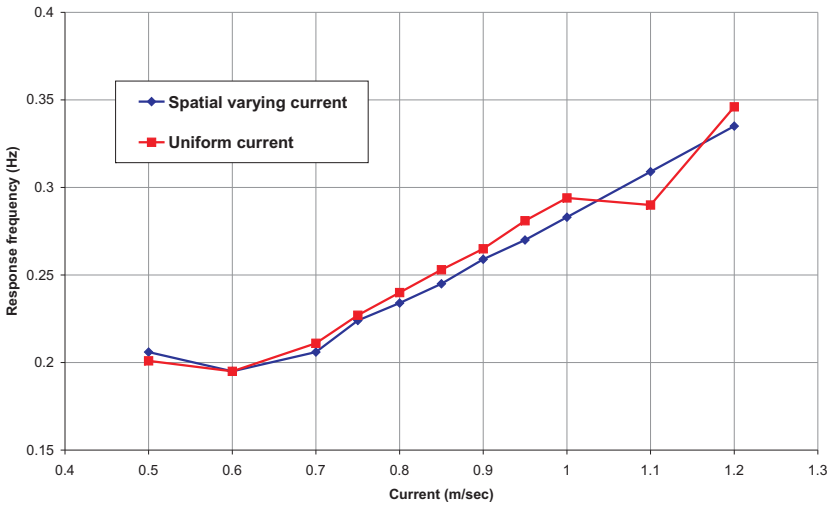

Figure 4.24: Response frequency versus reference current speed for single span pipeline, Span length $92m$

The last case is a double span pipeline with the same spans as the spans in the single span cases. It means that the longer span in the double span pipeline is 156 m and this value for the shorter one is 92 m.

Figure 4.25 and Figure 4.26 are illustrated the dimensionless response amplitude of the double span pipeline for both long and short span exposed to two different current conditions, respectively. One is the spatial varying current profile and the other is the uniform current with the same reference speed.

Figure 4.25 illustrates the results for the longer span with 156 m span. As seen in the figure, the pipeline with uniform current excited at 0.4 m/sec, while this value is 0.5 m/sec for the spatial current. A significant difference between the results from two current profiles is observed. The response amplitude is dropped for the spatial varying current after 0.8 m/sec where the pipe starts to vibrate in mode two.

Figure 4.26 shows the dimensionless response amplitude for the shorter span, 92 m of the double span pipeline. As seen from the figure, the pipeline with uniform current starts to vibrate at 0.4 m/sec, while this value is 0.5 m/sec for the spatial varying current. We can also see a significant difference in general between the response from the two current cases.

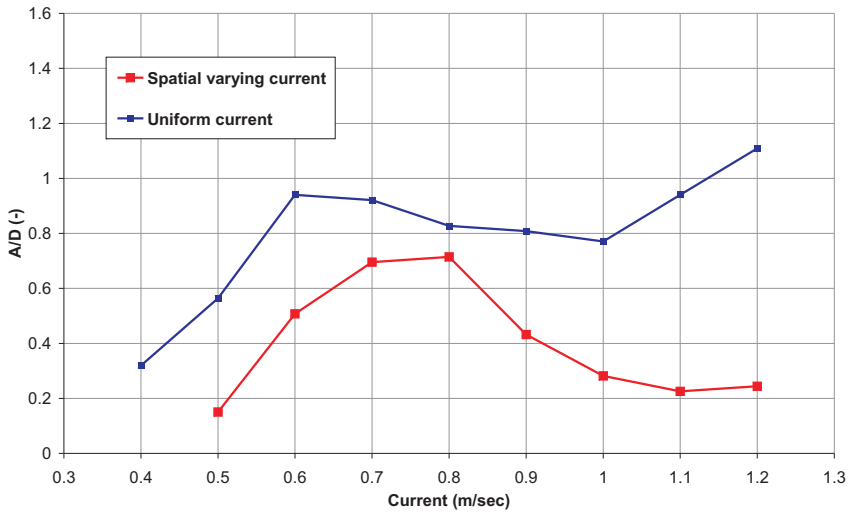

Figure 4.25: Dimensionless response amplitude versus reference current speed for double span pipeline, Span length 156m

More investigation have been made to find an explanation for this phenomenon.

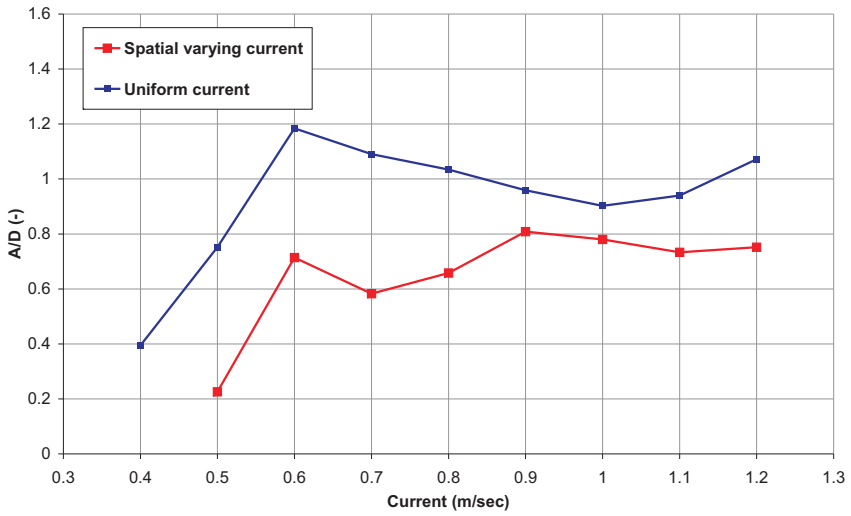

Figure 4.26: Dimensionless response amplitude versus reference current speed for double span pipeline, Span length $92m$

The reason is found to be the interaction between the neighbor spans as has already been explained in this chapter.

Figure 4.27 and Figure 4.28 show the VIV response amplitude and lift coefficient for the pipeline exposed to the spatial varying current at reference current speed 0.8 m/sec. Figure 4.29 and Figure 4.30 also show the VIV response amplitude and lift coefficient for the pipeline exposed to the spatial varying current at reference current speed 0.9 m/sec.

The same results for the uniform current are also shown in Figure 4.31, Figure 4.32, Figure 4.33 and Figure 4.34 for reference current speed 0.8 m/sec and 0.9 m/sec. The pipeline for all cases shown in the figures are excited at the second mode.

Refereing to Figure 4.27, the response amplitude is 0.38 m for the longer span and 0.35 m for the shorter one when the reference current speed is 0.8 m/sec. As seen in Figure 4.28 lift coefficient curve shows that the energy transfers from the shorter span to the longer span and then the longer span has magnification in response amplitude. The maximum negative lift coefficient in the larger span is -1.50.

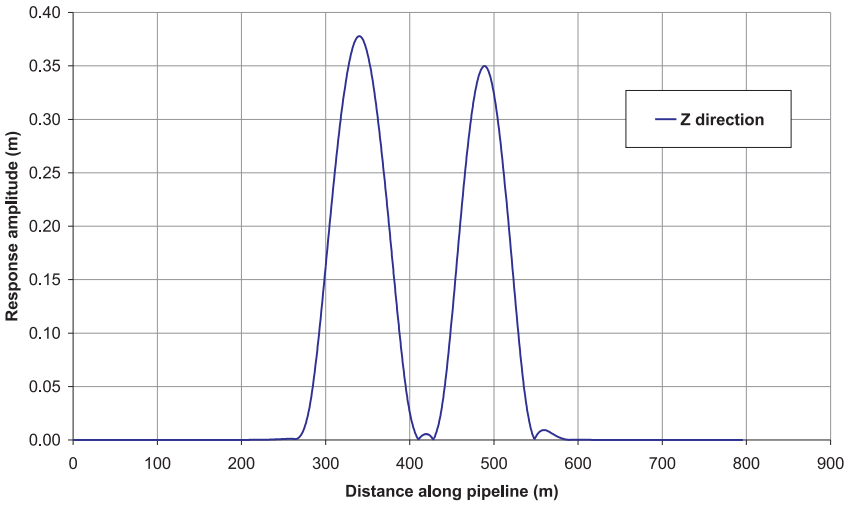

Figure 4.27: VIV response amplitude for double span pipeline, spatial varying current profile with reference current speed 0.8 m/sec

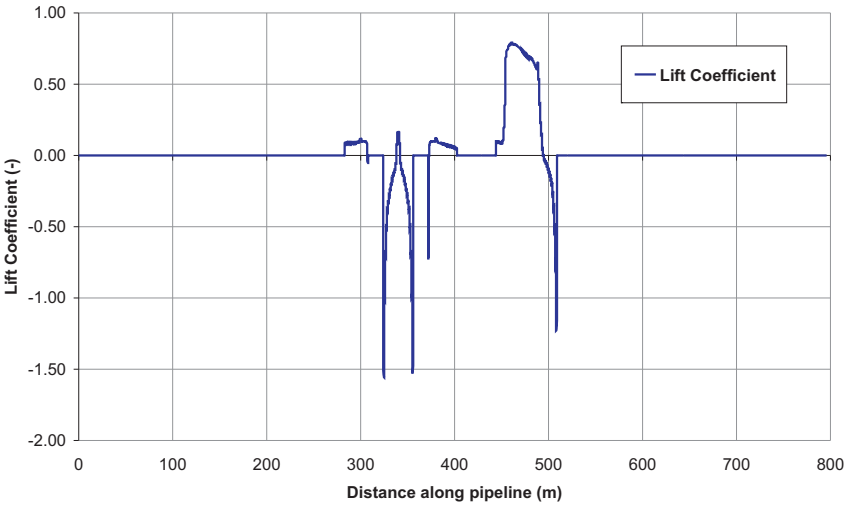

Figure 4.28: Lift coefficient for double span pipeline, spatial varying current profile with reference current speed 0.8 m/sec

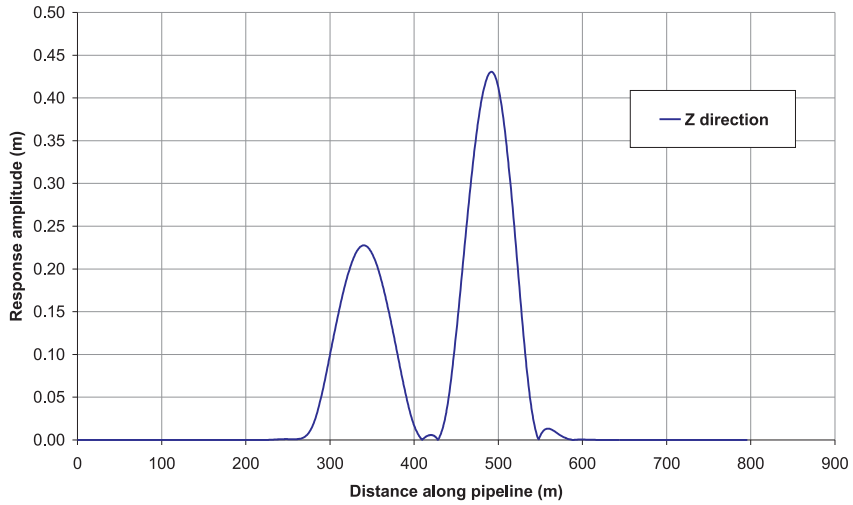

Figure 4.29: VIV response amplitude for double span pipeline, spatial varying current profile with reference current speed 0.9 m/sec

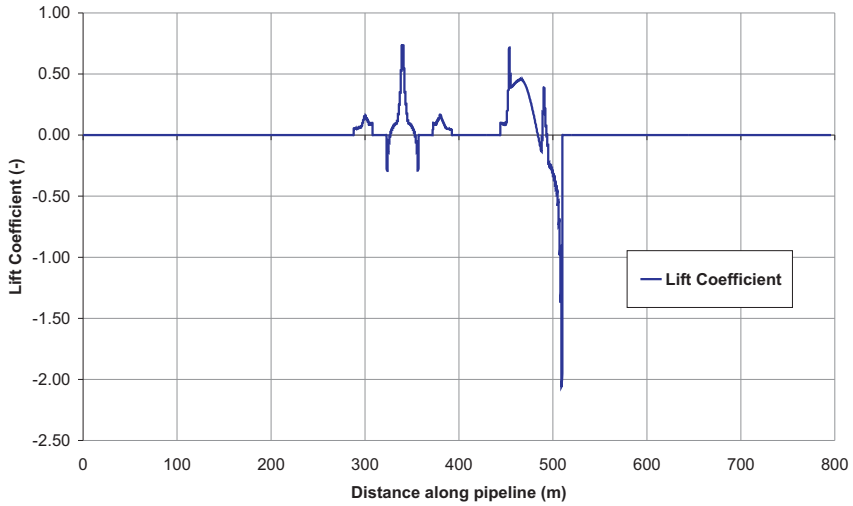

Figure 4.30: Lift coefficient for double span pipeline, spatial varying current profile with reference current speed 0.9 m/sec

At reference current speed 0.9 m/sec the response amplitudes are 0.23 m and 0.43 m showing a significant reduction in response amplitude for the longer span, (see Figure 4.29). As seen in Figure 4.30 the reason is the response amplitude in the longer span damped by the response in the shorter span and the energy transfer from the longer span to the shorter span.

The interactions from the adjacent span can also be seen in Figure 4.31 and 4.33. Lift coefficient curves in Figure 4.32 and 4.34 show the energy transfer from the longer span to the shorter span. The amount of the transfer energy between the adjacent span is depending on the relative span length and the relative amplitude of the dominating mode.

The response frequency of the double span pipeline is shown in Figure 4.35. The different response frequencies can be seen in this figure for two cases with spatial varying and uniform current speed.

All results show that applying the appropriate current profile is significantly important for multiple span pipelines.

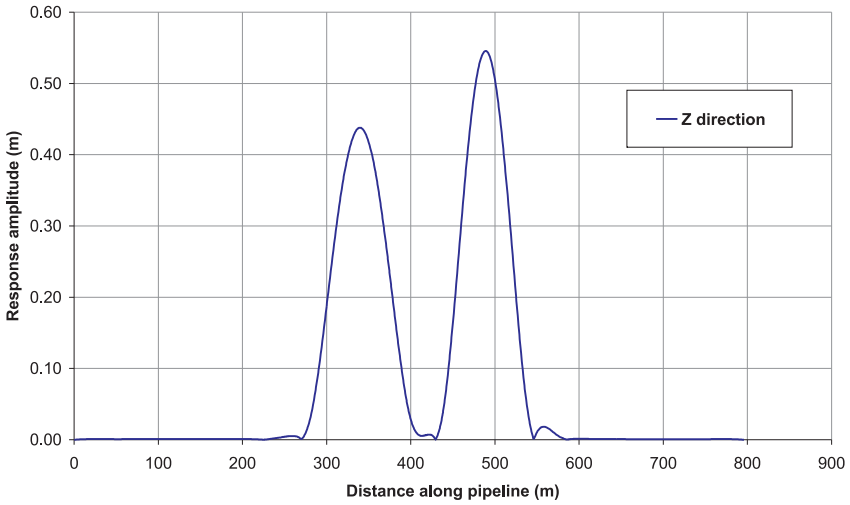

Figure 4.31: VIV response amplitude for double span pipeline, uniform current profile with reference current speed 0.8 m/sec

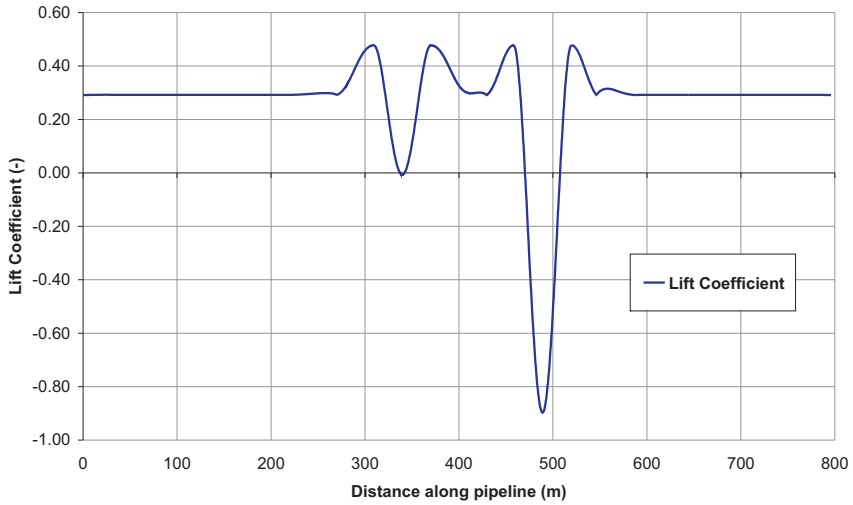

Figure 4.32: Lift coefficient for double span pipeline, uniform current profile with reference current speed 0.8 m/sec

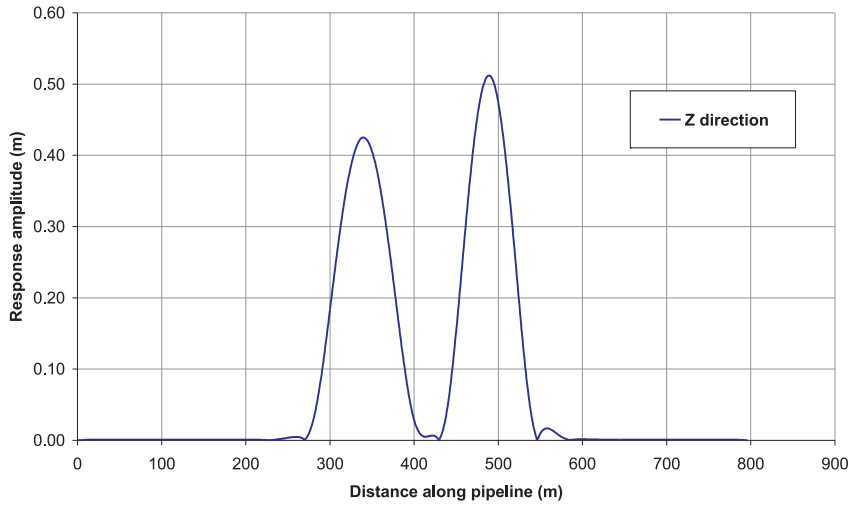

Figure 4.33: VIV response amplitude for double span pipeline, uniform current profile with reference current speed 0.9 m/sec

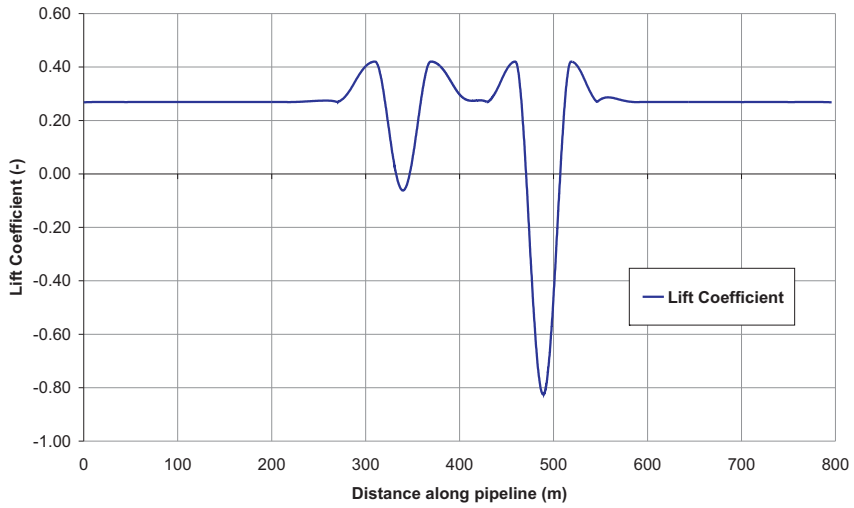

Figure 4.34: Lift coefficient for double span pipeline, uniform current profile with reference current speed 0.9 m/sec

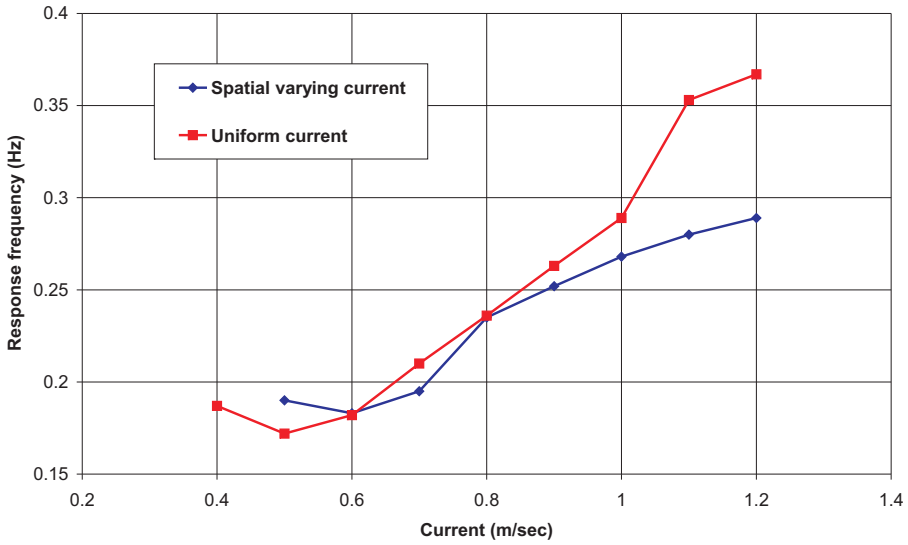

Figure 4.35: Response frequency versus reference current speed for double span pipeline

4.3 Influence from temperature variation

Varying temperature will change the stress-free length of a pipeline. Sag and tension in a free span will hence be influenced, but this influence will be controlled by the geometry of the pipe close to the free span and the interaction forces between the pipe and the sea-floor. The response frequency is influenced through changes in pipe tension and sag. If the pipe has a straight lined shape, the elongation will most likely accumulate in the free span and increase sag and decreases tension. If the pipe has a snaked geometry as seen in Figure 4.36, the elongation may be taken by increased snaking instead of being accumulated in the sag. Friction forces, pipe

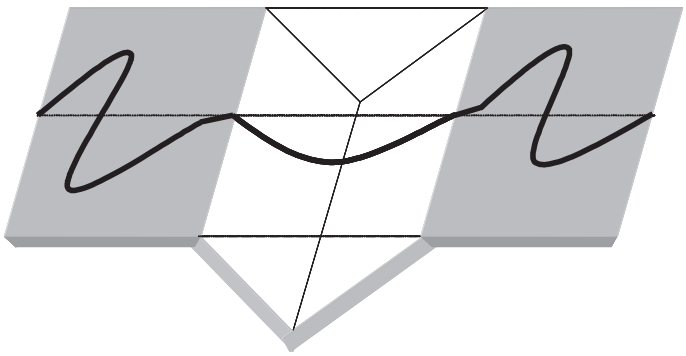

Figure 4.36: Free span pipeline with snaked geometry

stiffness and geometry will influence this process.

Two different cases have been analyzed; one straight lined pipeline and one with some snaking close to the free span. A 3D seafloor bottom profile combined with a 3D beam finite element model of the pipe have been applied. The entire pipeline model was 680 m long, and the pipe was laid over a rectangular trench of 156 m width, see Figure 4.36. Hence, the length of the free span will be almost constant and isolate the temperature effect to tension and sag deformation. Soil stiffness has been chosen from DNV recommended practice for free span pipelines (2001) for a very soft soil. Friction parameters are taken from subsea pipeline code (BS 8010). Both ends of the straight lined pipeline are positioned controlled for all degrees of freedom. For the snaked case, one end is positioned controlled but the other end has a force acting in the local axial direction. This arrangement has been used to obtain an almost identical tension for the two pipeline models. The water depth has been set to 1000 m. The initial temperature in all cases is $5°C$ and stepwise increased by $10°C$ up to a maximum of $65°C$. Other key data for the pipe can be found in Table 4.3.

Pipe properties		
Outer diameter	0.556	m
Inner diameter	0.508	m
Wall thickness	0.024	m
Modulus of elasticity	2.06E+11	N/m^2
Density of pipe material	7850	kg/m^3
Density of content	148.07	kg/m^3
Submerged weight	942	N/m

Table 4.3: Key data for the pipe

The influence of temperature variation on response frequency and eigenfrequency of a straight lined pipeline shown in Figure 4.37. In these cases the current speed was set to 0.6 m/s.

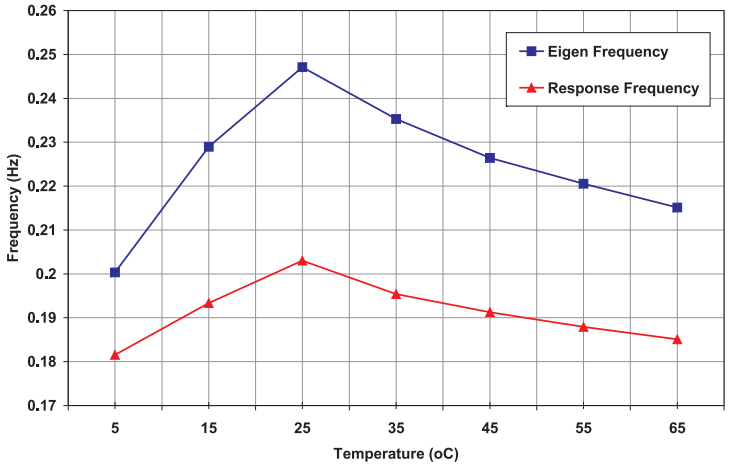

Figure 4.37: VIV response frequency and eigen frequency from the straight lined pipeline

Both response frequencies and eigenfrequencies are increased with increasing temperature up to 25°C. The rate of increase is higher for response frequency than for the eigenfrequency. After this point an opposite trend is seen. The explanation for the frequency trend may be found from Figure 4.38. Tension is seen to decrease for increasing temperature, while sag is increased. Increasing sag will give increasing eigenfrequency, while decreasing tension will give the opposite effect. None of these effects are linear. The combined action from tension and sag may therefore lead to

the behavior as seen on Figure 4.37. A more detailed study is, however needed to verify this hypothesis.

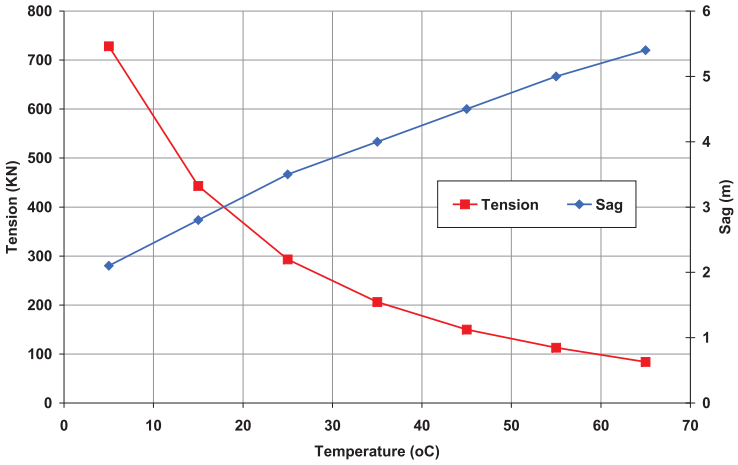

Figure 4.38: Tension and sag variation with temperature

Note that the span length is the same for all cases, which is illustrated in Figure 4.39. The trench and pipeline profile are shown for the highest and lowest temperatures, and the same node is in all cases the first one to have seafloor contact and hence being the end of the free span.

The effect from temperature variation has also been compared for a snaked geometry and a straight lined pipeline, and the results are shown in Figure 4.40. The differences between the response amplitudes for two cases can be seen in this figure. The response amplitude is significantly lower in the snaked geometry pipe since the thermal expansion in the pipe may be compensated in the snaked geometry part of the pipe, however, increasing the temperature in the straight lined pipe directly influence the length of the free span pipe and expand it.

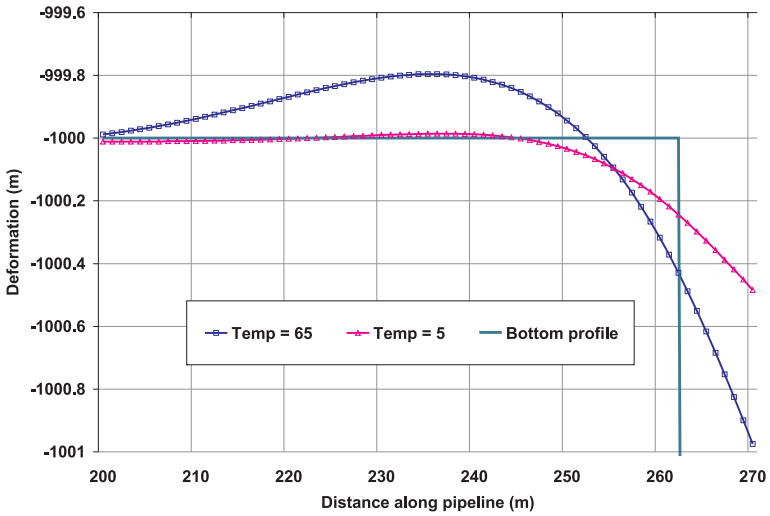

Figure 4.39: Pipe deformation related to bottom profile from different temperatures

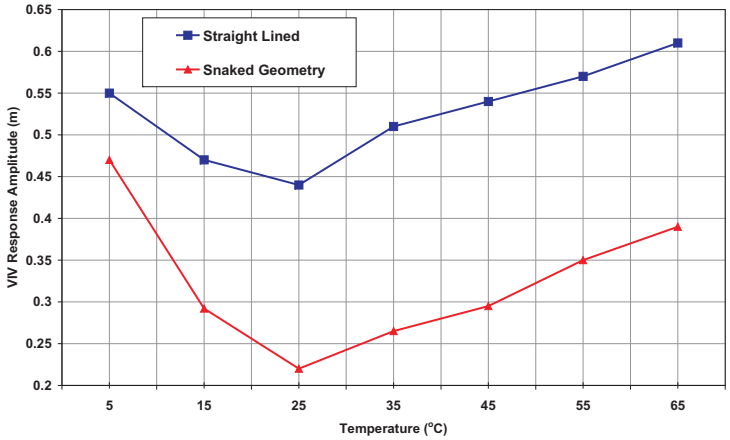

Figure 4.40: VIV response amplitude for straight lined and snaked geometry pipe

Chapter 5

Comparison between analysis and experiment

Uneven sea bed may introduce long and multiple free spans in pipeline where VIV response interaction between adjacent spans may occur for several modes.

For pipelines with short spans the beam effect of stiffness is dominant whereas for longer spans the cable effect is more likely to occur, e.g. Søreide, et al. (2001). Until recently, DNV Guideline No. 14 was commonly used to predict VIV response behaviour of a pipeline. This guideline had an acceptance criteria for response of a pipeline with short span and identical dynamic properties in horizontal and vertical directions. But this guideline was not suitable to cover the multi-mode VIV responses for long free spans, and interaction between adjacent spans. For such spans more than one mode may be excited and there are challenges to find the dominant response mode and the interactions between the modes and spans.

To improve the understanding of multi modal and multi span VIV some experiments were carried out at MARINTEK in connection with the Ormen Lange pipeline project. The test programs were conducted in three phases during years 2000 to 2003, Reinertsen (2003):

- Longer single spans with L/D up to 350. Both in-line and cross-flow response were considered. The response curves were found for prototype velocity up to $U_{(prototype)} = 2.40m/s$.
- Repeated single span tests with focus on in-line VIV and onset for cross flow response.

- Multiple span tests with focus on span interaction and shoulder effects.

The tests clearly proved that the VIV response mode interactions resulted in major reduction in cross-flow amplitudes. The test results were discussed by e.g. Nielsen, et al. (2002) and (2005).

Nielsen, et al. (2002) discussed the observed VIV response of long free spans during model testing and presented a hypotheses to explain the observed behaviour and outlined a format of new design principles for long free span pipelines. Nielsen also showed the importance of the interaction between the in-line and cross-flow response for long free spans which may reduce the responses in cross-flow.

Nielsen (2005), et al. discussed MARINTEK test results for multiple spans pipeline where multi-mode response is observed and established a hypotheses for modal interaction mechanisms.

The findings from these results were implemented in a design guideline for VIV response estimation as well as computer tools, see Søreide, et al. (2005).

Det Norske Veritas (2006) released a new recommended practice for design of free spanning pipelines, DNV-RP-F105 based on the major findings on MARINTEK test results, see also Fyrileiv, et al. (2004).

In the present section attempts will be made to compare measured response to analysis results from VIVANA. Built-in values for hydrodynamic coefficients will be used, but attempts will also be made to obtain a better agreement by adjusting some of the input parameters to VIVANA.

5.1 Experiment set-up

The experiments used in this study were conducted at MARINTEK. The rig consists of a truss girder of length 12m used as support for the model pipe. At one end of the pipe there is the mechanism for pretension and axial stiffness variation, while the other end is instrumented for axial force measurements. The truss girder is fixed to a moveable crane in the roof of the basing during tow.

The pipe is instrumented for strain measurements in two directions at ten sections, see Figure 5.1. The pipe model is clamped against twist rotation at the ends, thus the strain gauges maintain their global orientations during static offset due to current drag, Reinertsen (2003).

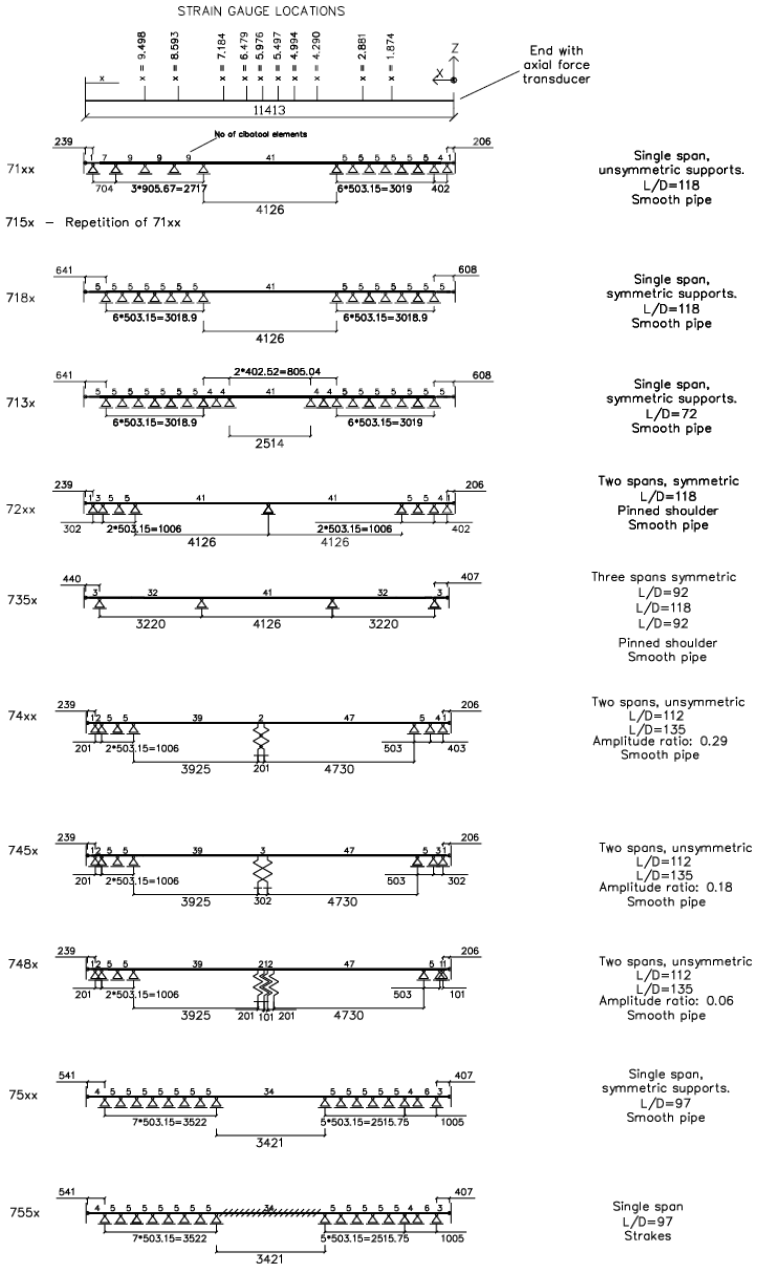

Figure 5.1: Test cases, MARINTEK

OD hydrodynamic	777 mm
PP coating, t	8 mm
OD steel pipe	761 mm
ID steel pipe	690 mm
EI steel	1.1046E09 Nm^2
Mass ratio	1.46
Content density	150 kg/m^3

Table 5.1: 30" prototype pipe properties

OD hydrodynamic	35.11 mm
EI brass	203 Nm^2
Mass	1.307 kg/m
Mass ratio	1.35
End tension	50 N

Table 5.2: Test model properties

5.1.1 Pipe properties and scaling

Table 5.1 and Table 5.2 correspond to the pipe properties of the prototype and test model respectively.

There are different ways to scale the test models, i.e based on outer diameters and based on bending stiffness. Scaling based bending stiffness gives factor $\lambda = 22.13$, where λ is the scale factor.

5.1.2 Spring stiffness

To provide reasonable boundary conditions from the pipe laying on soil some springs were introduced. The spring stiffness is calculated for the model according to the soil stiffness for the prototype model.

In the Ormen Lange field the seabed is very uneven with soil varying from very stiff to very soft clay. Table 5.3 shows the soil parameters as given by DNV-RP-F105 (2002).

According to Reinertsen (2003), a spring stiffness $k = 30000\ N/m$ has been chosen in model scale for both in-line and cross-flow which presents a very stiff clay.

This is chosen in accordance with DNV-RP-F105 which indicates multiple free spans interact more on stiff clay than softer clay, see Figure 5.2.

Soil type			Static	Dynamic
Very Soft Clay	*Stiffness*	*Vertical [N/m/m]*	$0.75 \cdot 10^5$	$2.0 \cdot 10^6$
		Lateral [N/m/m]		$1.35 \cdot 10^6$
		Axial [N/m/m]		$2 \cdot 10^6$
	Damping	*Vertical [%]*		2.0
		Lateral [%]		3.5
	Friction factor	*Lateral [-]*	0.85	
		Axial [-]	0.50	
Very Stiff Clay	*Stiffness*	*Vertical [N/m/m]*	$2.5 \cdot 10^6$	$11.5 \cdot 10^6$
		Lateral [N/m/m]		$8.25 \cdot 10^6$
		Axial [N/m/m]		$11.5 \cdot 10^6$
	Damping	*Vertical [%]*		0.6
		Lateral [%]		1.0
	Friction factor	*Lateral [-]*	0.80	
		Axial [-]	0.30	

Table 5.3: Soil conditions at Ormen Lange deep water section, Reinertsen (2003)

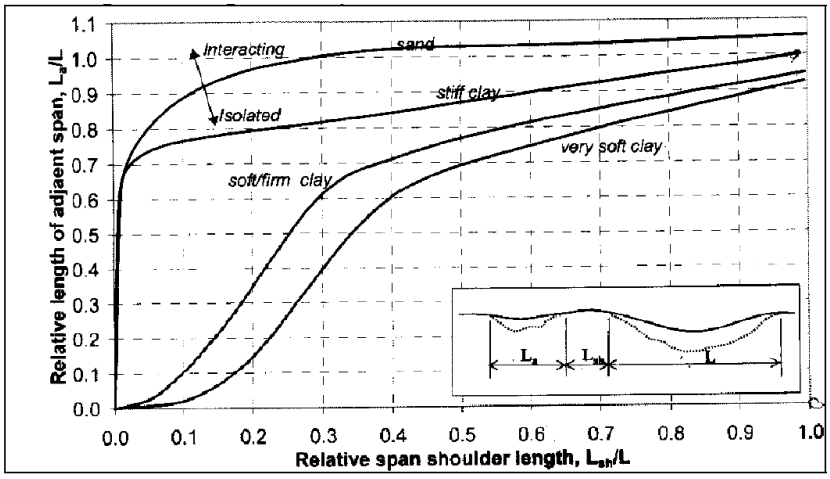

Figure 5.2: Classification of free spans DNV-RP-F105

OD hydrodynamic	35.11 mm
EI	203 Nm^2
Mass	1.307 kg/m
Mass ratio	1.35
End tension	50 N

Table 5.4: VIVANA model properties

5.2 Analysis model

VIVANA is used as a VIV software program for the comparison between analysis and experiments. One should note that VIVANA is an empirical program where hydrodynamic coefficients such as the lift coefficient and added mass are found from experiments.

Two models are applied in the VIVANA analyses. The models are made in accordance with test runs 71xx and 74xx in MARINTEK test program, see Figure 5.3.

The total length of each model is 11.41m. 71xx is a single span pipe with 4.126m free span. In the other hand, 74xx is a double span with two different span lengths 3.925m and 4.730m respectively.

Both pipes are free to rotate at each ends, but fixed for torsional rotation. As shown in Figure 5.3, 50N axial force applied at one end, whereas each end are fixed in vertical and lateral deflection.

VIVANA model properties are shown in Table 5.4.

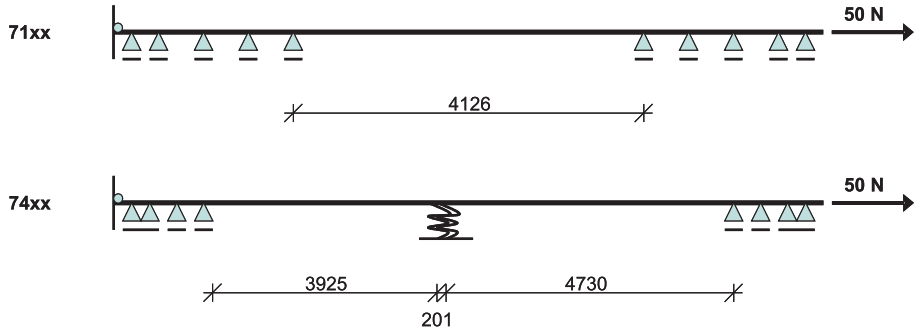

Figure 5.3: VIVANA test models

$U_{(model)}$	$U_{(prototype)}$
0.2	0.9408
0.25	1.1760
0.265	1.2466
0.275	1.2936
0.285	1.3407
0.3	1.4112
0.325	1.5288
0.35	1.6464
0.375	1.7640
0.4	1.8817
0.45	2.1169
0.5	2.3521

Table 5.5: Relation between $U_{(model)}$ and $U_{(prototype)}$

5.2.1 Spring stiffness

The clamps are modeled by springs with very high stiffness so both vertical and lateral displacements are zero. The shoulder between the spans of case 74xx modeled with elastic springs where the stiffness is $30000N/m$ for both cross-flow and in-line.

5.2.2 Current

Uniform current velocity along the pipe is applied. The study includes velocities above $0.2m/s$ ($U_{(prototype)} = 0.94m/s$) in order to be comparable with the test results.

The current velocities for prototype calculated using scale factor $\lambda = 22.13$ as

$$U_{(prototype)} = \sqrt{\lambda}.U_{(model)} \tag{5.1}$$

and shown in Table 5.5.

5.2.3 Hydrodynamic properties

Figure 5.4 shows the predefined Strouhal number relationship with the Reynolds number used in the VIVANA analysis.

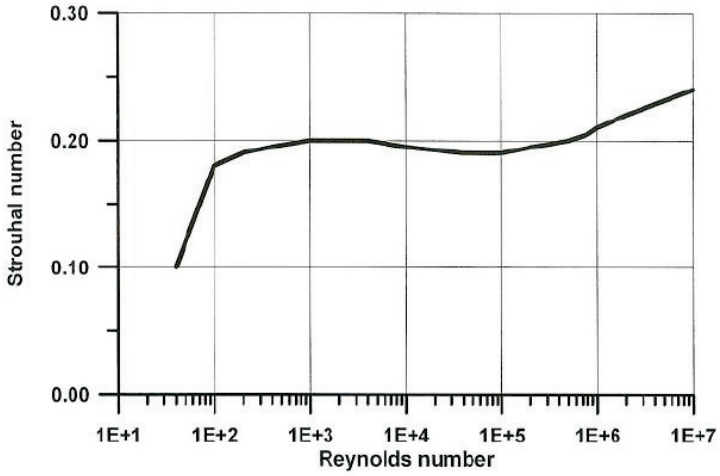

Figure 5.4: Strouhal number versus Reynolds number in VIVANA

The measured and calculated response have been compared and discussed in Section 5.3. In this section, the standard hydrodynamic parameters and curves have been applied in VIVANA models.

To get a better understandings of the results and in order to compare and discuss them the analysis model is tuned and the results compared with experiments in Section 5.4. That includes adjusting the Strouhal number, lift coefficient and added mass in each individual case. The variation of these parameters -whether the response frequencies are the same or not- and effects of them on VIV response have also been investigated and discussed.

As a reference, the predefined lift coefficient curves initially used in VIVANA analyses can be seen in Figure 3.10. The added mass as function of non-dimensional frequency applied in VIVANA shown in Figure 3.7. This is based on the results from Gopalkrishnan (1993).

5.2.4 Eigenfrequencies

Eigenfrequencies for case 71xx and 74xx are presented in Table 5.6 and Table 5.7. ω_{CF} and ω_{IL} refer to the circular frequency in cross-flow and in-line oscillation respectively. The analytical eigenfrequencies for the single span case is calculated

mode	ω_{CF} (rad/s)	ω_{IL} (rad/s)	ω_{EI} (rad/s)	ω_T (rad/s)	ω (rad/s)
1	11.218	11.236	5.476	4.709	7.223
2	30.591	30.594	21.905	9.419	23.844
3	59.840	59.840	49.286	14.128	51.271
4	98.332	98.334	87.620	18.838	89.622
5	149.06	149.07	136.91	138.91	138.92

Table 5.6: Eigen and analytical frequencies for case 71xx

mode	ω_{CF} (rad/s)	ω_{IL} (rad/s)
1	8.463	8.476
2	12.009	12.024
3	23.095	23.100
4	32.619	32.623
5	45.300	45.304

Table 5.7: Eigenfrequencies for case 74xx

based on the following equations:

$$\omega_{EI} = \frac{n^2\pi^2}{l^2}\sqrt{\frac{EI}{m}} \tag{5.2}$$

$$\omega_T = \frac{n\pi}{l}\sqrt{\frac{T}{m}} \tag{5.3}$$

$$\omega = \sqrt{\omega_{EI}^2 + \omega_T^2} \tag{5.4}$$

Note that these analytical eigenfrequencies are found from use of a hinged/hinged model. The real eigenfrequencies will be higher since the real model pipe has some rotation restriction at both ends. They are shown to illustrate how T and EI contribute to the total eigenfrequency. T is axial tension and EI is the bending stiffness of the pipe.

According to Table 5.6 and as seen in the next section, the single span pipe "prefers" to respond at the first mode CF and IL simply because the second eigenfrequency IL is too high, higher than 2 times the CF.

5.3 Comparison between results

The comparisons between the analysis and test results are given in this section for case 71xx and 74xx. Note that all results discussed here are related to cross-flow response and in-line response is not investigated here. For all cases in this section, the standard curves in VIVANA for the Strouhal number, lift and added mass coefficients have been used.

Figure 5.5 and Figure 5.6 illustrate the VIVANA analyses results versus the MARINTEK test results. The DNV-RP-F105 curves are also shown in these figures as a reference.

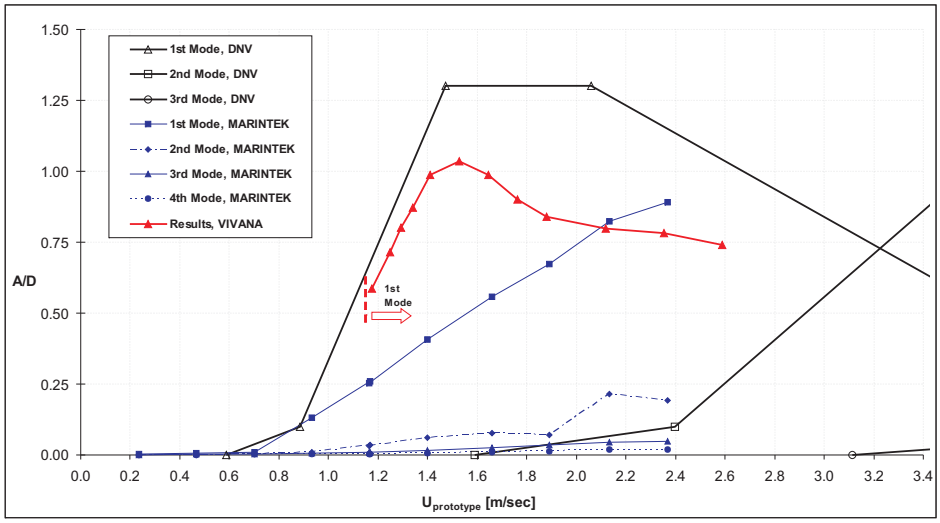

Figure 5.5: Comparison of MARINTEK test results with DNV-RP-F105 and VIVANA results for case 71xx

The comparison of results for case 71xx is illustrated in Figure 5.5. We observe that the test results generally show lower response in comparison with the VIVANA analyses and the DNV response prediction. The reason for this phenomena may be the VIV response mode interactions and interaction between in-line and cross-flow responses.

The key attention between VIVANA and model is the slope. Both IL and CF respond at mode 1, but $\omega_{IL} = 2\omega_{CF}$. This is what makes this case so special. This slope must probably caused by IL/CF interaction which is particular since both

have mode 1.

Figure 5.5 shows VIVANA results increase along the DNV curve for the first mode until the maximum non-dimensional amplitude, A/D at $U_{prototype} = 1.529m/s$ ($U_{model} = 0.325m/s$). But at this point could not reach the maximum response predicted by the DNV-RP-F105.

The VIVANA results are higher than the test measurements until $U_{prototype} = 2.117m/s$ ($U_{model} = 0.45m/s$). At this velocity the results are almost the same. Thereafter the test results are higher than the VIVANA results. This is the only location among the cases have been studied here that VIVANA predicts less response than the test results.

It is also seen that the experiment result curve has a lower slope than the analysis before $U_{model} = 0.3m/s$. The oscillation shape predicted by VIVANA in this figure are all dominated by the first mode.

Figure 5.6 shows the results for case 74xx. As seen the VIVANA results for the

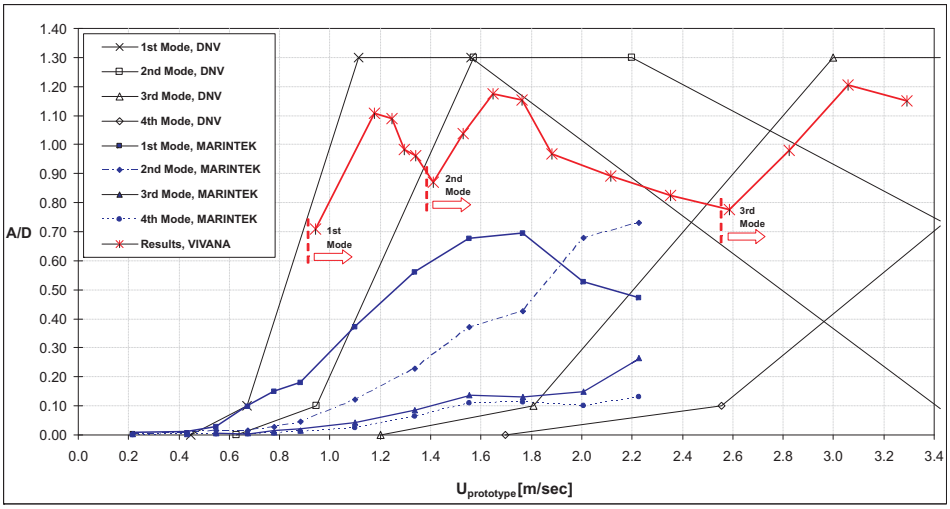

Figure 5.6: Comparison of MARINTEK test results with DNV-RP-F105 and VIVANA results for case 74xx

first mode follow the DNV curve until $U_{prototype} = 1.176m/s$, but could not reach the maximum response predicted by DNV.

The second and third mode curves are nicely following DNV curves until reaching to their peaks and thereafter reducing with the almost the same slopes as DNV

curves. Here, the analysis result peaks are also a little lower than the the maximum response predicted by DNV.

By these figures, it can be seen that the DNV-RP-F105 predicts the starting point of the modes correctly and is in agreement with VIVANA. The maximum A/D are close to the DNV results for the second and third mode. It shows VIVANA and DNV are consistent, but the real pipe behaves differently.

We observe that the test results are generally less than the VIVANA results. The reason may be explained that the response for low velocities is strongly dominated by the first mode in VIVANA, while the model has contributions from mode 1 and 2. This gives more transient effects and reduced response amplitude. A more complete discussion on the reasons for such a phenomena is given in the next section -on tuning of the results- where both A/D and response frequencies from IL and CF are discussed and compared on different modes.

To have a better understanding of the VIVANA results, the lift coefficient curves for case 74xx are shown in Figure 5.7 to Figure 5.9.

The lift coefficient curve in Figure 5.7 represents the energy transfers from the short to long span. It means when $C_L \geq 0$ energy goes into the system and for $C_L < 0$ energy goes out due to damping, hence energy transfers between the adjacent spans.

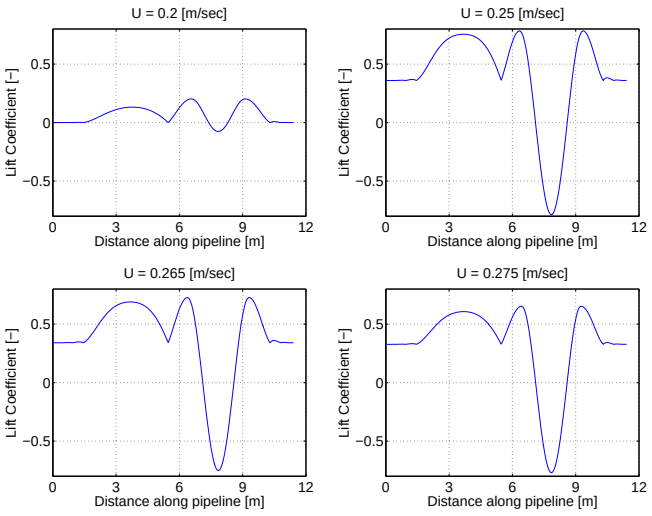

Figure 5.7: Lift coefficient curves for case 74xx, $U_{model} = 0.2 - 0.275 m/s$

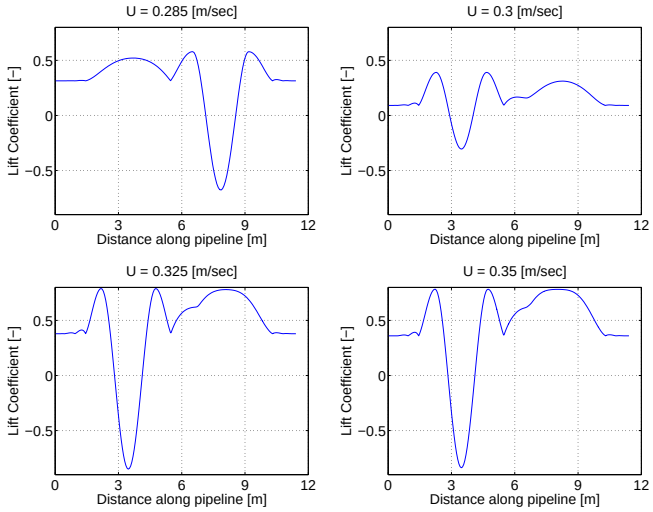

Figure 5.8: Lift coefficient curves for case 74xx, $U_{model} = 0.285 - 0.35m/s$

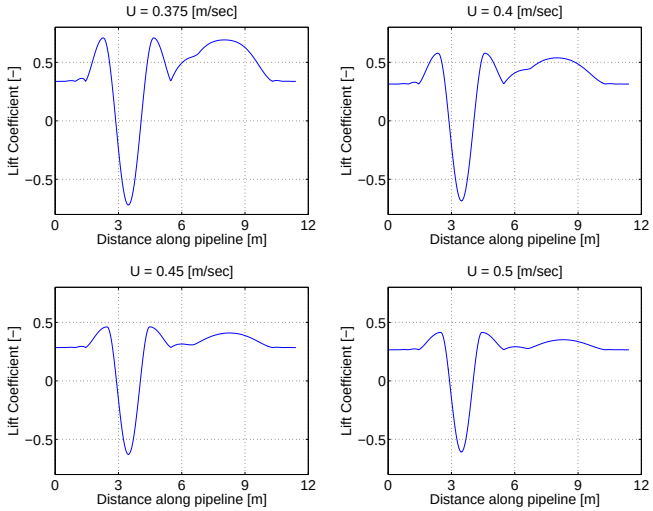

Figure 5.9: Lift coefficient curves for case 74xx, $U_{model} = 0.375 - 0.5m/s$

As seen in Figure 5.8 the maximum negative lift coefficient belongs to $U_{model} = 0.35m/s$ where the response is maximum.

Figure 5.8 clearly illustrates shifting from the first to second mode. From $U_{model} = 0.3m/s$ and after the energy must go from the span with $C_L > 0$ along its entire length to the span where $C_L < 0$ (where energy is dissipated).

As seen in Figure 5.6, the closest response between the test results and VIVANA are seen for the current velocity $U_{model} = 0.45m/s$ and $0.5m/s$. Two last cases in Figure 5.9 illustrate the lift coefficients for these current velocities.

The VIV response for the last case $U_{model} = 0.5m/s$ is shown in Figure 5.10. The maximum non-dimensional amplitude (A/D) is 0.83, which is in accordance with $U_{prototype} = 2.352m/s$ in Figure 5.6.

A/D in the time frame $334 - 352s$ for the test model at $U_{prototype} = 2.225m/s$ is also shown in Figure 5.11. It exhibits some beating, meaning the response spectrum around the dominating mode has a finite width. During tests, an approximation was done to take the *steady amplitude* as

$$A = \sqrt{\text{std}(timeseries(timewindow))} \tag{5.5}$$

which confers with a pure sinusoid where

$$A = \sqrt{\text{std}(\sin(t))} \tag{5.6}$$

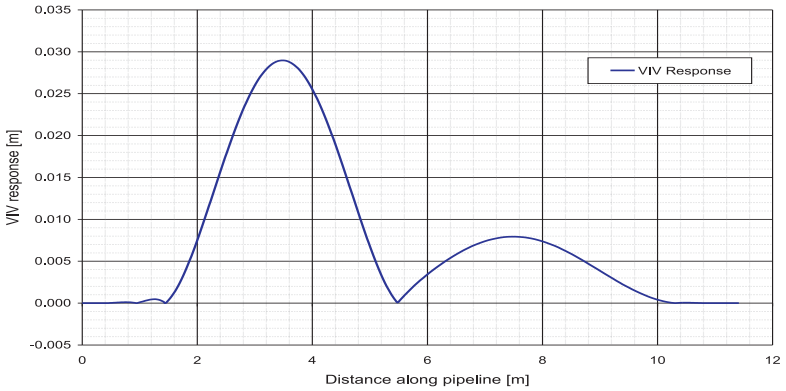

Figure 5.10: RMS VIV response for case 74xx, $U_{model} = 0.5m/s$

Figure 5.11 illustrates the non-dimensional amplitude for the test model at $U_{prototype} = 2.225m/s$. As seen for amplitude spectra Y, the first and third modes are broadbanded while the second mode is close to harmonic. The spectra in Z direction shows that the first mode is broadbanded and the second mode is close to harmonic, but the frequencies are not the same in the third mode and then gives beating.

Here, we observe that non-resonant modes creates a disturbance that leads to reduced stationary response, beating and irregular response. That is the reason the response is not large enough since that requires well organized response.

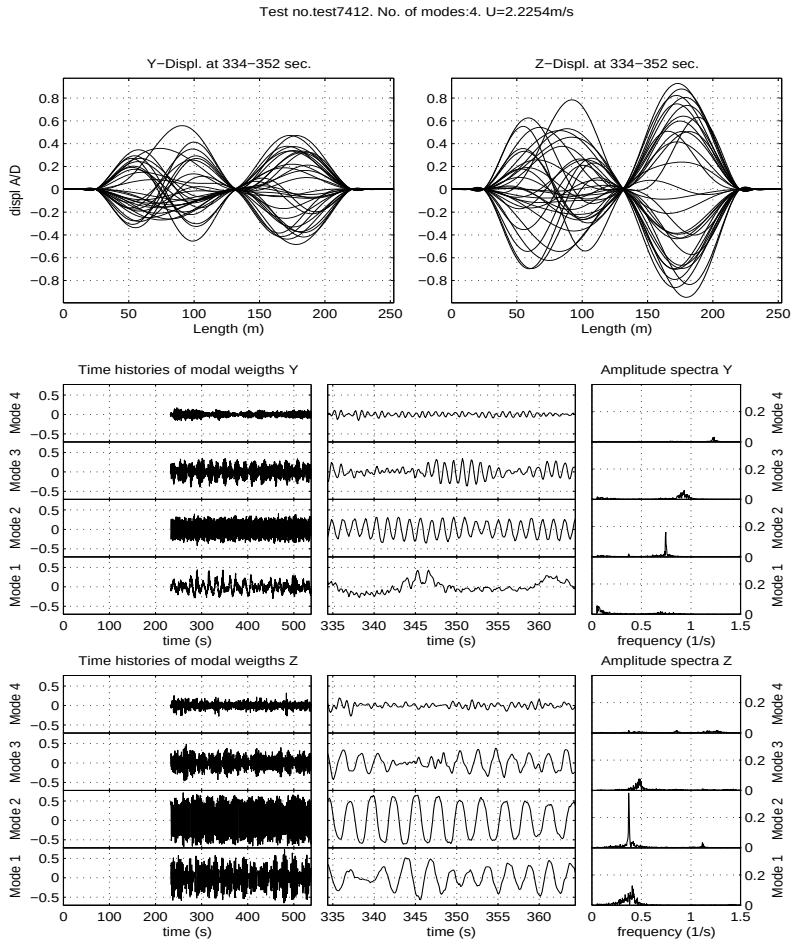

Figure 5.11: Test model non-dimensional amplitude for case 74xx, $U_{prototype} = 2.225m/s$, MARINTEK

5.4 Tuning of analysis model to compare with experiment

Some case studies have been made in order to improve the understandings on comparison between the VIVANA analysis and test results as follow:

- *Adjusting the Strouhal number*
  Firstly, the Strouhal number as a key parameter in VIVANA is tuned to provide a base for comparison of the test and analysis results. In this case the response frequency may be different for the test and analysis, however, the response amplitudes are in a good agreement.

- *Adjusting the lift coefficient*
  All $A_{(C_L=0)}$ and $A_{(C_L=max)}$ in the lift coefficient table in VIVANA are tuned and multiplied by a factor in order to get the same A/D on the test and analysis just for the reference point, i.e. $U_{(prototype)} = 1.764m/s$. Response frequencies for different cases are different than test results and calculated by VIVANA. The Strouhal number is VIVANA standard.

- *Adjusting the Strouhal number and lift coefficient, same response frequency for the reference point*
  Both St and C_L are tuned for the reference point, $U_{(prototype)} = 1.764[m/s]$. St for all cases is equal to 0.148 in order to get the same response frequency on the test and analysis only for the reference point. Accordingly, all $A_{(C_L=0)}$ and $A_{(C_L=max)}$ in the lift coefficient table are tuned to get the same A/D on the test and analysis just for $U_{(prototype)} = 1.764m/s$. St and C_L table used for the reference point have been applied for all cases and all modes.

- *Adjusting the Strouhal number and lift coefficient, same response frequency for all cases*
  Both St and C_L are tuned. St was tuned for all cases in order to get the same response frequencies in the first mode on the tests and analyses. All $A_{(C_L=0)}$ and $A_{(C_L=max)}$ in the lift coefficient table are tuned and multiplied by a factor to get the same A/D on the test and analysis just for the reference point, $U_{(prototype)} = 1.764m/s$. C_L table used for the reference point has been applied for all cases and all modes. St table for different cases are accordingly varied to get the same response frequency on the test and analysis, but are kept the same on different modes for each case.

- *Adjusting the added mass and lift coefficient, same response frequency for all cases*
  Instead of adjusting the Strouhal number the added mass is adjusted in order to get the same response frequency. The Strouhal number is set to 0.19 for all cases which is a well known value. The added mass is found to give the

correct response frequency at the reference point $U_{(prototype)} = 1.764[m/s]$. All $A_{(C_L=0)}$ and $A_{(C_L=max)}$ in the lift coefficient table are tuned and multiplied by a factor to get the same A/D on the test and analysis just for the reference point, $U_{(prototype)} = 1.764m/s$ table used for the reference point has been applied for all cases and all modes.

5.4.1 Adjusting the Strouhal number

In this study the Strouhal number is tuned in VIVANA to give the same response amplitude as the test model. Note that the response frequency in VIVANA may be different than the test. By adjusting the Strouhal number the actual non-dimensional frequency will be moved on the curve shown in Figure 2.13 to give a correct response amplitude. Note that this an attempt, but not actually a physically rational way of adjustment.

VIVANA results are based on Gopalkrishnan's tests, but since these were conducted with a small cylinder, some correction should be performed prior to calculating the non-dimensional frequency parameter. According to the standard curve for the Strouhal number as function of Reynolds number, the Strouhal number, St_G, must have been approximately 0.2 for these tests. If we have another Strouhal number and want to apply Gopalkrishnans results, we have to take this into account when calculating the non-dimensional frequency parameter. For more information see VIVANA Theory manual (2005).

$$\hat{f} = \frac{f_{osc}D}{U} \cdot \frac{St_G}{St} \tag{5.7}$$

The results by adjusting the Strouhal number are shown in Figure 5.12 and Figure 5.15 for case 71xx and 74xx respectively. As seen, the results are in a very good agreement. Case 71xx is excited in the first mode, but for case 74xx the first and second modes are excited.

The adjusted Strouhal number versus Reynolds number which found for case 71xx is seen in Figure 5.13. As shown in this figure the Strouhal number is varying from 0.1675 to 0.1175 which is a low value. These are the Strouhal numbers found in VIVANA that give the same response as the test results.

It is also important to compare the response frequencies for these cases. Figure 5.14 shows the response frequency for case 71xx with the actual and adjusted Strouhal number in comparison with test measurements. VIVANA models are excited at the first mode. As seen in this figure, the response frequency for the adjusted Strouhal number begins with a higher value ($1.626Hz$) than the actual case and is descending

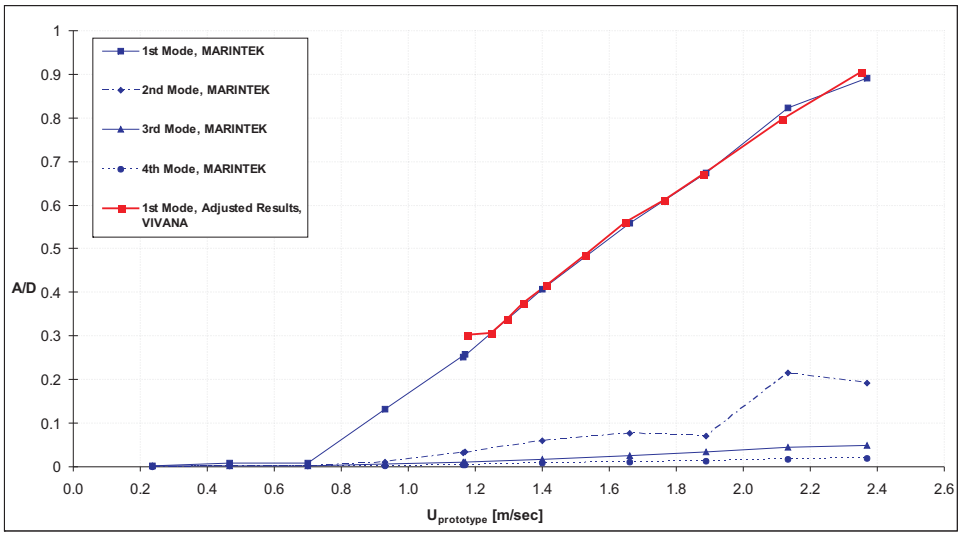

Figure 5.12: MARINTEK test results versus VIVANA results with adjusted Strouhal number for case 71xx

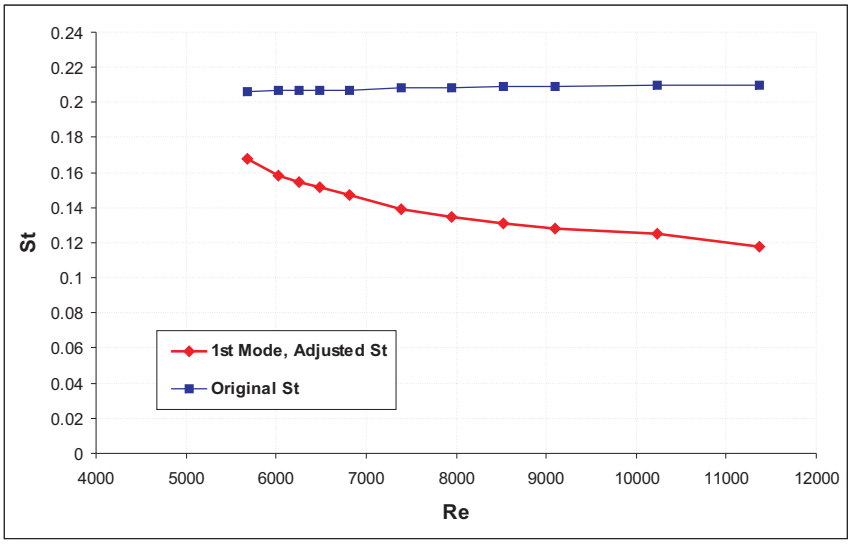

Figure 5.13: Adjusted Strouhal number versus Reynolds number for case 71xx in VIVANA

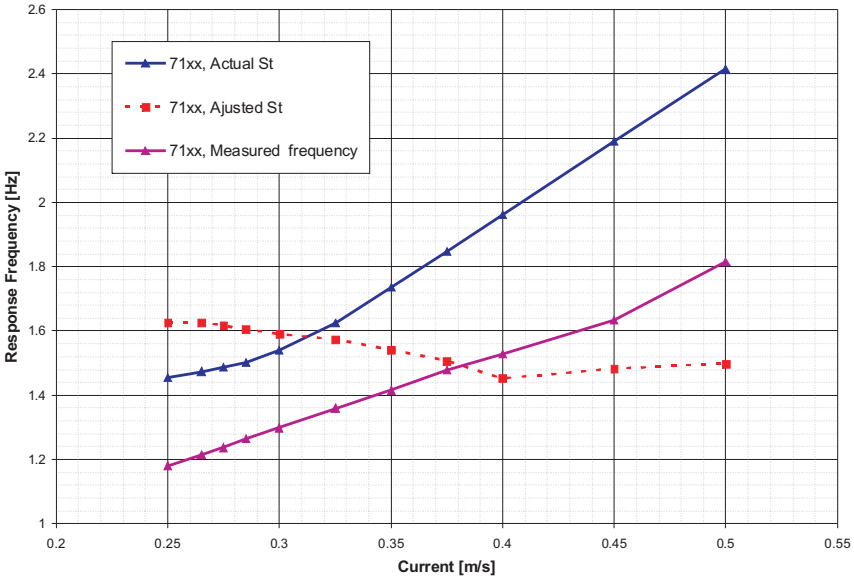

Figure 5.14: Response frequency for case 71xx with actual and adjusted Strouhal number in VIVANA

by increasing the current velocity until $0.4m/s$ ($U_{(prototype)} = 1.88[m/s]$). This is the point that added mass has the highest value. Thereafter, the response frequency is increasing a little. As a comparison with the actual case, the response frequency curve is rather flat and the frequency variation is not much in comparison with the actual case which is very steep. As seen, this trend for the actual case is different and increasing all the way until response frequency reaches $2.414Hz$.

It is very interesting to see that the measured frequency plot has almost the same trend as the actual case but at a lower value. It gives a hint for further investigation.

Figure 5.15 illustrates the results from the adjusted Strouhal number for case 74xx and for both first and second modes. It was more difficult to find a perfect match for the second mode and the results presented here are the closest results that may be found. Also note that in the tests the first and second modes are simultaneously excited, while the results from VIVANA analyses give first or second mode separately by applying a high and low St value.

The adjusted Strouhal number which gave the same response for case 74xx are presented in Figure 5.16. The Strouhal number is descending from 0.1579 to 0.066 for the first mode and 0.269 to 0.21 for the second mode. The Strouhal number

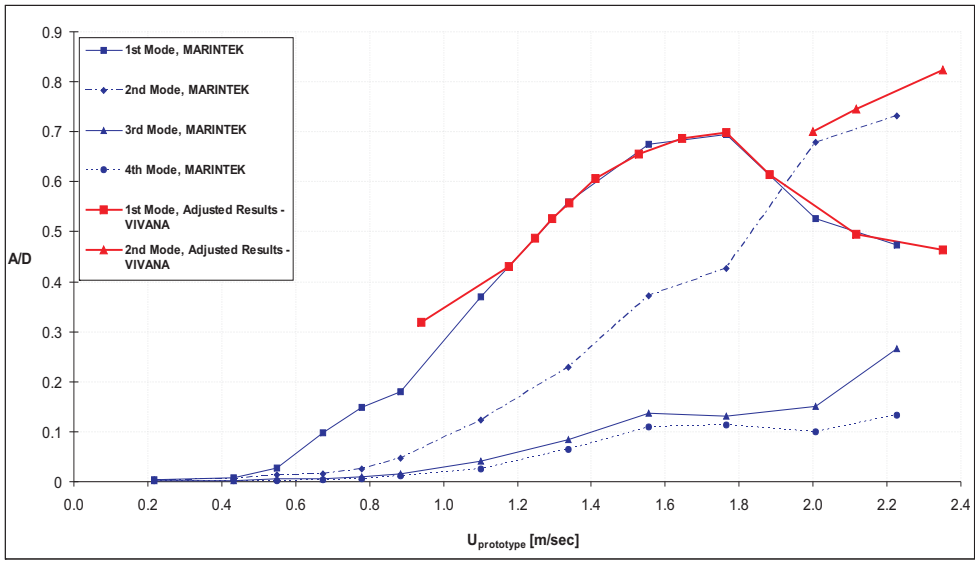

Figure 5.15: MARINTEK test results versus VIVANA results with adjusted Strouhal number for case 74xx

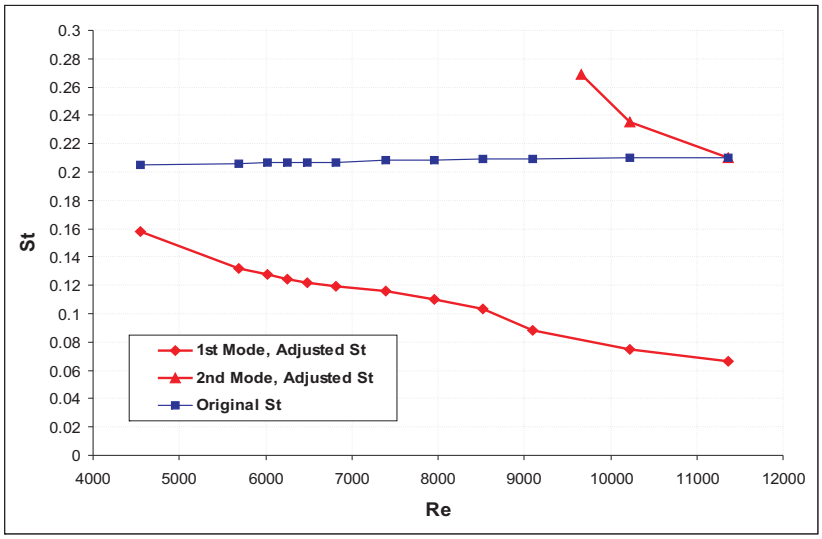

Figure 5.16: Adjusted Strouhal number versus Reynolds number for case 74xx

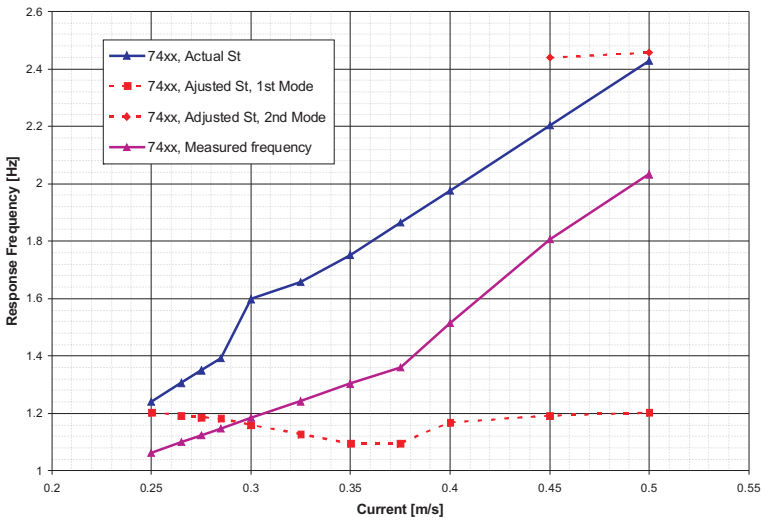

Figure 5.17: Response frequency for case 74xx with actual and adjusted Strouhal number

0.066 is an unrealistic low value, but one should note that changing the Strouhal number actually affects the non-dimensional frequency and consequently the standard predefined parameters in VIVANA such as lift coefficient and added mass. This phenomena is discussed more in detail later.

In Figure 5.16 the original Strouhal number is the one selected from the predefined source data by VIVANA. The adjusted Strouhal number found in order to give the same VIV response as the tests.

Figure 5.17 shows the response frequency for case 74xx with the actual and adjusted Strouhal number. As seen in this figure two modes were excited for the adjusted case by applying a high and low St value. The measured frequencies are also shown here.

Same as case 71xx, the measured frequency plot has almost the same trend as the actual case but at a lower value.

As already seen in Figure 5.6, the cases with the actual Strouhal number are excited in the first mode before $0.3m/s$ and hereafter in the second mode. The response frequency is ascending by increasing the current velocity.

The adjusted cases have also been shown in the first and second mode in Fig-

ure 5.17. In the first mode, the response frequency is descending by increasing of the current velocity until $0.35m/s$ hereafter the response is increasing a little until it returns to the initial response frequency ($1.203Hz$). In general, it shows not much variation. The response frequency in the second mode is increasing from $2.439Hz$ to $2.457Hz$.

This approach represents differences in the response frequencies but good agreements in the response amplitude due to choosing a correct lift coefficient by adjusting the Strouhal number and consequently added mass.

The lift coefficient curves for case 74xx with the adjusted Strouhal number are shown in Figure 5.18 to Figure 5.20. By comparisons of these figures with Figure 5.7 to Figure 5.9, it is observed that the negative lift coefficient for the first cases which excited in mode 1 is much lower than the cases with the actual Strouhal number. The positive lift coefficients for these cases are also much lower than the original cases.

Two last cases in Figure 5.20 with $U_{model} = 0.45$ and $0.5m/s$ are excited in the second mode. It is very interesting to see that the lift coefficient curves for these cases are very close to two last cases with the actual Strouhal number in Figure 5.9. As previously mentioned these two cases had the best match with the test results. Here, we realize that by adjusting the Strouhal number, in fact, it is mostly the lift

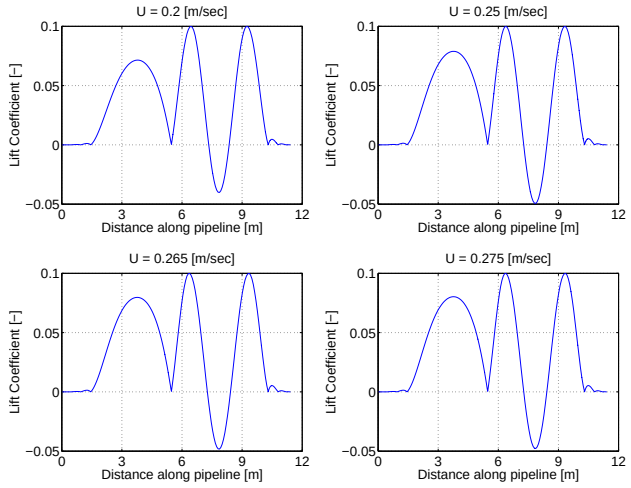

Figure 5.18: Lift coefficient curves for case 74xx with adjusted Strouhal number, $U_{model} = 0.2 - 0.275m/s$

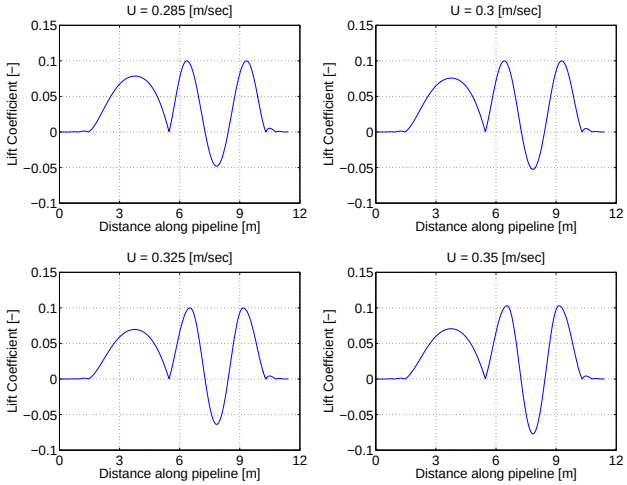

Figure 5.19: Lift coefficient curves for case 74xx with adjusted Strouhal number, $U_{model} = 0.285 - 0.35m/s$

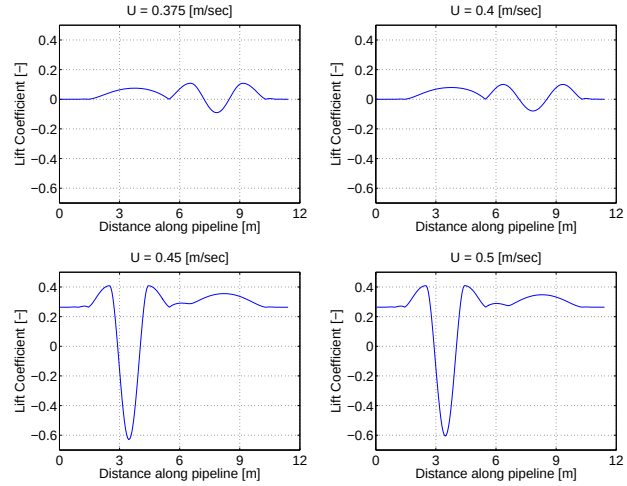

Figure 5.20: Lift coefficient curves for case 74xx with adjusted Strouhal number, $U_{model} = 0.375 - 0.5m/s$

coefficient contribution which causes the VIVANA results to match with the test measurements.

By looking at Figure 5.15 and Figure 5.16 we can observe that the Strouhal numbers needed to obtain a good agreement with experiments, decrease by increasing the current velocity. However the original Strouhal number in VIVANA is close to 0.2 for all cases which is in accordance with the relationship between the Strouhal number and the Reynolds number found by experiments in different flow regimes and reported in many references, e.g. Lienhard (1966). Therefore by accepting this relationship also for the VIV condition and by carrying in mind the VIVANA theory, see VIVANA Theory manual (2005), it may be concluded that the relationship between the Strouhal number and the other hydrodynamic coefficients and non-dimensional frequency may cause the response to match with the test results.

It should also be noted that this adjustment is a "*parametric exercise*" without any physical foundation. As explained for Figure 5.14, it is very interesting to see that the measured frequency plot has almost the same trend as the actual case but at a lower value. Then, further attempts have been done to adjust both response frequency and amplitude. The results are presented later in this chapter.

As a conclusion here, it is realized that adjusting the Strouhal number has the most effect on the selected lift coefficient curve by VIVANA.

5.4.2 Adjusting the lift coefficient

By varying the Strouhal number the non-dimensional frequency varies and that influences the selected lift coefficient curves and added mass data defined in VIVANA. Therefor there is obviously a need to investigate how other hydrodynamic coefficients will influence results from VIVANA. In the following the influence from variation of the lift coefficient and added mass on the results will be studied.

In this section, only the lift coefficient is tuned. All $A_{(C_L=0)}$ and $A_{(C_L=max)}$ in the lift coefficient table (see Table 5.8) are adjusted and multiplied by 0.675 for case 71xx and by 0.850 for case 74xx in order to get the same A/D on the test and analysis for the reference point, i.e. $U_{(prototype)} = 1.764m/s$. The Strouhal number is the VIVANA default values. The response frequencies found by VIVANA may hence become different from what was observed in the tests.

The reason to choose $U_{(prototype)} = 1.764m/s$ as the reference point is explained more later in case 74xx. There, this point has the maximum response in the test for the first mode.

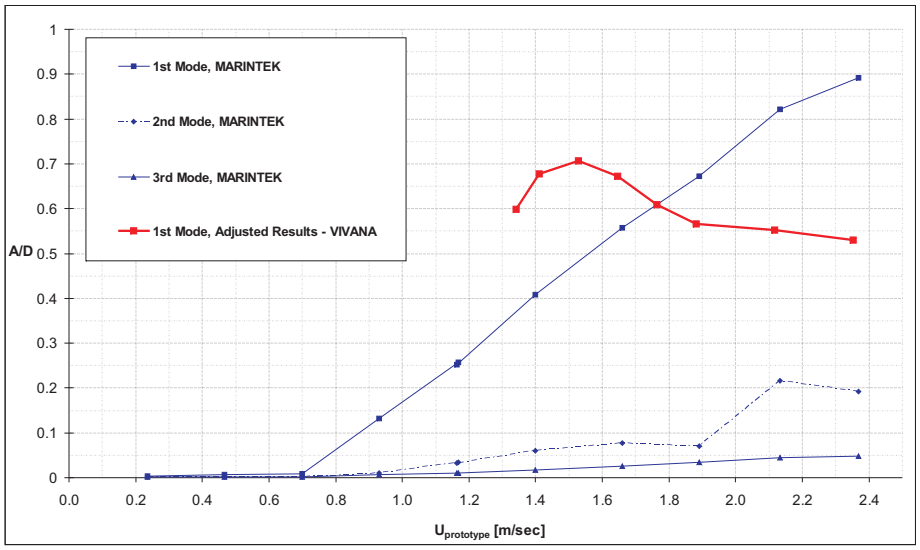

Figure 5.21: A/D versus $U_{(prototype)}$ for case 71xx with adjusted lift coefficient

Figure 5.21 shows A/D versus $U_{(prototype)}$ for case 71xx. As seen, the response displacement is the same for the reference point, $U_{(prototype)} = 1.764m/s$ by adjusting the lift coefficient data. The same C_L table is used for the other points.

$\hat{f}$	$A_{C_{L=0}}$	$A_{C_{L=max}}$	$C_{L_{max}}$	$C_{L_{A=0}}$
0.120	0.149	0.100	0.100	0.000
0.125	0.266	0.200	0.100	0.000
0.127	0.400	0.214	0.100	0.016
0.130	0.451	0.235	0.100	0.040
0.135	0.505	0.270	0.100	0.080
0.140	0.530	0.350	0.140	0.110
0.150	0.588	0.450	0.200	0.180
0.160	0.658	0.500	0.350	0.240
0.165	0.746	0.500	0.500	0.300
0.168	0.890	0.460	0.780	0.350
0.172	0.900	0.430	0.800	0.400
0.175	0.837	0.400	0.700	0.200
0.180	0.761	0.400	0.400	0.100
0.185	0.706	0.400	0.300	0.000
0.190	0.666	0.400	0.200	0.000
0.200	0.615	0.380	0.100	0.000
0.210	0.592	0.350	0.100	0.000
0.220	0.575	0.313	0.100	0.000
0.230	0.539	0.275	0.100	0.000
0.240	0.504	0.238	0.100	0.000
0.250	0.420	0.200	0.100	0.000
0.270	0.312	0.160	0.100	0.000
0.280	0.247	0.140	0.100	0.000
0.290	0.186	0.120	0.100	0.000
0.300	0.160	0.100	0.100	0.000
0.310	0.136	0.090	0.100	0.000

Table 5.8: The original lift coefficient table in VIVANA

By using an option in VIVANA, case 71xx is forced to be excited in mode 1, but it was impossible to be excited in mode 2 and 3 up to the maximum current velocity range, i.e. $U_{(prototype)_{max}} = 2.352m/s$. However, case 74xx is successfully forced to be excited in mode 1, 2 and 3 by using this option.

As shown in Figure 5.21 tuning of C_L curve to maximum response does not work well since the A/D curve has a different trend from the analysis than from the tests.

The response frequencies in the tests are shown in Figure 5.22. For the velocities higher than the reference point the response in the tests is higher than expected. The reason may be the interaction between the cross-flow and the in-line response.

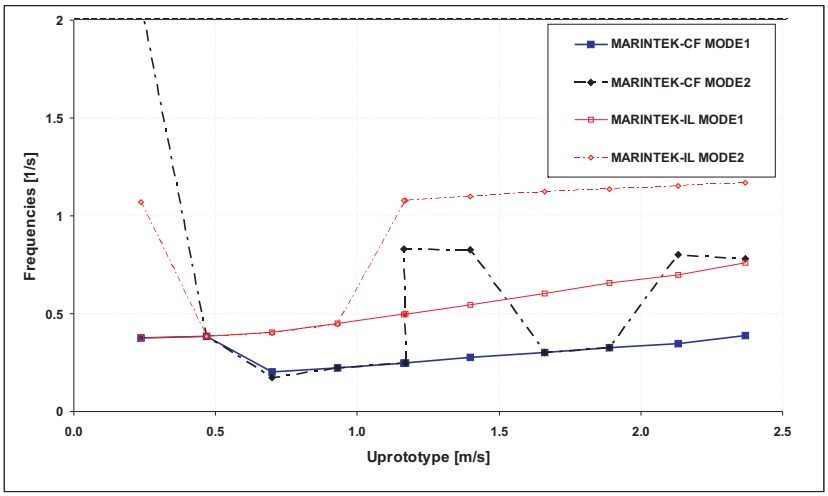

Figure 5.22: Test model frequencies for case 71xx, MARINTEK

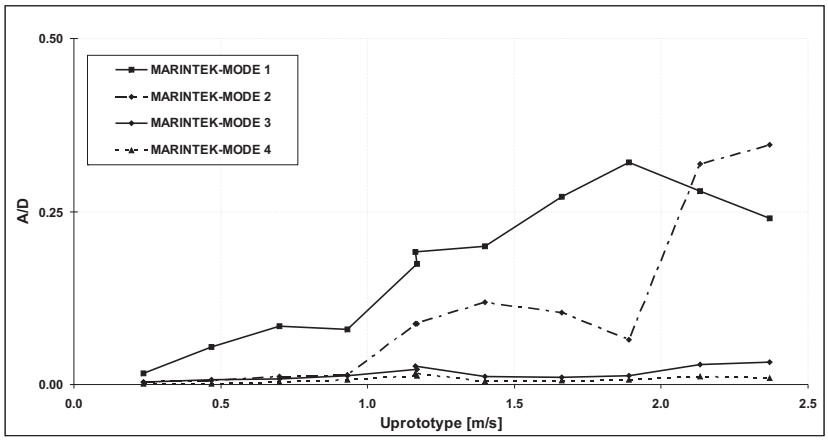

Figure 5.23: Test model in-line response for case 71xx, MARINTEK

Figure 5.22 shows that $\omega_{IL} = 2x\omega_{CF}$ for mode 1 in both directions, which leads to a well organized response of the beam, and hence also large amplitudes.

Figure 5.23 shows that the in-line response in mode 2 gets quite high for the velocities larger than the reference point which may cause the cross-flow response in mode 2 also gets higher after this point in the test. This response may amplify the

$U_{(model)}$	$U_{(prototype)}$	$f_{(osc)test}$	$f_{(osc)analysis}$	St
0.285	1.340	1.265	1.502	Default
0.300	1.411	1.298	1.539	Default
0.325	1.528	1.360	1.626	Default
0.350	1.646	1.416	1.737	Default
0.375	1.764	1.477	1.848	Default
0.400	1.881	1.529	1.962	Default
0.450	2.116	1.632	2.189	Default
0.500	2.352	1.816	2.414	Default

Table 5.9: Response frequency mode 1 in test and analysis for case 71xx with adjusted lift coefficient

cross-flow response in mode 1 as well. The in-line response mode 1 also influences the cross-flow response in mode 1 specially after the reference point.

Mode 1 in the cross-flow response creates $\omega_{1(CF)}$, while the load distribution gives mode 1 in the in-line response, $\omega_{1(IL)}$ and that can be a reason the in-line response inclines steeply as well.

Table 5.9 shows the response frequency for mode 1 from the test and analysis. Here the Strouhal number is the VIVANA default values and calculated during the analysis. As seen the response frequencies are different. This must be caused by an added mass variation in the experiments that is not captured by VIVANA.

The lift coefficient curves are shown for different current velocities on the analyses models in Figure 5.24 and Figure 5.25 for case 71xx.

As shown, the maximum negative lift coefficient belongs to $U_{(model)} = 0.325m/s$ ($U_{(prototype)_{max}} = 1.528m/s$) that corresponds to the maximum energy which goes out of the system. It is in accordance with the highest response as seen in Figure 5.21 for the analysis, but the maximum response in the test model occurs for a higher velocity due to the interaction between the in-line and cross-flow response.

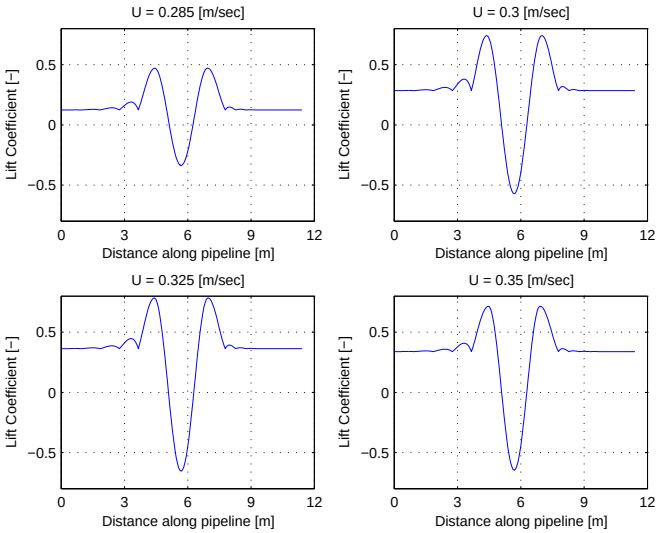

Figure 5.24: Lift coefficient curves for case 71xx with adjusted lift coefficient

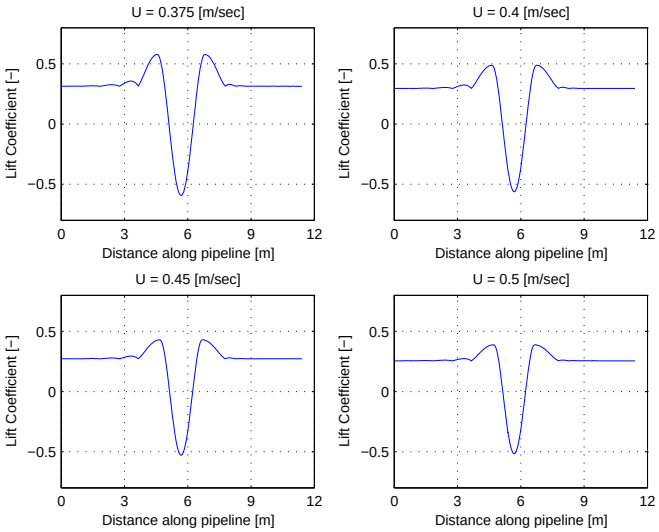

Figure 5.25: Lift coefficient curves for case 71xx with adjusted lift coefficient

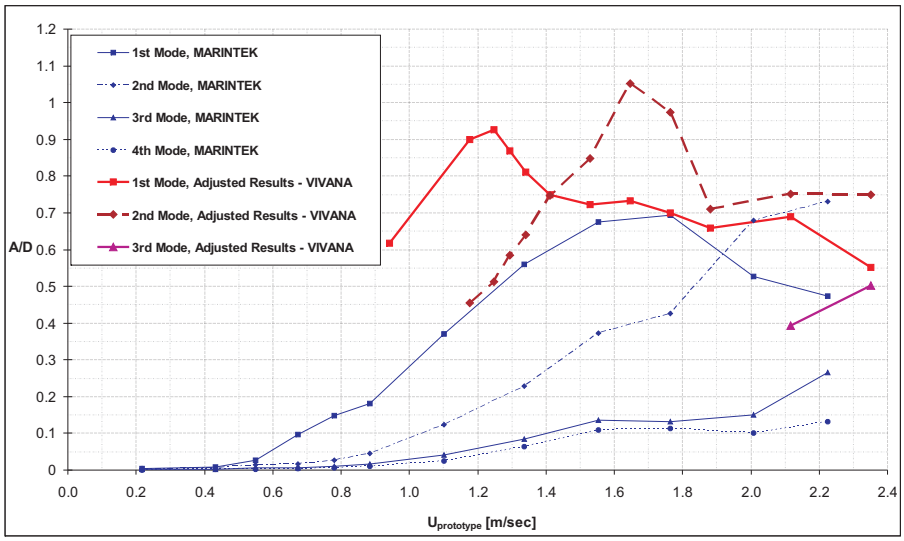

Figure 5.26: A/D versus $U_{(prototype)}$ for case 74xx with adjusted lift coefficient

Figure 5.26 shows A/D versus $U_{(prototype)}$ for case 74xx. As shown, response displacement is the same for the reference point, $U_{(prototype)} = 1.764m/s$ on the test and analysis by adjusting the lift coefficient data. The same C_L table is used for the other current velocities. Here, the factor to adjust the lift coefficient is 0.850.

As seen in Figure 5.26 the reference point, $U_{(prototype)} = 1.764m/s$ has been chosen since it has the maximum response in the tests for mode 1 and can be a good point for comparing with the VIVANA results. But as shown in this figure tuning of C_L curve to maximum response does not work due to experiencing higher response for the lower velocity. The non-dimensional frequency for the reference point is $\hat{f} = 0.127$, while the non-dimensional frequency for the maximum response is $\hat{f} = 0.172$. We observe that the maximum response in the test occurs for a higher velocity than expected.

It should be noted that the VIVANA analyses will not give *"modes"*, but the response will have a dominating mode that normally is identical to the mode associated to the actual response frequency (which always is an eigenfrequency). The measured response has been analysed and modal components are calculated. These modes are acting simultaneously. The VIVANA response from one analysis is compared with the measured mode which is a component of the total response. As seen in Figure 5.6 VIVANA standard will probably give the second eigenfrequency as response frequency at the reference point.

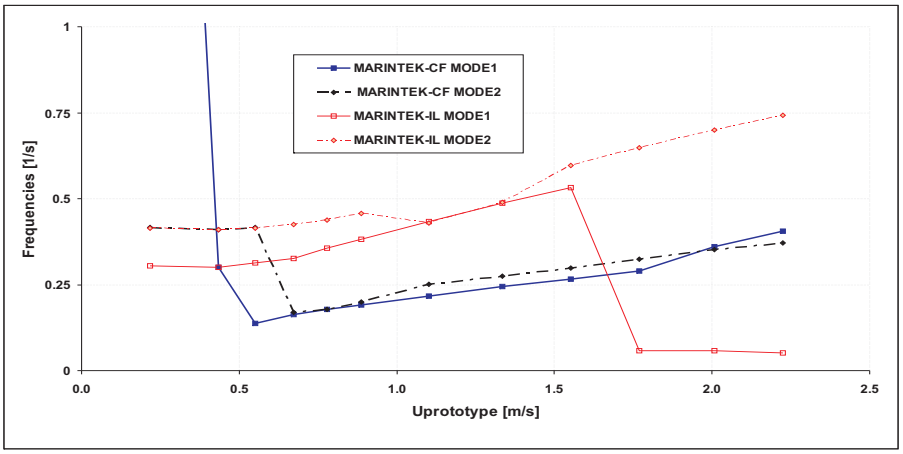

Figure 5.27: Test model frequencies for case 74xx, MARINTEK

Figure 5.26 shows maximum cross-flow response is lower in the test than VIVANA. The reasons may be the interaction between the cross-flow and the in-line response, and also the strong influence from mode 2 at almost the same frequency, see Figure 5.27.

As seen in this figure mode 1 in the cross-flow response in the test is weaker than expected. In the contrary, mode 2 in the cross-flow response is stronger than expected. The reason may be the in-line response at mode 1, 2 and 3, see Figure 5.28. The in-line response mode 2 is the strongest and that is the reason mode 2 in the cross-flow response also is strongly represented. It is an interesting shift of the response composition at approximately $U_{(prototype)} = 1.6m/s$ in Figure 5.27. The first mode have reduced response, and becomes non-resonant; the response frequency becomes very low, slowly varying which is not ordinary VIV. The second mode becomes dominating for IL, and appears at 2x$\omega_{(CF)}$, see Figure 5.28.

Mode 1 in the cross-flow response creates $\omega_{1(CF)}$, while the load distribution gives mode 1 in the in-line response, $\omega_{1(IL)}$. Moreover, the resonance gives mode 2 in the in-line response, $\omega_{2(IL)}$ and the load distribution in the cross-flow response will give mode 2 in addition to mode 1 due to combination of closely spaced eigenfrequency. Mode 1 and 2 in the cross-flow and the load distribution give mode 2 in the cross-flow response as well. The first and second eigen frequency -after the added mass iteration- from the VIVANA model are $1.36Hz$ and $1.56Hz$ respectively which are also close.

Table 5.10 is shown the response frequency in mode 1 of the test and analysis

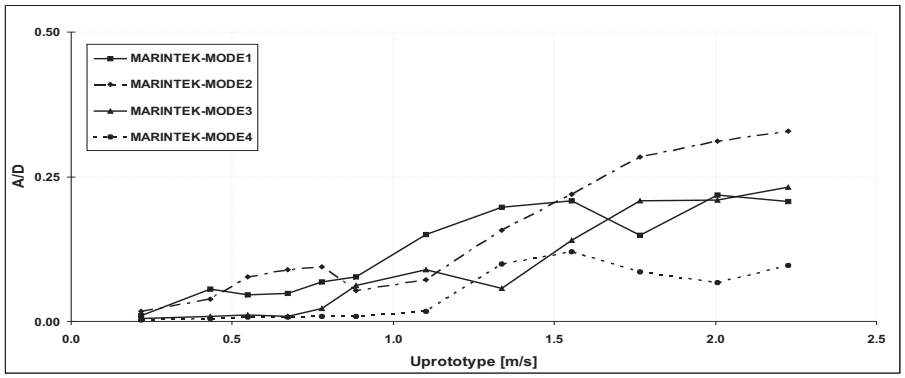

Figure 5.28: Test model in-line response for case 74xx, MARINTEK

$U_{(model)}$	$U_{(prototype)}$	$f_{(osc)test}$	$f_{(osc)analysis}$	St
0.250	1.176	1.063	1.240	Default
0.265	1.246	1.101	1.306	Default
0.275	1.293	1.124	1.350	Default
0.285	1.340	1.148	1.393	Default
0.300	1.411	1.185	1.460	Default
0.325	1.528	1.242	1.571	Default
0.350	1.646	1.303	1.685	Default
0.375	1.764	1.360	1.798	Default
0.400	1.881	1.515	1.915	Default
0.450	2.116	1.806	2.119	Default
0.500	2.352	2.032	2.289	Default

Table 5.10: Response frequency mode 1 in test and analysis for case 74xx

for case 74xx with adjusted lift coefficient. The Strouhal number shown here is VIVANA standard which calculated during the analysis. The lift coefficient curves for case 74xx are shown in Figure 5.29 to Figure 5.30 for different current velocities on the analyses models. The lift coefficient curves here are presented for the first mode. It is observed in these figures that the maximum response happens at the longer span and on $U_{(model)} = 0.275m/s$. But as seen in Figure 5.26 the maximum response in the test model occurs for $U_{(model)} = 0.375m/s$.

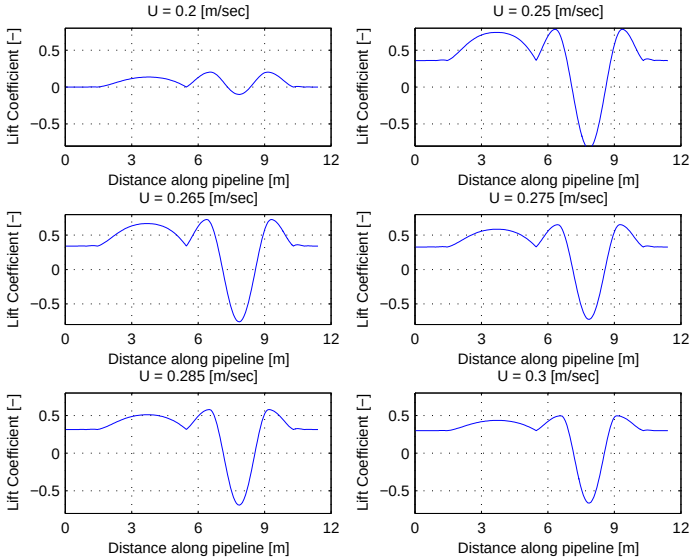

Figure 5.29: Lift coefficient curves for case 74xx with adjusted lift coefficient

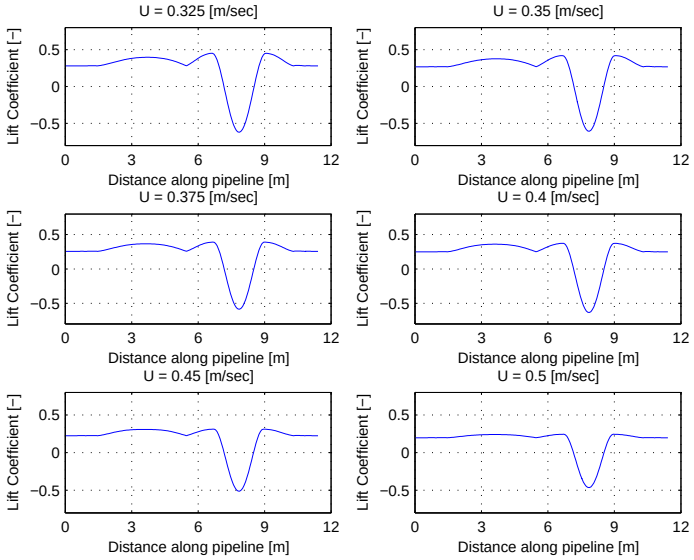

Figure 5.30: Lift coefficient curves for case 74xx with adjusted lift coefficient

5.4.3 Adjusting the Strouhal number and lift coefficient, same response frequency for reference point

The response frequency was different in the test than found from the analysis in the previous section. Here, both St and C_L are tuned to get the same response amplitude and frequency for the reference point, $U_{(prototype)} = 1.764m/s$. Same St and C_L has been used for all cases. St for all velocities is equal to 0.148 for case 71xx and 0.153 for case 74xx. Accordingly, all $A_{(C_L=0)}$ and $A_{(C_L=max)}$ in the lift coefficient table (see Table 5.8) are tuned and multiplied by 0.780 for case 71xx and 0.675 for case 74xx to get the same A/D for the test and analysis at $U_{(prototype)} = 1.764m/s$. These St and C_L values have been applied for all velocities and all modes. Case 71xx was always found to respond at the first eigenfrequency in VIVANA, even if the second frequency was given priority. The reason for this is the low Strouhal number, which leads to a low response frequency that can not be linked to the second mode for realistic variation of added mass. Case 74xx is forced to be excited in mode 1 and 2 successfully.

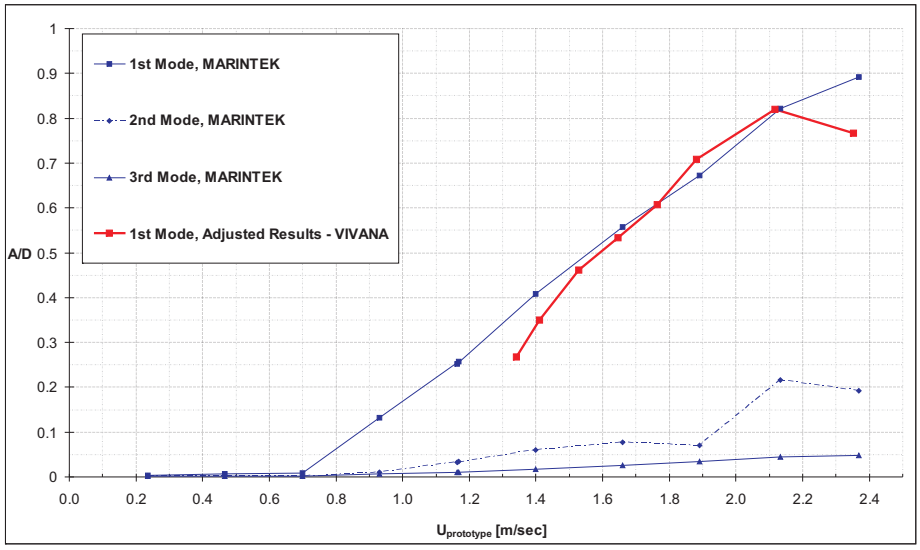

Figure 5.31: A/D versus $U_{(prototype)}$ for case 71xx with adjusted Strouhal number and lift coefficient, same response frequency for reference point

Figure 5.31 shows A/D versus $U_{(prototype)}$ for case 71xx. As shown, response displacement is the same for the reference point, $U_{(prototype)} = 1.764m/s$ on the test and analysis by adjusting the lift coefficient data. The same C_L table is used for the other current velocities. Here, the factor to adjust the lift coefficient is 0.780.

$U_{(model)}$	$U_{(prototype)}$	$f_{(osc)test}$	$f_{(osc)analysis}$	St	$\hat{f}_{(internal)}$
0.285	1.340	1.265	1.622	0.148	0.211
0.300	1.411	1.298	1.587	0.148	0.205
0.325	1.528	1.360	1.524	0.148	0.198
0.350	1.646	1.416	1.456	0.148	0.192
0.375	1.764	1.477	1.478	0.148	0.187
0.400	1.881	1.529	1.504	0.148	0.181
0.450	2.116	1.632	1.607	0.148	0.172
0.500	2.352	1.816	1.759	0.148	0.171

Table 5.11: Response frequency mode 1 in test and analysis for case 71xx with adjusted Strouhal number and lift coefficient, same response frequency for reference point

The Strouhal number is also adjusted here to give a correct response frequency for the reference point. St is set to 0.148 for all cases.

The results in Figure 5.31 in comparison with the previous results show a better agreement. The trend on analysis results illustrates the same slope as the test, but at the top deviates a little. It has a peak at $U_{(prototype)} = 2.116m/s$.

Table 5.11 represents the response frequency for mode 1 for the test and analysis. As seen the Strouhal number is 0.148 for all cases in order to give the same response frequency at the reference point. The internal non-dimensional frequency is also presented in this table. This is the non-dimensional frequency internally calculated by VIVANA. The program results are based on Gopalkrishnan's tests which were conducted for the Strouhal number, $St_G = 0.2$ and if we get another Strouhal number during the analysis the non-dimensional frequency, $\hat{f}$ shall be corrected as:

$$\hat{f}_{(internal)} = \frac{St_G}{St}.\hat{f} = \frac{0.2}{St}.\frac{f_{(resp)}.D}{U} \tag{5.8}$$

where $f_{(resp)}$ is the response frequency found from added mass iteration in VIVANA.

According to Table 5.8 and Table 5.11 the maximum response should occur for $U_{(prototype)} = 2.116m/s$ where $\hat{f}_{(internal)} = 0.172$. This is also in agreement with the trend shown in Figure 5.31 as the response is increased by increasing the current velocity until $U_{(prototype)} = 2.116m/s$ and hereafter reducing a little.

The lift coefficient curves are shown for different current velocities on the analyses models in Figure 5.32 and Figure 5.33 for case 71xx.

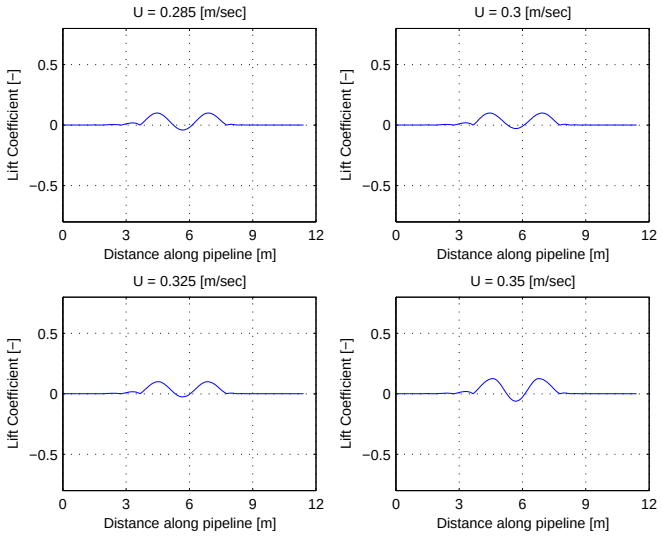

Figure 5.32: Lift coefficient curves for case 71xx with adjusted Strouhal number and lift coefficient, same response frequency for reference point

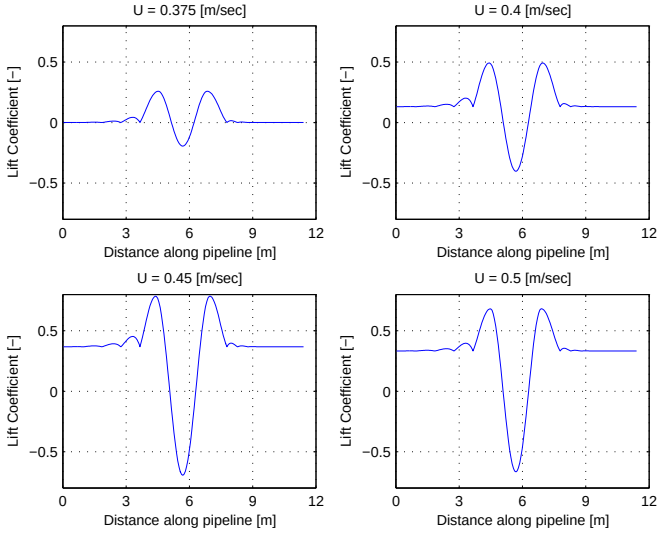

Figure 5.33: Lift coefficient curves for case 71xx with adjusted Strouhal number and lift coefficient, same response frequency for reference point

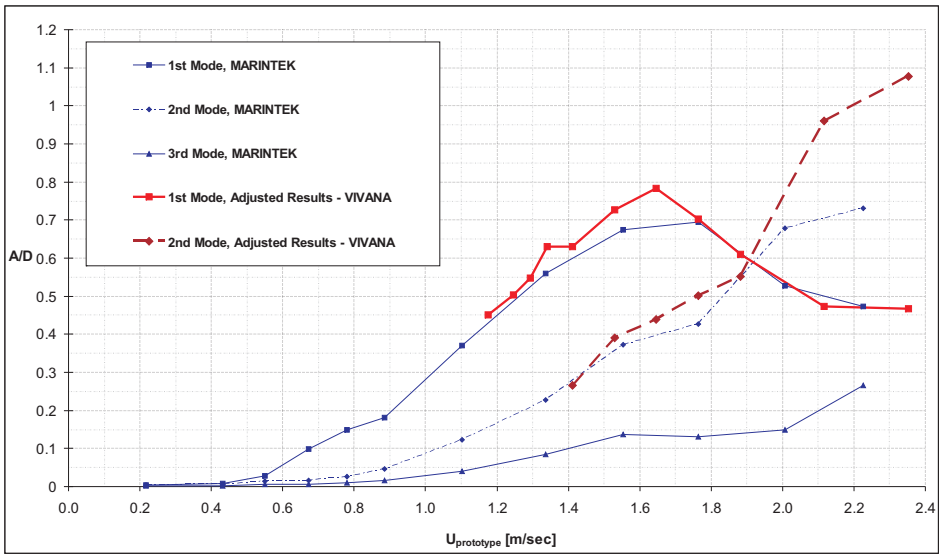

Figure 5.34: A/D versus $U_{(prototype)}$ for case 74xx with adjusted Strouhal number and lift coefficient, same response frequency for reference point

Figure 5.34 shows A/D versus $U_{(prototype)}$ for case 74xx. As shown, response displacement is the same for the reference point, $U_{(prototype)} = 1.764m/s$ on the test and analysis which happens by tuning of the lift coefficient data. The same C_L table is used for the other current velocities. Here, the factor to adjust the lift coefficient is 0.675. The Strouhal number is also adjusted here to give a correct response frequency for the reference point. St is 0.153 for all cases.

Again it should be noted that the experiments show response at mode 1 and 2 simultaneously, while VIVANA gives only mode 1 at the same time.

Table 5.12 represents the response frequency in mode 1 for the test and analysis. As seen the Strouhal number is 0.153 for all cases in order to give the same response frequency for the reference point. The internal non-dimensional frequency is also presented in this table and for the reference point can be calculated as:

$$\hat{f}_{(internal)} = \frac{St_G}{St}.\hat{f} = \frac{0.2}{0.153}.\frac{1.36.(0.03511)}{0.375} = 0.166 \tag{5.9}$$

According to Table 5.8 and Table 5.12 the maximum response should occur for $U_{(prototype)} = 1.646m/s$ where $\hat{f}_{(internal)} = 0.172$. By looking at these tables one can understand that the response is increased by increasing the current ve-

$U_{(model)}$	$U_{(prototype)}$	$f_{(osc)test}$	$f_{(osc)analysis}$	St	$\hat{f}_{(internal)}$
0.250	1.176	1.063	1.105	0.153	0.195
0.265	1.246	1.101	1.108	0.153	0.191
0.275	1.293	1.124	1.116	0.153	0.188
0.285	1.340	1.148	1.125	0.153	0.185
0.300	1.411	1.185	1.149	0.153	0.181
0.325	1.528	1.242	1.200	0.153	0.175
0.350	1.646	1.303	1.281	0.153	0.171
0.375	1.764	1.360	1.360	0.153	0.166
0.400	1.881	1.515	1.440	0.153	0.174
0.450	2.116	1.806	1.601	0.153	0.184
0.500	2.352	2.032	1.762	0.153	0.187

Table 5.12: Response frequency mode 1 in test and analysis for case 74xx with adjusted Strouhal number and lift coefficient, same response frequency for reference point

locity until the maximum response $1.646m/s$, and hereafter gets a different trend and decreased. This is completely in agreement with the trend shown in Figure 5.34. The maximum response for the test model happens at a little higher velocity $U_{(prototype)} = 1.764m/s$ due to the interaction between the in-line and cross-flow response.

The lift coefficient curves are shown for different current velocities on the analyses models in Figure 5.35 to Figure 5.37 for case 74xx. It is seen that the maximum

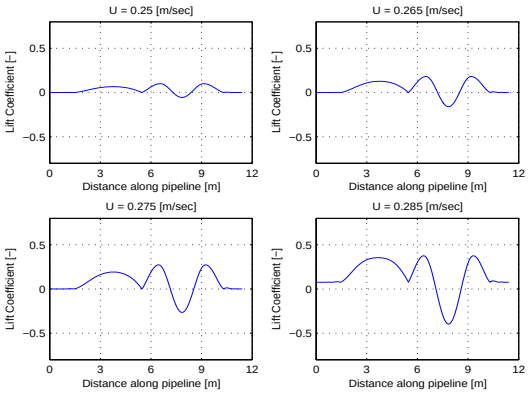

Figure 5.35: Lift coefficient curves for case 74xx with adjusted Strouhal number and lift coefficient, same response frequency for reference point

energy transfer occurs at $U_{(model)} = 0.35m/s$ which has the maximum negative lift coefficient. That is in agreement with the maximum response shown in Figure 5.34 at this point. But, the maximum response on the test model occurs at $U_{(model)} = 0.40m/s$ probably due to the interaction between the in-line and cross-flow vibrations.

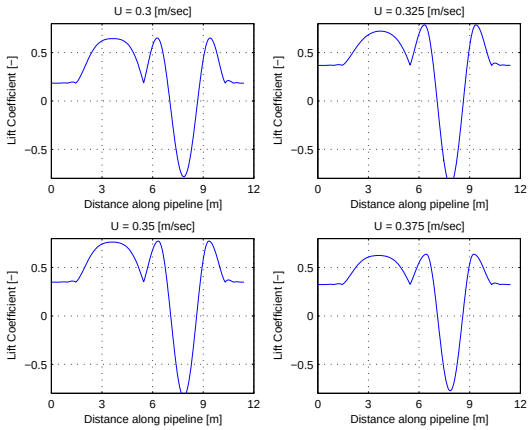

Figure 5.36: Lift coefficient curves for case 74xx with adjusted Strouhal number and lift coefficient, same response frequency for reference point

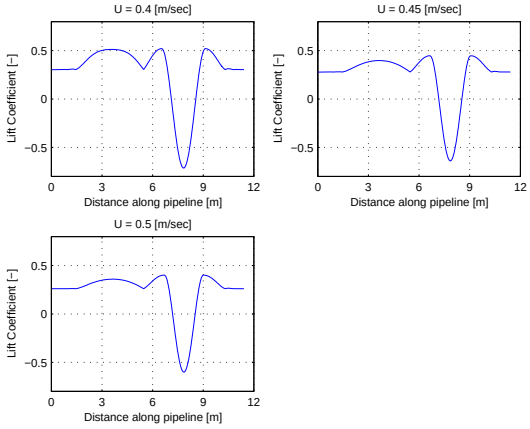

Figure 5.37: Lift coefficient curves for case 74xx with adjusted Strouhal number and lift coefficient, same response frequency for reference point

5.4.4 Adjusting the Strouhal number and lift coefficient, same response frequency for all cases

As shown in Table 5.11 and 5.12 the response frequencies -in exception of reference point- are not the same for the test and analysis. To have a more robust comparison an approach should be taken in order to get the same response frequencies for all cases.

In this study, both St and C_L are tuned. St was tuned for all cases in order to get the same response frequencies in the first mode. All $A_{(C_L=0)}$ and $A_{(C_L=max)}$ in the lift coefficient table (see Table 5.8) are tuned and multiplied by 0.780 for case 71xx and 0.675 for case 74xx to get the same A/D on the test and analysis at the reference point, i.e. $U_{(prototype)} = 1.764m/s$. C_L table used for the reference point has been applied for all cases and all modes. St table for different cases are accordingly varied in VIVANA to get the same response frequency on the test and analysis, but are kept the same on different modes for each case. Case 71xx is forced to be excited in mode 1, but it was not able to be excited in mode 2 and 3 as the same reason is explained in the previous section. Case 74xx is forced to be excited in mode 1, 2 and 3.

Figure 5.38 shows A/D versus $U_{(prototype)}$ for case 71xx. As shown, response dis-

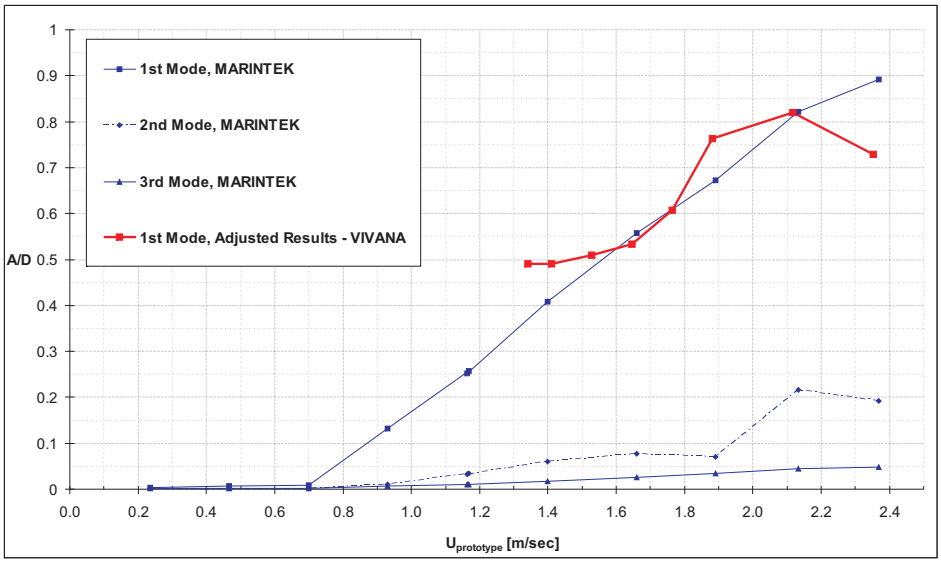

Figure 5.38: A/D versus $U_{(prototype)}$ for case 71xx with adjusted Strouhal number and lift coefficient, same response frequency for all cases

$U_{(model)}$	$U_{(prototype)}$	$f_{(osc)test}$	$f_{(osc)analysis}$	St	$\hat{f}_{(internal)}$
0.285	1.340	1.265	1.452	0.1790	0.174
0.300	1.411	1.298	1.452	0.1700	0.179
0.325	1.528	1.360	1.452	0.1570	0.187
0.350	1.646	1.416	1.456	0.1480	0.192
0.375	1.764	1.477	1.478	0.1480	0.187
0.400	1.881	1.529	1.529	0.1535	0.175
0.450	2.116	1.632	1.634	0.1510	0.169
0.500	2.352	1.816	1.817	0.1535	0.166

Table 5.13: Response frequency mode 1 in test and analysis for case 71xx with adjusted Strouhal number and lift coefficient, same response frequency for all cases

placement is the same for the reference point, $U_{(prototype)} = 1.764m/s$ on the test and analysis by adjusting the lift coefficient data. The same C_L table is used for the other current velocities. Here, the factor to adjust the lift coefficient is 0.780. The Strouhal number is adjusted here to have a correct response frequency for all points. The adjusted Strouhal number are shown in Table 5.13 for all cases.

Table 5.13 is shown the response frequency in mode 1 for the test and analysis. As seen the Strouhal number and the internal non-dimensional frequency are also presented in this table for all cases. The Strouhal number is varying between 0.148 till 0.179. The response frequencies are in a very good agreement in exception of three first cases. It was not possible to get a better match for those cases in VIVANA. As seen $\hat{f}_{(internal)} = 0.169$ for the case with maximum response, i.e. $U_{(model)} = 0.45m/s$ which corresponds to the high lift coefficient value in Table 5.8. The response frequency is 1.634 for this point which achieved by tuning the Strouhal number to 0.151. As seen in Figure 5.38 in previous section, it was predictable that St remains almost the same as the case presented there since the response frequency was almost similar for this point on the test and analysis and also the response was in a good agreement with the test model.

The lift coefficient curves are shown for different current velocities on the analyses models in Figure 5.39 and Figure 5.40 for case 71xx. The lift coefficient curves show the maximum lift force occurs at $U_{(model)} = 0.45m/s$ which is in agreement with analysis curve in Figure 5.38. But as seen, the test model has a peak at a higher velocity which as earlier explained in this chapter may be due to the interaction between the in-line and cross-flow vibrations.

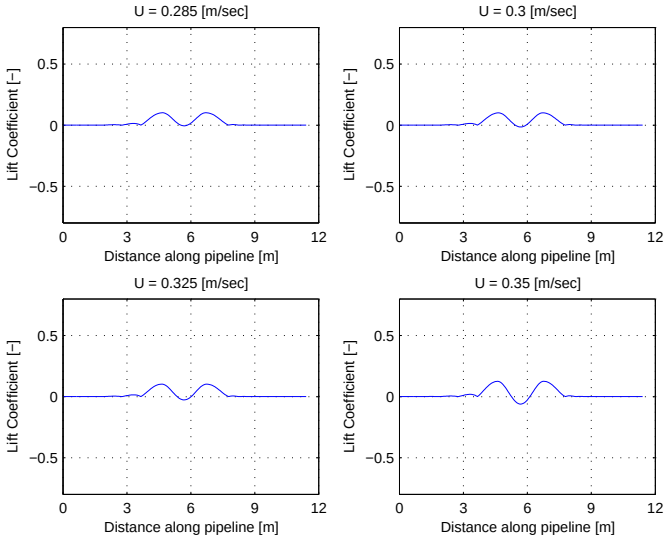

Figure 5.39: Lift coefficient curves for case 71xx with adjusted Strouhal number and lift coefficient, same response frequency for all cases

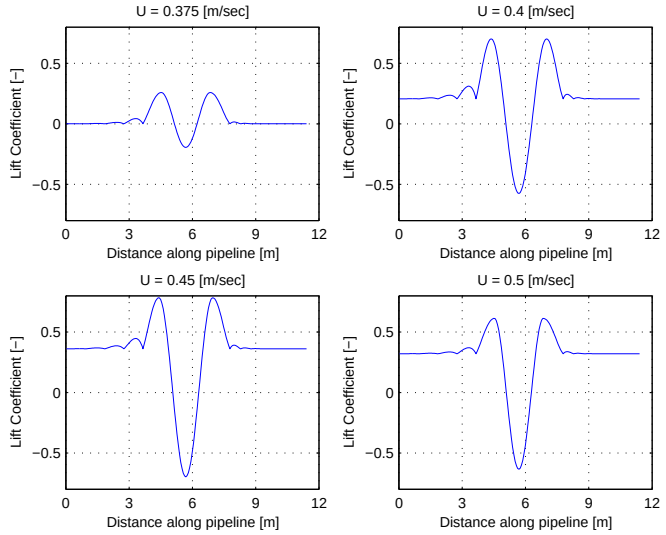

Figure 5.40: Lift coefficient curves for case 71xx with adjusted Strouhal number and lift coefficient, same response frequency for all cases

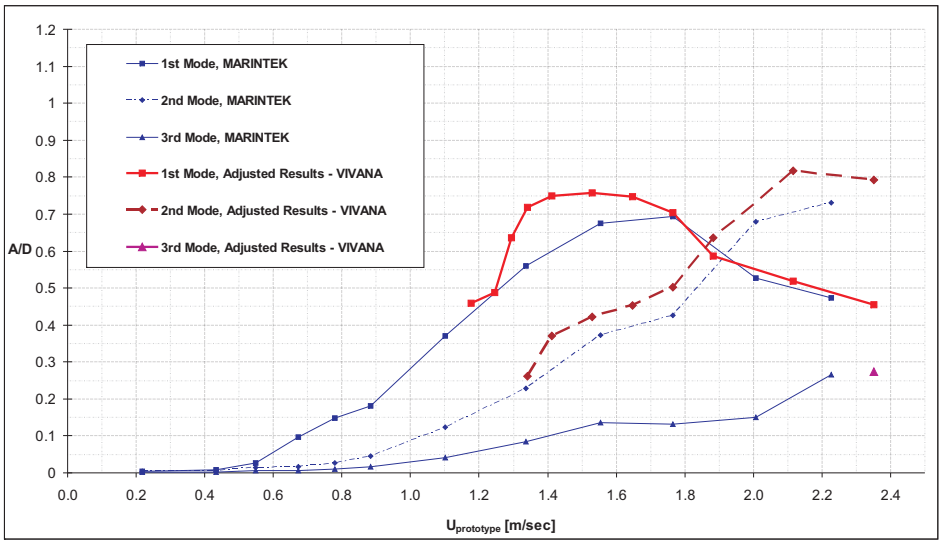

Figure 5.41: A/D versus $U_{(prototype)}$ for case 74xx with adjusted Strouhal number and lift coefficient, same response frequency for all cases

Figure 5.41 shows A/D versus $U_{(prototype)}$ for case 74xx. As shown, response displacement is the same for the reference point, $U_{(prototype)} = 1.764m/s$ on the test and analysis which happens by adjusting the lift coefficient data. The same C_L table is used for the other current velocities. Here, the factor to adjust the lift coefficient is 0.675. The Strouhal number is adjusted here to have a correct response frequency for all points. The adjusted Strouhal number are shown in Table 5.14 for all cases.

Figure 5.41 illustrates a higher response for the velocities less than the reference point. The maximum response occurs at $U_{(model)} = 0.325m/s$ where $\hat{f}_{(internal)} = 0.169$. The cases with high responses have almost the same $\hat{f}_{(internal)}$ around 0.170. According to this figure, mode 2 also shows a good trend and have a peak at $U_{(model)} = 0.45m/s$ where $\hat{f}_{(internal)}$ is close to 0.172. There is only one point excited at mode 3, i.e. $U_{(model)} = 0.5m/s$ and the response is very close to the test model in this mode.

Table 5.14 is shown the response frequency in mode 1 for the test and analysis. As seen the Strouhal number and the internal non-dimensional frequency are also presented in this table for all cases. The response frequencies are in a very good agreement.

$U_{(model)}$	$U_{(prototype)}$	$f_{(osc)test}$	$f_{(osc)analysis}$	St	$\hat{f}_{(internal)}$
0.250	1.176	1.063	1.096	0.1545	0.193
0.265	1.246	1.101	1.103	0.1500	0.194
0.275	1.293	1.124	1.124	0.1580	0.182
0.285	1.340	1.148	1.149	0.1610	0.176
0.300	1.411	1.185	1.185	0.1635	0.170
0.325	1.528	1.242	1.242	0.1591	0.169
0.350	1.646	1.303	1.303	0.1560	0.168
0.375	1.764	1.360	1.360	0.1530	0.166
0.400	1.881	1.515	1.515	0.1620	0.164
0.450	2.116	1.806	1.806	0.1746	0.161
0.500	2.352	2.032	2.038	0.1790	0.159

Table 5.14: Response frequency mode 1 in test and analysis for case 74xx with adjusted Strouhal number and lift coefficient, same response frequency for all cases

The lift coefficient curves are shown for different current velocities on the analyses models in Figure 5.42 to Figure 5.44 for case 74xx. It is interesting to see that the lift coefficient curves for $U_{(model)} = 0.3m/s$ to $0.375m/s$ have negative values which lead to high amount of energy that goes out of the system. That is the consequence these velocities encounter high responses. For the test model the maximum response happens at $U_{(model)} = 0.375m/s$ (i.e. the point which chosen as the reference point) and has a higher velocity value than the maximum response point for the analysis case. One of the reason may be the interaction between the in-line and cross-flow vibrations. More reasons are given in Section 5.5 (Conclusion) in this chapter.

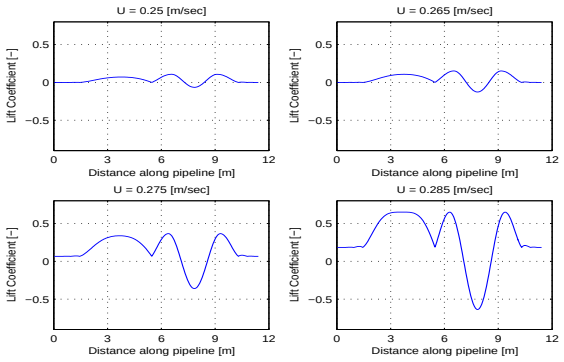

Figure 5.42: Lift coefficient curves for case 74xx with adjusted Strouhal number and lift coefficient, same response frequency for all cases

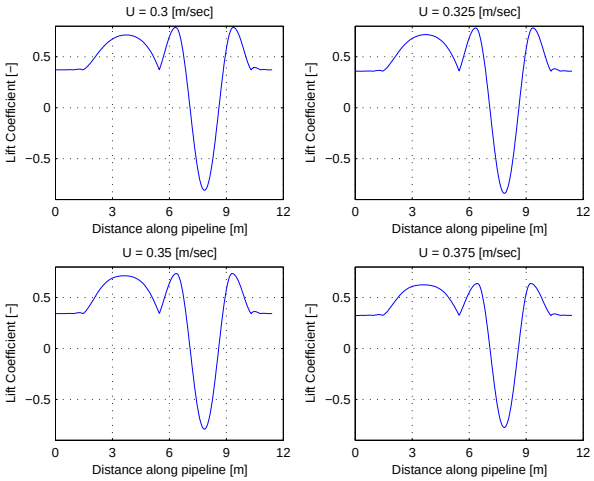

Figure 5.43: Lift coefficient curves for case 74xx with adjusted Strouhal number and lift coefficient, same response frequency for all cases

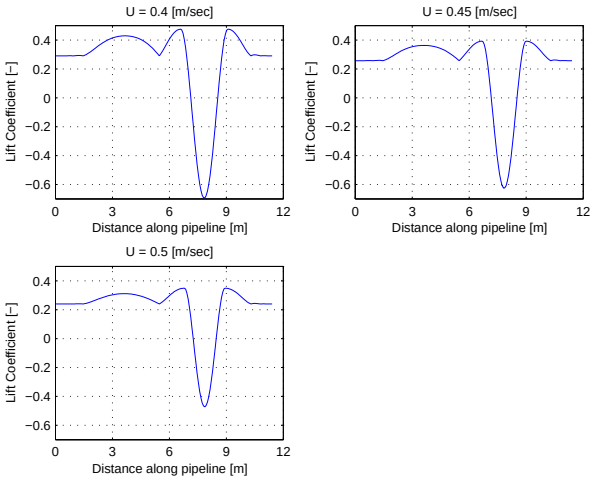

Figure 5.44: Lift coefficient curves for case 74xx with adjusted Strouhal number and lift coefficient, same response frequency for all cases

5.4.5 Adjusting the added mass and lift coefficient, same response frequency for all cases

Instead of adjusting the Strouhal number one might adjust added mass to get the same response frequency. The added mass curve which is defined as default in VIVANA has a maximum value of 2.2, while the values above 4 are possible in particular for low amplitudes, see Gopalkrishnan's curves (1993), and also for combined IL and CF response.

In this study, we specify $St = 0.19$ which is a well known value and find the added mass value that gives the correct response frequency at all points. All $A_{(C_L=0)}$ and $A_{(C_L=max)}$ in the lift coefficient table are tuned and multiplied by 1.01 for case 71xx and 1.2 for case 74xx to get the same A/D on the test and analysis just for the reference point, $U_{(prototype)} = 1.764m/s$. C_L table used for the reference point has been applied for all cases. Both case 71xx and 74xx are forced to be excited in mode 1.

Figure 5.45 shows A/D versus $U_{(prototype)}$ for case 71xx. As shown, response displacement is the same for the reference point, $U_{(prototype)} = 1.764m/s$ on the test and analysis by adjusting the lift coefficient data. The same C_L table is used for the other current velocities. Here, the factor to adjust the lift coefficient is 1.01.

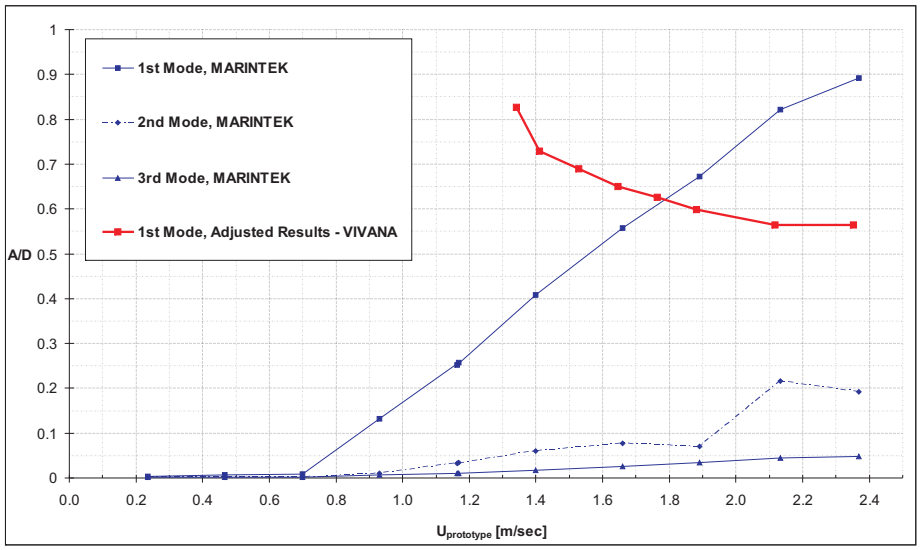

Figure 5.45: A/D versus $U_{(prototype)}$ for case 71xx with adjusted added mass and lift coefficient, same response frequency for all cases

The added mass is adjusted here to give a correct response frequency for all points. The adjusted added mass value are shown in Table 5.15 for all cases. It varies from 0.93 till 3.30.

We observe in Figure 5.45 that mode 1 continues to increase for velocity values to higher than what VIVANA predicts as a maximum response velocity. This must be caused by IL/CF interaction and is not possible to be reproduced by adjusting the added mass and lift coefficients as the case here.

A/D is 0.83 at $U_{(prototype)} = 1.340m/s$ and reducing by increasing the velocity. This is against the trend we can see for the test model. We also observe a different trend as shown in Figure 5.38 even the response frequencies are the same. The reason is different in St which causes a different non-dimensional frequency. Here $\hat{f}_{(internal)}$ varies between 0.134 till 0.164 (see Table 5.15) and as shown in Table 5.13 $\hat{f}_{(internal)}$ is from 0.166 till 0.192 so the higher velocities peak the maximum C_L.

However it is very interesting to see that the trend is similar to Figure 5.21 where St used as VIVANA standard, i.e. $St = 0.2$ which is very close to what we chose in the analysis here, i.e. $St = 0.19$. Note that the response frequencies are not the same and here is lower but the lift coefficient factor applied there is also different, i.e. 0.675.

The reason for this phenomena can be explained by VIVANA theory. The lift coefficient curve is almost symmetric around point $\hat{f} = 0.172$, see Figure 3.10. What happens here is the non-dimensional frequencies are located at both side of this peak point for these two cases. Here the non-dimensional frequency is lower and picks up the value below 0.172 as seen in Table 5.15. In the contrary, the non-dimensional frequencies for the case in Section 5.4.2 are higher but picks almost the same value. Thus, even the frequencies are different both cases give almost the same lift coefficient curve. By applying a different lift coefficient factor we actually balance these two curves and that is the reason we see the same trend in these cases.

Figure 5.45 shows that the maximum response on the test model occurs for a much higher velocity. We may conclude that adjusting St gives a better comparison between the results than adjusting the added mass. It means that the hypothesis about high added mass value is not working here.

According to the analysis results, we should expect that the maximum response on the test model happens at lower velocity value, however the response amplification occurs at higher response due to IL/CL interactions.

$U_{(model)}$	$U_{(prototype)}$	$f_{(osc)test}$	$f_{(osc)analysis}$	St	$\hat{f}_{(internal)}$	$Added, mass$
0.285	1.340	1.265	1.267	0.190	0.164	3.300
0.300	1.411	1.298	1.298	0.190	0.160	3.080
0.325	1.528	1.360	1.362	0.190	0.155	2.680
0.350	1.646	1.416	1.419	0.190	0.150	2.360
0.375	1.764	1.477	1.477	0.190	0.146	2.080
0.400	1.881	1.529	1.529	0.190	0.141	1.850
0.450	2.116	1.632	1.632	0.190	0.134	1.460
0.500	2.352	1.816	1.814	0.190	0.134	0.930

Table 5.15: Response frequency mode 1 in test and analysis for case 71xx with adjusted added mass and lift coefficient, same response frequency for all cases

Table 5.15 is shown the response frequency in mode 1 for the test and analysis. As seen the Strouhal number is 0.19 in order to represent a realistic value for all cases. The internal non-dimensional frequencies and adjusted added mass are also presented in this table. As shown the response frequencies are in a very good agreement.

The lift coefficient curves are shown for different current velocities on the analyses models in Figure 5.46 and Figure 5.47 for case 71xx.

The lift coefficients are high for lower velocities and decreased by increasing the velocity. Comparing this figure with Figure 5.40 shows that even the response amplitude is the same in the reference point but the lift coefficient curves are different due to different $\hat{f}_{(internal)}$ which corresponds to different lift coefficient parameters.

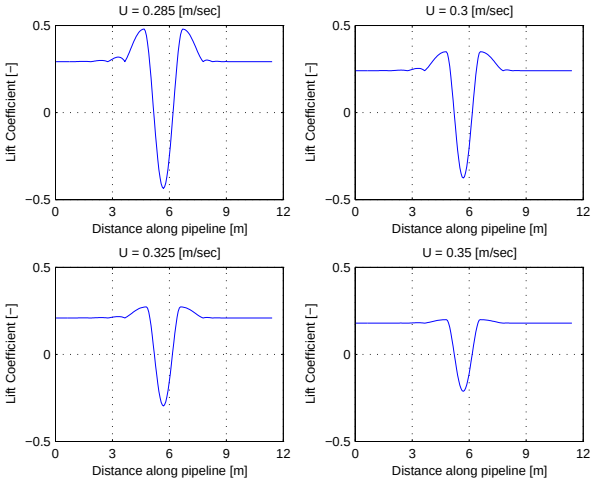

Figure 5.46: Lift coefficient curves for case 71xx with adjusted added mass and lift coefficient, same response frequency for all cases

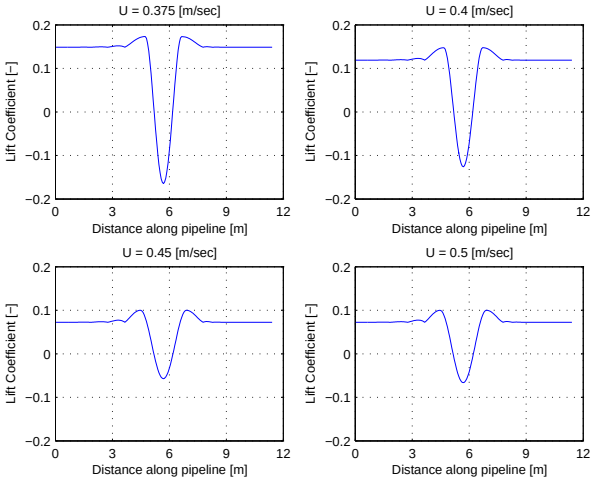

Figure 5.47: Lift coefficient curves for case 71xx with adjusted added mass and lift coefficient, same response frequency for all cases

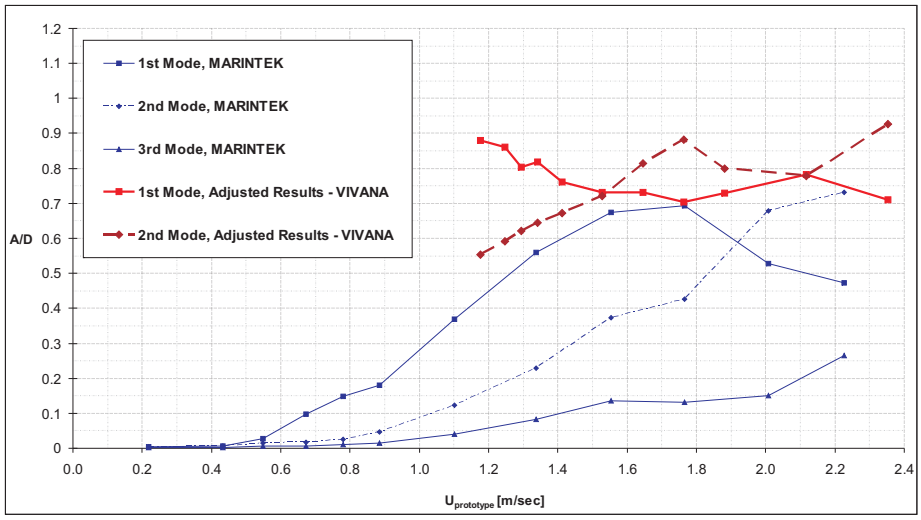

Figure 5.48: A/D versus $U_{(prototype)}$ for case 74xx with adjusted added mass and lift coefficient, same response frequency for all cases

Figure 5.48 shows A/D versus $U_{(prototype)}$ for case 74xx. As shown, response displacement is the same for the reference point, $U_{(prototype)} = 1.764m/s$ on the test and analysis by adjusting the lift coefficient data. The same C_L table is used for the other current velocities. Here, the factor to adjust the lift coefficient is 1.20. The added mass is adjusted here to have a correct response frequency for all points. The adjusted added mass value are shown in Table 5.16 for all cases.

A/D is maximum at $U_{(prototype)} = 1.176m/s$ and decreases until the reference point. After this point the response increases till $U_{(prototype)} = 2.116m/s$. This trend is against what we observe for the test model which has the highest response at the reference point. However -the same as for case 71xx- it is very interesting to see that the trend is similar to Figure 5.26 where St used as VIVANA standard, i.e. $St = 0.2$ which is very close to what we chose in the analysis here. Note that the response frequencies are not the same with that case but the lift coefficient factor applied there is also different, i.e. 0.85. The reason for this phenomena is already given for case 71xx.

We also observe that the maximum response on the analysis occurs for a much different velocity than the test model. Again, we may conclude that adjusting St gives a better comparison between the results than adjusting the added mass. It means that the hypothesis about high added mass value is not working here too.

As seen in this figure, mode 2 has a better trend agreement compare to the test

$U_{(model)}$	$U_{(prototype)}$	$f_{(osc)test}$	$f_{(osc)analysis}$	St	$\hat{f}_{(internal)}$	$Added, mass$
0.250	1.176	1.063	1.062	0.190	0.157	2.420
0.265	1.246	1.101	1.101	0.190	0.154	2.160
0.275	1.293	1.124	1.124	0.190	0.151	2.020
0.285	1.340	1.148	1.148	0.190	0.149	1.880
0.300	1.411	1.185	1.184	0.190	0.146	1.690
0.325	1.528	1.242	1.241	0.190	0.141	1.420
0.350	1.646	1.303	1.304	0.190	0.138	1.160
0.375	1.764	1.360	1.360	0.190	0.134	0.960
0.400	1.881	1.515	1.514	0.190	0.140	0.520
0.450	2.116	1.806	1.787	0.190	0.148	0.000
0.500	2.352	2.032	1.787	0.190	0.150	0.000

Table 5.16: Response frequency mode 1 in test and analysis for case 74xx with adjusted added mass and lift coefficient, same response frequency for all cases

model but has a peak at the reference point. Thereafter, decreases till $U_{(prototype)} = 2.116m/s$ and increases again. It predicts the VIV response higher than the test model. The trend for mode 2 is very similar to what we have seen in Figure 5.26. But, it is very interesting to see that the experiments shows two competing modes, and that the frequency has a large change where mode 2 dominates over mode 1. It can be commented that VIVANA's criteria for selecting dominating frequency is questioned.

The response frequency is shown in Table 5.16 for mode 1 from the test and analysis. As seen the Strouhal number is 0.19 in order to represent a realistic value. The internal non-dimensional frequency and adjusted added mass are also presented in this table for all cases. It varies between a very low value and 2.42. As shown the response frequencies are in a very good agreement in the exception of two highest velocities. It was not possible to get a better match for those velocities.

The lift coefficient curves on mode 1 are shown for different current velocities on the analyses models in Figure 5.49 and Figure 5.51 for case 74xx.

It shows high energy transfer which goes out of the system at the larger span and transfers to the shorter span at $U_{(model)} = 0.250m/s$. In the contrary, the maximum response occurs at $U_{(model)} = 0.375m/s$ for the test model, see Figure 5.48.

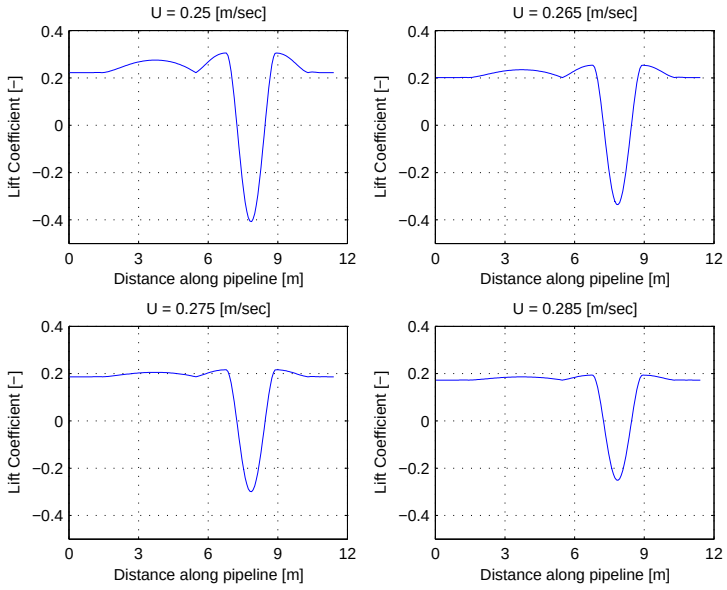

Figure 5.49: Lift coefficient curves for case 74xx with adjusted added mass and lift coefficient, same response frequency for all cases

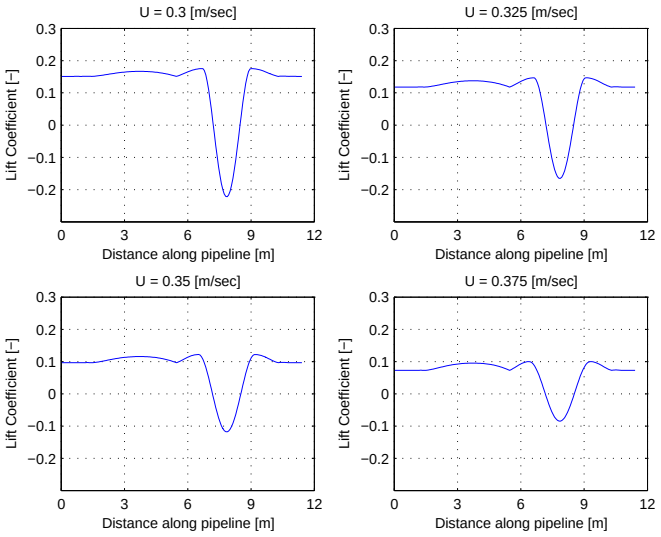

Figure 5.50: Lift coefficient curves for case 74xx with adjusted added mass and lift coefficient, same response frequency for all cases

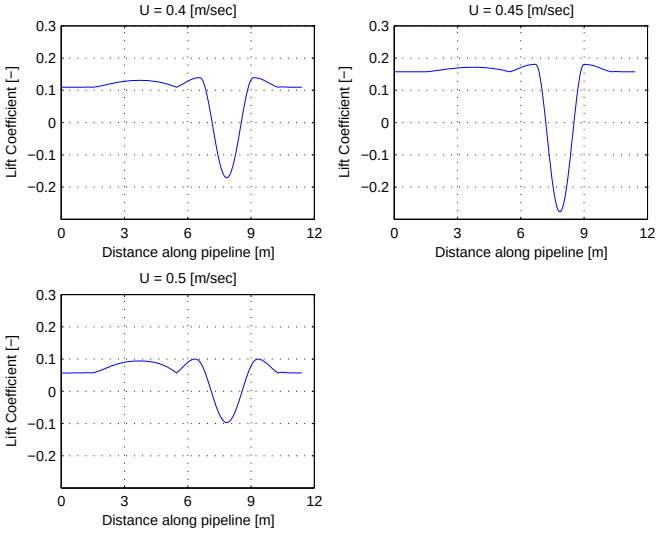

Figure 5.51: Lift coefficient curves for case 74xx with adjusted added mass and lift coefficient, same response frequency for all cases

5.5 Conclusion

The comparison of VIVANA analysis results with MARINTEK tests represents that VIVANA predicts the cross-flow response generally much higher than the test measurements, especially for the higher mode responses. The reasons to explain this phenomena may be categorized as follow:

- **In-line and cross-flow interaction**

  In-line oscillation may have some influence on cross-flow response. Different modes of oscillation may happen for in-line and cross-flow which cause the different points of span vibrate in the different ways. Consequently, the hydrodynamic forces must become different, and a perfect asymmetric response is impossible. The MARINTEK results also confirm this interaction, but the implications on response amplitude is not fully understood yet.

  The modal shape of the in-line response may differ from the cross-flow response. This will reduce the correlation of vortex shedding along the span, causing a reduced flow responses, Nielsen et al. (2002).

- **Synchronization along the pipe**

  The vortex induced vibration is a 3D phenomena. The strength of vortices depend on the relative velocity between the pipe cross-section and water. It means if the shedding process is not synchronized along the span the response amplitudes may not be comparable to 2D response, Nielsen et al. (2005).

- **Multi mode response**

  If multi mode responses happen, one can not expect all response candidates to achieve a full response amplitude. Meaning that when the eigen frequencies are closely spaced, more than one frequency can participate in VIV excitation and the response for each mode may not have enough energy to achieve the maximum amplitude expected. Modes are competing and that leads to reduced amplitudes.

- **Conservatism in VIVANA**

  In VIVANA each response frequency is assumed to excite alone which is a conservative assumption. Also, the basis for VIVANA has been risers -rather than pipelines- which normally respond at higher mode orders. There are also the other conservative assumptions in VIVANA which are natural for a commercial software widely used in industry.

- **Re/St dependency**

  Reynolds number may influence on the VIV response amplitude, Swithenbank, et al. (2007). The Reynolds/Strouhal number relationship and lift coefficient in VIV condition which are predefined in VIVANA have also much influence on the results.

The other conclusion from this study is that the method used by VIVANA is not able to describe VIV for free spanning pipelines adequately. It is not possible to find a set of parameter in a rational way that will give reasonably correct results. Tuning of parameters like the Strouhal number, lift coefficient curves and added mass may give correct results with regard to amplitude, dominating mode and response frequency for a specific flow velocity. However, the gradients for the response with respect to flow velocity will in general be incorrect which means that the predicted response parameters becomes incorrect for flow velocities different from what has been used for parameters tuning.

The reason for this rather pessimistic conclusion is that the parameters applied in VIVANA are insufficient for a correct description of this type of oscillations. The influence from IL oscillation is strong, and will for the most free spanning pipelines be different from what takes place in long risers which constitute the empirical basis for VIVANA. Keywords here are short spans, strong influence from bending stiffness relative to tensions and low mode orders.

The hydrodynamic parameters used in VIVANA analysis are dependent on the Reynolds/Strouhal number relationship. More experiments should be done to find these parameters in relation with the variation of the other hydrodynamic parameters in VIV condition.

Chapter 6

Time domain analysis of VIV for free span pipelines

Most empirical models are based on frequency domain dynamic solutions and linear structural models, Larsen (2000). A free span pipeline has, however, important non-linearities that should be taken into consideration. Both tension variation and pipe-seafloor interaction will contribute to non-linear behaviour, which means most empirical models will have significant limitations when dealing with a free span case. The need for time domain methods is therefore obvious.

The purpose of this part of the thesis is to discuss nonlinear effects related to VIV of free span pipelines and describe how a best possible linear model can be established. An improved strategy for non-linear analysis will also be outlined. This is based on combined use of a traditional linear VIV analysis and a subsequent non-linear time domain simulation where information from the linear case is utilized. The proposed model is based on existing knowledge on VIV and dynamics of free span pipelines.

The response analysis in VIVANA applies the frequency response method that is limited to structures with linear stiffness, while non-linear time domain methods are available in RIFLEX. The new method for VIV analysis will introduce a new type of links between the two programs. Results from VIVANA will be transferred to RIFLEX in such a way that a time domain analysis can be carried out where structural non-linearities can be accounted for. This will in particular be important for free span pipelines, but also for other type of structures like catenary risers and risers on a SPAR buoy.

6.1 Outline of standard approach

The computer programs VIVANA, Larsen et.al. (2000) and RIFLEX, Fylling et.al. (1998) have been used in the present study. The VIV analysis program VIVANA applies RIFLEX modules for system modeling and static analysis, and RIFLEX has been used for all time domain simulations. A complete VIV analysis of a free span pipeline must include steps as follows:

- Static analysis to define tension and shape of the span. Geometry of the seafloor and a model for pipe/seafloor interaction are essential features of this analysis.
- Eigenvalue analysis for the actual static condition
- VIV analysis to identify response frequency and amplitudes for a given current condition. Some details on these steps will be given in the following.

6.1.1 Static analysis

A 3D tensioned beam finite element model of the pipe is applied. The analysis will start from a stress free (horizontal straight lined) configuration without any seafloor contact. One end is positioned controlled for all degrees of freedom. The other end has all degrees of freedom positioned controlled except for the local axial direction where an external load identical to the applied laying tension is introduced. A sequence of loads will be applied in such a way that the final condition will represent the real pipeline as accurate as possible. Non-linear bottom springs and friction elements take care of the pipe-seafloor interaction. A large number of load increments may be needed in order to maintain a stable solution during all intermediate conditions. The final load sequence will introduce current forces perpendicular to the plane defined by the pipe under influence form gravity and buoyancy loads. Hence, a correct 3D shape of the pipeline span is obtained, see Figure 6.1.

6.1.2 Eigenvalue analysis

Eigenvalue analysis can be carried out on the basis of the static solution. This is straightforward for the still water case since the added mass coefficient is well known. The effect of seafloor proximity may be taken into account, cf. Jensen et.al. (1993), but this effect has been neglected in the present study. Eigenvalue analyses are also applied in order to identify the response frequency for a given current condition. The response frequency will in general appear as a compromise

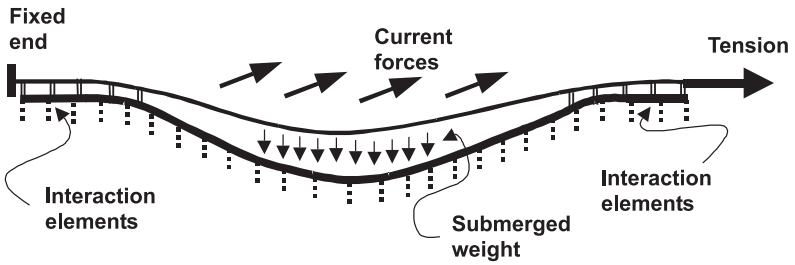

Figure 6.1: Model for static analysis of free span pipeline

between the still water eigenfrequency and the vortex shedding frequency for the fixed cylinder, Larsen et.al. (2001). This frequency is found from an iteration where the added mass coefficient is given as a function of the non-dimensional frequency, $\hat{f}$. Convergence is obtained when consistency between the added mass and eigenfrequency is obtained.

6.2 Outline of combined approach

The free span pipeline case involves several types of non-linearities, while the standard VIV model as described in the previous section is linear with respect to structural response. A non-linear time domain analysis procedure is hence wanted. The main reason for this is that maximum stress variations and hence also fatigue damage, will often occur at the shoulders where the influence from non-linear pipe/soil interaction is large. However, empirical data for hydrodynamic coefficients are almost exclusively given as functions of amplitude and frequency, meaning that the response is assumed to be strongly dominated by one harmonic component. A time domain model must hence identify the frequency and amplitude in order to find the proper coefficients during a simulation. System identification techniques have been used, cf. Finn et.al. (1999), but the present work follows a completely different approach. In order to carry out a VIV analysis where non-linear structural effects can be accounted for, the analysis must be carried out in a sequence as follows, (see also Figure 6.2):

6.2.1 Description of new analysis procedure

- **Step 1** *Static analysis*

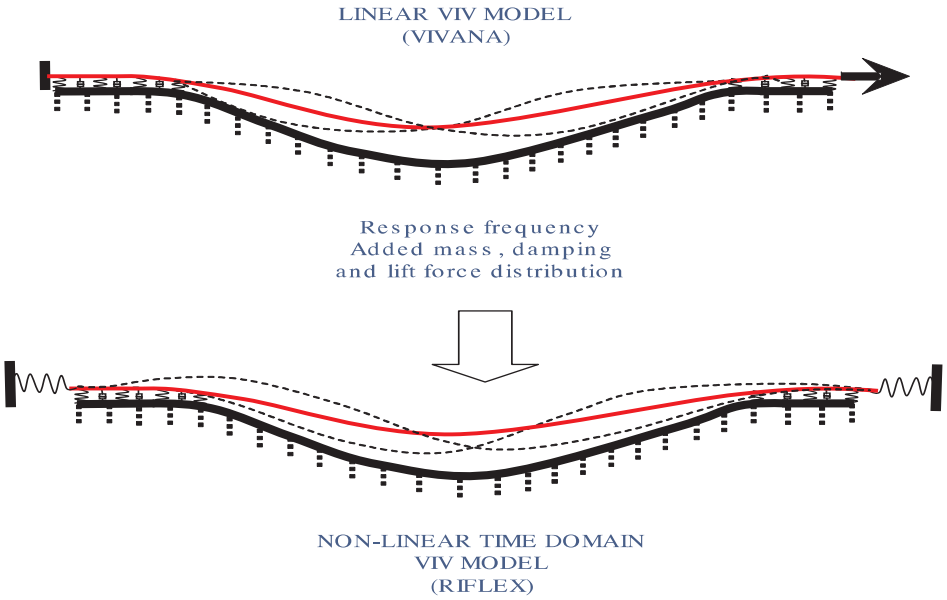

Figure 6.2: Frequency and time domain models

The static shape of the pipeline needs to be found.

- **Step 2** *Eigenvalue analysis*

  The eigenfrequencies and mode shapes of the pipeline are found. Added mass is applied as for a non-responding pipe in still water according to data given by the user. The results will be given in terms of discrete eigenvectors and associated eigenfrequencies.

- **Step 3** *Identification of possible and dominating excitation frequencies*

  A subset of all calculated eigenfrequencies will define the complete set of possibly active eigenfrequencies. Added mass under VIV conditions will, however, become different from the still water case as applied for the initial eigenvalue analysis. Hence, iterations must be performed for each response frequency candidate to find the actual response frequency. The iteration has converged when there is consistency between the modified eigenfrequency and modified added mass distribution since added mass depends on the oscillation frequency and flow speed. A criterion is applied to identify the dominating response frequency if there are more than one possible frequency.

- **Step 4** *Analysis of the response at the dominating frequency*

The frequency response method is used to calculate the dynamic response at the dominating frequency identified in step 3. The analysis applies an iteration that converges when the response is in accordance with the non-linear models for excitation and damping. The result of this analysis is hence complete information of exciting forces and damping coefficients.

- **Step 5** *Response analysis for other frequencies than the dominating frequency*

  In case of non-uniform flow profile the result from Step 4 may show an excitation zone for the dominating frequency that does not cover the total pipe length. Consequently excitation may take place at other frequencies in zones outside the initially identified zone. A similar analysis as for Step 4 must now be carried out for each frequency, but the excitation zone will now become the original zone for the new frequency with a reduction according to the zone taken by the more dominating frequencies.

- **Step 6** *Transformation of frequency domain results to time domain format*

  The results from the frequency domain analysis (VIVANA) give a complete description of added mass, lift forces and hydrodynamic damping forces along the pipeline. Loads are known in terms of frequency, amplitudes and phase angles and can hence be described in time domain. This transformation must be performed according to the RIFLEX load description format. All data needed for a non-linear time domain simulation are hence available.

- **Step 7** *Non-linear time domain simulation by use of RIFLEX*

  The finite element model applied by VIVANA was originally established by RIFLEX. The model is now transmitted back to RIFLEX, but with dynamic loads as identified by VIVANA. The non-linear time domain simulation can take tension variations, modified boundary conditions and friction forces into account. Hence, a more realistic result for VIV can be found.

This approach is only valid if the oscillation amplitudes at segments along the pipe with significant vortex shedding activity is almost the same from the frequency domain analysis (VIVANA) as from the time domain simulation (RIFLEX). The response at the free span shoulders may however vary significantly from frequency to time domain. Fatigue is known to be most significant at the shoulders, meaning that the new procedure improves the results where improvements are mostly needed. In the case of experiencing a large deviation between frequency and time domain, some type of iteration have been performed. This might be obtained by adding concentrated dampers at the shoulders in the frequency domain analysis.

Combined use of frequency domain (VIVANA) and non-linear time domain (RIFLEX) analyses for calculation of vortex induced vibrations of free span pipelines can be described more in detail as follows:

1. Static analysis of the span with known effective tension, current and volume forces. Seafloor interaction modeled by non-linear springs.

2. Traditional VIVANA analysis where the response frequency and added mass, damping and lift force distributions are found. The stiffness matrix found at static equilibrium is applied and not modified during this calculation. Linear springs and dashpots at nodes with bottom contact will be introduced.

3. Establish a non-linear finite element model with identical static configuration as for the linear model, and the same added mass, damping and load distribution as found by VIVANA.

4. Non-linear time integration with updating of bottom contacts (spring and dashpots), pipe geometry and tension consistent with calculated response at every time step. Time integration should continue until a steady state solution for the actual frequency is found.

   The results after these steps will represent an improved stress analysis as compared to the original VIVANA result. However, the force distribution found in VIVANA might be inconsistent to the new response since force coefficients depend on the response amplitude. It is possible to improve the result by an iteration procedure as follows:

5. Redefine damping and lift force coefficients according to the new results and perform a second time integration until steady state is obtained. Note that the load frequency will be kept constant and identical to the frequency found by VIVANA for all time domain computations.

6. If the results are consistent with the assumptions for selecting lift and damping coefficients, the process has converged. A consistent result that takes all types of structural, damping and load non-linearities into account has been obtained.

The difference between step 2 and 4 is that non-linearities from dynamic tension variation and interaction between pipe and seafloor at shoulders are neglected in step 2 but accounted for in step 4. Since the loads from VIVANA are functions of the response, one can not apply this method if the response in step 4 is significantly different from what was found in step 2. The benefit from step 4 is therefore not to have a better result for the overall response, but to have improved results for local stresses at the shoulders. These stresses are essential for fatigue life prediction and are strongly influenced by seafloor interaction.

6.2.2 Mathematical approach - time domain

The dynamic equilibrium equation in time domain can formally be written as

$$(M_s + M_H)\ddot{r}(t) + (C_s + C_H)\dot{r}(t) + K(r).r(t) = R(t) \tag{6.1}$$

The hydrodynamic mass and damping matrices are identical to what was found by VIVANA in the frequency domain analysis. The stiffness matrix will now become a function of the displacements r due to change of geometry and varying contact between the pipe and the seafloor.

The equation is solved by a conventional step by step integration scheme where K is updated and iteration for equilibrium is carried out for each step. A Newmark β-family algorithm has been applied. The load vector R contains all terms from the complex load vector in Equation 3.11, but the complex representation is now changed to harmonic components with individual phase.

The present program version does not take in-line forces into account. For free spanning pipelines this means that only vertical forces will be present in the dynamic load vector X. In the non-linear time domain analysis, however, one must include the total loads, including the in-line static drag component. This is needed in order to keep the pipe in the same average position as found by the initial static analysis. Since there will be dynamic motions also in the in-line direction, these drag forces may vary in time according to the standard Morison's equation. Amplification of these forces due to cross-flow response is not taken into account.

The load frequency is as mentioned before identical to an eigenfrequency for the pipe in its static position.This means that the response takes place at resonance, which means the result will be strongly influenced by damping. For cases with uniform current speed along the pipeline, there will not be any hydrodynamic damping except for negative lift forces due to large response amplitudes. Since these forces are included in the load vector, C_H in Equation 3.11 and 6.1 is zero, and the only contribution to damping is the structural damping matrix C_S.

6.3 System modeling in case studies

The purpose of the case study is to compare results from the various models and thereby illustrate shortcomings and modeling possibilities and show the influence on stresses from interaction model. The models were made in order to be analyzed in RIFLEX and VIVANA. In this section, the system modeling of such analysis is described.

6.3.1 Bottom topography

One of the bottom topography for a single free span pipeline is shown in Figure 6.3. It is a model of a sea-bed depression and is defined by parallel profiles. As you

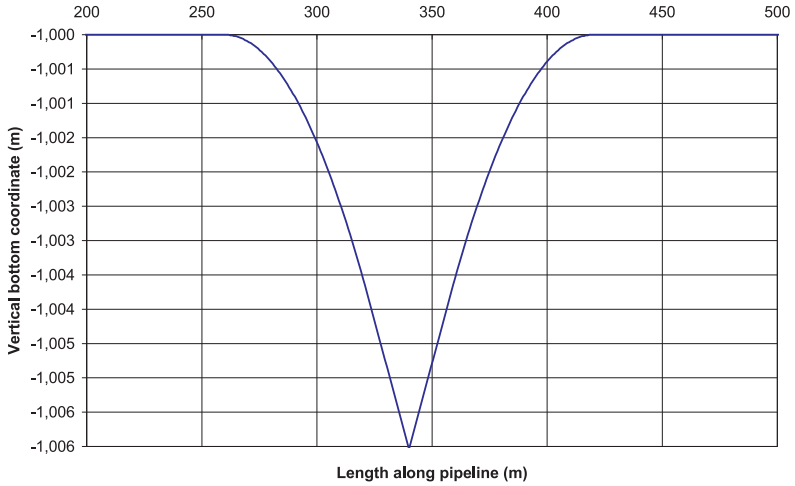

Figure 6.3: Typical bottom profile

can see in Figure 6.4, each profile consist of a flat part (shoulder), L_{fb}, a curved part denoted by the horizontal length, L_{cb}, and an inclined part with the horizontal length, L_{db}. The bottom model can be described mathematically as

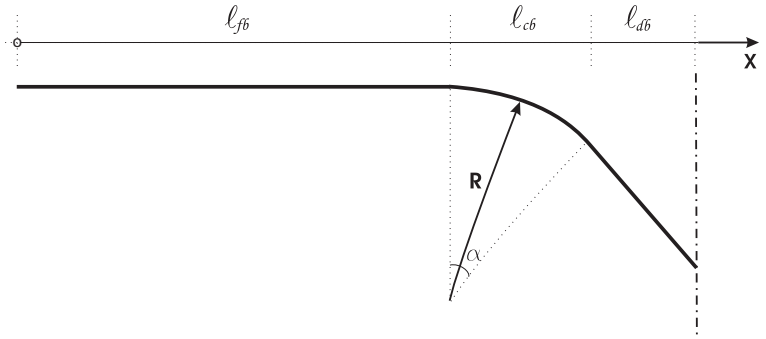

Figure 6.4: Bottom profile

Clay type	$C_v(kN/m^{5/2})$	$C_l(kN/m^{5/2})$	$K_{v,s}(kN/m/m)$
Very soft	1800	1200	50-100
Soft	4200	2800	160-260
Firm	9000	6000	500-800
Stiff	15000	10000	1000-1600
Very stiff	33000	22000	2000-3000
Hard	36000	24000	2600-4200

Table 6.1: Dynamic stiffness factor and static stiffness for pipe-soil interaction in clay with OCR=1

$$\begin{cases} Z_b & : \quad x < \ell_{fb} \\ Z_b - (R - \sqrt{R^2 - x_i^2}) & : \quad \ell_{fb} < x < \ell_{fb} + \ell_{cb}; x_i = x - \ell_{fb} \\ Z_b - (R - \sqrt{R^2 - x_i^2}) - x_i \tan\alpha & : \quad x > \ell_{fb} + \ell_{cb}; x_i = x - (\ell_{fb} + \ell_{cb}) \end{cases}$$

where Z_b is the water depth, R is the radius of curvature, x is the x-coordinate in a global coordinate system and x_i is the x-coordinate in a local coordinate system.

6.3.2 Soil-pipeline interaction

Many uncertainties still exist in soil-pipe interaction. Most available data on the behaviour of soil is empirically based and highly dependent on test condition. For this reason conservative approaches should be used in design, by employing soil parameters so that the associated displacements and forces are calculated as upper bounds.

The soil stiffness, k_s can be obtained on the basis of simple settlement theory, Lambe (1969). Soil stiffness may be given by defining as the ratio of the normal force per unit length to the corresponding soil settlement

$$k_s = \frac{E_s}{2(1-\nu_s^2)} \tag{6.2}$$

where E_s is the modulus of elasticity and ν_s is the Poisson's ratio of the soil.

In the present work, DNV (2001) and BS (1993) have been used for determining the soil parameters. Table 6.1 and Table 6.2 correspond to the typical ranges of axial pipe-soil friction coefficients for various types of soil which are taken from DNV (2001) and BS (1993) respectively.

Soil Type	Longitudinal Coefficient Friction (μ)
Sand	0.3 - 1.2
Silt	0.3 - 0.9
Clay	0.2 - 0.6
Rock	0.6

Table 6.2: Axial pipe/soil friction coefficients

6.3.3 Applied forces

The forces are applied to the model by an incremental loading procedure from a stress free configuration (AR configuration). Those are categorized according to RIFLEX User Manual (Fylling et.al. 1998) as:

- Specified forces
- Specified displacement
- Volume forces (gravity and buoyancy)
- Friction forces
- Current forces

6.3.4 Non-linear and linear pipe model

Pipe-seafloor interaction is modeled by discrete springs in the linear model. These springs are found in vertical, axial and lateral directions. The pipe is fixed at one end and has a constant tension at the other end.

The key data for the pipe are given in Table 6.3, while the profile of the pipe relative to the seafloor is seen in Figure 6.5.

The non-linear model applies the same springs to represent the initial stiffness, but a dry friction model is introduce for axial and lateral directions. This will allow the pipe to slide under constant restoring force. The vertical springs are non-linear, meaning that if tension occurs in the spring the pipe is allowed to leave the bottom. Hence, the associated spring to the unconnected node will be off. This spring will be activated again if bottom contact is obtained during the dynamic simulation.

Dynamic oscillations of the pipe will lead to three non-linear effects:

Pipe properties			
Density of pipe material	ρ_s	7850	kg/m^3
Mass	m	314.86	kg/m
Young's modulus	E	2.06E+11	N/m^2
Moment of inertia	I	1.422E-03	m^4
Axial stiffness	AE	8.26E+06	kN
Bending stiffness	EI	2.93E+05	$kN.m^2$
Wall thickness	t	0.024	m
Outer diameter	OD	0.556	m
Inner diameter	ID	0.508	m
Axial tension	T	250	kN

Table 6.3: Pipe properties

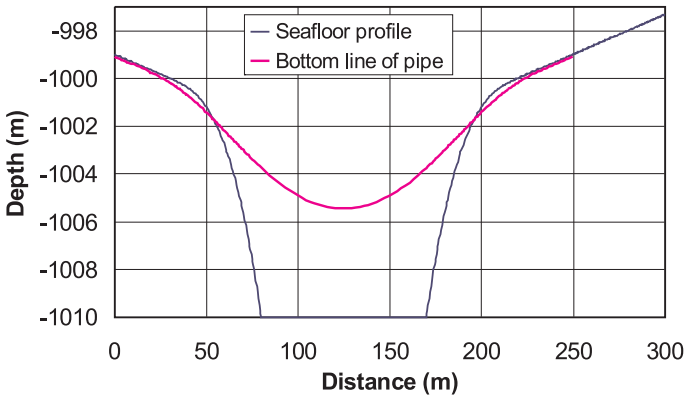

Figure 6.5: Geometry of free span pipeline

1. The lateral oscillations will lead to axial oscillations at ends (for a fixed boundary condition) that will give tension variations in the pipe. Tensions will influence the geometric stiffness matrix, meaning that this effect demands a non-linear time integration to be properly taken into account.

2. The contact zone between the pipe and seafloor will change as illustrated on Figure 6.5. The pipe will therefore have local bending stresses at the shoulders that are controlled by the shape of the seafloor and its stiffness properties.

3. The pipe-sea-floor interaction will introduce some damping to the pipe. The correct way of modeling this effect is to introduce damping elements into the

damping matrix and in addition, friction must be modelled by a non-linear spring since the force is independent on the velocity. But these elements must be updated in the same way as the interaction springs in order to consider the time varying contact between the pipe and seafloor. Damping will have contribution from friction (sliding of the pipe on the seafloor) and viscous effects in the soil.

6.4 New approach based on tuning of the linear model

In this section, the non-linear time domain analyses were not really VIV analyses, but used a load pattern that gave response amplitudes similar to VIV. The purpose was to demonstrate the potential for the combined time/frequency domain strategy and influence from damping models, cfr. Larsen et.al. (2002).

6.4.1 Use of standard model in VIVANA

The illustration of effects by an ideal example is shown here. Figure 6.6 and Figure 6.7 present key results from VIV analyses according to the standard VIVANA procedure. Current speed is varied from a very low value up to 1.1 m/s. Initial cross-flow VIV is seen at a speed of 0.21 m/s. This corresponds to a reduced velocity of 3.1, which is in good agreement with DNV Guidelines (1998).

The first mode is seen to dominate up to a current speed of 0.6 m/s, corresponding to a reduced velocity of 8.8. At this point the second mode takes over. Reduced velocity for the corresponding eigenfrequency is 4.5. Similarly, the shift between the second and third mode takes place at a current speed between 1.0 and 1.1 m/s, where the reduced velocity for the second mode is between 8 and 9, and approximately 4.5 for the third. Non-dimensional response amplitudes are seen to reach a maximum value around 1.1, and experience some reduction with increasing speed before the next mode takes over.

Eigenfrequencies and response frequencies as function of current speed are shown on Figure 6.7. Eigenfrequencies found by use of still water added mass will experience some influence from current speed since current forces will influence static shape and contact forces. This effect is not significant in the present study.

The trend for the response frequency is however, more interesting. At low current speed the response frequency is seen to be lower than the still water value. This is caused by the very high added mass coefficient for this condition. Increased

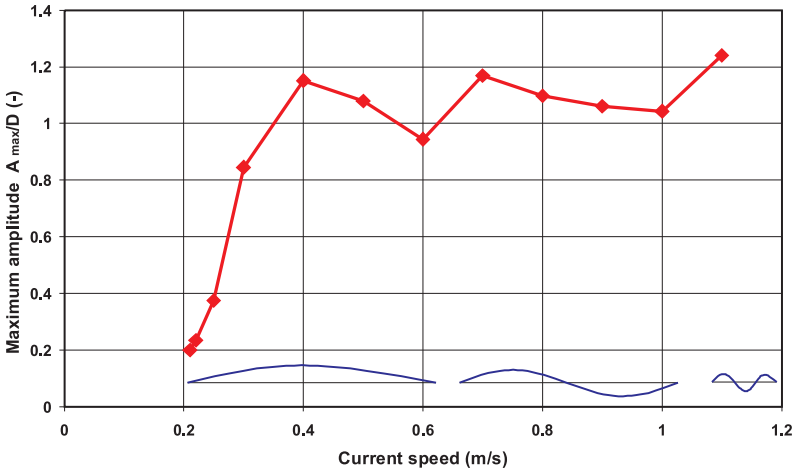

Figure 6.6: Response amplitudes and dominating modes as function of current speed

speed leads to reduced added mass and hence also to increased response frequency.

The shift of dominating mode from first to second and from second to third is seen to appear without any dramatic change of response frequency, which is a consequence of the added mass modeling. This trend needs verification from experiments with flexible beams since the added mass curve is based on tests with short cylinders.

It is seen that a new dominating mode takes over at a response frequency slightly lower than the corresponding still water frequency, and that the response frequency is close to linear with respect to current speed. One may interpret this trend as a fixed Strouhal number effect, valid for an oscillating beam. If so, one will arrive at a Strouhal number of 0.19. Note that this value is not an input value to VIVANA but a result of the analysis. VIVANA applies a Strouhal number valid for a fixed cylinder determined from Reynolds number, and the response frequency follows from an added mass/eigenfrequency iteration where the mass ratio will be an important parameter.

6.4.2 Influence from linear soil damping

The same pipeline model was used to illustrate the influence from alternative damping assumptions. Three cases were analyzed:

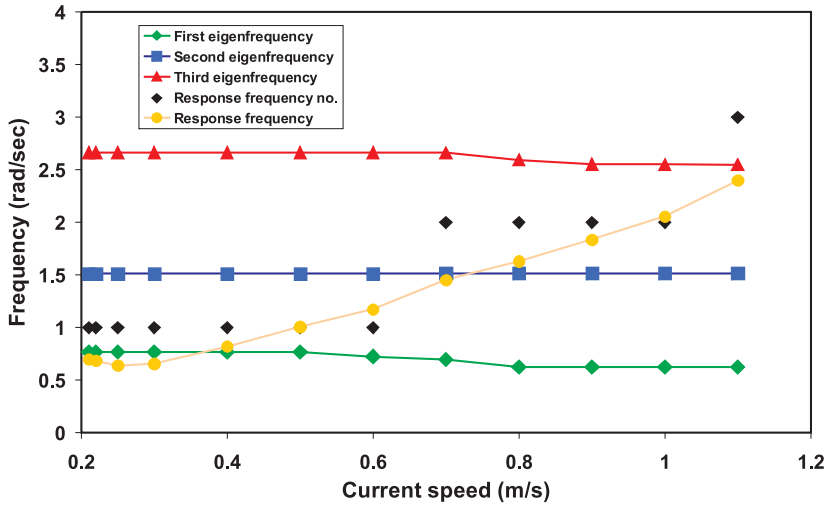

Figure 6.7: Eigenfrequencies for still water added mass and response frequencies as functions of current speed. Response frequency order indicated.

- No damping except for negative lift forces for large amplitudes.
- 10% damping modeled as a damping matrix proportional to the stiffness matrix. This model is often referred to as global damping or Rayleigh damping.
- Linear damping elements at all nodes with contact between the pipe and the seafloor. The magnitude of these dampers was tuned to obtain the same maximum response amplitude as for the global model. This model will be referred to as the local damping model.

Figure 6.8 shows the lift coefficient along the pipe for all cases. Case 1 is seen to have negative lift at the mid section caused by the large amplitudes found here. Energy is hence transported from the end sections to the mid section as illustrated on Figure 3.12. The lift coefficient distributions for the other two cases are seen to be near identical, which is a consequence of the intended similarity of response amplitude.

Response amplitudes are compared on Figure 6.9. 10 % damping is seen to give approximately 40 % reduction of the response. Amplitudes for the two damped cases are seen to be near identical, but minor differences are still seen. Amplitudes at the shoulders for the local model is significantly higher than for the global model. This follows from the fact that the only way energy can dissipate is by activating

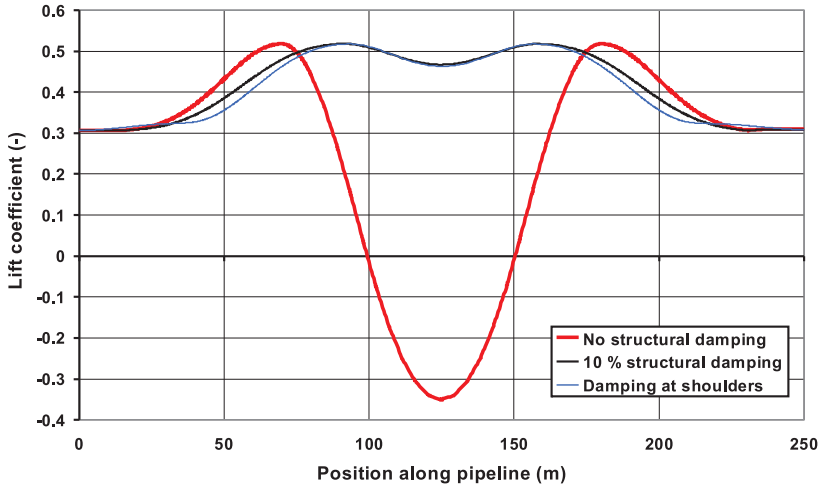

Figure 6.8: Distribution of lift coefficient along the pipe

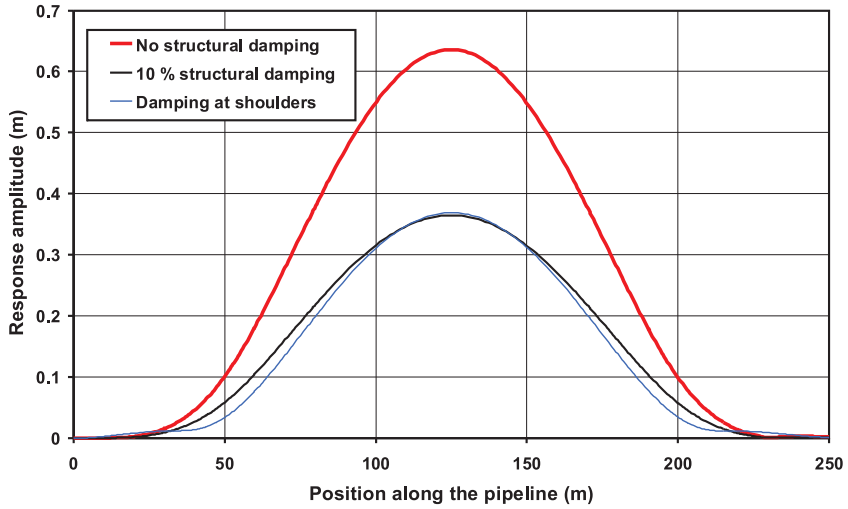

Figure 6.9: Response amplitudes

the dampers at the shoulders. Hence, amplitudes must be large enough to provide

this dissipation.

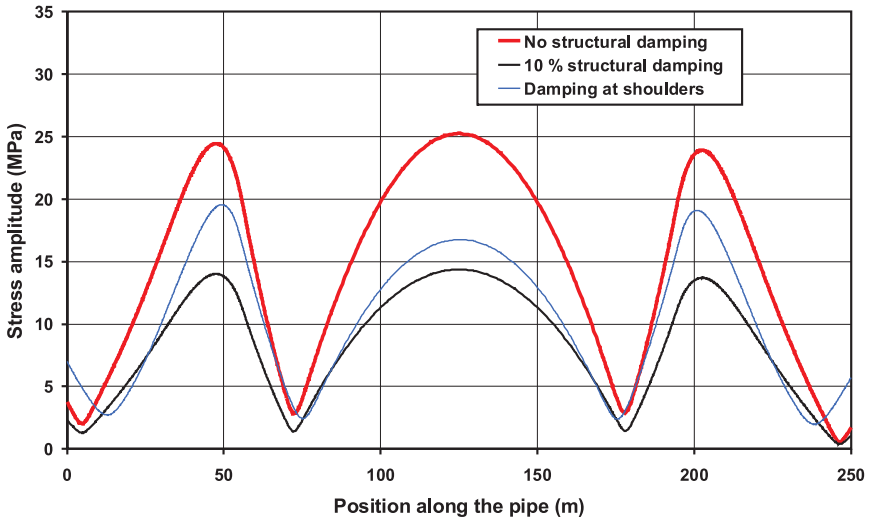

Figure 6.10: Bending moments

Figure 6.10 shows the bending moment along the pipe for all models. The global damping case is seen to have a uniform reduction of the moment as compared to the undamped case of the same magnitude as the oscillation amplitude. The local damping case has, however, a much smaller reduction at the shoulders than at the mid span. The consequence is that maximum dynamic stress has moved from the mid span to the shoulders, and is significantly higher than for the global model. The conclusion from this very simple study is that a global damping model may lead to under-prediction of bending stresses even if the response amplitude is correctly described. By introducing a local damping model, the response shape is altered and a simple modal approach will fail.

6.4.3 Influence from non-linear boundary condition

The results from the new approach are illustrated here. A simple case study using time domain models have been carried out. The purpose is to illustrate some aspects of modeling, and firm conclusions on how to establish a good time domain model for VIV analysis of free span pipelines. This model demonstrate effects of damping and interaction models.

The attempt have been made to have a smooth touch-down zone that will allow the touch-down point to have some movements during dynamic response. This was done in order to simulate the effect from local settlements under the pipe that will take place after installation. The distribution of contact forces will strongly depend on the local geometry of the seafloor in this area. This effect is easily observed from analyses.

Pipe/seafloor interaction is modeled by discrete springs in the linear model. These springs are found in vertical, axial and lateral directions. The pipe is fixed at one end and has a constant tension at the other end. The non-linear model applies the same springs to represent the initial stiffness, but a dry friction model is introduced for axial and lateral directions. This will allow the pipe to slide under constant restoring force. The vertical springs are non-linear allowing the pipe to leave the bottom if tension occurs in the spring. A node without bottom contact at static equilibrium will initially not have springs, but these will be introduced if contact is obtained during the dynamic simulation.

The total model is more than 400 meters long, but the free span section at the mid part is slightly less than 100 meters. The bottom profile is symmetric.

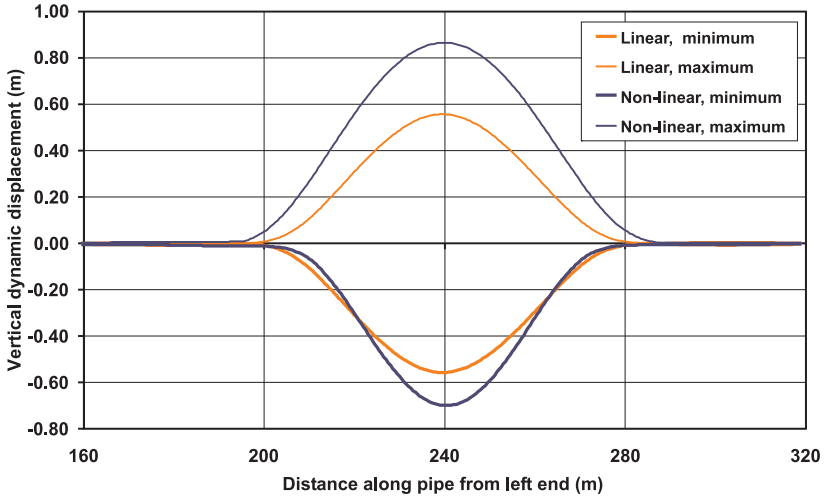

Figure 6.11: Vertical displacement envelope curves from linear and non-linear analyses

Figures 6.11 to 6.14 show results from the linear and non-linear analyses. The

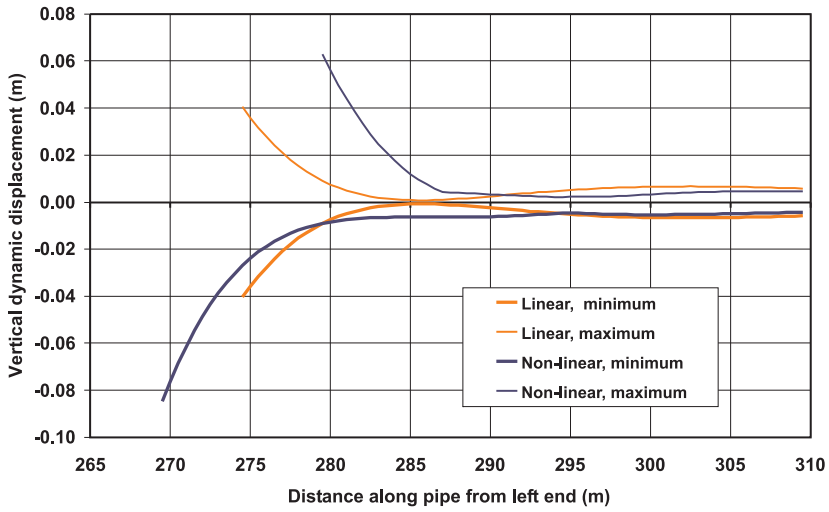

Figure 6.12: Displacements at the touch-down zone

loads are identical for the two cases, and no attempts were done in order to tune the models to give similar results. Figure 6.11 gives envelope curves for vertical displacements for the mid section of the pipe. The linear results are seen to be symmetric as expected, while the non-linear vertical springs have resulted in an asymmetric response for the non-linear model. Figure 6.12 illustrates the uplifting and restrained downwards displacements as compared to linear response by zooming in the touch-down zone. Note that these curves are envelopes and do not represent actual displacement shapes (snapshots). The non-linear response is also seen to be significantly higher than the linear. The reason for this will be commented later.

Bending moment

Bending moments and stress ranges are presented on Figure 6.13 and Figure 6.14 respectively. Moments are shown in terms of envelope curves, meaning maximum recorded values during one load cycle and not actual moment diagrams. The stress range curves shows that the non-linear stresses at the mid span is highest for the non-linear case, which is an obvious consequence of the response amplitudes at this part of the pipe. At the shoulders, however, the two models have given almost the same stress range. The linear case have almost the same result for the mid span as for the shoulders, while the non-linear response is relatively lower at the shoulders. The reason for this is that the non-linear contact formulation will represent a more

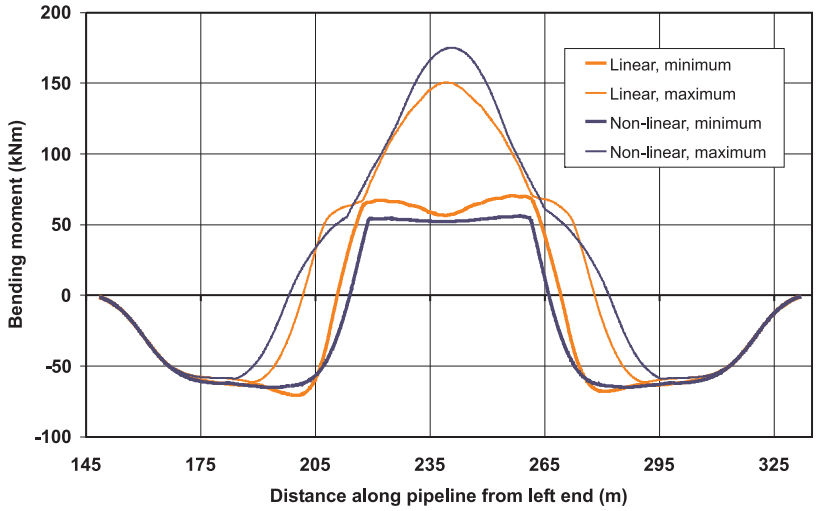

Figure 6.13: Bending moment from linear and non-linear analyses

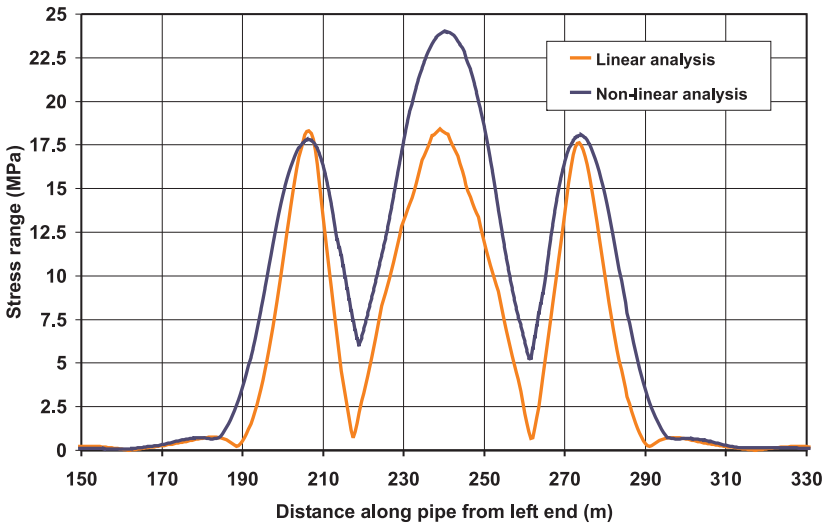

Figure 6.14: Stress range from linear and non-linear analyses

soft boundary condition than linear springs. The linear model will not allow the pipe to leave the bottom, but allow penetration at nodes without static seafloor contact.

The large difference between linear and non-linear displacements at the mid span needs an explanation. The reason is not the difference in vertical contact formulation, but how interaction is modeled in axial direction. The springs in the linear model will act as a restriction for the sagged pipeline and give small axial displacements. Axial forces will, however, build up. This effect is prevented in the non-linear model where the friction formulation will limit axial contact forces and allow sliding and hence give larger response amplitudes.

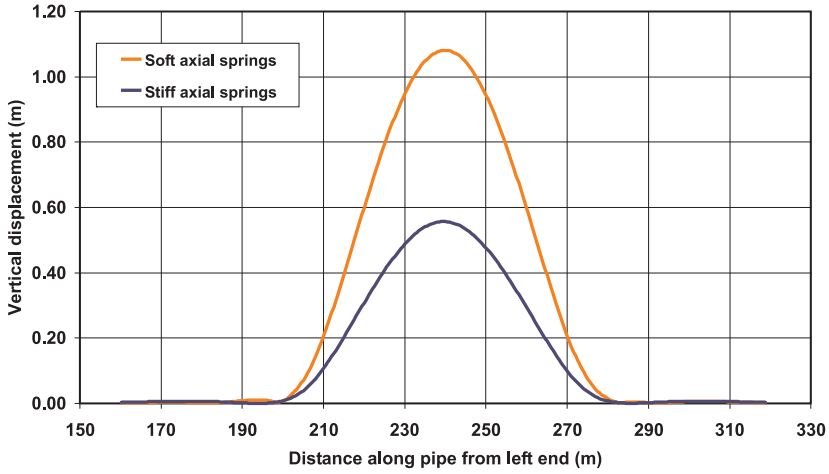

Figure 6.15: Vertical displacements from soft and stiff axial springs

A linear model may be tuned to give the same effect by adjusting the stiffness of the axial contact springs. This is illustrated on Figures 6.15 and 6.16, where results from models with different stiffness are presented. The "stiff spring" model is identical to the original, and the "soft spring" model applies springs with 10% stiffness as compared to the originals. The response is seen to increase considerably by reducing the stiffness of axial springs. It is easy to find linear springs that will give the same displacements as the more sophisticated friction model, but one should keep in mind that the effect is non-linear and hence amplitude dependent. It is also important to note that the local stresses at the shoulders will be over-predicted by a linear model even if the response amplitude at the mid span is correctly predicted.

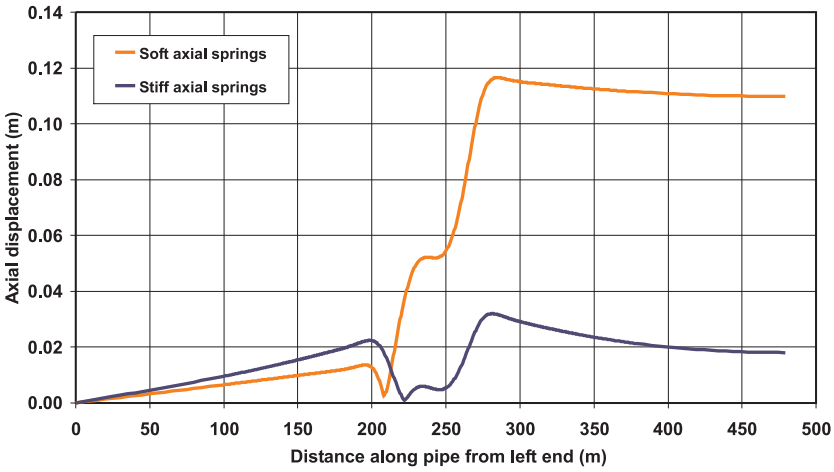

Figure 6.16: Axial displacements from soft and stiff axial springs

6.5 Combined approach

One of the aim of the current project was to investigate the potential of the new analysis method for time domain analysis of free span pipeline. At the beginning of this project, RIFLEX was not capable of doing time domain analysis with true VIV forces. Therefore, as explained in the previous section, the linear model tuned in order to give a correct prediction of response amplitude. Later, MARINTEK coded RIFLEX based on the combined approach and the findings during this project. The following results are based on the concept that lift forces and key parameters from VIVANA were taken into RIFLEX, cfr. Larsen et.al. (2004).

6.5.1 Simple model

In order to approach a better understanding of the difference between the time domain and frequency domain analysis of pipeline, a simplified pipe model with hinged ends at point supports have been applied and then some more realistic analyses of a pipe on an uneven sea bottom performed. The first cases are included in order to illustrate some basic differences between linear and non-linear analyses, while the realistic case will illustrate the significance of non-linearities for offshore pipelines.

Note that the structural damping has been set to 2% in these case studies. The frequency domain analysis can handle this situation without any problems since the iteration will ensure consistency between loads and response. In time domain,

however, we have less control of possible sources of inaccuracy that may influence damping. Experience with time integration of non-linear systems has shown that some negative or positive damping may occur. We have therefore been forced to adjust the structural damping level in time domain analyses in order to obtain the same global response in time and frequency domain.

The simplified pipe model is a beam with moment free supports at both ends. One end is kept in a fixed position, while the other is free to move axially. A constant force is introduced at this end, which will give an effective tension in the pipe and hence contribute to its lateral stiffness. Two cases are analyzed, one with a neutrally buoyant pipe, and one with increased weight that will give a static sag between the end supports. Static drag forces are excluded in the first case, which means that the pipe is perfectly straight in the static condition. Key data for the pipe are given in Table 6.4. The L/D ratio for this pipe is approximately 230.

PIPE PROPERTIES			
Length	L	8.0	m
External diameter	D	0.035	m
Axial stiffness	AE	5.6E+03	kN
Bending stiffness	EI	0.2	$kN.m^2$
Mass per unit length - Heavy pipe	m	1.3	kg/m
Mass per unit length - Neutral pipe	m	0.835	kg/m
End tension	T	50	N
Current speed	C	0.2	m/s
drag coefficient	C_D	1.0	$-$

Table 6.4: Data for simplified pipe model

This implies that the neutrally buoyant pipe will behave perfectly linear under VIV conditions. This case can therefore serve as a test of the analysis procedures. The response shape was found to be almost identical to the second mode, and the time and frequency domain amplitudes were very close after tuning the damping for the time domain model. Figure 6.17 shows a set of response snapshots. No in-line component or axial response was seen - as expected. From Figure 6.18 it is seen that bending stresses from linear and non-linear analyses are in excellent agreement.

The second case has static sag due to the submerged weight of the pipe, and also in-line static displacements from drag forces. Snapshots of cross-flow (vertical) displacements from the linear analysis are identical to Figure 6.17, and the mid-point of the pipe acts as a perfect node for this response component.

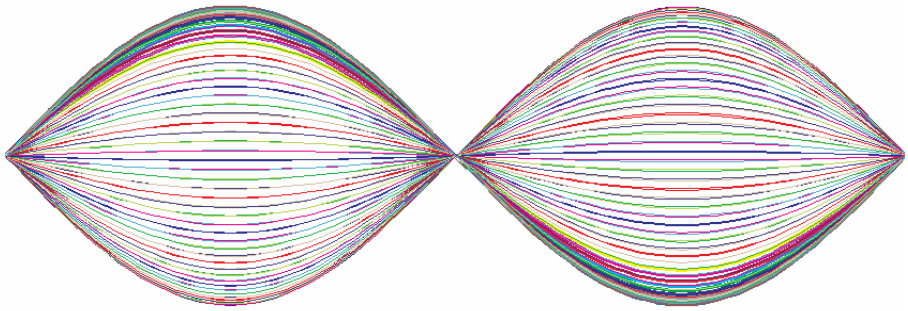

Figure 6.17: Oscillation shape snapshots, neutrally buoyant pipe, time and frequency domain

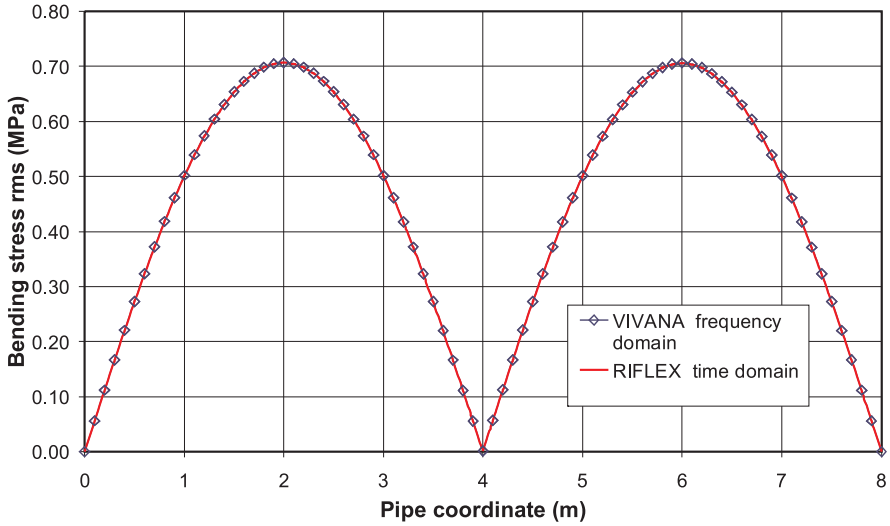

Figure 6.18: Comparison of bending stress, frequency and time domain analysis

Figure 6.19 shows snapshots for the dynamic response from the non-linear analysis. Both cross-flow and axial components are included. Comparisons of rms values for both response components are shown on Figure 6.20. The only difference between time and frequency domain results appears close to the mid-point. Linear theory will describe the oscillation at this point as an oscillation in axial direction only, while non-linear theory will show an elliptic orbit. These effects are

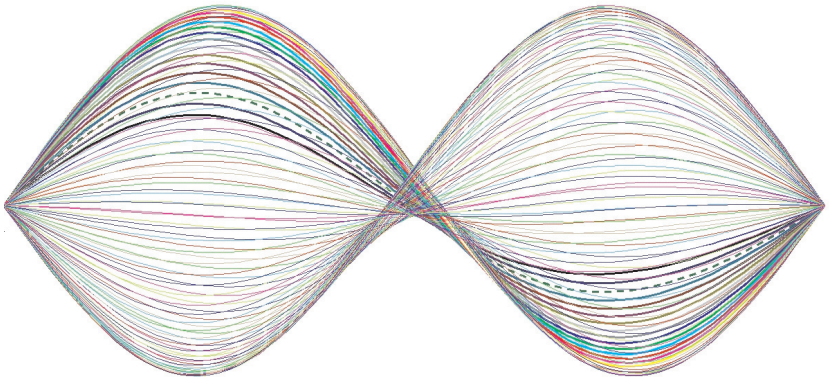

Figure 6.19: Lateral response snapshots, non-linear time domain analysis of pipeline with sag

results of the static geometry and the difference between time and frequency domain results is caused by the asymmetric behaviour of an arch subjected to inwards and outwards displacements. This asymmetry can not be found from linear theory.

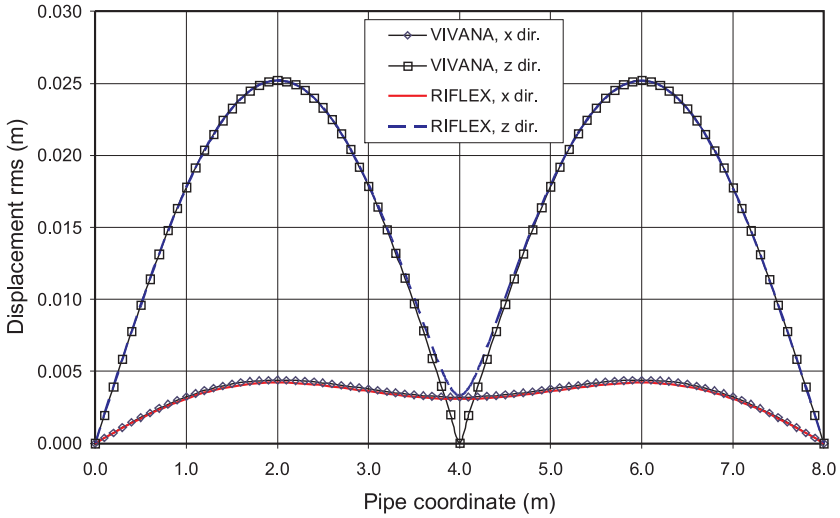

Figure 6.20: Comparison of displacements, frequency and time domain analysis

Figure 6.21 presents the rms values of bending stresses. The overall picture shows a good agreement, but some difference is seen close to the midpoint, which of course is a consequence of the difference between the displacements in this zone. The main conclusion from these analyses is that the software system behaves as intended. Linear and non-linear methods give identical results for a linear system, and the non-linear method can capture non-linear effects.

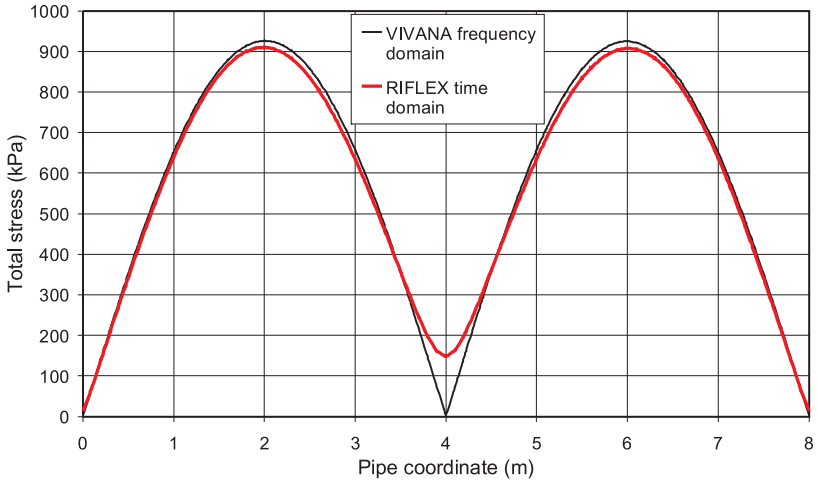

Figure 6.21: Comparison of axial + bending stress, frequency and time domain analysis

6.5.2 Realistic model with varying bottom profiles

Key data for the offshore pipeline model are given in Table 6.5.

The pipeline model is 380 m long, but the length of the free span will depend on the bottom geometry. All analyzed cases in this study had free spans of approximately 100 m long. Hence, pipe sections at shoulders have been longer than the free span itself. This is needed in order to obtain realistic boundary conditions for the pipe.

Different bottom profiles have been applied in order to show the difference in the results from linear and nonlinear analysis. Based on these bottom profiles, different cases have been carried out. Figure 6.22 shows three different bottom profiles that

PIPE PROPERTIES			
Length	L	380.0	m
External diameter	D	0.55	m
Axial stiffness	AE	8.2E+06	kN
Bending stiffness	EI	2.9E+05	$kN.m^2$
Mass per unit length	m	315	kg/m
Effective weight	w	0.7	kN/m
End tension	T	750	N
Current speed	C	0.7	m/s
Bottom stiffness - Hard bottom	k	400	kN/m^2
Bottom stiffness - Soft bottom	k	40	kN/m^2

Table 6.5: Data for offshore pipeline model

have been applied in this study. The radius of curvature at the shoulders is seen to decrease from Case 1 to 3.

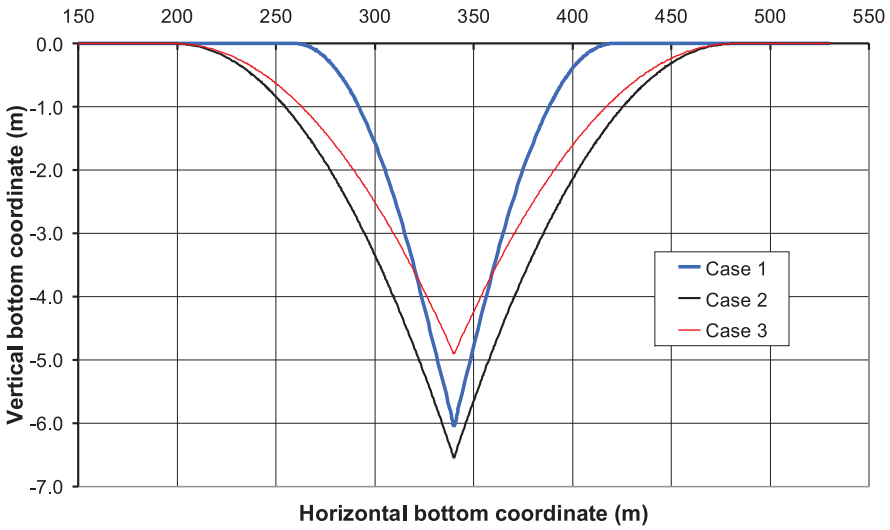

Figure 6.22: Bottom profiles for case study

It is possible to indicate the sensitivity to varying boundary conditions when performing free span analyses by varying the bottom geometry. For each case, a linear and a nonlinear dynamic RIFLEX analysis is performed. The load condition during

these simulations has been equal for both the linear and nonlinear model. The simulations have been performed in time domain analysis format recently implemented in RIFLEX.

The response has been dominated by the fundamental cross-flow mode for all analyzed cases. Figure 6.23 shows a typical distribution for the lift coefficient along the pipe. Referring to Figure 3.9 it is seen that $C_{L,0}$ is 0.24 and found at the shoulders, while 0.35 is the maximum C_L value. The response amplitude is seen to exceed $(A/D)_0$ at the mid segment of the pipe. This is seen to give a negative lift coefficient and hence contribute to hydrodynamic damping. Note that this lift coefficient distribution is found for the actual value of the non-dimensional frequency, see Figure 3.10.

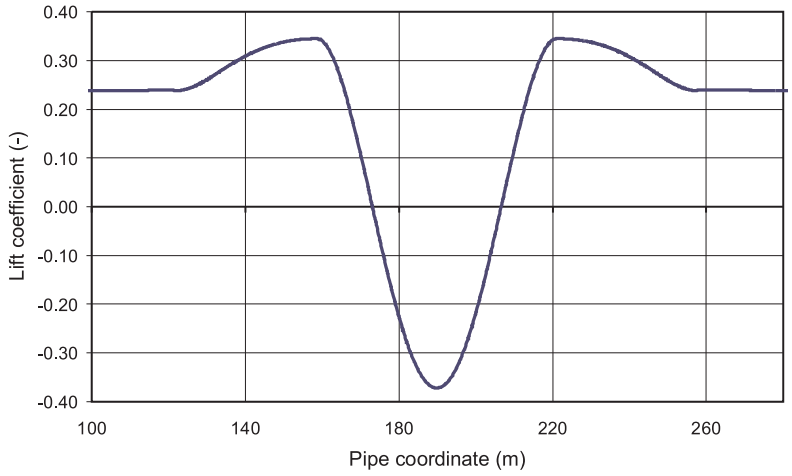

Figure 6.23: Lift coefficient distribution along the free spanning pipeline

Figure 6.24 and Figure 6.25 illustrate the difference between pipe deformations at the shoulders as computed from linear and non-linear methods. A perfect symmetric response is seen for the linear case. The pipe is linked to the bottom by linear springs at nodes with contact in the static condition. Nodes without static contact will never come into contact with the bottom in a linear analysis.

Consequently, a free node may have a large penetration into the seafloor without meeting any stiffness, and a node with bottom contact will not be able to lift off. The result is large tension forces in some springs and large curvature in the pipe where bottom springs should have been introduced. This behaviour is in contrast

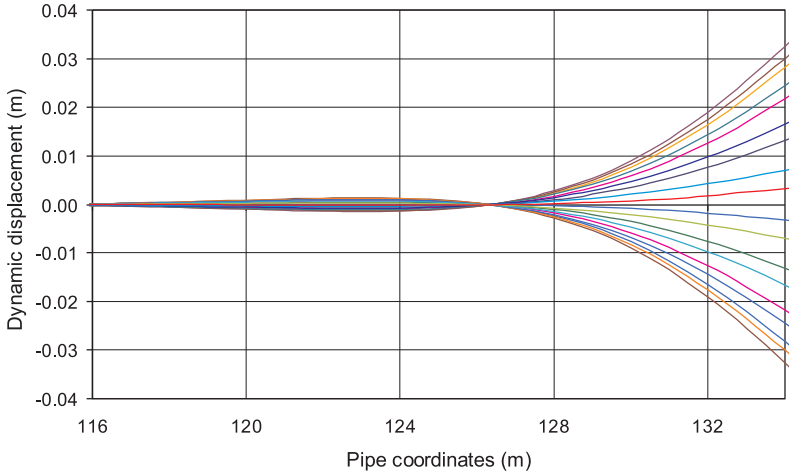

Figure 6.24: Snapshots of dynamic response at shoulder, linear frequency domain

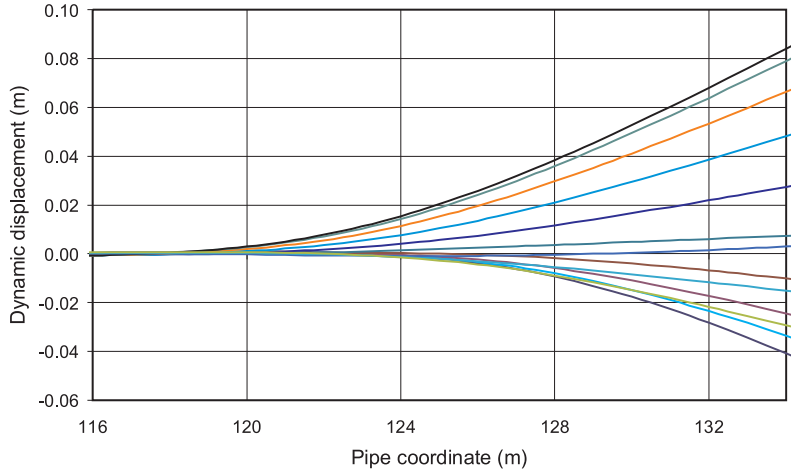

Figure 6.25: Snapshots of dynamic response at shoulder, non-linear time domain

to the result form non-linear time domain analysis. It is easily seen from Figure 6.25 that uplifting takes place and that pipe deformations will follow the bottom profile.

Refereing to Figure 6.22, it is seen that the radius of curvature at the shoulders is decrease from Case 1 to 3. This will influence the interaction between the bottom and the pipe. The touch-down point will tend to move a longer distance for larger radius of curvature. Hence, non-linear effects must therefore be expected to be more pronounced for case 3 than case 2 and 1.

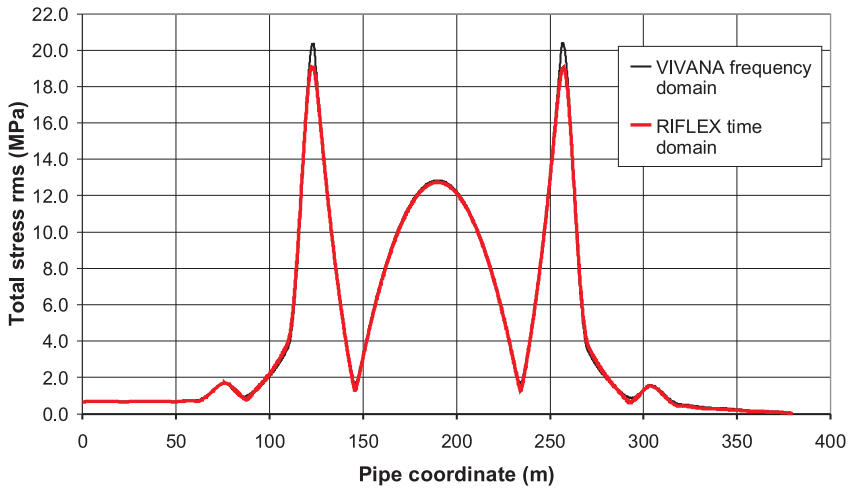

Figure 6.26: Comparison of stresses, bottom profile 1

Results from the analyses are presented in Figure 6.26, 6.27 and 6.28 in terms of RMS values for axial plus bending stresses from both analysis methods. The large peaks are caused by the interaction forces at the shoulders and are seen to be significantly influenced by non-linearities. The difference between linear and non-linear analyses is seen to be larger for case 3 than the other cases, cfr. Larsen et.al. (2005).

Figure 6.29 illustrates the influence from bottom stiffness. The stiffness is reduced from 400 kN/m^2 to 40 kN/m^2, which means that the static penetration for the actual pipe is increased from 0.002 to 0.02 m. Bottom profile 1 is applied, and the result can hence be compared to Figure 6.26. The softer bottom is seen to give a significant stress reduction at the shoulders, and the difference between linear and non-linear analysis is seen to be slightly reduced.

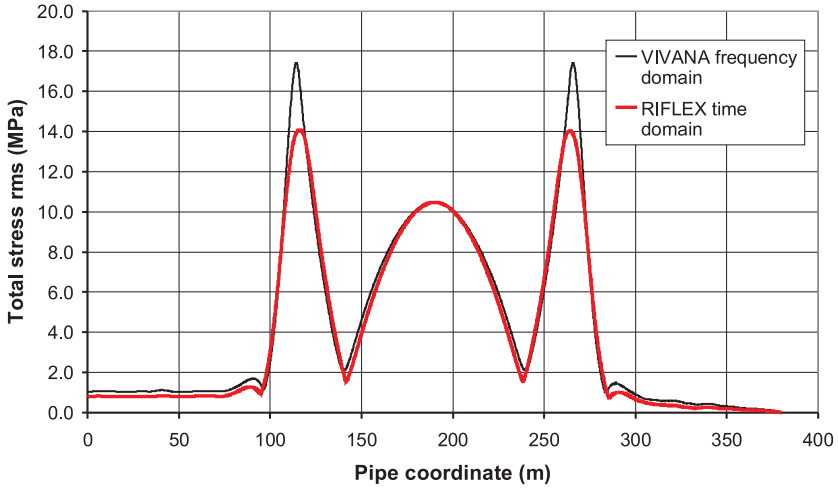

Figure 6.27: Comparison of stresses, bottom profile 2

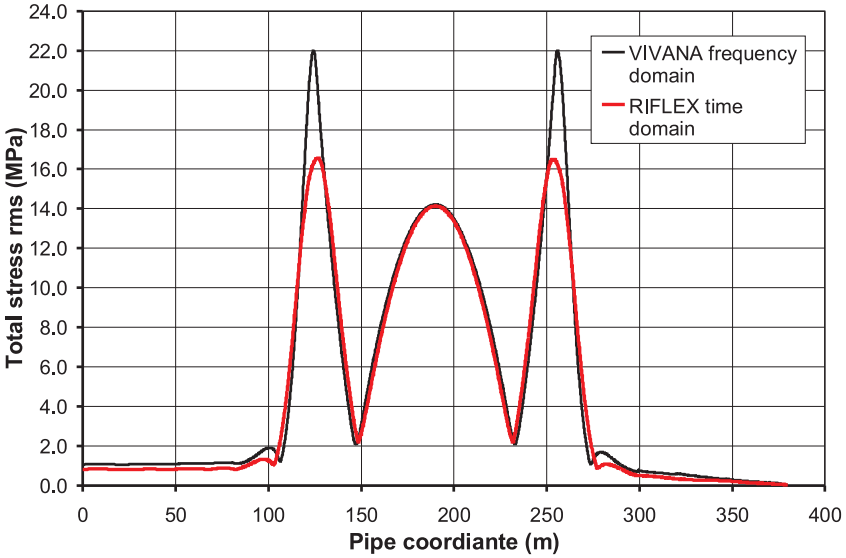

Figure 6.28: Comparison of stresses, bottom profile 3

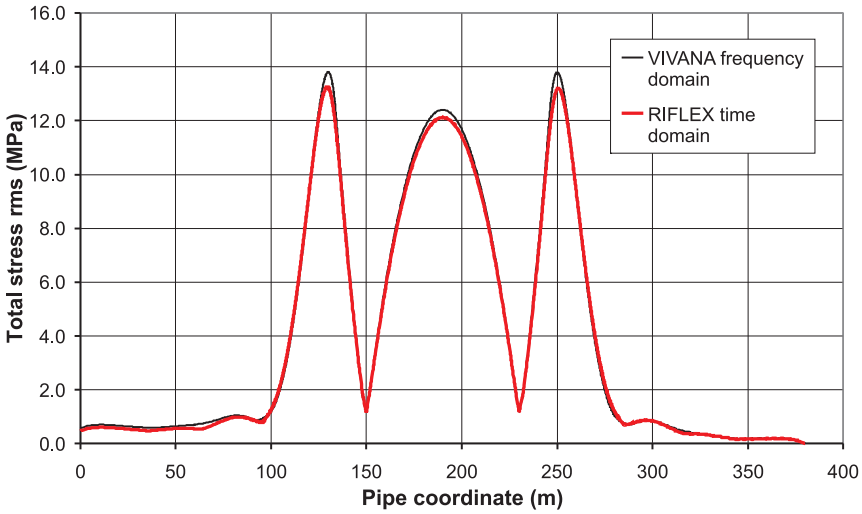

Figure 6.29: Comparison of stresses, bottom profile 1, soft clay

6.5.3 Realistic model with varying pipe weights

Following the last section in order to show the difference between the non-linear to linear analyses for free span pipelines, in this section the attempt has been made to investigate the differences caused by pipe weight variation. According to this, the same pipeline as the last section with bottom profile 3 was chosen (see Figure 6.22). The original weight of pipeline is 314 Kg/m. Time domain analyses have been performed with increasing and decreasing of the original pipeline weight by 2% in order that the pipeline weight varies from 301 Kg/m to 339 Kg/m.

Figures 6.30 to 6.36 show the comparison of the results performed by time domain and frequency domain analyses on the pipeline with different weights.

The difference between the total stress RMS is presented in Figure 6.30 for the pipeline with 301 Kg/m weight considering axial plus bending stresses. The amount of this stress at the mid span is the same for both analysis methods, meaning that the hydrodynamic parameters correctly transferred from VIVANA to RIFLEX. The difference can be seen at the shoulders where the total stress RMS is 18.2 MPa for linear analysis compare to 13.9 MPa for non-linear analysis. This significant difference is due to non-linearities which already explained in the last section.

The influence of the weight variation on the non-linearity effect can be seen in

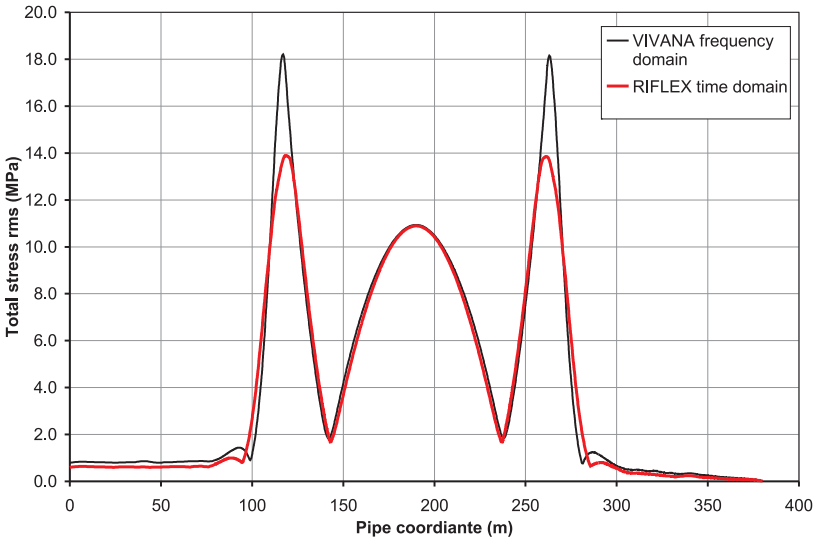

Figure 6.30: Comparison of stresses, $\bar{M} = 301 Kg/m$

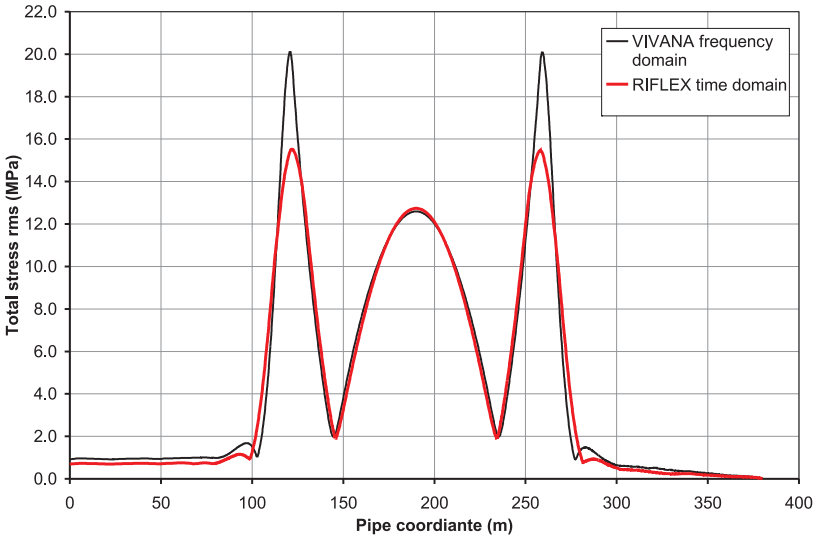

Figure 6.31: Comparison of stresses, $\bar{M} = 307 Kg/m$

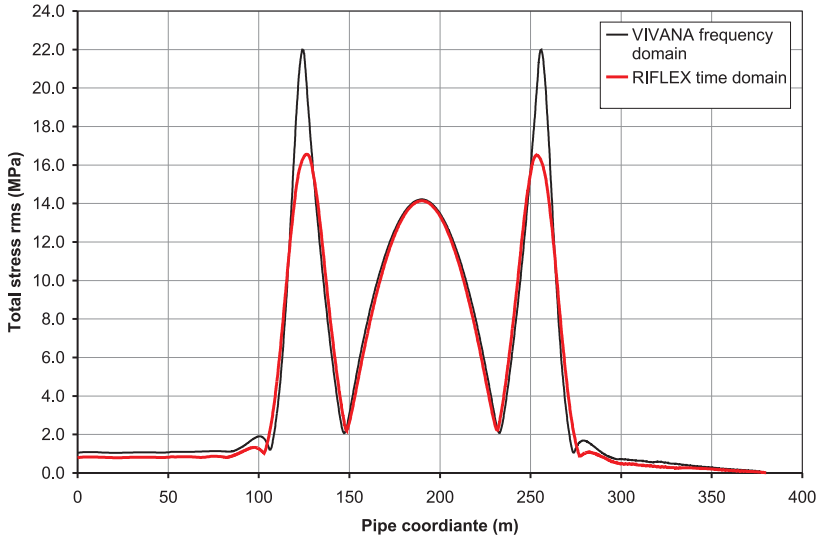

Figure 6.32: Comparison of stresses, $\bar{M} = 314Kg/m$

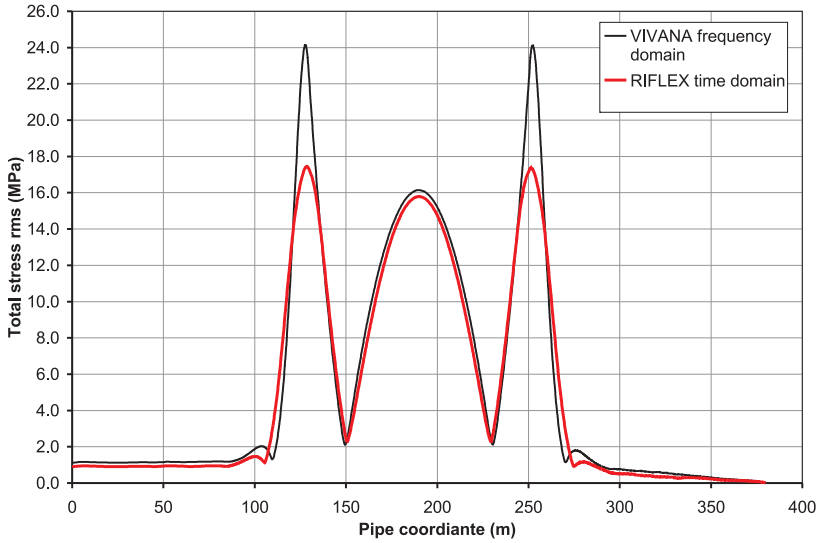

Figure 6.33: Comparison of stresses, $\bar{M} = 320Kg/m$

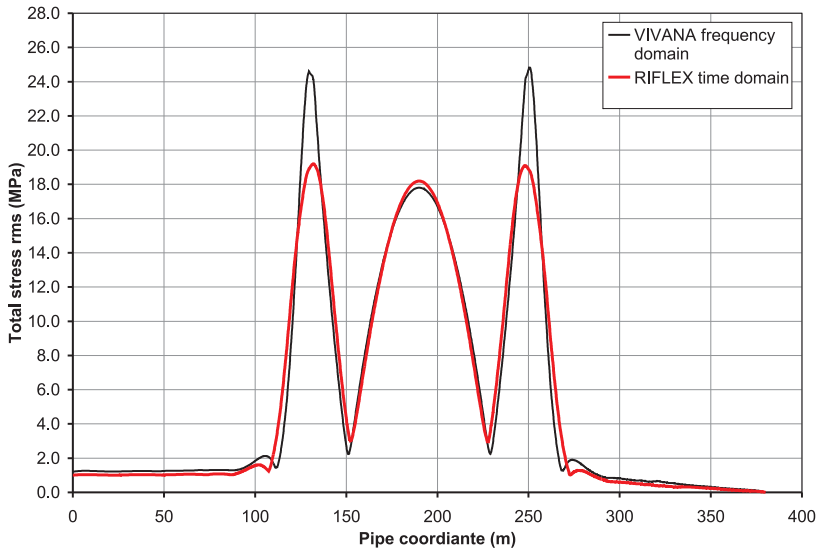

Figure 6.34: Comparison of stresses, $\bar{M} = 327Kg/m$

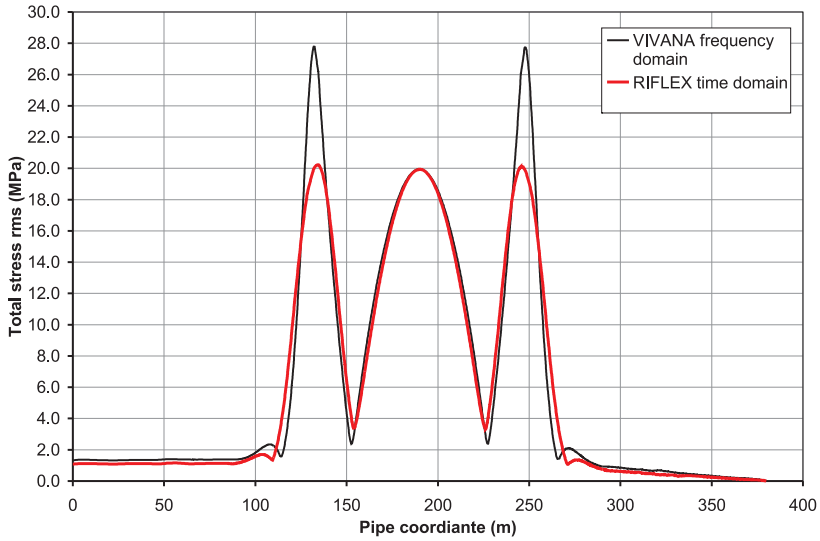

Figure 6.35: Comparison of stresses, $\bar{M} = 333Kg/m$

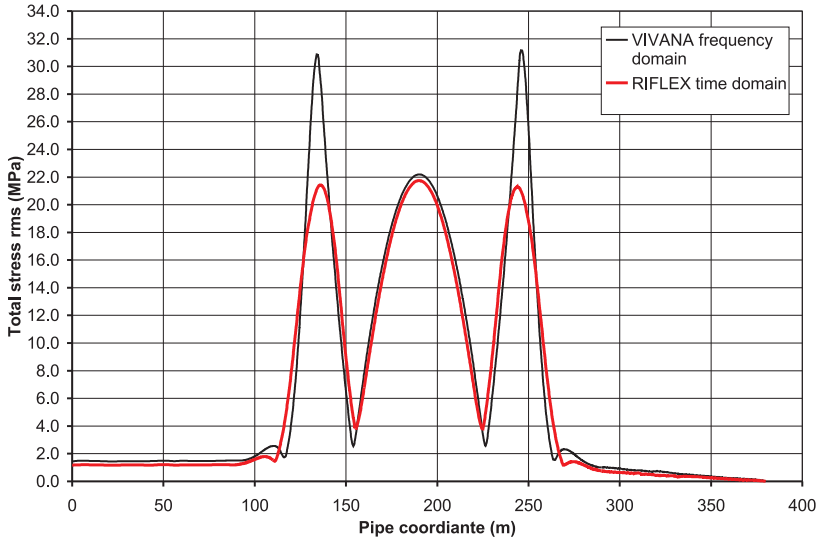

Figure 6.36: Comparison of stresses, $\bar{M} = 339 Kg/m$

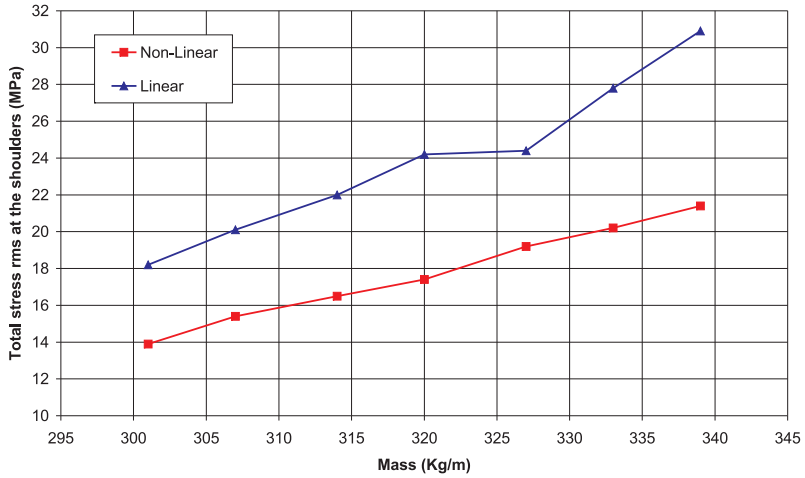

Figure 6.37: Comparison of stresses with varying weights

Figure 6.37. The maximum difference is seen when weight of the pipeline is 339 Kg/m (see also Figure 6.36). In this figure RMS value is given 30.9 MPa by VI-

VANA frequency domain analysis, whereas this value is 21.4 MPa by RIFLEX. The difference as shown in Figure 6.37 is 9.5 MPa presenting 58 % higher in RMS value than in the pipeline which we chose as an original with 314 Kg/m weight (see Figure 6.32).

6.5.4 Realistic model with varying pipe areas

In this section the investigation is continued to compare linear and non-linear analysis methods by changing the area of the pipeline.

The pipe model is the same as the pipeline described in Table 6.5, the only parameter changed is the external diameter of the pipe. The new outer diameter is 516 mm. As the last section, the bottom profile 3 is chosen (see Figure 6.22). The weight of the pipeline is 314 Kg/m.

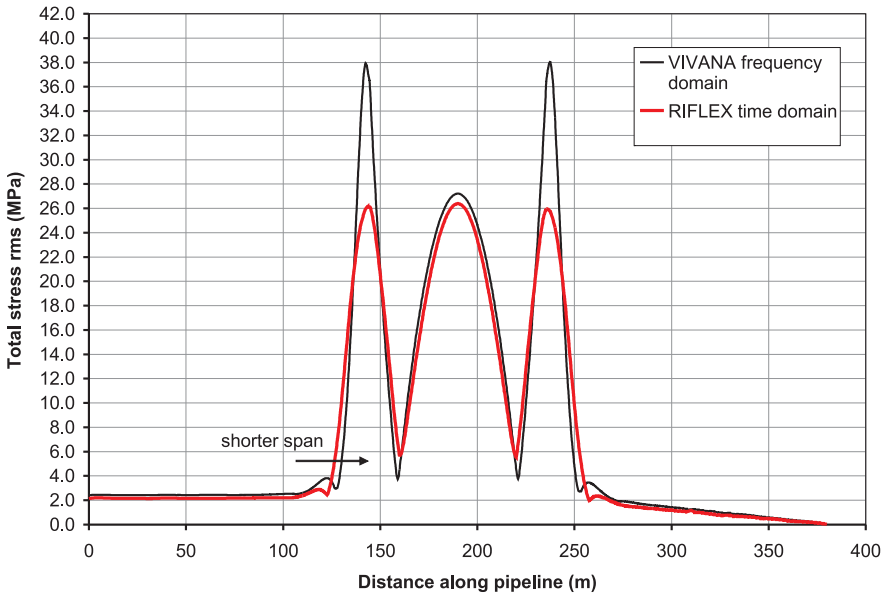

Figure 6.38: Comparison of stresses, D=516 mm

Figure 6.38 illustrates results of both time domain and frequency domain analyses. As seen in the figure, the difference between two methods is even more significant than previous. At the shoulders, the RMS value is 37.8 MPa by time domain

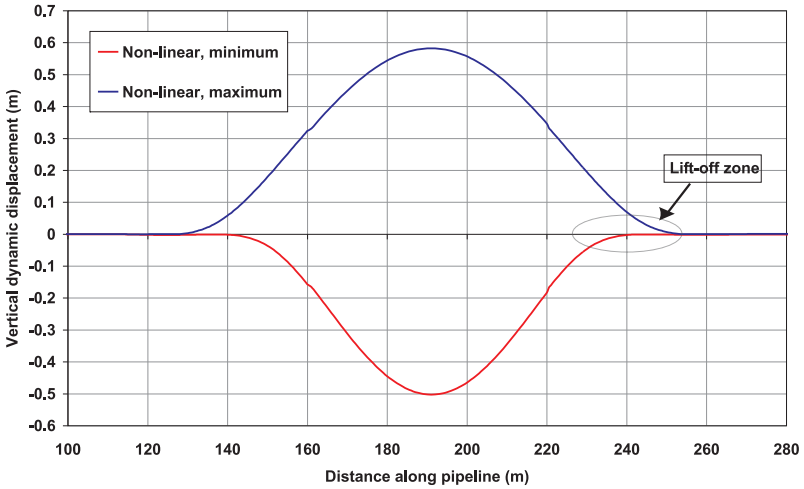

Figure 6.39: Dynamical displacement versus distance along pipeline

analysis compare to 26 MPa by frequency domain presenting 11.8 MPa difference. The reason may be that the pipe with less area gets lighter and less stiff and those make the pipeline to be laid more smoothly on the bottom profile. This increases non-linear effects. In the other meaning, the free span length gets shorter compare to other cases and it causes more pipe/soil interaction as well as more penetration at the shoulders and then in consequence, higher non-linearities.

The non-linear effect is illustrated more in Figure 6.39. This figure shows envelope curves (maximum and minimum vertical displacements records during one regular wave cycle) for the pipeline. It is seen that the non-linear model gives a strongly asymmetric solution. Nodes at the shoulders that have bottom contact and therefore also a spring attached at static equilibrium are able to lift off and have large vertical displacements since the spring will be released if tension is observed. On the other hand, no nodes are able to penetrate since springs will be introduced as soon as new contact is obtained. Computed stress will of course also be significantly different from the two different analyses.

Figures 6.40 to 6.42 show lift coefficient, mode frequency and VIV response amplitude for the pipeline.

Figure 6.40 shows the lift coefficient distribution along the pipe. Refereing to Figure 3.9, in this figure $C_{L,0}$ is 0.326 and found at the shoulders, while maximum C_L value is 0.644. There is seen a negative lift coefficient at the mid span of the

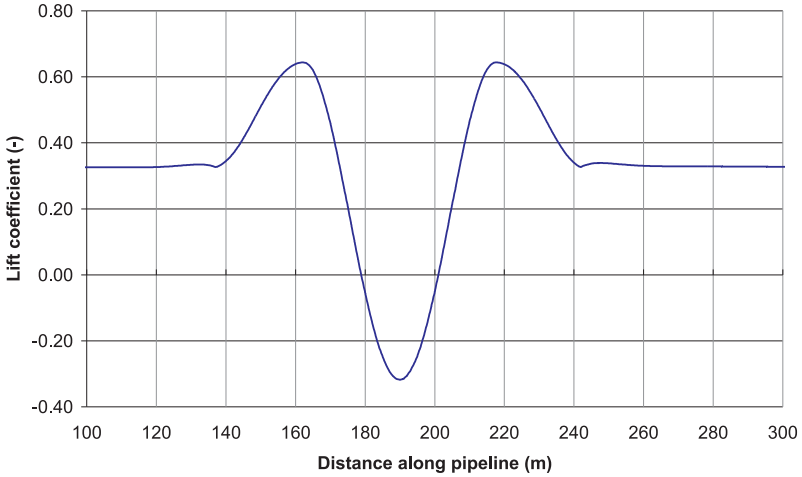

Figure 6.40: Lift coefficient distribution along the free span pipeline

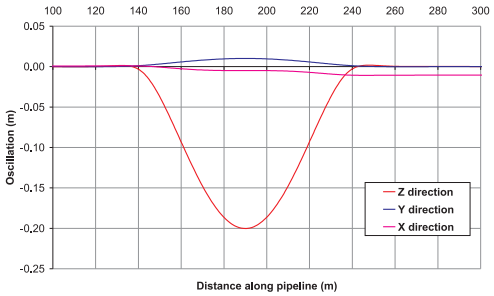

Figure 6.41: The first mode frequency along the span of pipeline

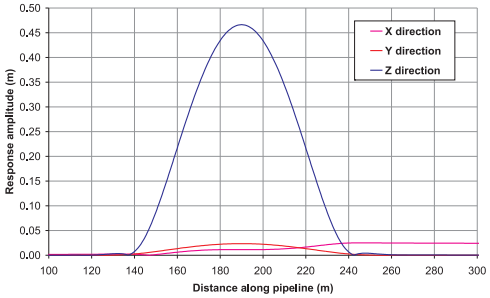

Figure 6.42: VIV response frequency along the span of pipeline

pipe showing that the response amplitude is exceed $(A/D)_0$ and the lift coefficient contributes to hydrodynamic damping.

The dominating first mode shape of the pipe is illustrated in Figure 6.41 for a static condition corresponding to a current speed of 0.7 m/sec for x,y and z directions, where z axes is perpendicular to the horizontal plane xy including current direction and the pipe axes. x is in the direction of the pipe axes and y is perpendicular to x axes.

Figure 6.42 shows the response amplitude for the pipe. The maximum response for the cross-flow direction is seen to be 0.466 m. Note that VIVANA only is capable to calculate the response for the cross-flow and not for the in-line, but one may note that the response in cross-flow direction may also have component on x and y axes.

6.5.5 Influence from axial tension variation on VIV

Following the last sections, the influence from variation of axial tension on non-linear time domain analysis has been investigated.

The key data for the pipe model is given in Table 6.6. The outer diameter of

Pipe properties			
Length	L	380.0	m
External diameter	D	0.516	m
Axial stiffness	AE	8.2E+06	kN
Bending stiffness	EI	2.9E+05	$kN.m^2$
Mass per unit length	m	315	kg/m
Effective weight	w	0.7	kN/m
End tension	T	Varried	N
Current speed	C	0.7	m/s
Bottom stiffness - Hard bottom	k	400	kN/m^2

Table 6.6: Data for offshore pipeline model

the pipe is the same as the previous section. Figure 6.43 to 6.48 are the results from non-linear analyses of the pipeline with applying 6 different axial tensions from 500 to 1000 kN, where each axial tensions increased by 100 kN. The pipe is started to excite when the tension reaches 500 kN. Note that the original pipe tension in the previous sections was 750 kN.

The results are fascinating showing significant differences between linear and non-linear analysis of free span pipeline. The maximum difference seen in Figure 6.43 where tension is 500 kN. The stress RMS is 30.2 MPa for non-linear analysis, while this value is 49.4 MPa for the linear model, means 19.2 MPa difference and showing 39% decrease in RMS value from linear analysis.

Looking at more figures, by increasing of axial tension, the difference decreases but is still significant. The reason is that the pipe with less axial tension has more smoothly and longer contacts with the bottom profile curve and this makes the non-linear effects to be increased. In the other meaning, in linear model, the pipe

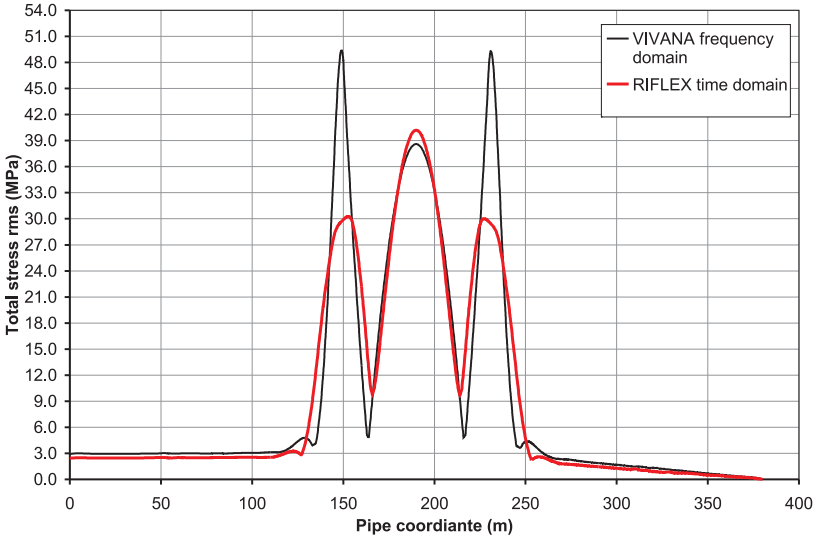

Figure 6.43: Comparison of stresses, T=500 kN

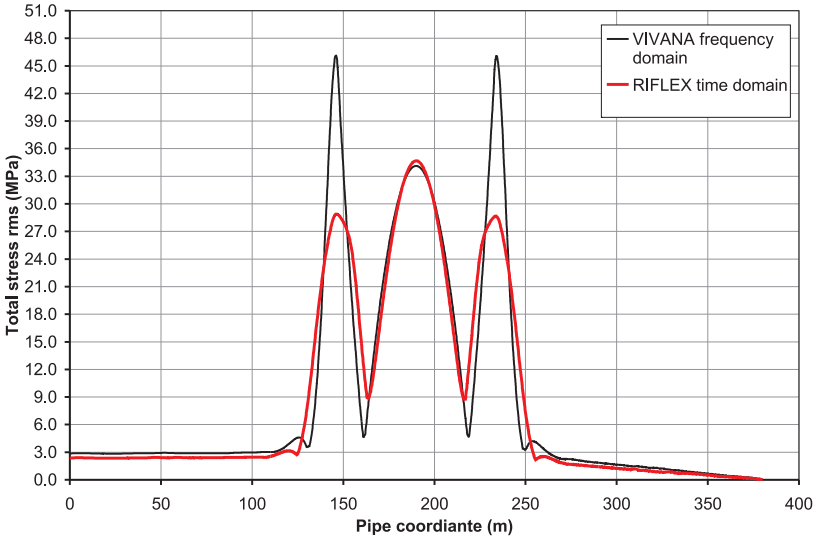

Figure 6.44: Comparison of stresses, T=600 kN

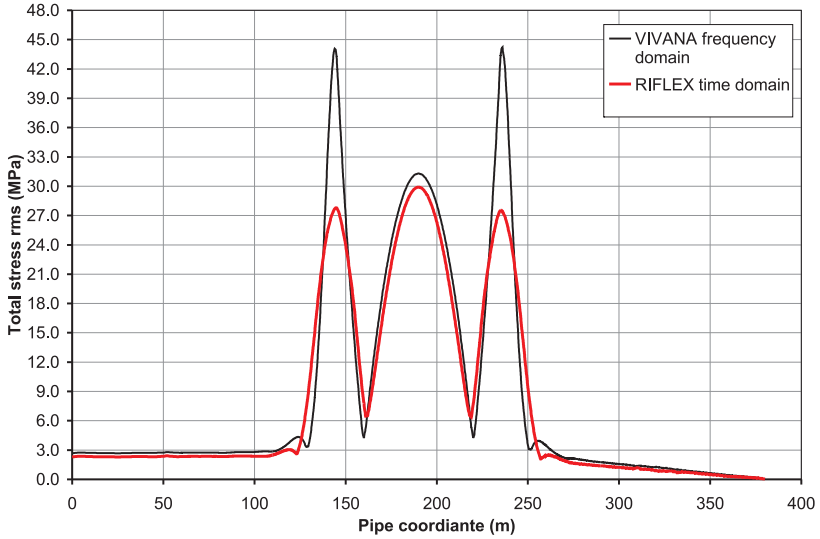

Figure 6.45: Comparison of stresses, T=700 kN

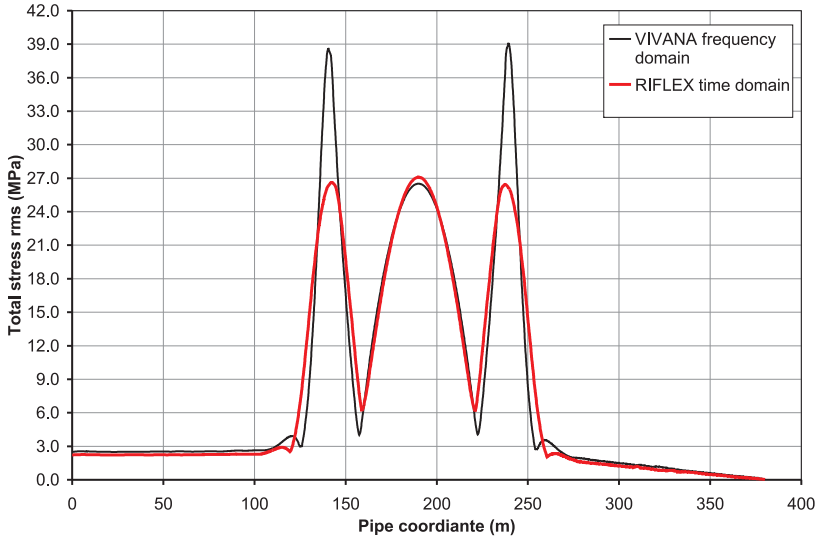

Figure 6.46: Comparison of stresses, T=800 kN

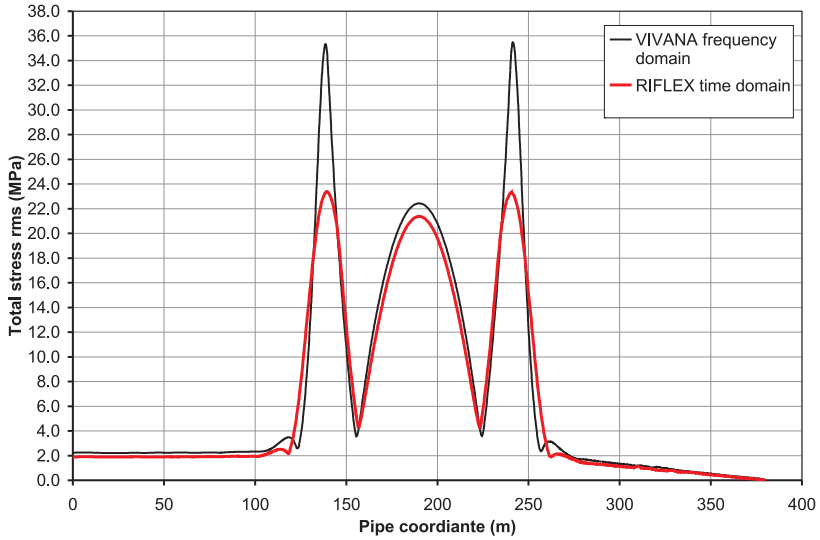

Figure 6.47: Comparison of stresses, T=900 kN

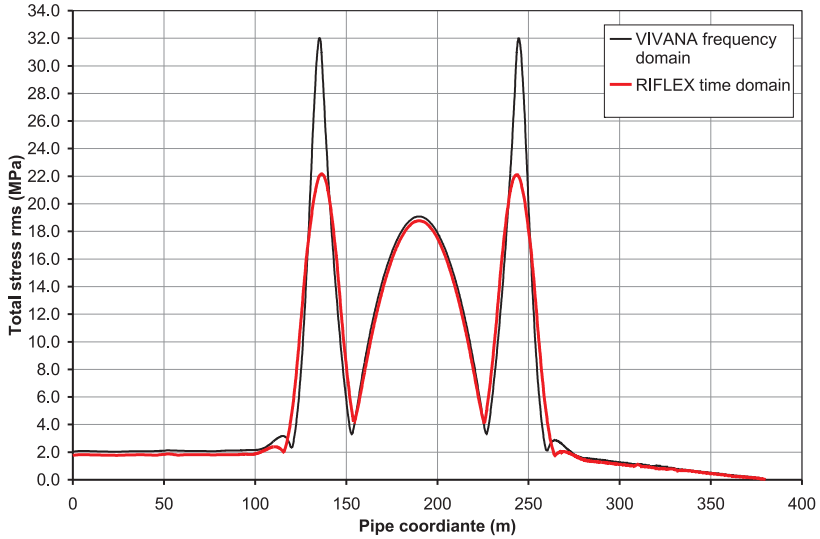

Figure 6.48: Comparison of stresses, T=1000 kN

experiences the soil interaction (i.e. from soil stiffeners) both by penetrating and lifting off from the seafloor, while in the non-linear model the interaction from soil is dispersed when the pipe is lifting off. Longer and smoother the pipe laid on the bottom profile curve, more non-linear effects appear.

Important conclusion from these results is how different can be the behavior of a free span pipeline modeling in linear or non-linear analysis. However, this fact has not been accounted by the guidelines worldwide yet. Free span pipelines can be quite long (i.e. thousands kilometers), therefore efficient analysis of these pipelines are obviously in outmost importance both technically and economically. Further, the above results show the significant difference between stresses caused by VIV at the each end of the span. Since fatigue is high at these points, then the importance of considering this effect is more obvious.

Chapter 7

Summary and future perspectives

An empirical model for prediction of VIV have been applied on the free span pipeline case. Calculation of the static condition is important since this will be the basis for calculation of eigenfrequencies for the pipe.

The model predicts on-set of cross-flow VIV and the transition from one dominating mode to another consistently, but verification from comparisons with experiments are needed.

Damping from pipe/seafloor interaction at the span shoulders should not be introduced as a global (modal) damping parameter since the effect of this damping mechanism is local in its nature and may increase stresses at the shoulders.

The stresses at the shoulders will depend strongly on the local geometry of the bottom profile underneath the pipe. The only way of modeling this interaction in a dynamic analysis is to apply a non-linear formulation.

Axial interaction plays an equally important role. Tuning of linear models may lead to correct prediction of response amplitudes, but over-prediction of bending stresses at the shoulders. The presented model does not represent an ideal solution. The model for added mass and hence also response frequency prediction needs verification. Further work should also be done on interaction between in-line and cross-flow response. Hydrodynamic coefficients for oscillating pipes close to the seafloor are also needed. It is also necessary to study all aspects of pipe/seafloor interaction in order to identify parameters for interaction elements in a finite ele-

ment model.

One way of combining frequency and time domain model has been outlined and a new set of lift coefficients suited for VIV analysis of free span pipelines is proposed. Excitation range and lift coefficients are demonstrated to give results in good agreement with the empirical curve applied by Det Norske Veritas. The potential of the analysis method should be further explored.

An analysis tool for non-linear analysis of free spanning pipelines under VIV conditions has also been applied. The method is based on combined use of frequency and time domain models, and can capture the non-linear interaction between the bottom and the pipeline at the free span shoulders. The results demonstrate that non-linear effects can be significant, in particular for pipelines on a hard and smoothly curved bottom. Pipe properties such as pipe weight and area as well as variation of axial tension play an important role to feature non-linear effects, especially when the pipe is laid on the seafloor with longer and smoother contact at each end of the span.

The results from the time domain analysis with compare to the frequency domain show how important is to consider the difference between the behavior of a free span pipeline modeling in linear or non-linear analysis. However, this fact has not been accounted by the guidelines worldwide yet, e.g. DNV. Pipelines can be quite long (i.e. thousands kilometers), therefore efficient analysis of these pipelines are obviously in outmost importance both technically and economically. Further, the results show the significant difference between stresses caused by VIV at each end of the span. Since fatigue is high at these points, then the importance of taking this effect into account is more obvious.

Bending stresses at the shoulders can be higher or lower than at the mid section of the span, and linear theory will normally over predict these stresses.

The present approach needs tuning of structural damping in time domain in order to obtain the same response as found in frequency domain. This topic should be studied more in detail, and guidelines on how to use the software need to be given. The damping correction is small, and experiments so far indicates that one will always need higher damping in time than in frequency domain.

The analysis method need to be further developed. Work should be done in order to include in-line vibrations both in time and frequency domain. Modeling of damping at the shoulders in a linear analysis needs to be improved by introducing damping elements in all directions, i.e. axial, lateral and vertical. The analysis programs can easily account for such effects, but realistic data must be available in order to produce meaningful results.

The comparison of VIVANA analysis results with MARINTEK experiments rep-

resents that VIVANA predicts the cross-flow response generally much higher than the test measurements, especially for the higher mode responses.

The VIVANA model was tuned to the test model and results are compared in different cases. The analysis results in comparison with tests have been shown while the reference point is tuned by changing various hydrodynamic properties, i.e. C_L, St and added mass. The response frequencies are also tuned to give a better agreement on the results. It can be concluded that the method used by VIVANA is not able to describe VIV for free spanning pipelines adequately. It is not possible to find a set of parameter in a rational way that will give reasonably correct results.

The discrepancy between the analysis and test results are highlighted which confirm the interaction between the in-line and cross-flow vibrations. Discussions are given and addressed on different reasons which may cause this phenomena.

The hydrodynamic parameters used in VIVANA analysis are dependent on the Reynolds/Strouhal number relationship. More experiments should be done to find these parameters in relation with the variation of the other hydrodynamic parameters in VIV condition.

Analyses of a double span pipeline shows that the response of each span might be amplified due to vortex shedding on the adjacent span. This amplification can be illustrated by a transfer energy hypothesis. The amount of the transfer energy between the adjacent span is depending on the relative span length and the relative amplitude of the dominating mode. A more systematic study of the behavior of multiple span pipelines is recommended.

The presented results are found by use of computer programs that are able to model complex geometries and include advanced models for pipe/seafloor interaction. The advantage of using such tools in addition to simplified guidelines in practical design is obvious, but results need to be verified by experiments. This is in particular true for the interaction effect between spans in a multi span pipeline case.

The influence from temperature variation on vortex induced vibrations has also been demonstrated. The response frequency and amplitude is influenced through changes in pipe tension and sag. Both increase and decrease of the response frequency and amplitude may be experienced. A more systematic study on this effect is recommended.

The influence from snaking of the pipe on the temperature effect is significant. This effect should be further investigated for other pipe data and friction models.

Other aspects of VIV for free spanning pipelines has also been studied. This includes the influence from current speed gradients within the boundary layer close

to the bottom, axial force variation for various boundary conditions, and study of response for varying pipe properties and bottom stiffness as well as bottom profile.

The influence of spatial varying current profile on single span and multiple spans is also studied and the importance of considering this influence is illustrated. The results show a significant difference between applying the spatial varying current profile compare to using the uniform current. This is more significant for multiple span pipelines since the tendency of interaction between the neighbor spans can be different.

Bibliography

Anagnostopoulos, P. and Bearman, P. W. (1992). Response characteristics of a vortex-excited cylinder in a uniform stream. *Journal of Fluid and Structures, 8, 367-390.*

Ashley, H. and Havilaud, G. (1950). Bending vibrations of a pipeline containing flowing fluid. *Journal of Applied Mechanics, 17, 229-232.*

Bearman, P. W. (1969). On vortex shedding from a circular cylinder in the critical reynolds number regime. *Journal of Fluid Mech. , Vol. 34, 577-585.*

Bearman, P. W. and Zdravkovich, M. M. (1978). Flow around a circular cylinder near a plane boundary. *Journal of Fluid Mechanics, Vol. 89, 33-47.*

Bishop, R. E. D. and Hassan, A. Y. (1964). The lift and drag forces on a circular cylinder oscillating in a flowing fluid. *Proceeding of the Royal Society of London, Series A 277, 51-75.*

Blasius, H. (1908). *Grenzschichten in Flussigkeiten mit kleiner Reibung.* Z. Math. Phys. vol 56, pp. 1-37.

Blevins, R. D. (1977). *Flow-induced Vibrations.* Van Nostrand Reinhold Company.

Braza, M., Chassaing, P., and Minh, H. H. (1986). Numerical study and physical analysis of the pressure and velocity fields in the near wake of a circular cylinders. *Journal of Fluid Mechanics, 165, 79-130.*

Brika, D. and Laneville, A. (1993). Vortex-induced vibrations of a long flexible circular cylinder. *Journal of Fluid Mechanics, 250, 481-508.*

Bruschi, R., Montesi, M., Tura, F., Vitali, L., and Accerboni, E. (1989). Field tests with pipeline free spans exposed to wave flow and steady current. *OTC-6151, Offshore Technology Conference, Houston.*

Bryndum, M. B., Bonde, C., Smitt, L. W., Tura, F., and Montesi, M. (1989). Long free spans exposed to current and waves; model tests. *OTC-6153, Offshore Technology Conference, Houston.*

Choi, H. S. (2001). Free spanning analysis of offshore pipelines. *Ocean Engineering, 28, 1325-1388.*

Crandall, S. H. (1968). *Dynamics of Mechanical and Electromechanical Systems.* McGraw-Hill, New York, 300-395.

de Silva, W. (2000). *"Vibration Testing", Vibrations: Fundamentals and practice.* CRC press LLC.

Deau, R. B. and Wootton, L. R. (1977). An analysis of vortex shedding problems in offshore engineering. *Report No. 77/14, Atkins Research and Development, Epsom, UK.*

DNV (1981). Rules for submarine pipeline systems. *Det Norske veritas, Appendix A.*

DNV (1991). Enviromental condition and enviromental loads. *Det Norske veritas, Classification Notes No. 30.5.*

DNV (1998). Free spanning pipelines. *Guidelines No. 14, Det Norske Veritas, Høvik.*

DNV (2001). Free spanning pipelines. *Recommended practice DNV-RP-F105, Det Norske Veritas, Høvik.*

DNV (2002). Free spanning pipelines. *Recommended practice DNV-RP-F105, Det Norske Veritas, Høvik.*

DNV (2006). Free spanning pipelines. *Recommended practice DNV-RP-F105, Det Norske Veritas, Høvik.*

Feng, C. C. (1968). *The measurements of vortex-induced effects in flow past stationary and oscillating circular and D-section cylinders.* Masters thesis, University of British Columbia.

Finn, L., Lambrakos, K., and Maher, J. (1999). Time domain prediction of riser viv. *The 4th International Conference on Advances in Riser Technologies.*

Fylling, I., Larsen, C. M., Sødahl, N., Passano, E., Bech, A., Engseth, A. G., Lie, E., and Ormberg, H. (1998). Riflex user's manual. *MARINTEK report, Trondheim.*

Gerrard, J. H. (1966). The mechanics of the formation region of vortices behind bluff bodies. *Journal of Fluid Mechanics, 25, 401-413.*

Gopalkrishnan, R. (1993). *Vortex-Induced Forces on Oscillating Bluff Cylinders.* Msc. thesis, Dept. of Ocean Eng., MIT, And Dept. Applied Ocean Phys. and Eng., WHOI, USA.

Green, R. B. and Gerrand, J. H. (1993). Vorticity measurements in the near wake of a circular cylinder at low Reynolds numbers. *Journal of Fluid Mechanics, 246, 675-691.*

Greenhow, M. and Yanbao, L. (1987). Added masses for circular cylinders near or penetrating fluid boundaries: review, extension and application to water-entry -exit and slamming. *Ocean Engineering 14(4), 325-348.*

Griffin, O. M. (1980). OTEC Cold Water Pipe Design for problems caused by

vortex -excited oscillations. *NRL Memorandum Report 4157, March 14*.

Griffin, O. M. (1985). Vortex shedding from bluff bodies in a shear flow - A review. *Journal of Fluids Engineering, 107, 298-306*.

Griffin, O. M. (1995). A note on bluff body vortex formation. *Journal of Fluid Mechanics, 284, 217-224*.

Griffin, O. M. and Koopmann, G. H. (1977). The vortex-excited lift and reaction forces on resonantly vibrating cylinders. *Journal of Sound and Vibration, 54(3), 435-448*.

Griffin, O. M. and Rambeng, S. E. (1982). Some recent studies of vortex shedding with application to marine tubulars and risers. *Journal of Energy Resources Tech., 104 , 2-13*.

Halse, K. H. (1997). *On vortex shedding and prediction of vortex induced vibration of circular cylinders*. Ph.D. thesis, Faculty of Marine Technology, NTNU, Trondheim.

Halse, K. H. and Larsen, C. M. (1998). Prediction of vortex induced vibrations of a free-spanning pipeline by direct numerical simulation of the flow field. *OMAE98-575, 17th International Conference on Offshore Mechanics and Arctic Engineering, Lisboa*.

Herfjord, K. (1996). *A study on two-dimensional separated flow by a combination of the FEM and Navier-Stokes equations*. Ph.D. thesis, Faculty of Marine Technology, NTNU, Trondheim.

Housher, G. W. (1952). Bending vibrations of a pipeline containing flowing fluid. *Journal of Applied Mechanics, 19, 205-208*.

Huse, E., Nielsen, F. G., and Søreide, T. (2002). Coupling between in-line and transverse viv response. *OMAE2002-28618, 19th International Conference on Offshore Mechanics and Arctic Engineering, Lisboa*.

Ilstad, T., Søreide, T., and Nielsen, F. G. (2005). Fatigue calculations of multimode viv. *The 24th International Conference on Offshore Mechanics and Arctic Engineering, OMAE, Halkidiki, Greece*.

Jensen, B. L., Sumer, B. M., and Fredsøe, J. (1993). Forces on a pipeline oscillating in transverse direction in steady current. *Proceedings of the third International Symposium on Offshore and Polar Engineering (ISOPE), Singapore*.

Kariadakis, G. E. and Triantafyllou, G. S. (1989). Frequency selection and asymptotic states in laminar wakes. *Journal of Fluid Mechanics, 199, 441-469*.

Karman, T. (1912). *Über den Mechanismus des Wider standes den ein bewegfer Körper in einen Flussigheit Erfahrt*. Nachr. Königl, Gesellschaft.

Karniadakis, G. E., Bullister, E. T., and Patera, A. (1985). A spectral element method for solution of the two- and three-dimensional time-dependent in compressible navier-stokes equations. *In proc. Europe-US Conference on Finite Ele-*

ments Methods for Non-linear Problems, 803-817.

Karniadakis, G. E. and Triantafyllou, G. S. (1992). Three-dimensional dynamics and transition to turbulence in the wake of bluff objects. *Journal of Fluid Mechanics, 238, 1-30.*

Kenny, J. P. (1993). Structural analysis of pipeline spans. *Offshore Technology Information, HMSO.*

Keulegan, G. H. and Carpenter, L. H. (1958). Forces on cylinders and plates in an oscillating fluid. *Journal Res., Nat. Bureau Standards , 60, No. 5, 423-440.*

King, R. (1977). A review of vortex shedding research and its application. *Ocean Engineering Vol. 4, 141-171.*

Koushan, K. and Larsen, C. M. (2003). Influence from temperature variation and multiple spans on vortex induced vibrations for free span pipelines. *3rd International Confrenece on Hydroelasticity in Marine technology, Oxford, UK.*

Larsen, C. M. (2000). Empirical viv models. *Invited lecture at Workshop on Vortex Induced Vibrations of Offshore Structures, Sao Paulo.*

Larsen, C. M. (2005). *Vortex induced vibrations (VIV), Fundamental concepts, Simplified model for VIV analysis, VIVANA.* Lecture Notes, NTNU.

Larsen, C. M. and Koushan, K. (2005). Empirical model for the analysis of vortex induced vibrations of free spanning pipelines. *The Sixth European Conference on Structural Dynamics, EURODYN, Paris, France.*

Larsen, C. M., Koushan, K., and Passano, E. (2002). Frequency and time domain analysis of vortex induced vibrations for free span pipelines. *OMAE02-28064, 21st International Conference on Offshore Mechanics and Arctic Engineering, Oslo.*

Larsen, C. M., Passano, E., and Koushan, K. (2004). Non-linear time domain analysis of vortex induced vibrations for free span pipelines. *The 23rd International Conference on Offshore Mechanics and Arctic Engineering, OMAE, Vancouver, Canada.*

Larsen, C. M., Vikestad, K., Yttervik, R., and Passano, E. (2001). Empirical model for analysis of vortex induced vibrations - theoretical background and case studies. *OMAE01-1203, 20th International Conference on Offshore Mechanics and Arctic Engineering, Rio de Janeiro.*

Larsen, C. M., Vikestad, K., Yttervik, R., and Passano, E. (2005). Vivana theory manual. *MARINTEK report, Trondheim.*

Lienhard, I. H. (1966). Synopsis of lift, drag and vortex frequency data for rigid circular cylinders. *Washington State University ,college of Engineering , Research Division Bulletin 300.*

Marchesani, F., Gianfelici, F., Bruschi, R., and Bryndum, M. B. (1995). Response of very long and multi span pipelines in turbulent flows - experimental results.

OMAE 95, 14th International Conf. on Offshore Mechanics and Arctic Engineering, Copenhagen.

Matteelli, R. and Mazzoli, A. (1982). Deep water pipeline : Intervention requirements, before, during and after laying. *Snamprogetti, Italy, OTC 4235.*

Meirovich, L. (2001). *Fundamentals of Vibrations.* McGraw-Hill Higher Education.

Meneghini, J. R. (1993). *Numerical simulation of bluff flow control using a discrete vortex method.* Ph.D thesis , university of London.

Moe, G. and Wu, Z. J. (1990). The lift force on a cylinder vibrating in a current. *Journal of Offshore Mechanics and Arctic Engineering 112, 297-303.*

Monhagen, H. (1980). Fishing gear loads and effects on submarine pipelines. *Proc. 12th Annual Offshore Technology Conference, Houston, Texas, OTC paper 3782.*

Mørk, K. J., Fyrilriv, O., Chezhian, M., Nielsen, F. G., and Søreide, T. (2003). Assessment of viv induced fatigue in long free spanning pipelines. *The 22nd International Conference on Offshore Mechanics and Arctic Engineering, OMAE, Cancun, Mexico.*

Mørk, K. J., Fyrilriv, O., Verley, R., Bryndum, M., and Bruschi, R. (1998). Introduction to the new dnv guideline for free spanning pipelines. *OMAE98-1054, 17th International Conf. on Offshore Mechanics and Arctic Engineering, Lisboa.*

Newman, J. N. (1977). *Marine Hydrodynamics.* The MIT Press, The Massachusetts Institute of Technology.

Nielsen, F. G., Søreide, H. T., and Kvarme, S. O. (2002). Viv response of long free spanning pipelines. *The 21st International Conference on Offshore Mechanics and Arctic Engineering, OMAE, Oslo, Norway.*

Nielsen, F. G. and Søreide, T. H. (2005). Dynamic response of pipeline in long free spans or multi-spans. *The Sixth European Conference on Structural Dynamics, EURODYN, Paris, France.*

NPL (1968). Strouhal number of model stacks free to oscillate. *National Physics Laboratory, NPL Aero Report No.1257.*

Paidoussis, M. P. and Issid, N. T. (1974). Dynamic stability of pipes conveying fluid. *Journal of Sound and Vibration, 33, 267-294.*

Pantazopoulos, M. S. (1994). Vortex induced vibration parameters : Critical review. *In proceeding Of the 13th conference on Offshore Mechanics and Arctic Engineering, 199- 255.*

Prandtl, L. (1904). Über flüssigkeitsbewegung bei sehr kleiner reibung. *Verh. Int. Math. Kongr., 3rd , Heidelberg, 484-91 (also NACA Memo V. 452, 1928-in English).*

Reinertsen (2003). *Ormen Lange Project, Pipeline Engineering, Technical Note, Single and Multispan VIV, Model Test Proposal 2003.* Reinertsen Engineering.

Reynolds, O. (1888). *An experimental investigation of the circumstances Which determine whether the motion of water shall be direct or sinuous and of the law of resistance in parallel channels.* Phil Trans. Roy. Soc., 174, 935-982.

Roshko, A. (1961). Experiments on the flow past a circular cylinder at very high reynolds number. *Journal Fluid Mechanics, Vol. 10 , 345-356.*

Sarpkaya, T. (1977). Inline and transverse forces on cylinders near a wall in oscillatory flow at high reynolds number. *Offshore Tech. Conf . Proceeding , OTC paper no. 2898, Houston, Texas.*

Sarpkaya, T. (1978). Fluid forces on oscillating cylinders. *Journal of Waterway, Port, Costal and Ocean Division, 104(WW4), 275-290.*

Sarpkaya, T. (1979b). Vortex induced oscillations - A selective review. *Journal of Applied Mechanics, 46, 241-258.*

Sarpkaya, T. and Isaacson, M. (1981). Mechanics of wave forces on offshore structures. *Van Nostrand Reinhold Company.*

Schewe, G. (1983). On the force fluctuations acting on a circular cylinder in crossflow about stationary and transversely oscillating circular cylinders. *Technical Report NPS- 69 SL 79011, Naval Postgraduate School, Monterey, CA.*

Schlichting, H. (1987). *Boundary Layer Theory.* 7th ed., New York, NY:McGraw-Hill Book Company.

Schulz, K. W. and Meling, T. S. (2004). Multi-strip numerical analysis for flexible riser response. *23rd International Conference on Offshore Mechanics and Arctic Engineering, OMAE, Vancouver, Canada.*

Schulz, K. W. and Meling, T. S. (2005). Viv analysis of a riser subjected to step and multi-directional currents. *The 24th International Conference on Offshore Mechanics and Arctic Engineering, OMAE, Halkidiki, Greece.*

Sheppard, D. M. and Omar, A. F. (1992). Vortex induced loading on offshore structures : A selective review of experimental work. *In proceeding of the 24th Offshore Technology Conference, Houston, Texas, 103-112, OTC paper no.6817.*

Skaugset, K. B. (2003). *On the suppression of vortex induced vibrations of circular cylinders by radial water jets.* Ph.D. thesis, Department of Marine Technology, NTNU, Trondheim.

Soni, P. K. and Larsen, C. M. (2005). Dynamic interaction between spans in a multi span pipeline subjected to vortex induced vibrations. *The 24th International Conference on Offshore Mechanics and Arctic Engineering, OMAE, Halkidiki, Greece.*

Søreide, T. H., Ilstad, T., Paulsen, G., and Nielsen, F. G. (2005). Dynamic response of pipeline in long free spans or multi-spans. *The Sixth European Conference on Structural Dynamics, EURODYN, Paris, France.*

Soulsby, R. (1997). *Dynamics of marine sands.* Thomas Telford Publication, Lon-

don.

Standards, B. (1993). Code of practice for pipelines. pipelines subsea: design, construction and installation. *BS 8010, British Standard, England*.

Staubli, T. (1983). Calculation of the vibration of an elastically mounted cylinder exposed ta oscillating flow. *In proceeding of the Sixth Int-offshore Mechanics and Arctic Engineering Symposium, Houston, Texas, 165-173*.

Stokes, G. G. (1851). *On the effect of the internal friction of fluids on the motion of pendulums*. Trans. Cambrige Phil. Soc., 9, (II), 8-106.

Strouhal, V. (1978). *Über eine besondere Art der Tonerregung*. Ann. Physik (Leipzig).

Sumer, B. M., Fredsøe, J., and Jensen, B. L. (1994). Forces on vibrating cylinder near wall in current and waves. *Journal of Waterway,Port, Costal and Ocean Engineering, 115(4)*.

Swithenbank, S. B. and Larsen, C. M. (2008). The importance of mode number on in-line amplitude of vortex-induced vibration of flexible cylinder. *The 27th International Conference on Offshore Mechanics and Arctic Engineering, OMAE, Estorli, Portugal*.

Swithenbank, S. B., Vandiver, K., Lie, H., and Larsen, C. M. (2007). Reynolds number dependence of flexible cylinder data. *Journal of Fluid and Structures*.

Traintafyllou, G. S., Triantafyllou, M. S., and Chryssostonids, C. (1986). On the formation of vortex streets behind stationary cylinders. *Journal of Fluid Mechanics, 170, 461-477*.

Tura, F. and Vitali, L. (1990). Non-linear behavior of free spanning pipelines exposed to steady current; model tests and numerical simulations. *EUROMS-90-276, European Offshore Mechanics Symposium, Trondheim*.

Vandiver, J. K. (1993). Dimensionless parameters important to the prediction of vortex induced vibration of long flexible cylinders in ocean currents. *Journal of Fluid and Structures, 7 , 423-455*.

Venugopal, M. (1996). Damping and responses prediction of a flexible cylinder in a current. *Ph.D. Thesis, Department of Ocean Engineering, MIT, USA*.

Vikestad, K. (1998). *Multi-frequency response of a cylinder subjected to vortex shedding and support motions*. Ph.D. thesis, Faculty of Marine Technology, NTNU, Trondheim.

White, F. M. (1991). *Viscous Fluid Flow*. 2nd ed., New York, NY: Mc Graw-Hill Book Company.

Willden, R. H. and Graham, M. R. (2005). Cfd simulations of the vortex-induced vibrations of model riser pipes. *The 24th International Conference on Offshore Mechanics and Arctic Engineering, OMAE, Halkidiki, Greece*.

Williamson, C. H. K. (1985). Sinusoidal flow relative to circular cylinders. *Journal*

of Fluid Mechanics, 155, 141-174.

Williamson, C. H. K. and Roshka, A. (1988). Vortex formation in the wake of an oscillating cylinder. *Journal of Fluid and Structures, 2, 355-381.*

Zdravkovich, M. M. (1981). Review and classification of various aerodynamic and hydrodynamic means for suppressing vortex shedding. *Journal of Wind Engineering and Industrial Aerodynamics , 7, 145-189.*

Appendix A

Allowable span lengths by DNV

For a safe operation of offshore gas or oil pipeline during and after installation, the free span lengths should be maintained within the allowable lengths, which are determined during the design stage. Once a free span longer than the allowable span length occurs, the free span may suffer the vortex-induced vibration (VIV) and consequently suffer the fatigue damages on the pipe due to the wave and current. The vortex shedding phenomenon results in two kinds of periodic forces on a free span of a pipe. Symmetrical vortices are shed when the flow velocity is low. A pipe will start to oscillate in-line with the flow when the vortex shedding frequency is about one-third of the natural frequency of a pipe span. Lock-in occurs when the vortex shedding frequency is half of the natural frequency. As the flow velocity increases further, the cross-flow oscillation begins to occur and the vortex shedding frequency may approach the natural frequency of the pipe span. Amplified responses due to resonance between the vortex shedding frequency and natural frequency of the free span may cause fatigue damage. Thus, the determination of the critical allowable span lengths under the various environments becomes an important part of pipeline design, Choi (2001).

Allowable span lengths are governed by the code limitations regarding maximum allowable stresses and by the onset of vortex shedding criteria. The allowable pipe span lengths can be chosen as the lesser lengths found from the span length criteria of the ANSI code: allowable stress (static), and the DNV code: onset of VIV (dynamic).

Choi (2001) calculated the allowable span length governed by the onset of VIV

and can be referred to for more information.

A.1 Calculation of allowable span lengths

A.1.1 In-line motion

According to the DNV (1981), DNV (1991) and DNV (1998), in-line vortex shedding may occur when $1.0 < U_r < 3.5$ and $K_s < 1.8$. Once the range of the in-line oscillations has been established, based on the upper and lower bound values of U_r, the corresponding pipe spans can be determined. Figure A.3 in the DNV code (1981) is used to obtain the lower bound value of U_r based on K_s for the onset of in-line motion.

The upper bound value of U_r is set at 3.5. The natural frequency of the pipe can then be calculated using the aforementioned relationship. The allowable pipe spans (lower bound values) are then computed by solving for the span length L, the following formula:

$$L = \left(\frac{EI}{m}\right)^{0.25} \left(\frac{CU_rD}{2\pi U}\right)^{0.5} \tag{A.1}$$

where E is the modulus of elasticity, I is the moment of inertia, and C is the end boundary coefficient.

A.1.2 Cross-flow motion

For cross-flow oscillations, vortex shedding may occur when $K_s < 16$ and U_r falls within the range as determined in Figure A.5 in the DNV code. The allowable pipe spans are then determined using the same procedure as Equation A.1 and cross-flow U_r.

A.2 Maximum amplitude of vibration

A.2.1 In-line motion

In-line motion Once the stability parameter is determined, the maximum amplitude of motion can be directly obtained from Figure A.4 in the DNV code (1981).

A.2.2 Cross-flow motion

The maximum amplitude of cross-flow motion can be determined by Figure A.6 in the DNV code (1981). The mode shape parameters are required to get the maximum amplitude of cross-flow motion.

A.2.3 Mode shapes

Free transverse vibration of the Bernoulli-Euler beam is governed by:

$$\frac{d^2}{dx^2}\left(EI\frac{d^2y}{dx^2}\right)+\rho A\frac{d^2y}{dt^2}=0 \tag{A.2}$$

where y is the displacement of the beam and A is the mass per unit length of the beam. Assuming a harmonic motion given by

$$y(x,t)=Y(x)\cos(\omega t-\alpha) \tag{A.3}$$

and substituting Equation A.3 into Equation A.2, one gets the eigenvalue equation:

$$EI\frac{d^4Y}{dx^4}-\rho A\omega^2Y=0 \tag{A.4}$$

On substituting

$$\beta^4=\frac{\rho A\omega^2}{EI} \tag{A.5}$$

the fourth-order differential equation is obtained for a vibration of a uniform beam:

$$\frac{d^4Y}{dx^4}-\beta^4Y=0 \tag{A.6}$$

The general solution of Equation A.6 may be written in the form

$$Y(x)=C_1\sinh\beta x+C_2\cosh\beta x+C_3\sin\beta x+C_4\cos\beta x \tag{A.7}$$

The four constants and β can be obtained using boundary conditions:

Fixed end boundary condition:

$$Y=0,\frac{dY}{dx}=0 \tag{A.8}$$

Pinned end boundary condition:

$$Y=0,\frac{d^2Y}{dx^2}=0 \tag{A.9}$$

Free end boundary condition:

$$\frac{d^2Y}{dx^2} = 0, \frac{d^3Y}{dx^3} = 0 \tag{A.10}$$

The mode shapes for each boundary condition are as follows:

Fixed-free boundary condition:

$$Y(x) = C\{\cosh\beta x - \cos\beta x - K_r(\sinh\beta x - \sin\beta x)\} \tag{A.11}$$

where

$$K_r = \frac{(\cosh\beta L + \cos\beta L)}{(\sinh\beta L + \sin\beta L)} \tag{A.12}$$

Pinned-pinned boundary condition:

$$Y(x) = C\sin\frac{r\pi x}{L} \tag{A.13}$$

Fixed-pinned boundary condition:

$$Y(x) = C\{\cosh\beta x - \cos\beta x) - K_r(\sinh\beta x - \sin\beta x)\} \tag{A.14}$$

where

$$K_r = \frac{(\cosh\beta L - \cos\beta L)}{(\sinh\beta L - \sin\beta L)} \tag{A.15}$$

Fixed-fixed boundary condition:

The equation of motion is the same as Equation A.14, but the different boundary conditions result in a different form of the mode shape.

A.2.4 Mode shape parameter, γ

The mode shape parameter,γ is defined as:

$$\gamma = Y_{max}\left\{\frac{\int_0^L Y^2(x)dx}{\int_0^L Y^4(x)dx}\right\}^{1/2} \tag{A.16}$$

where Y_{max} is the maximum value of the mode shape. Once the mode shape parameter is obtained from Equation A.16, the maximum amplitude of cross-flow motion can be obtained from the DNV code (1981).

Appendix B

Beat Phenomenon

During the investigation about the time domain analysis, in some cases we faced a phenomenon so called *Beating* when the structural damping of the pipeline was set to zero. This phenomenon can be observed in the result of displacement time series, such as the one in Figure B.1.

This figure shows the amplitude variation pattern of the pipeline in terms of time in 400 *sec*. This pattern is repeating itself with a period of 188 *sec*. The model used to show this phenomenon is a pipeline with 144 m span and hinged support at both end.

Beating is a complex phenomenon to be completely explained here. But, it can be said that such a time-varying nature of the response amplitude is a result of the participation of multiple frequencies along the pipeline.

In a more simple definition, when two periodic signals are close in frequency, the sum of the signals exhibits an interference that is sometimes constructive, and sometimes destructive. This results in an oscillation of the amplitude envelope of the sum that has a frequency of the difference of the two initial signals. This low frequency oscillation is termed the beat frequency. There is also another higher beat frequency that has a frequency of the sum of the two initial frequencies, Silva (2000). According to Silva (2000), when two identical single-degree-of-freedom systems are connected by means of a weak spring the resulting two-degree-of-freedom system is characterized by natural frequencies very close in value. The response of such a two-degree-of-freedom system to a certain initial excitation exhibits a phenomenon known as the *beat phenomenon*, whereby the displacement of one mass decreases from some maximum value to zero, while the displacement of the other mass increases from zero to the same maximum value, and then the roles are reversed, with

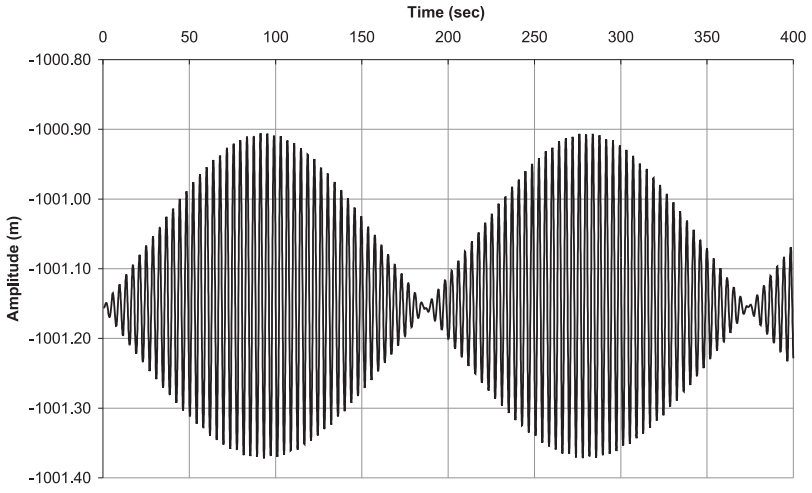

Figure B.1: Beating phenomenon

the pattern repeating itself continuously.

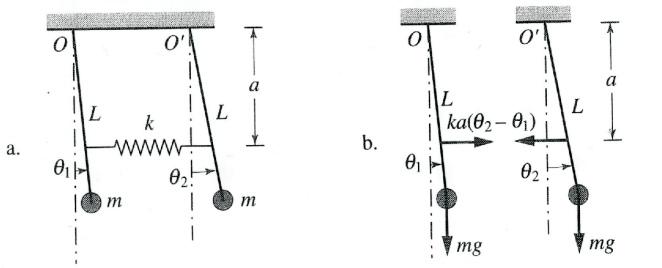

Figure B.2: (a) Two identical pendulums connected by a spring, (b) Free-body diagrams

One of these cases is a system consisting of two identical pendulums connected by a spring (see Figure B.2a). The corresponding free-body diagrams for the two masses are shown in Figure B.2b, in which the assumption of small angles θ_1 and θ_2 is applied. By making the moment equations of pendulums 1 and 2 about the points o and o' and solving the differential equations of motion, the response of the pendulums demonstrated in Figure B.3.

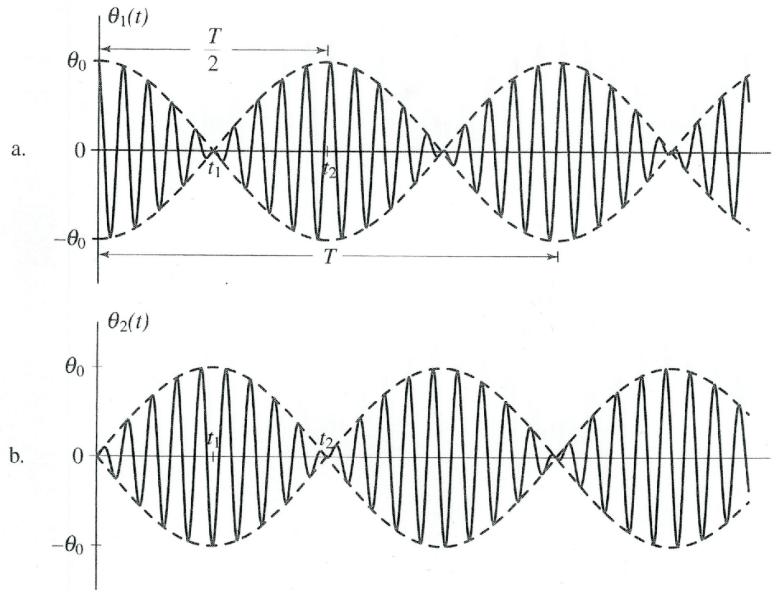

Figure B.3: Response of the pendulums, demonstrating the beat phenomenon, Silva (2000)

Although in our particular case the beat phenomenon results from the weak coupling of two pendulums, the phenomenon is not exclusively associated with two-degree-of-freedom systems. Indeed, the beat phenomenon is purely the result of adding two harmonic functions of equal amplitudes and nearly equal frequencies. For example, the beating phenomenon can occur in twin-engine propeller aircraft if the speed of rotation of the two propellers differs slightly. In this case, the propeller noise grows and admonishes in intensity as the sound waves generated by the two propellers reinforce and cancel each other in turn, Meirovitch (2001).

Another example of a system exhibiting the beat phenomenon is the *amplitude-modulated* cylinder oscillation which in the simplest case is dual-frequency *beating*. It can be expressed in two mathematically ways. One way is a superposition of two sinusoids at different frequencies f_1 and f_2 which can be determined as

$$y(t) = Y_1 \sin(2\pi f_1 t) + Y_2 \sin(2\pi f_2 t) \tag{B.1}$$

The Equation B.1 can be written differently if $Y_1 = Y_2$ as

$$y(t) = 2Y_1 \sin(2\pi f_c t) \cos(2\pi f_m t) \tag{B.2}$$

This Equation is a product of a rapidly varying sinusoid at the *carrier frequency* f_c modulated by a slowly varying sinusoid at the *modulation frequency* f_m.

The relation between the above component in Equations B.1 and B.2 can be determined as

$$f_c = \frac{f_2 + f_1}{2} \tag{B.3}$$

$$f_m = \frac{f_2 - f_1}{2} \tag{B.4}$$

$$f_1 = f_c - f_m \tag{B.5}$$

$$f_2 = f_c + f_m \tag{B.6}$$

The modulation ratio can be expressed as the rate of modulation which is defined here as the ratio of unity to the number of oscillations at the carrier frequency contained in one beat packet. In other meaning if the modulation ratio is equal to 1:N, where N can be defined as

$$N = \frac{f_c}{2f_m} \tag{B.7}$$

Appendix C

Correction of non-dimensional frequency

Gopalkrishnans tests were carried out with a small cylinder. According to the standard curve for Strouhal number as function of Reynolds number, the Strouhal number, St_G, must have been approximately 0.2 for these tests. If we have another Strouhal number and want to apply Gopalkrishnans results, we have to take this into account when calculating the non-dimensional frequency parameter, VIVANA theory manual (2005).

General case: St^*

$$f_v = \frac{St_G \cdot U}{D} \tag{C.1}$$

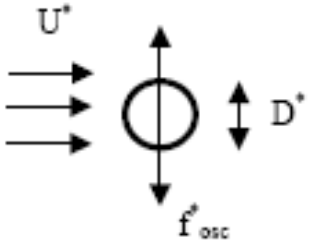

Gopalkrishnans case: St_G

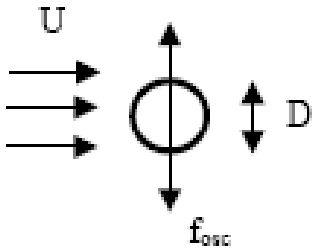

Non-dimensional frequency

$$\hat{f}^* = \frac{f^*_{osc} \cdot D^*}{U^*} \tag{C.2}$$

Vortex shedding frequency

$$f^*_v = \frac{St^* \cdot U^*}{D^*} \tag{C.3}$$

Non-dimensional frequency

$$\hat{f} = \frac{f_{osc} \cdot D}{U} \tag{C.4}$$

The general case is assumed to be equivalent to Gopalkrishnans case if

$$\frac{f^*_{osc}}{f^*_v} = \frac{f_{osc}}{f_v} \tag{C.5}$$

The non-dimensional frequency can now be defined from parameters in the general case:

$$\frac{f^*_{osc}}{\frac{St^* \cdot U^*}{D^*}} = \frac{\frac{\hat{f} \cdot U}{D}}{\frac{St_G \cdot U}{D}} = \frac{\hat{f}}{St_G} \tag{C.6}$$

Hence:

$$\hat{f} = \frac{f^*_{osc} \cdot D^*}{U^*} \cdot \frac{St_G}{St^*} \tag{C.7}$$

By using this definition for the non-dimensional frequency in all operations we can use Gopalkrishnans data directly.

If we calculate the reduced velocity from the standard definition

$$U_R = \frac{U}{f_o \cdot D} \tag{C.8}$$

for a system with Strouhal number = St^* that is different from St_G , and want to compare such values to values obtained from the relation between the added mass and reduced velocity,

$$U_R = \frac{1}{\hat{f}}\sqrt{\frac{\overline{m}+1}{\overline{m}+\frac{C_a}{C_{a0}}}} \tag{C.9}$$

we have to correct U_R in order to take care of the difference in Strouhal number. If we assume that the ratio f_0/f_v should be constant, the correction will be as follows

With standard Strouhal number:

$$\frac{f_0}{f_v} = \frac{\frac{U}{U_R \cdot D}}{\frac{St_G \cdot U}{D}} = \frac{1}{U_R \cdot St_G} \tag{C.10}$$

At a different Strouhal number:

$$\frac{f_0}{f_v} = \frac{1}{U_R^* \cdot St^*} \tag{C.11}$$

We can now define a modified U_R that will give the same ratio. This must be as follows:

$$U_R^* = U_R \cdot \frac{St_G}{St^*} \tag{C.12}$$

By using this definition of the reduced velocity we can compare U_R^* directly to values found from the standard relation between U_R and the non-dimensional frequency in Gopalkrishnans experiments.